Dynamics of Tissue Patterning in *Hydra*

Inauguraldissertation

zur Erlangung der Würde eines Doktors der Philosophie

vorgelegt der Philosophisch-Naturwissenschaftlichen Fakultät

der Universität Basel

von

Jaroslav Ferenc

2022

Originaldokument gespeichert auf dem Dokumentenserver der Universität Basel
https://edoc.unibas.ch

Genehmigt von der Philosophisch-Naturwissenschaftlichen Fakultät auf Antrag von

Prof. Dr. Dirk Schübeler

Dr. Charisios D. Tsiairis

Prof. Dr. Engelbert Hobmayer

Basel, den 14. 12. 2021

Prof. Dr. Marcel Mayor (Dekan)

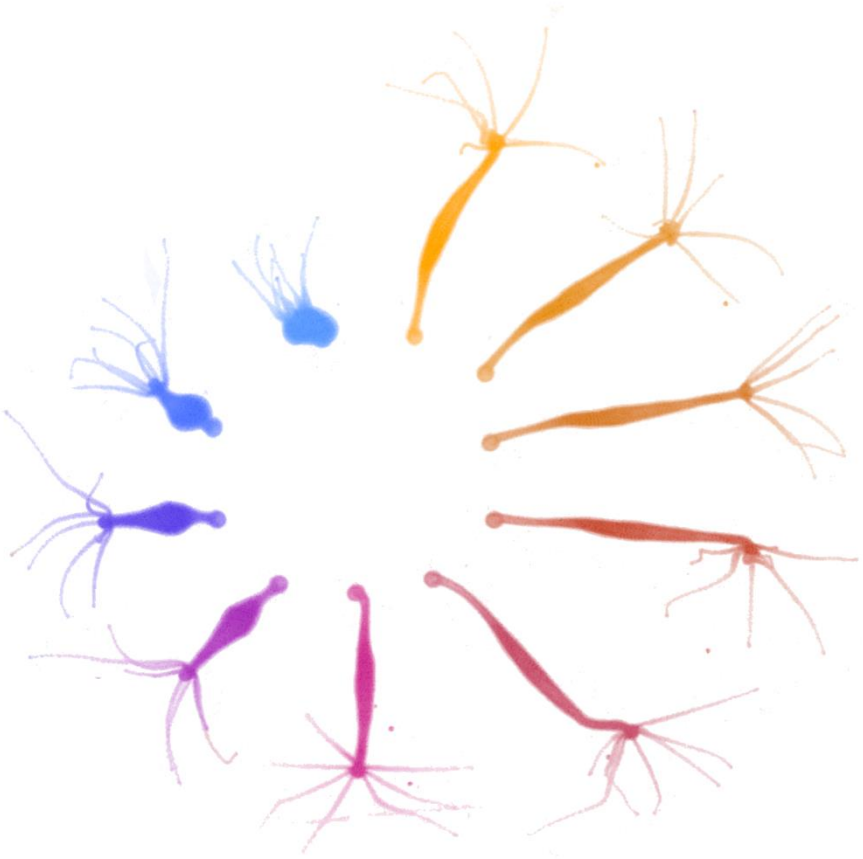

Acknowledgements

When looking for a PhD position at different institutions, I sometimes interviewed with group leaders who seemed to have lost their passion for science long ago. This would manifest as sentences full of fluff in reply to my question about why they are doing science. Thankfully, the person, whose lab I decided to join was very different. "To have fun" he said swiftly, and it was clear that this was indeed the case. After five years in the lab, I can say that that it was (mostly) fun and much more! Therefore, I wish to thank first and foremost Charisios, my advisor. Not only for his visible passion for science but also for being an amazing mentor always ready to brainstorm ideas, discuss results, help with experiments, and yet not micromanaging or forcing his own views and ideas.

Many thanks to the *Hydra* crew in the lab for all their help with experiments, and especially to Jacqueline, our lab manager, for her excellent work to keep the lab running smoothly. I am also very thankful to all the past and present group members for their scientific input on my work and pleasant time together both in and outside of the lab. Special place among them belongs to Giorgos, who became one of my closest friends.

I wish to thank all the members of our technical platforms, whose outstanding support makes doing science in the FMI a very smooth and enjoyable experience. Pan for his invaluable help with data analysis and Iskra for performing all the many *Hydra* electroporations. Throughout my doctoral work I have also relied heavily on all the members of the genomics and imaging facilities – without them obtaining a large part of the presented data would have been much more difficult. I am thankful for all the constructive feedback received during the thesis committee meetings, as well as during joint lab meetings with the Liberali and Grosshans Labs.

I would also like to thank my previous teachers who nourished my scientific curiosity. A special thanks goes to all my friends, particularly those whom I met in Basel and who made the last five years so enjoyable.

Na záver patrí veľké „ďakujem" mojím rodičom a babke, ktorí ma vždy podporovali a tešili sa z mojich úspechov.

Summary

In this work we explored regeneration and homeostatic body patterning of the simple cnidarian *Hydra*. Thanks to its evolutionary position, this animal is well suited to identify cellular and molecular mechanisms of tissue organization conserved among metazoans.

In the first part, we used regenerating *Hydra* tissue spheroids as a model for understanding how mechanical signals affect cellular self-organization and tissue patterning. In this system, the specification of missing body parts is accompanied by tissue stretching generated through periodic osmotically driven inflation and deflation cycles. However, their role in regeneration was not known. We found that these oscillations are not only accompanying but required for successful symmetry breaking and regeneration. The data also indicated that the cellular readout is continuous rather than cyclic as the spheroids did not seem to have a mechanism for counting the oscillations. We identified this readout to be the transcription of a key organizer-defining factor *Wnt3*, which is quantitatively related to the overall amount of tissue stretching experienced by the spheroid. Moreover, when supplied externally, Wnt3 enables successful regeneration without mechanical stimulation. Beyond elucidating the role of mechanical oscillations for *Hydra* regeneration, the work points out a potentially conserved mechanism for translating mechanical stretching into chemical signals. Since tissue stretching also triggers the expression of Wnt ligands in in various developmental contexts in vertebrates, it can represent a conserved feature of this signaling pathway.

The second part used unbiased approaches to identify factors downstream of the Wnt organizer, regulating the differentiated cell identities. This led to the discovery of a conserved zinc-finger transcription factor Zic4 to be a crucial cell fate regulator in *Hydra*. Upon its knockdown, tentacle battery cells transdifferentiate to the basal disk cells, likely in a cell-cycle dependent manner. These findings suggested a possible general framework for the connection of fate specification and axial position of epithelial cells in the *Hydra* body. We also explored new strategies to find new small molecules, such as metabolites, involved in patterning and discuss one putative example.

Table of Contents

Acknowledgements I
Summary III
Prologue 7

I. Introduction
I.1. How to Make Tissues and Bodies 8
I.1.1. Mechanical Clues 10
I.1.2. Biochemical Signals 11
I.1.3. Epithelial Lumens: Hubs of Mechanochemical Crosstalk 13
I.2. *Hydra* as a Model of Tissue Patterning 16
I.2.1. Self-Organization of *Hydra* Cells 18
I.2.2. Wnt Signaling and Organizing Centers 19
I.2.3. Axial Patterning in *Hydra*: Gierer-Meinhard Model and Beyond 21
I.2.4. Stem Cells and Differentiation in *Hydra* 24
I.3. Outstanding Questions and Scope of this Work 28

II. Results and Discussion
II.1. Mechanical Oscillations during *Hydra* Regeneration 29
II.1.1. Mechanical Oscillations Orchestrate Axial Patterning through Wnt Activation in Hydra (accepted manuscript) 29
II.1.2. β-catenin as a Potential Link between Wnt Signaling and Tissue Stretching 75
II.1.3. Wnt3 Promoter Analysis to Uncover Candidate Mechanoresponsive Transcription Factors 79
II.1.4. Discussion 82
II.2. Body Patterning in Homeostatic *Hydra* 87
II.2.1. Positional RNA-sequencing to Uncover Downstream Effectors of Wnt Signaling Involved in Body Patterning 87
II.2.2. Zic4, a Key Regulator of Epithelial Differentiation 90
II.2.3. Using Mass-spectrometry Imaging to Identify Small Molecules Potentially Involved in Patterning 100
II.2.4. Discussion 102

III. Material and Methods
III.1. Studying Mechanical Oscillations during Whole Body Regeneration in *Hydra* (book chapter in press) 107
III.2. Additional Methods 123

Epilogue 129

Appendices

1. Alignment of *Wnt3* promoter sequences from the wild type 105 and *reg-16 Hydra* strains 130
2. Predicted transcription factor binding sites in the *Wnt3* promoter affected by the mutations found in the *reg-16* strain 132
3. Genes up- and downregulated in the original tentacles upon *Zic4* and/or *Sp5* knockdown 133
4. Functional annotation of genes from Appendix 3 135

References and Abbreviations

References 138
Abbreviations 150

Curriculum vitae 151

Prologue

Music of Chances

When I hear what we call music, it seems to me that someone is talking… But when I hear traffic, I have the feeling that sound is acting. And I love the activity of sound. I don't need sound to talk to me… In my music nothing takes place but sounds: those that are notated and those that are not. Those that are not notated appear in the written music as silences, opening the doors of the music to the sounds that happen to be in the environment. John Cage

The most amazing thing about mammalian development is not that it sometimes goes wrong, but that it ever succeeds Veronica van Heyningen

The American experimental composer John Cage is probably best known for his controversial work for any instrument and any number of players, named 4'33". That is 4 minutes and 33 seconds of silence. Or, as he would like us to view it, 4 minutes and 33 seconds of allowing sounds to express themselves. Here, ambient sounds are supplemented by the expectant audience coughing, chatting, and laughing as they wait for the performer to start playing. However, Cage also realized that "composing" silence of different durations would be pointless and tried to find other means of forcing his listeners to pay attention to the sounds themselves rather than their organization. For example, by eliminating traditional organization from his music. He would compose short snippets of melodies and then arrange them with the help of random processes – coin tosses, or randomness simulators. Using these "chance operations" he created pieces that others have called music of chances.

Surely, Cage would have been astonished and perplexed if, despite his randomization efforts, the resulting music sounded organized and always rather similar. Seeing a clump of scrambled sponge or *Hydra* cells self-organize back into an animal, or stem cells build an organoid for the first time, biologists probably experienced similar astonishment and perplexion. Developmental processes seem so obviously and precisely choreographed that it is only natural to assume complex programs behind them. Yet, as these examples demonstrate, cells are not simply record players playing a CD but active participants in creating the organization through their interactions. While often relying on self-organizing principles, development not only manages to succeed but also create rather stereotypical outcomes most of the time. All that not only despite the inherent random variability but often thanks to it. A true music of chances!

Introduction

I.1. How to make tissues and bodies

Approximately 700 million years ago, the evolution of obligate multicellularity laid the groundwork of the astounding animal diversity we observe today. Instead of living loosely associated in colonial clumps, the cells begun forming bodies with cell types specialized for certain functions and unable to exist on their own outside the body (reviewed in greater detail in Brunet and King, 2017). This division of labor then allowed building more complex and varied body plans.

Animal embryonic development, responsible for building the body plan, starts in most animals by a series of zygote divisions, producing several smaller cells. Through orchestrated collective behaviors, these cells give rise to tissues and organs of the developing individual. Thus, the diversity of animal developmental modes can be viewed as variations on a theme of building a body from a clump of cells. In some cases, like during initial polarization of the *Drosophila* embryo, cellular behavior coordination results from responding to preexisting signaling cues (prepattern). The zygote is already polarized by maternally loaded factors, which are asymmetrically distributed among the daughter cells and underlie the differences of their behaviors (Driever and Nüsslein-Volhard, 1998). Alternatively, groups of cells can coordinate through self-organizing mechanisms. This is the case in mammalian embryos, where no evident zygote polarity exists (reviewed in Hu, 2019). Polarization is instead achieved in a spontaneous symmetry-breaking event, when a subgroup of cells, different from the rest of the embryo, emerges. These cells then function as an organizing center which specifies the posterior body axis pole (Bedzhov et al., 2015).

Self-organization is a widespread natural phenomenon where the global organization of a system emerges solely from the local interactions of its components (Camazine et al., 2020). Instead of reacting to the global system dynamics, individual components can be envisioned as following simple rules, depending on the behavior of their interactors (Hemelrijk and Hildenbrandt, 2012). Much like humans creating a Mexican wave traveling around a stadium, simply by jumping up when their neighbors jump, cells in an embryo do not need to reference its global organization. Instead, each cell perceives the signals from the neighborhood and adjusts its behavior accordingly. With the right set of rules, which harness and amplify existing biological variability, coordinated cellular behaviors can emerge.

During development, self-organizing mechanisms and prepatterns alternate on different spatial and temporal scales to produce the final morphogenetic outcomes. Developmental progression thus results from their successive iterations and crosstalk. For instance, new organizers can appear by self-organization, and subsequently drive downstream events by secreted signals, as in the mammalian embryo polarization discussed above (Zhu and Zernicka-Goetz, 2020).

Interestingly, the repertoire of cellular behaviors, serving as tools for patterning and morphogenesis is relatively small and shared across the animal kingdom. Their combinations, however, can produce a wide variety of outcomes (Fig. I.1-1.). Consequently, both developmental similarities and differences can often result from differentially regulating the same set of underlying cellular behaviors. In chicken and duck leg primordia, a combination of differential adhesion and apoptosis drives the emergence of comparable skeletal anatomy through cartilage condensation and separation into individual pieces that will later ossify (Oberlender and Tuan, 1994; Saunders, 1966). However, differences in apoptosis also account for the anatomical differences between the feet of these two species. While in the chick the cells between digits are destined to die, they are retained in the duck embryos, generating the webbed foot used for swimming (Zuzarte-Luis and Hurtle, 2004).

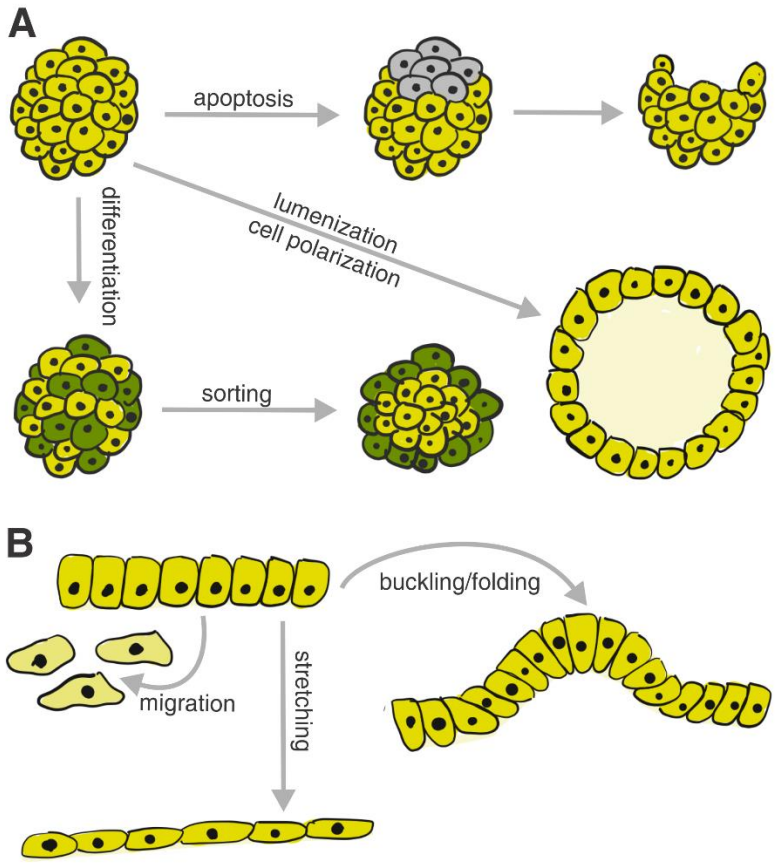

Fig. I.1-1. Examples of morphogenetic transformations driven by different cellular behaviors. (**A**) Cell clump example. The shape of the clump can be remodeled by collective apoptosis of a subpopulation of cells or stratified in two layers through sorting driven by differential adhesion. The cells can also create a lumen by secreting liquid into the center of the aggregate and breaking cell-cell contacts. (**B**) Epithelial sheet example. Sheets of cells can buckle/fold or stretch both because of external mechanical forces, and cell shape changes, such as apical/basal constriction. Some epithelial cells can also become migratory and leave the epithelium.

On the other hand, combinations of different cellular behaviors can coalesce into similar outcomes, such as in different basic gastrulation mechanisms. To turn a single-layered blastula into a double-layered gastrula, some cells can leave the epithelium, migrate inside the blastula, and reestablish another tissue layer there (ingression), or the whole tissue might fold on itself (invagination), generating a similar result (Solnica-Krezel and Sepich, 2012). Importantly, apart from moving cells to a different place, such morphogenetic movements are frequently involved in their functional specification (Shabhazi, 2020; Hannezo and Heisenberg, 2019), such as generating distinct embryonic layers in the case above. Conversely, different cell types within the same structure can also alter the morphogenetic outcome (Yang et al., 2021) and generate dynamics feedkack loops.

Recently, several bio-inspired engineering approaches, utilizing the knowledge of developmental principles, have emerged (Teague et al. 2016). Ranging from producing artificial tissues and organs (Gartner and Hu, 2021) to autonomous robots (Pfeifer et al., 2007), they demonstrate that understanding how cell collectives build tissues and organs is not only one of the most fascinating questions in biology but can have substantial practical implications.

I.1.1. Mechanical Clues

Many changes of tissue morphology, such as folding and stretching, also generate mechanical forces. Despite pioneering classical works (Bremer, 1932; Thompson, 1917), it was not until recently that these forces were widely recognized as affecting patterning. New technological advances allowed us to recognize that all cells react to mechanical signals as part of probing their environment (Heisenberg and Bellaiche, 2013). These cues, mainly perceived by the cytoskeleton, cell membrane, and cell-matrix or cell-cell junctions, are then integrated with other signals to drive cellular decisions (reviewed in Vining and Mooney, 2017).

Early demonstrations of such mechanosensing included the observation that different substrate stiffness can direct lineage specification in stem cells (Engler et al., 2006) or individual and collective migration of motile cells – a phenomenon termed durotaxis (Sunyer and Trepat, 2020; Lo et al., 2000). In the context of cell groups, mechanical cues are an important source of information about the global organization. For example, a clump of cells would have a very different geometry of cell-cell contacts compared to epithelial spheroids, resulting in perceiving different mechanical forces (Dumortier et al., 2019). Similarly, cells in a confined space can use mechanical forces resulting from neighbor contact to measure crowding. Defects in such mechanisms

can have dramatic impact on tissue homeostasis. In tumors, experimental evidence not only suggests that mechanical signals generated by overcrowding can enhance their aberrant phenotypes but that a growing solid tumor can mechanically induce oncogenic changes in the surrounding healthy cells (Fernandez-Sanchez, 2015). Changes of tissue mechanics can also serve as a feedback mechanism to verify the execution of a previous developmental step. In gastrulating animal embryos, the expression of endomesodermal markers in the cells moving inside the embryo not only accompanies the morphogenetic movement but is often driven by it (Schwarz and Hadjantonakis, 2020). When this movement is prevented, the expression of endomesodermal markers will not initiate. However, it is possible to rescue the defect by artificial mechanical stimulation (Pokhlyakova et al., 2018; Brunet et al., 2013), suggesting that the cell fate change is a response to the previous morphological change (and resulting mechanical forces).

I.1.2. Biochemical Signals

To influence cellular behaviors, all types of cues that the cells perceive inevitably have to be transformed into the "language" of biochemical signals. In case of tissue mechanics, several ways of accomplishing this task have been discovered. Since junctional proteins are often associated with signaling factors, such as kinases, their mechanically driven clustering can facilitate crossing the kinase activation threshold and stimulate downstream pathways (Li et al., 2016; Roca-Cusachs et al., 2009). Alternatively, mechanical stress can cause proteins to unfold or otherwise change conformation, revealing or abolishing binding sites for other protein partners (Johnson et al., 2007). Similar mechanism is also at work in mechanosensitive ion channels. Under low membrane tensions, the channel is closed, but changes conformation and opens when membrane tension increases, leading to the influx of ions into the cell (Murthy et al., 2017).

Several different effector molecules can be found downstream of these mechano-chemical relay mechanisms. One particularly well studied case is the transcriptional coactivator YAP1 (Dupont et al., 2011). This protein integrates mechanical signals from the actin cytoskeleton, changing its subcellular localization as a result (Aragona et al., 2013). Stimuli such as increased actin contractility (Panciera et al., 2017), stiff substrates (Calliari et al., 2016), and cell stretching (Benham-Pyle et al., 2015) can all drive YAP1 nuclear localization, resulting in gene expression changes. Interestingly, mechanical forces also seem to be capable of modifying gene expression through changes of chromatin structure (Tajik et al., 2016). Cell deformations due to the action

of mechanical forces are transmitted through the cytoskeleton and influence the nuclear shape (Ramdas and Shivashankar, 2015). It has been suggested that such deformations would then also impact chromatin packaging and interactions, leading to transcriptional output changes (Kirby and Lammerding, 2018; Uhler and Shivashankar, 2017).

Importantly, developmental and morphogenetic processes are also regulated by a wide variety of dedicated biochemical signals, often termed morphogens, which have been extensively studied. Since morphogens are commonly graded in tissues and can induce different cellular behaviors in different concentrations, a simple paradigm known as positional information was proposed to explain these observations (Wolpert, 1969). In this view, the source cells are spatially segregated and produce a morphogen that diffuses into the tissue, generating a gradient. The receiver cells then behave according to the perceived morphogen concentration. Thus, the sender cells function as an organizing center spatially patterning the receivers simply by encoding distance as a function of gradient concentrations. Although some cases, such as the drosophila embryo patterning by the morphogen Bicoid seem to fit this elegant model well (Porcher and Dostatni, 2010), subsequent research also pointed out several problems. Due to the inevitable variations of morphogen concentration, as well limits of cellular sensitivity to it, generating sharp boundaries between different cell fates (behaviors) just based on absolute morphogen concentration seems unlikely (Barkai and Shilo, 2009). Similarly, since morphogen diffusive properties are mostly stable, such mechanism would not be able to efficiently cope with scaling the morphogenetic field that is often necessary during development (Gregor et al., 2005). Moreover, many graded morphogens do not seem freely to diffuse freely and generating their gradients might require additional coordinated behaviors such as morphogen transport or cell movement (Wartlick et al., 2009).

Combining morphogen diffusion with interactions can produce more complex patterns, as demonstrated by the reaction-diffusion (RD) models first postulated by Alan Turing (Turing, 1952). Despite being long viewed as competing ideas, RD models can be easily reconciled with positional information, especially because they can explain how organizing centers of sender cells can appear from homogeneous initial conditions (Green and Sharpe, 2015). In a simple RD system, two morphogens – an activator and inhibitor of a certain cellular behavior – interact and generate a regular pattern. The key to this outcome are their diffusive properties and interactions that result in a combination of short-range activation and long-range inhibition. This dynamic system thus amplifies random fluctuations of morphogen concentrations and generates domains where the activator dominates, separated by the inhibitor-

controlled exclusion zones. When translated into the output cellular behavior (e.g. pigment production), the outcome is a regular spatial pattern, like the ones seen on animal bodies (Watanabe and Kondo, 2015). Fine tuning the system parameters and the interplay with boundary conditions then allow variable outcomes, such as spots and stripes (Dillon et al., 1994). RD type models were used to model a wide spectrum of patterning phenomena beyond color patterns. Examples include hair follicle spacing (Sick et al., 2006) or limb morphogenesis (Miura et al., 2006). The predominant model of *Hydra* body patterning that will be described later in greater detail is also RD based. However, despite being able to successfully reproduce the patterning outcomes in the modelled cases, the underlying biological mechanism often seems hardly reconcilable with the model. Many proposed morphogen pairs do not fit the model predictions, and consequently, the suspected regulatory molecules remain unidentified despite decades of effort (Vogg et al., 2019a). Moreover, experimental data that would effectively distinguish between concurrent patterning models are largely unavailable (Hiscock and Megason, 2015).

While both positional information and RD models are simplified concepts, they reveal fundamental principles that can be applied in more complex ways in real biological systems. For example, the short-range activation coupled with long-range inhibition can be realized without having to rely purely on a system of two diffusible morphogens (Brinkmann et al., 2018). On the other hand, both models present variations of one patterning paradigm, where cells read out an external coordinate system set up by the morphogens. However, cell-intrinsic mechanisms such as molecular oscillations or division timing can also be used to produce patterns without relying on an external reference grid, representing a fundamentally different type of patterning logic (Negrette and Oates, 2021; Puram and Bonni, 2013). These two complementary systems can even function in combination, as in the vertebrate somitogenesis, where signaling gradients modulate a self-organizing patterning system based on an oscillating genetic network (Aulehla et al., 2008).

I.1.3. Epithelial Lumens: Hubs of Mechanochemical Crosstalk

Epithelial lumens are a particularly interesting and relevant instance illustrating the complex interplay of principles described above. Most animal embryos have a stage where they resemble an epithelial spheroid with a central lumen. Moreover, many of the future organs are also initiated as cyst-like structures, making the epithelial lumen one of the fundamental motifs in animal development.

The tightly connected epithelial cells that create a boundary between the lumen and the surrounding space are all coupled both mechanically and chemically through their contact with the lumen. This creates a unique environment for the crosstalk between mechanical and biochemical signals (Fig. I.1-2.). For example, the cells can cause tissue stretching by increasing luminal fluid amounts as in the the mammalian morula to blastocyst transition (Ruiz-Herrero et al., 2017). In this system, connections between the morula cells partially break through liquid secretion to create several small lumens that eventually coalesce into a single big lumen, which continues expanding, causing the cells to stretch (Ryan et al., 2019). Since some cells do not participate in creating the epithelial wall but form a clump attached to it inside the lumen (inner cell mass), they experience very little stretching. Interestingly, these cells will form the embryo while the stretched surrounding epithelial layer will form extraembryonic tissues. Available evidence suggests that differential stretching is involved in specifying the different fates of these cell populations (Chan and Hiiragi, 2020). Even in cases when cells are part of the same epithelial layer, tension differences can drive them to behave differently, as in the the developing zebrafish heart. Here, more contractile cells migrate inward and create corrugated structures in the inner myocardial wall (Priya et al., 2020).

All these instances illustrate the influence of the luminal pressure driven stretching on cell fate decisions. However, reciprocal feedback mechanisms also exist. In some contexts, ceasing the liquid influx into the lumen once the cells have differentiated might be advantageous. Tuning the equilibrium between the force required for differentiation and switching off pumping by differentiated cells, could even be used to regulate the fraction of cells allowed to differentiate. Moreover, cellular adaptions to stretching could change their response to signaling molecules by effecting the amount of exposed plasma membrane surfaces or cellular connectivity (Hannezo and Heisenberg, 2019). Although such mechanisms have not yet been shown to operate *in vivo*, several studies already described other ways in which cell fate can feed back on tissue mechanics and patterning outcomes (Yang et al., 2020, Sanchez-Esteban et al., 2001). Among the precursors of alveolar cells in the developing lung, for example, two pre-specified populations can be identified. These cells are driven to differentiate by the amniotic fluid pressure. However, cells of one subgroup change their connectivity within the tissue before the onset of stretching, thus avoids most of its effects (Li et al., 2018). This way the previously established differences are reinforced, and two distinct populations of differentiated cells emerge. Apart from cell fate changes, other cellular behaviors, such as division, can also affect mechanics of the luminal wall. Weak spots, created in the epithelium by dividing cells, can lead

to luminal fluid leakage, concomitant luminal pressure decrease, and less stretching experienced by the cells (Chan et al., 2019)

Another interesting property of lumen architecture is the segregation of intra- and extra-luminal spaces, which allows separating the signals that cells perceive by their apical and basal ends. Signaling molecules secreted into the lumen are only accessible to the cells connected to it. A particularly elegant mechanism of this kind functions in the zebrafish lateral line development (Durdu et al., 2014). Here a group of migrating cells leaves behind equally spaced smaller clumps that will become individual sensory organs. This is accomplished by concentrating the FGF ligand in the lumens of the small clumps, which prevents their further migration. Interestingly, the self-organized lumen assembly (and thus the size of the clumps) is regulated by the geometry of the system. In similar cases, where morphogens are secreted into the luminal space, several interactions with tissue mechanics can be envisioned. The morphogen, secreted inside the lumen, could influence mechanical properties of the cells and so change their response to the secretion-driven stretching. Alternatively, cells could also regulate the morphogen concentration by secreting more luminal fluid and diluting the morphogen for the cost of experiencing more stretching.

Taken together, several different possibilities for useful mechanochemical crosstalk in epithelial lumens exist, but most of them are currently speculative. Future experimental work will be needed to investigate which of them have been implemented in biological systems, and to uncover the unifying principles of such regulations.

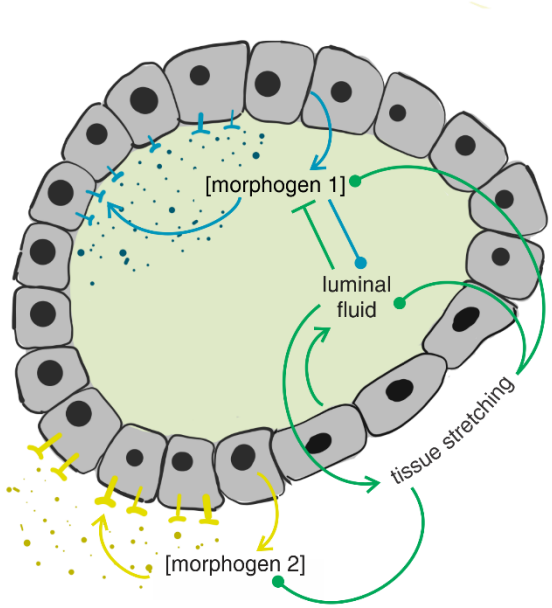

Fig. I.1-2. The interplay of mechanical clues and chemical signals in an epithelial lumen. Pointed arrows indicate positive regulation. Flat arrows indicate negative regulation. Lines ending in dots indicate that either mode of regulation is possible. Based on Hannezo and Heisenberg (2019).

II.2. *Hydra* as a Model of Tissue Patterning*

Cnidarians are an early-branching metazoan phylum, sister to all bilaterians (Fig, I.2-1. A). This evolutionary position makes them suited to uncover basic biological principles, broadly conserved among more complex animals (Technau and Steele, 2011). *Hydra*, one of the freshwater representatives, is a simple animal with a long history as an experimental model system (Vogg et al., 2019a). Its tube-like body is organized along a single oral-aboral axis (Fig. I.2-1. B). The oral (upper) pole consists of a mouth opening (hypostome) surrounded by tentacles, which the animal uses to catch prey. Once food has been digested inside of the body cavity, the mouth also serves as the exit route for undigested leftovers. The opposite side of the axis (aboral pole) is specialized for attaching the animal to the substrate and is referred to as the foot (comprising the peduncle and the basal disc). Its body wall is only two layers thick, consisting of two sheets (ectoderm and endoderm) of epithelio-muscular cells, separated by a thin layer of extracellular matrix (mesoglea). Cells of a third cell lineage, known as the interstitial cells (i-cells), are also interspersed among the epithelia, which give rise to other cell types, such as the stinging cells (nematocytes), gland cells, and neurons. Even though capable of sexual reproduction, *Hydra* predominantly reproduces asexually by budding (Otto and Campbell, 1977). During this process, a miniature daughter animal forms perpendicular to the parental body column. When fully developed, the clone detaches from the parent, and continues living freely. Interestingly, budding only happens in a spatially restricted body region, adjacent to the foot, termed the budding zone.

As early as in the 18th century, the extensive regenerative capacity of *Hydra* was described and studied by Abraham Trembley, marking the dawn of experimental biology (Trembley, 1744). Since most of the body cells are not terminally differentiated, the regeneration process mostly relies on cell specification and movement without the need for dedifferentiation or significant proliferation and tissue growth (morphallactic regeneration, reviewed e.g. in Bosch, 2007). When bisected in the middle, the oral half of the animal will regenerate the missing foot at the injured site, while the aboral half will regenerate a head, producing two complete half-sized animals. Remarkably, even very small pieces (~ 1/20 body size), without an obvious polarity memory, can regenerate into full animals (Peebles, 1897), suggesting a possibility of *de novo* body

* *Modified fragments of this section appear in the chapter "Self-organization of Tissues through Biochemical and Mechanical Signals" (Misailidis, G., Ferenc, J. & Tsiairis, C. D.) as a part of the book "Modeling Biomaterials" (Malek, J., Suli, E., eds. 2022. Springer/Birkhäuser, in press)*

pattern establishment. This is indeed the case as shown by the ability of dissociated and reaggregated body column cells to regenerate a full animal (Noda, 1971, Gierer et al., 1972).

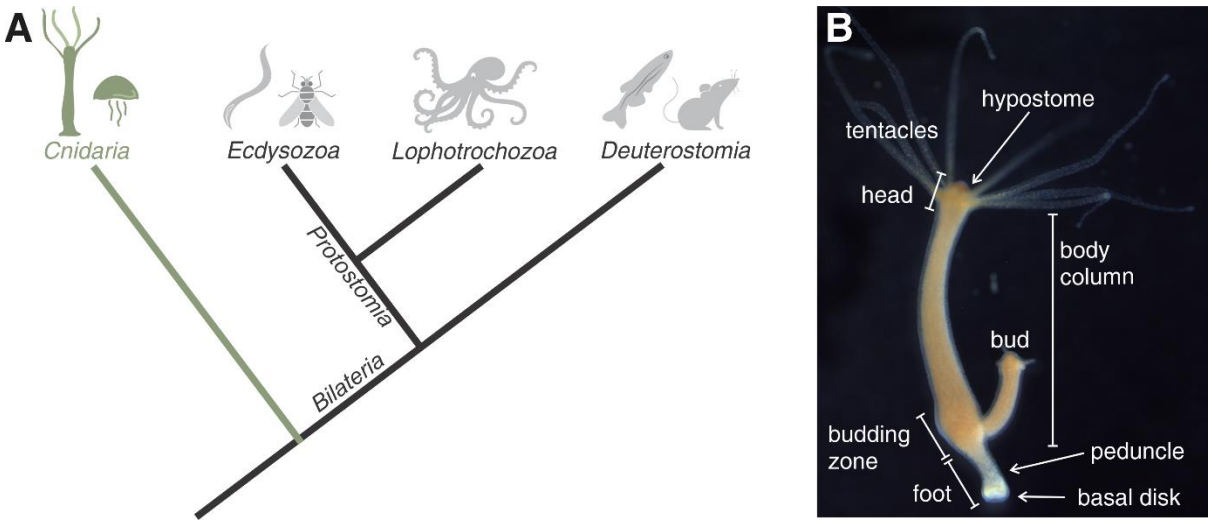

Fig. I.2-1. The *Hydra* body plan and phylogenetic position. (**A**) Phylogenetic position of cnidarians with respect to major bilaterian clades. Phylogenetic tree topology according to the Three of Life Project (tolweb.org). (**B**) Morphology of the *Hydra* body.

Another experimental manipulation that is easy to perform in *Hydra,* and served as a powerful tool for understanding the principles of patterning, is tissue grafting. Such transplantation experiments lead to the first identification of a biological organizer in the hypostome of Hydra (Browne, 1909). This small group of cells around the mouth opening controls patterning through biochemical signals. When transplanted into the body column of another animal, it will induce an ectopic head formation and generate an ectopic body axis perpendicular to the recipient's body. Importantly, this new head contains mostly host cells, responding to the presence of the grafted organizing center (Yao, 1945). We now known that the organizer identity is determined by the canonical Wnt signaling (Broun et al., 2005; Hobmayer et al., 2000). Subsequent experimental work has also shown that transplanted pieces of the body column are sometimes capable of forming an ectopic head (Webtster, 1966). Further analysis of these and similar results was then crucial for developing influential theoretical models of patterning (Wolpert et al., 1974; Gierer and Meinhardt, 1972).

More recently, these traditional techniques were combined with molecular tools. Advancements such as the *Hydra* genome sequencing and annotation (Chapman et al., 2010), approaches for gene knockdowns (Lohmann and Bosch, 2006) and transgenesis (Wittlieb et al., 2006), allowed probing the regeneration and patterning

phenomena at a deeper level. Single-cell transcriptomic data (Siebert et al., 2019), as well as epigenetic datasets (Cazet et al., 2021; Murad et al., 2019) also became available, bringing new insights about cell differentiation trajectories and the regulatory connections in gene expression.

I.2.1. Self-Organization of *Hydra* Cells

As mentioned above, *Hydra* cells from a dissociated body column can regenerate an entire animal when reaggregated (Fig. 1 in section III.1.). Remarkably, unlike organoid systems, they do not require the external addition of signaling factors, thus being a prime self-organization example. The reaggregated cells first reestablish the two epithelial layers by cell sorting, which transforms the clump into a hollow spheroid (Gierer et al., 1972). As both ecto- and endodermal cells already need to be present in the original aggregate for successful regeneration, cell identity changes do not seem to play a significant role (Kishimoto et al, 1996). Spontaneous symmetry breaking then follows and the spheroid establishes one or several new body axes. The number of emerging heads depends on the size of the aggregate, suggesting an intrinsic spatial scale of the patterning process (Technau et al. 2000). Hollow tissue spheroids can also be created from small rectangular pieces of the body column. When cut, the tissue fragments quickly fold into spheroids, developing similarly as the spheroids prepared by reaggregation (Fig.1A in II.1.1.).

Interestingly, both types of spheroids experience mechanical oscillations on the way to symmetry breaking and regeneration (Kücken et al. 2008). Since *Hydra* is a freshwater animal, cells constantly experience an influx of water from the environment. To maintain osmotic balance, they excrete the surplus water into the body cavity. In fully formed animals, the accumulated water is then expelled through the mouth by spontaneous contractions (Benos et al. 1977). Regenerating spheroids, however, lack a mouth. With the increasing volume of liquid excreted into the spheroid lumen, pressure builds up, resulting in spheroid expansion. Eventually, a threshold of tissue strength is reached and the tissue ruptures. Several such cycles are typically necessary before the spheroid breaks symmetry, which leads to mechanical inflation and deflation oscillations. One of the symmetry breaking hallmarks is the stabilization of the new mouth opening (Soriano et al. 2009). This causes the oscillatory pattern to change as the mouth provides a weak point through which the accumulated water can be released. Thus, the spheroid inflates less before deflating, causing shortening of the oscillation period and decrease of amplitude (Fig. 1C in II.1.1). On the molecular level, one of the earliest signs of symmetry breaking

is the appearance of a small group of cells, expressing high levels of Wnt signaling ligands (Technau et al., 2000).

I.2.2. Wnt Signaling and Organizing Centers

Wnt signaling is a common name for several interconnected signaling pathways that utilize Wnt proteins as their ligands. The pathways have been traditionally divided based on their downstream mediator molecules to canonical and non-canonical. Canonical Wnt signaling relies on the multifunctional protein β-catenin, whereas the noncanonical pathways, such as Wnt/planar polarity and Wnt/calcium signaling rely on different means. While both non-canonical pathways are present in *Hydra* and have been implicated in processes such as budding and tentacle formation (Philipp et al., 2009), the canonical Wnt signaling has a prime importance for axial patterning. We will thus further focus on this pathway.

B-catenin, the main mediator of canonical Wnt signaling, is a multifunctional protein that serves both as a component of cell-to-cell junctions and transcriptional coactivator (reviewed in Valenta et al., 2012). However, in the absence of Wnt signal, most of its cellular pool is found in the junctions. This is due to the constant degradation by a cytoplasmic degradation complex (Spink et al., 2001). One of the important components of this complex is the glycogen synthase kinase-3 beta, which phosphorylates β-catenin, targeting it for proteasomal degradation (Yost et al., 2006). Several chemical activators of the canonical Wnt signaling (e.g. paullones, CHIR compounds) function by inhibiting this kinase (Naujok et al, 2014; Leost et al., 2000). Similarly, when a Wnt ligand binds its receptor (one of the members of the frizzled protein family), the degradation complex is inactivated, leading to the increase in cytoplasmic β-catenin levels. The protein can then also move into the nucleus, where it associates with the Tcf transcription factors to promote the expression of downstream target genes (Fig I.2-2. A). Thanks to its junctional function, β-catenin also connects the canonical Wnt pathway with tissue mechanics. For example, β-catenin molecules are recruited into newly assembling junctions under mechanical tissue stress (Röper et al., 2018; Dorland and Huveneers, 2017). When in junctions, the protein gets phosphorylated on a different aminoacyl residue than in the cytoplasm. This phosphorylation leads to β-catenin exiting the junctions and enhances its transcription-stimulating activity (Fang et al., 2007)

Despite being relatively small proteins (molecular weight usually ranging between 35 and 50 kDa; Willert and Nusse, 2012), the Wnt ligands have a limited diffusivity due to palmitoylation in the endoplasmic reticulum before being secreted. This lipophilic

modification tethers them to cellular membranes, restricting their diffusion range (Komekado et al., 2007). It has been suggested that, thanks to this property, the Wnt proteins are excellent symmetry breaking drivers that could have been one of the first molecular signals used to organize metazoan bodies (Loh et al., 2016). In accordance with this hypothesis, the origins of the canonical Wnt signaling appear to be intertwined with the origins of multicellularity. Moreover, the primary body axis specification in extant metazoans relies almost universally on this signaling pathway (Petersen and Reddien, 2009). Thus, we not only find it expressed in the oral end of *Hydra* body axis but also in the dorsal ends of vertebrate embryos (Fig. I.2-2. B). Consistently with this role, genetic or chemical activation of the canonical Wnt signaling results in branched animals with ectopic organizers (Gee et al., 2010). Transplanted tissue pieces, treated with β-catenin stabilizing drugs, also have an organizer-like behavior, and induce ectopic axis formation (Wang et al., 2020).

Among the canonical Wnt proteins in *Hydra*, Wnt3 seems to have the most prominent role. Not only is its expression specific to the organizer cells, but it also marks the spots of future heads in reaggregates before any morphological changes occur (Technau et al. 2000). *Wnt3* expression is also crucial for head regeneration in bisected animals, and in both regenerative systems it is the first Wnt ligand to be expressed in a spatially restricted manner (Lengfeld et al. 2015). Thanks to a direct positive feedback loop through β-catenin/Tcf, the *Wnt3* expression in *Hydra* is self-sustaining and potentially involved in the organizer maintenance (Nakamura et al., 2011).

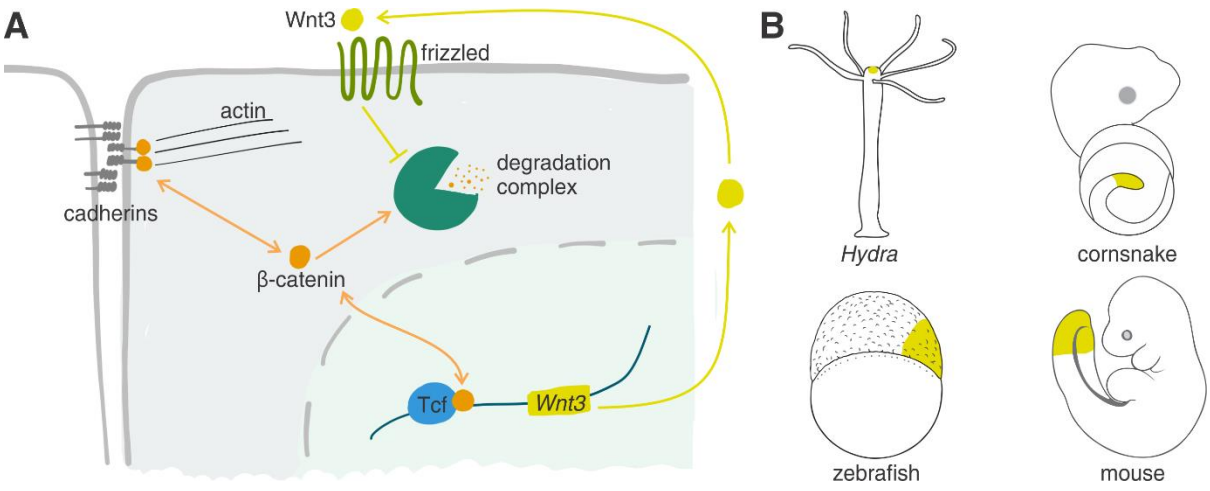

Fig. I.2-2. The canonical Wnt signaling and its role in axial patterning. (**A**) Simplified scheme of the canonical Wnt pathway function in *Hydra*, highlighting the positive feedback loop in *Wnt3* expression. (**B**) The position of the Wnt developmental organizer in *Hydra* and various animal embryos. Based on data in Hobmayer et al. (2000), Lu et al. (2011), Gomez et al. (2007).

I.2.3. Axial Patterning in *Hydra*: Gierer-Meinhard Model and Beyond

Thanks to the ease of transplanting tissue pieces and clear morphological readout of head formation, grafting experiments made it possible to make inferences about the patterning mechanisms in *Hydra* long before the underlying molecular players were known. As mentioned previously, apart from grafting the mouth organizer itself, pieces of the body column can also sometimes establish an ectopic head when grafted into another individual. Interestingly, this ability is the strongest in pieces originating close to the head and decays as a function of distance from it (MacWilliams, 1983a, MacWilliams, 1982; Webster 1966). Conversely, positions distant form the host head have the highest probability of ectopic head formation after receiving a graft. Next to an existing head, the probability of such event is negligible (MacWilliams, 1983b). Thus, both the head activation and the head inhibition capacity of the body tissue peak at the oral end and decrease towards the aboral pole (Fig. I.2-3. A).

Along with the experiments uncovering the foundations of *Hydra* patterning, Albrecht Gierer and Hans Meinhardt developed a theoretical framework, aiming to explain the observations (Fig. I.2-3. B). The Gierer-Meinhardt model sought to unify the results of different experiments by an underlying reaction-diffusion mechanism (Gierer and Meinhardt, 1972). It postulates two chemical morphogens (head activator and head inhibitor) produced by the organizer and diffusing into the body, generating gradients. The activator is a less diffusive molecule and provides local activation. The inhibitor, on the other hand, diffuses further away and generates long-range inhibition. Additionally, the two morphogens interact in a negative feedback loop. The activator as well as inhibitor production is enhanced by the activator, while, at the same time, the inhibitor prevents activator production.

This simple framework can successfully explain both the morphology of homeostatic animals, as well as the transplantation experiments. Moreover, the inherent pattern length scale, dictated by the morphogen diffusion properties, would also account for the need of a freshly budded *Hydra* to grow first, before being capable of budding itself. It could also explain the positive correlation between the reaggregate size and the number of emerging heads. Morphogen source density, which the model also introduces, can additionally account for regeneration phenomena. This property is modelled as graded similarly to a particular morphogen but being less dynamic than its concentration. Morphogen-induced cell states, for example, have been envisioned to form such a gradient. This positional identity gradient would then persist even after the morphogen source removal and could be responsible for maintaining the correct body polarity during regeneration.

The elegance of the GM model and its ability to explain a wide range of experimental observations have served as a catalyst for efforts trying to identify the proposed substances. Even though many pioneering studies were looking for the head activator in extracts of small peptides from the *Hydra* body (e.g. Schaller and Gierer, 1973; Schaller, 1973), the most promising candidate turned out to be the Wnt3 protein (Hobmayer et al. 2000). Once Wnt3 was accepted to be the head activator, the search for head inhibitor also concentrated on homologs of endogenous Wnt signaling inhibitors. The first proposed candidate was the Dkk protein, a competitive inhibitor of Wnt binding to its receptor (Guder et al., 2006). While this small secreted protein could act as a diffusible morphogen, its expression pattern in the body does not correspond with the model prediction because it peaks in the body column and not in the hypostome itself. Another, more recent, candidate is the transcription factor Sp5, which inhibits the expression of Wnt3 yet, at the same time, is positively regulated by it (Vogg et al. 2019b). When Sp5 is downregulated artificially, it phenocopies the Wnt3 activation phenotype of ectopic head formation. It is also expressed in a graded manner along the body column with a peak in the hypostome region; however, as a transcription factor, it cannot diffuse between cells.

Moreover, although the ectopic head phenotypes of Wnt3 activation or Sp5 suppression demonstrate their central role in head specification, such results are not consistent with the GM model. According to the theoretical predictions, only the morphogens' diffusive properties, but not their concentrations, should influence the pattern spacing (Hiscock and Megason, 2015). Thus, despite decades of efforts, no molecules precisely fitting the bill of the GM model activator and inhibitor were found. On the other hand, any efforts to update the model should also be able to integrate the existing knowledge of molecular players. Perhaps the simplest way to reconcile the GM model with the current data would be to simply assume that the Wnt3/Sp5 feedback loop operates downstream of the actual morphogens, which remain unknown. In this case, the genetic network would function predominantly as a readout of the patterning mechanism, and, possibly, be responsible for establishing the source density gradient. Several alternative updates of the GM model, which try to accommodate known molecules into the patterning mechanism, have also been proposed. Examples include proposing additional loops of slow- vs. fast-diffusing Wnt3 (Meinhardt, 2012), having Wnt-signaling control a competence gradient that decides which patterning centers will manifest as heads (Meinhardt 2008), or separating the canonical Wnt-signaling and its main mediator β-catenin into two interconnected loops (Mercker et al., 2021). While all these models represent interesting conceptual developments, their assumptions and predictions also require

careful validation. Experimental setups that could distinguish between the different options would be critical. Alternatively, another class of models suggests mechanisms very different from the GM model. For example, several mechanochemical models have been proposed, inspired by the potential role of mechanical cues in regenerating *Hydra* spheroids and data from other systems. Here, tissue mechanical properties, such as curvature (Mercker et al. 2013) or strain (Mercker et al. 2015), operate to change the expression of chemical morphogens and thus drive patterning.

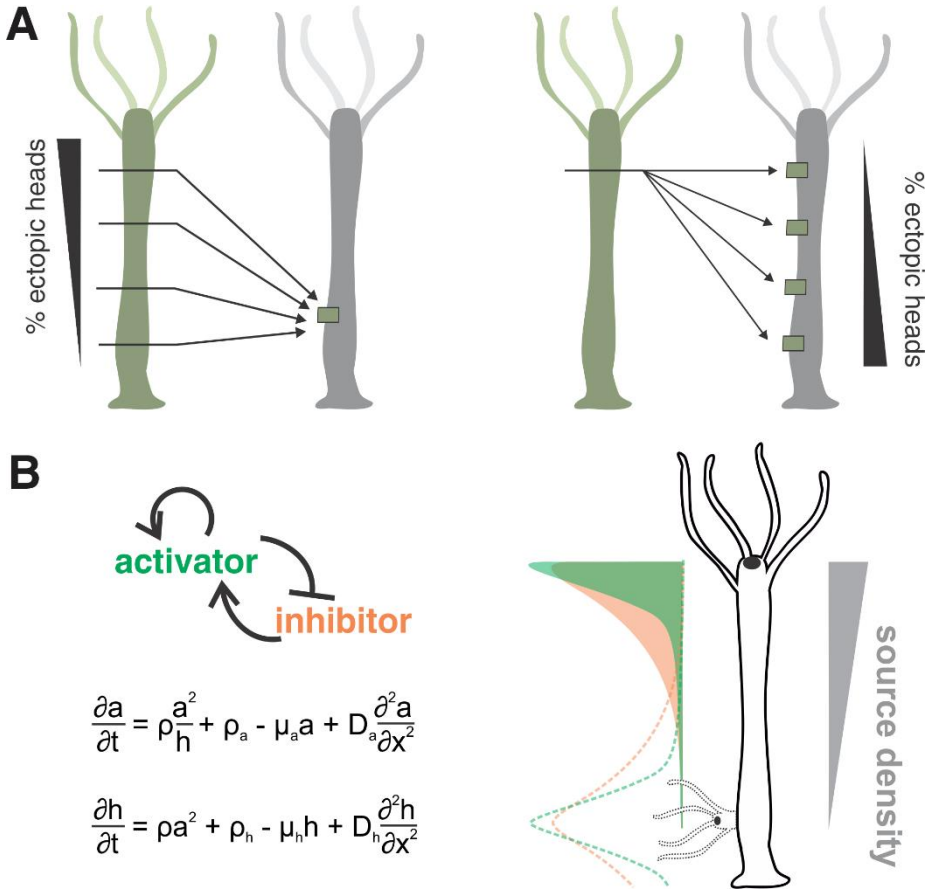

Fig. I.2-3. The Gierer-Meinhard model of *Hydra* patterning. (**A**) Grafting experiments demonstrating head activation (left) and inhibition (right) gradients. After Shimizu (2012). (**B**) A summary of the Gierer-Meinhard model. Black dot in the *Hydra* head denotes the organizer. Dotted lines indicate secondary peaks occurring in big enough animals, that would be the basis for ectopic axis generation during budding. Activator and inhibitor concentrations are denoted by a(*x,t*) and h(*x,t*) respectively. D denotes diffusion constant, μ the degradation rate, and ρ source density. Equations from Gierer and Meinhardt (1972).

I.2.4. Stem Cells and Differentiation in *Hydra*

Cell differentiation is one of the crucial outputs (and tools) of patterning mechanisms. In the body of *Hydra*, terminally differentiated cells are mostly found at the extremities, while the body column is largely composed of undifferentiated stem-like cells, which can readily differentiate (Dübel and Schaller, 1990). This property is also thought to be responsible for *Hydra's* substantial regenerative capacity (Bosch, 2010).

As mentioned before, the epithelial stem cells belong to two lineages – ectodermal, covering the outside of the body, and endodermal, lining the body cavity. Within the body column, these cells are constantly dividing and being passively displaced towards the extremities (Fig. I.2-4. A-B; Campbell, 1974), along with the mesoglea to which they are attached (Sarras et al., 1991). After arriving at the body ends, they stop dividing, differentiate terminally, and eventually die and are replaced. This constant renewing of the *Hydra* body is thus reminiscent of mammalian epithelia with high turnover, such as the skin or intestinal wall. The cell cycle of *Hydra* epithelial cells is relatively long, lasting on average ~ 75 h (David and Campbell, 1972), most of which are spent in the G2 phase (Bugzariu et al., 2014). Interestingly, the cells can also terminally differentiate in this phase, without the need of dividing first (Dübel and Schaller, 1990).

Despite not being terminally differentiated, these cells also support vital functions of the animal, such as active movement (both layers) and digestion (endoderm), since they constitute most of the body column. Their muscle function is mediated by supracellular actin fibers that span the basal ends of the cells, creating an organized network (Muller, 1950). The ectodermal fibers run parallel to body axis and the endodermal perpendicular to it, creating longitudinal and circular "muscles" (Wang et al., 2020). Recent studies have indicated that the organization of these fibers might also function as a pattering cue (Maroudas-Sacks et al., 2021; Livshits et al., 2016).

Differentiated epithelial cells can be found in the hypostome (organizer cells), tentacles, and the foot (Fig. I.2-4. C). Out of these cell types, the two best described are basal disk mucus cells and tentacle battery cells, both ectoderm derivatives. Basal disk cells have a typical inverted cone shape and, unlike undifferentiated cells, are ciliated (Davis, 1973). They contain many secretory granules, the content of which acts as a glue when secreted, and mediates the animal's substrate adhesion (Rodrigues et al., 2016). Battery cells, on the other hand, are specialized for catching prey and sensory functions, and harbor a complex assembly of nematocytes (stinging cells) and neurons, which are themselves derived from the interstitial lineage (Hobmayer et al., 1990).

Interstitial stem cells (i-cells) have several features distinguishing them from their epithelial counterparts – shorter cell cycle, active mobility, and differentiation in G1/G0

phase of the cell cycle (Buzgariu et al., 2014; David, 2012). They also generate progenitors for several different somatic cell populations (gland cells, neurons, nematocytes), as well as the germline (Fig. I.2-4. D). The fast cell cycle (14 – 24 h, Cambell and David, 1974) of interstitial cells makes it possible to selectively eliminate them from the *Hydra* body by drug treatments killing actively dividing cells (Sacks and Davis 1979). Animals prepared this way are viable but unable of active movement or feeding. To maintain them in culture, they must be force-fed. Surprisingly, they are still capable of budding and regeneration, suggesting that i-cells are dispensable for patterning processes in *Hydra* (Campbell., 1979).

A special class of the i-cell derivatives are the nematocytes (stinging cells) – a sensory cell type characteristic for cnidarians (Hausmann and Holstein, 1985). Several nematocyte subtypes, specialized for different functions, exist, sharing a general morphology. They all have an oval shape, densely condensed nucleus, and possess a nematocyst. Nematocyst is an organelle that develops in a secretory vesicle and contains a coiled stinging fiber, capable of rapid discharge (Nüchter et al., 2006). The discharge is regulated by a small mechanosensory protrusion known as the cnidocil (Cormier and Hessinger, 1980). Different types of nematocytes use the fiber either to catch prey and inject it with venom, for defensive purposes, or for substrate attachment during active locomotion (Chapman and Tilney, 1959a-b). Nematocytes are a single use cells and have to be replaced upon fiber discharge. To meet the high turnover demand, their progenitors (nematoblasts) have a very fast cell cycle (~ 15 h, David and Gierer, 1974). These cells divide synchronously and develop in groups connected by cytoplasmic bridges, termed nests. Once the nematocyst development finishes, individual cells separate and move into the tenacles, where they are engulfed by battery cells (Bode and Flick, 1976). A minority of differentiated nematocytes also remains in the body column.

While nematocytes and their progenitors are only intercalated in the ectoderm, neurons are found in both tissue layers. They are interconnected in a disperse network without apparent organization, which is, however, functionally compartmentalized (Dupre and Yuste, 2017). Given the ease of live imaging of the entire network activity (Lagache et al., 2020), and thanks to the recent identification of distinct neuronal subtypes (Siebert et al., 2019), *Hydra* has become an emerging model to study the principles of nervous system organization. The third type of differentiated i-cell progeny are the gland cells. These cells are intercalated between the epithelial cells and produce digestive enzymes (Schmidt and David, 1986). Interestingly, both their morphology and secretory content change as they move towards the extremities (Siebert et al., 2008). Since the undifferentiated i-cells reside in the ectoderm, some

of the precursors migrate into endoderm to supply neurons and gland cells. Recent molecular data have suggested the existence of a common precursor subpopulation that can give rise to both the gland cells and endodermal neurons (Siebert et al., 2019).

Hydra stem cells also share several molecular similarities with their counterparts in more complex organisms. For example, all three undifferentiated cell types express the transcription factor FoxO, which has been implicated in stemness maintenance (Soh et al., 2021). Consistently with this assumption, the differentiated body domains begin to expand upon its knockdown in *Hydra* (Boehm et al., 2012). Other well-known stemness regulators expressed in the *Hydra* stem cells are the two *myc* homologues (*myc1* predominantly in i-cells, and *myc2* in epithelia), which regulate the balance between differentiation and self-renewing cell divisions (Wilson et al., 2004). Interestingly, these two genes are also differentially regulated by canonical Wnt signaling, which represses *myc1* but not *myc2*, suggesting that it might enhance i-cell proliferation (Hartl et al., 2019). However, since expression of Wnt inhibitors in i-cells also increases, as they approach the Wnt domain (Guder et al., 2006), it remains to be understood how this regulation functions.

Hydra stem cells also express components of the PIWI-piRNA pathway, which are predominantly found in the germline and stem cells in other animals (Lim et al., 2014; Thomas et al., 2013; Bennecke et al., 2007). This pathway is crucial for silencing transposons and its defects often lead to fertility loss (Heyn et al., 2012) or reduced stem-cell proliferative capacity (Cox, 2000). Similarly, knockdown of the *Hydra piwi* homolog *hywi* is lethal, due to the lysis of epithelial cells (Juliano et al., 2014). It has also been proposed that high expression of *piwi* homologs contributes to the maintenance of such high stock of stem cells in the *Hydra* body and the non-senescence of the animal (Vogg et al., 2021).

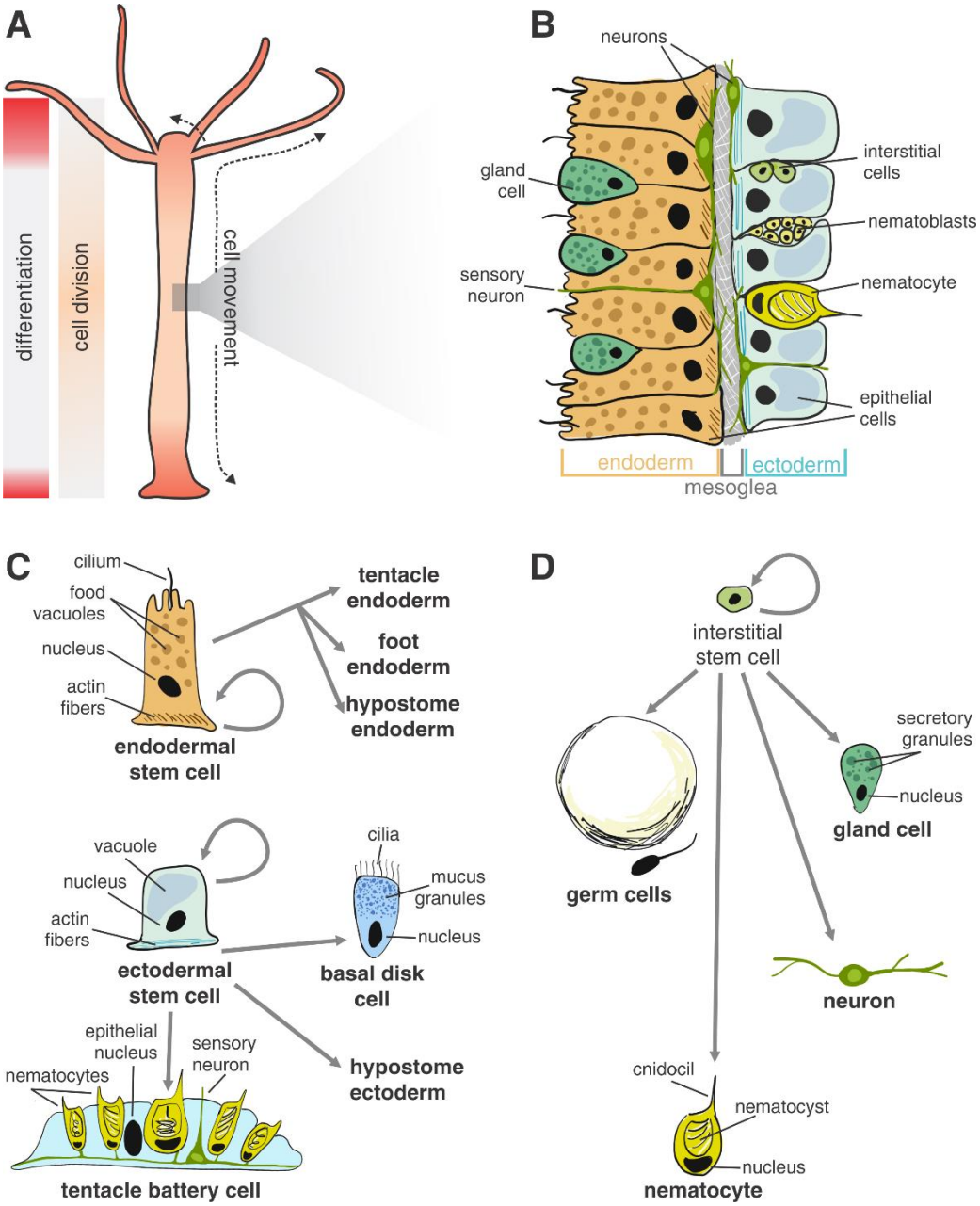

Fig. I.2-4. *Hydra* cell types. (**A**). A scheme of the *Hydra* body with indicated directions of cellular movements (arrows) and zones of differentiation (red) and division (orange). Based on Campbell (1974) and Bosch et al. (2010) (**B**) Zoomed-in picture of the body wall architecture. Modified from Technau and Steele (2011). (**C**) The epithelial stem cells and their progeny. (**D**) The interstitial cell lineage and its derivatives. Battery cell drawing based on Hobmayer et al. (1990).

II.3. Outstanding Questions and Scope of this Work

Hydra is often viewed as a textbook example of reaction-diffusion patterning, yet many challenges to this view keep emerging. One of them is the question of integrating mechanical cues into the patterning processes. Ever since the description of the mechanical oscillations, accompanying the *de novo* patterning of *Hydra* spheroids, their potential role for creating the pattern has been speculated about (Fütterer et al., 2003). Since the cells in these two-layered epithelial lumens generate dramatic tissue-level mechanical changes, it would be natural to assume that such mechanical cues also feed back on their behaviors. However, the models proposed so far (Sander et al., 2020; Gamba et al., 2012; Soriano et al., 2009) only relied on correlative evidence and did not provide a connection to the underlying molecular pathways.

The aim of the first part of this thesis was twofold. First, to understand the role of mechanical oscillations for *de novo* axial patterning in *Hydra* spheroids. Additionally, if the oscillations indeed played a role in development, to find connections between the mechanical cues generated by them and the signaling pathways involved in patterning.

Once established, the organizing centers coordinate the behaviors of other cells to build and maintain the body. For example, cells in the body column should be prevented from differentiating, and cells close to the head organizer should differentiate into tentacle structures. While, we have some understanding about how stemness is maintained in *Hydra* cells, not much is known about the regulation of differentiation, especially in epithelia. Moreover, although graded diffusible factors upstream of these decisions were proposed from the early days of *Hydra* patterning research, their identity remains elusive. Several studies have suggested these signals to be diffusible peptides (Fujisawa and Hayakawa; 2012; Bosch and Fujisawa, 2001; Lohmann and Bosch; 2000). However, due to technical limitations, most of them only investigated expression profiles and biological activities of the putative morphogens, rather than their distribution withing the body. Thus, it is hard to evaluate whether these molecules really are the suggested upstream activators, or rather another part of the downstream patterning output.

In the second part of the thesis, we therefore set out to investigate downstream targets of canonical Wnt signaling that could be regulating the cell specification in the extremities. We also instigated a mass-spectrometry imaging approach that could be used to identify small molecules acting as possible patterning regulators.

II. Results and Discussion

II.1. Mechanical Oscillations during *Hydra* Regeneration

II.1.1. Mechanical Oscillations Orchestrate Axial Patterning through Wnt Activation in Hydra (accepted manuscript)

The following manuscript was accepted for publication in the journal Science Advances

Authors

Jaroslav Ferenc[1,2], Panagiotis Papasaikas[1,3], Jacqueline Ferralli[1], Yukio Nakamura[4†], Sebastien Smallwood[1], Charisios D. Tsiairis[1*]

Affiliations

[1] Friedrich Miescher Institute for Biomedical Research, Maulbeerstrasse 66, 4058 Basel, Switzerland.
[2] University of Basel, Petersplatz 1, 4001 Basel, Switzerland.
[3] SIB Swiss Institute of Bioinformatics, 4058 Basel, Switzerland.
[4] Institute of Medical Sciences, University of Aberdeen, AB25 2ZD Aberdeen, United Kingdom.
[†] Current address: Repertoire Genesis Inc., 567-0085, Osaka, Japan.
* Corresponding author: charisios.tsiairis@fmi.ch

Abstract

Mechanical input shapes cell fate decisions during development and regeneration in many systems, yet the mechanisms of this crosstalk are often unclear. In regenerating *Hydra* tissue spheroids, periodic osmotically driven inflation and deflation cycles generate mechanical stimuli in the form of tissue stretching. Here we demonstrate that tissue stretching during inflation is important for the appearance of the head organizer – a group of cells that secrete the Wnt3 ligand. Exploiting time series RNA expression profiles, we identify the upregulation of Wnt signaling as a key readout of the mechanical input. In this system, the levels of Wnt3 expression correspond to the levels of stretching, and Wnt3 overexpression alone enables successful regeneration in the absence of mechanical stimulation. Our findings enable the incorporation of mechanical signals in the framework of *Hydra* patterning and highlight the broad significance of mechanochemical feedback loops for patterning epithelial lumens.

Introduction

Animal bodies and organs display an overwhelming variability of forms, yet their development relies on a relatively small repertoire of key processes such as folding, branching, and lumenization (*1*, *2*). These morphogenetic processes often generate mechanical forces that can in turn guide cellular behaviors, thus creating mechanochemical feedback loops (*3*). In such crosstalk, the patterning phenomena bridge organization scales as tissue properties like elasticity or curvature influence individual cell biochemistry and vice versa. Epithelial lumen expansion is a characteristic case, where the fluid accumulation in the cavity increases pressure globally and affects patterning of the surrounding epithelium. Differential fate decisions of individual cells are then often driven by local heterogeneities of the global tissue properties and can further modify them (*4*). Mechanically driven inflation and deflation events have been observed to influence the patterning of mammalian blastocysts (*5*, *6*), lung alveoli (*7*), otic vesicles (*8*), and diverse organoid systems(*9*, *10*). To understand the conserved general principles of this luminal patterning, anatomically simple systems with well-defined cell differentiation processes, and amenable to experimental manipulation, are particularly handy. The critical questions are what type of mechanical signals the cells react to, and how they modify their identity, i.e. gene expression profile. Regenerating *Hydra* tissue spheroids are such a simple, experimentally tractable system, derived from an animal whose phylogenetic position makes it suited to uncover broadly conserved mechanisms (*11*). Here mechanics and cell fate decisions coincide but their connection has remained elusive thus far (*12*, *13*).

Hydra is a simple organism organized along a single oral/aboral axis. Two epithelial layers, the ectoderm and the endoderm (also termed epidermis and gastrodermis), form a tubular structure with a mouth surrounded by tentacles on one end, and a foot on the opposite. Wnt signaling is critical for the patterning of the animal with ligands expressed on the oral end, the hypostome area (*14*). Ectopic activation of Wnt signaling induces ectopic axes formation (*15*). Moreover, Wnt signaling is critical during the morphallactic regeneration of *Hydra* (*16*). When a small fragment is taken from the body of *Hydra*, the two-layered epithelial tissue folds into a spheroid with a lumen in the center. This spheroid gradually re-establishes the full body plan as the head (hypostome) with tentacles, and the foot (peduncle and basal disk) of the animal appear, marking the opposite ends of its body axis (Fig. 1A). The uniformity of the epithelial cells is first broken when a small subpopulation stably expresses the Wnt3 ligand, differentiating into the head organizer which guides the morphogenesis of the surrounding tissue (*17*, *18*).

Previous work has shown cycles of osmotically driven mechanical oscillations accompanying the regeneration process of such small fragments (*19*)(Movie S1). Since *Hydra* is a freshwater animal, the cells need to maintain their osmotic balance against water that enters from the hypotonic environment. They excrete the surplus water into the spheroid lumen (*20*). Thus, the spheroid inflates, and the tissue is stretched at the same time (Fig. S1A-D). Once the stretching reaches a critical threshold, the tissue ruptures, causing the spheroid to deflate. Variable numbers of inflation and deflation cycles have been observed before a change of this oscillatory behavior marks the break of symmetry and mouth establishment (*21*). For example, experimental evidence shows that it is possible to bias the position of the future head but only before the oscillatory behavior transition (*22*). It has also been demonstrated that the mouth opening is stabilized after this transition (*23*) resulting in earlier release of the accumulated liquid and smaller spheroid expansions. The oscillation pattern thus changes from a high-amplitude, low-frequency regime (termed Phase I) to a low-amplitude and high-frequency one (Phase II, Fig. 1c). However, whether and how the mechanical oscillations are linked to the establishment of the hypostome organizer remained unknown.

In the current work, we used imaging and mechanical perturbations to investigate the role of inflation and deflation cycles and found that the stretching level of the tissue during inflation is essential for the downstream patterning of the epithelia. Then, through a time series RNA sequencing of the regenerating spheroids, we identify the impact of mechanical signals specifically for the appearance of the oral end of the body axis, with the *Wnt3* gene being a key target. The expression of *Wnt3* is quantitatively related to the amount of tissue stretching and the expression of this gene enables patterning in the absence of mechanical stimulation. These results facilitate incorporation of mechanical signals in a coherent framework that will explain *Hydra* patterning. Moreover, it underscores the evolutionary conserved connection between Wnt signaling and mechanical stimuli, and indicates that a lumen expansion could be a general mechanism for epithelial patterning.

Results

Mechanical oscillations are required for the head organizer establishment

Given the osmotic nature of inflation mechanism, oscillations can be perturbed by manipulating environmental osmotic pressure. Including additional osmolytes (e.g. sucrose) in the medium slows down the spheroid inflation rate in a concentration-dependent manner (*19*), and in isotonic conditions, the oscillations cease completely

(Fig. S1E-G, Movie S2). Using this approach, we observed a progressive loss of regeneration capacity (measured by the appearance of new tentacles) with increasing osmolarity. Under isotonic conditions (70 mM sucrose), spheroids completely fail to regenerate (Fig. 1B-D). However, they remain viable for several days and can reinitiate the regeneration program when transferred back to normal medium (Fig. S1H-I), indicating that isotonic environment is not inherently toxic. Rather, it suggests that the absence of mechanical input puts a temporary halt to the regeneration program.

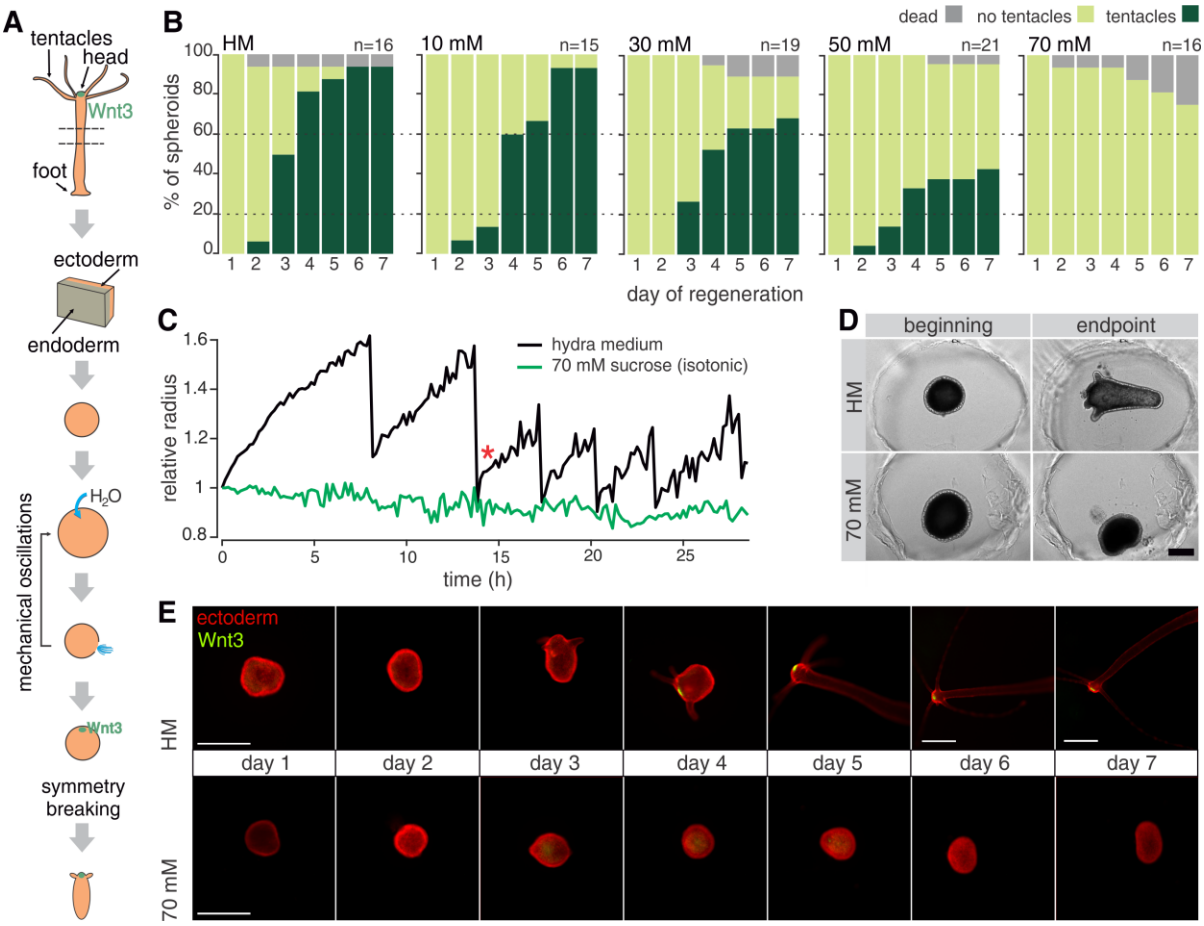

Fig. 1. The impact of mechanical stimulation on head regeneration. (A) Spheroid preparation and regeneration. **(B)** Regeneration success decreases in media with increasing osmolarities. Cumulative plots for n animals from 3 independent experiments. The concentration of sucrose in *Hydra* medium is indicated above each plot, 70 mM being isotonic. HM – *Hydra* medium. **(C)** Quantifications of the size of representative spheroids from Movies S1-S2. Note the absence of oscillations in isotonic conditions. Asterisk marks PhaseI/II transition. **(D)** Snapshots of the initial (t = 0 h) and final time points (t > 50 h) from Movies S1 and S2, demonstrating the inability to regenerate in isotonic conditions (70mM sucrose). **(E)** Fluorescent imaging of representative spheroids from a Wnt3-reporter line in normal, and isotonic conditions without oscillations. There is a known delay in the reporter visibility, which causes it to be observable only after tentacle appearance (*22*). All scale bars, 500 µm.

To answer whether mechanical input is required for the emergence of the $Wnt3^+$ organizer cells, we used a reporter line, where GFP is expressed under the Wnt3 promoter recapitulating the normal Wnt3 expression pattern (*24*). Remarkably, all spheroids lacked GFP-positive foci under isotonic conditions (Fig. 1E, and Fig. S1J). Thus, mechanical input is required for the differentiation of the head organizer rather than the execution of the downstream morphogenetic program of tentacle development. Surprisingly, even in the absence of oscillations, many spheroids elongate in the isotonic medium over time (Fig. S1K). Acquiring an asymmetric shape is, therefore, not a hallmark of molecular symmetry breaking, as previously suggested (*21*). Head regeneration in bisected animals, is also hindered in isotonic conditions, indicating that some level of mechanical stimulation is a general requirement for *Hydra* regeneration (Fig. S1L-M, Movie S3).

The readout of mechanical oscillations is continuous rather than periodic

To understand the role of these mechanical oscillations we examined the range of Phase I cycle numbers among spheroids. Such differences can result from intrinsic symmetry breaking variability among the tissue pieces. To investigate the source of this variability, we looked at the behavior of spheroids originating from different axial positions. Classical grafting experiments have demonstrated gradients of head formation and inhibition capacity along the axis. Tissue originating closer to the head is able to establish a new organizer more efficiently when grafted but, as a host environment, it is less conducive to a new organizer appearance (*25*, *26*). Therefore, we examined whether the axial origin of the regenerating spheroids also impacts their mechanical dynamics. Indeed, spheroids derived from tissue closer to the head require more cycles before breaking the symmetry than those originating further away. These results thus likely reflect the persistence of an inhibitory property bestowed by the proximity of an existing head (Fig. 2A-B). In contrast, other oscillation properties, such as cycle duration or inflation rate do not vary significantly among the measured axial positions (Fig. S2A-D).

Having established that mechanical input is indispensable for successful regeneration and that the number of Phase I oscillations correlates with an inhibitory axial gradient, we then asked whether spheroids require a specific number of cycles to be able to regenerate (a "periodic counting" model). Alternatively, they might sense the overall amount tissue stretching experienced during the oscillations, disregarding deflation events (a "continuous" model). To distinguish between these options, we imaged spheroids in a medium with intermediate osmolyte concentration (30 mM sucrose), which slows down the rate of inflation and, consequently, prolongs each cycle's

duration (Fig. S2E-H). Only spheroids from the R1 position were used, since they have the highest number of cycles on average. Assuming a counting mechanism, all cycles should be executed irrespective of their duration. Instead, we observed a decrease in the average number of Phase I oscillations in higher osmolarity (Fig. 2D). This argues that a continuous mechanism relying on the overall amount of tissue stretching is more plausible. This metric can be approximated by quantifying the area under the plot of Phase I oscillations (hereafter Phase I area, Fig. 2B-C). Indeed, sister spheroids, derived from the same axial position and from the same animal, tend to have a very similar Phase I area even in different medium osmolarities, where the number of oscillations is different (Fig. 2E-F). These results underscore the crucial role of sustained mechanical tissue stretching during inflation for successful symmetry breaking and regeneration.

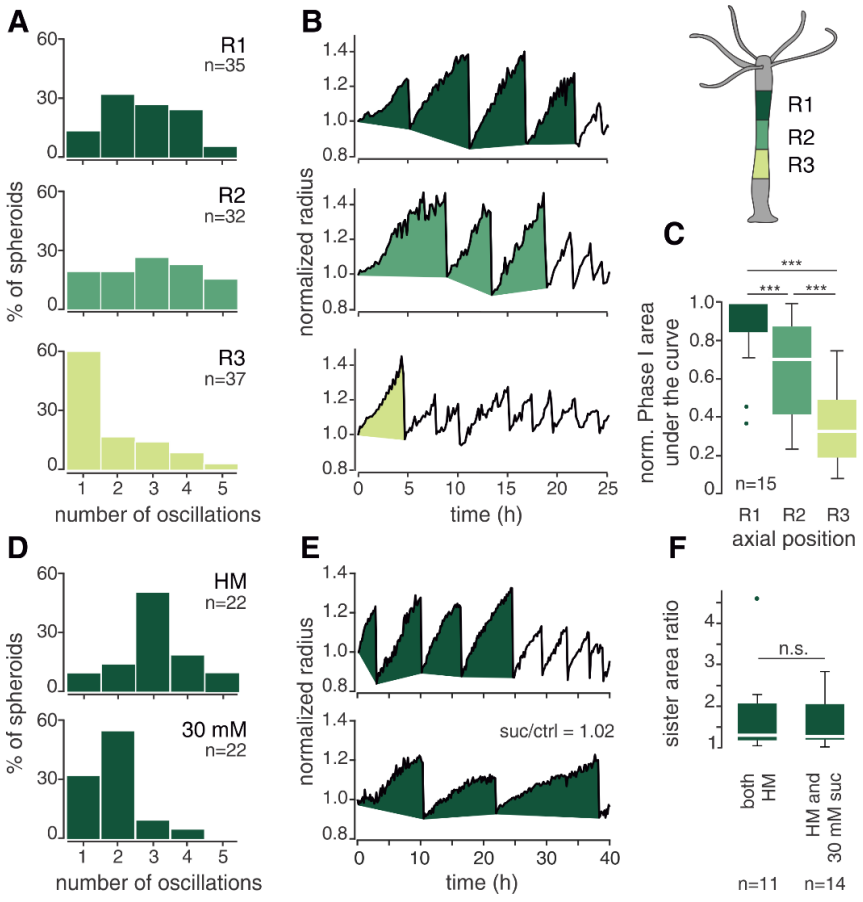

Fig. 2. Features of mechanical oscillations important for regeneration. (A) Distributions of the number of Phase I oscillations for spheroids from different axial positions (R1 – R3, see schematic). Data of n samples pooled from 3 independent replicates. **(B)** Representative examples of oscillation patterns for three spheroids derived from different axial positions of the same individual. Filled parts correspond to Phase I oscillations. **(C)** Quantification of the Phase I area under the curve for 15 animals from **(A)** for which data were available for all three positions. Measurements for each animal were normalized to the R1 position. **(D)** Comparison of the oscillation number distribution for R1 spheroids in HM vs. 30 mM sucrose (n samples from 5 independent experiments). **(E)** A representative example of two spheroids from the identical axial position of a single animal (sister spheroids) showing a similar

Phase I area in different media. **(F)** Area ratios for pairs of sister spheroids. They were either both cultured in *Hydra* medium or one of the pair was put into 30 mM sucrose. The ratios for each pair are always normalized to the sister with a smaller Phase I area, irrespective of the conditions (n samples pooled from 3 independent experiments). Data in C and F were analyzed using the Mood's median test. *** $p < 0.0005$ ($p_{R1/R2}$=1.0322e-4, $p_{R1/R3}$=2.9061e-08, $p_{R2/R3}$=8.7409e-04)

Head, but not foot, regeneration transcriptional program shows a strong mechanical dependence

To understand the molecular impact of tissue stretching, we performed a time course of RNA-sequencing in spheroids (Fig. S3A-D) under both control and isotonic conditions. This identified ~ 2300 genes exhibiting at least a 2-fold change in expression over the course of normal regeneration. Strikingly, we could not detect any periodic changes associated with spheroid deflations (Fig. S3B), further corroborating the previous findings of a continuous readout. Neither was there an indication of the samples experiencing osmotic stress in 70 mM sucrose (Fig. S3C). We then combined these temporal data with a positional RNA-sequencing of isolated body pieces from individual animals (Fig. S4A-B). The body parts' transcriptomes allowed us to map gene expression profiles onto positional identities along the axis (Fig. 3A). When projected into this map, the time course data of >150 individual spheroids per condition revealed their regeneration trajectories. Under normal conditions, spheroids follow a relatively straightforward path from a body-like state towards a regenerated animal with both ends of the axis established (Fig. 3B). However, in isotonic medium, without mechanical input, the trajectory lacks directionality and follows an undulating path that eventually turns toward a foot-like identity (Fig. 3C).

We then looked at the top 10 % of genes (n=115) most severely affected by the removal of mechanical input (Fig. S3E), to gain insight into the transcriptional changes behind the observed developmental differences. The majority (n=73) of these genes were increasing over time during normal regeneration, while a smaller portion (n=37) showed a decreasing trend (Fig. 3D). Interestingly, these groups of genes also have very different axial expression profiles. The rising genes show a clear enrichment in the head region, consistent with their role in setting up the body part most affected by the lack of mechanical oscillations. On the other hand, the group of decreasing genes shows enrichment in the undifferentiated body column, highlighting the failure to differentiate properly when oscillations are inhibited (Fig. 3E). Looking at functional annotations within the rising cluster (Table S1 and S2), we found an enrichment of extracellular matrix related genes, which likely reflects the tissue remodeling that has to occur in order to tolerate the mechanical stress and to regenerate.

More importantly, several components of the Wnt signaling pathway were also enriched, including three ligands of the canonical Wnt signaling (Fig. 3F).

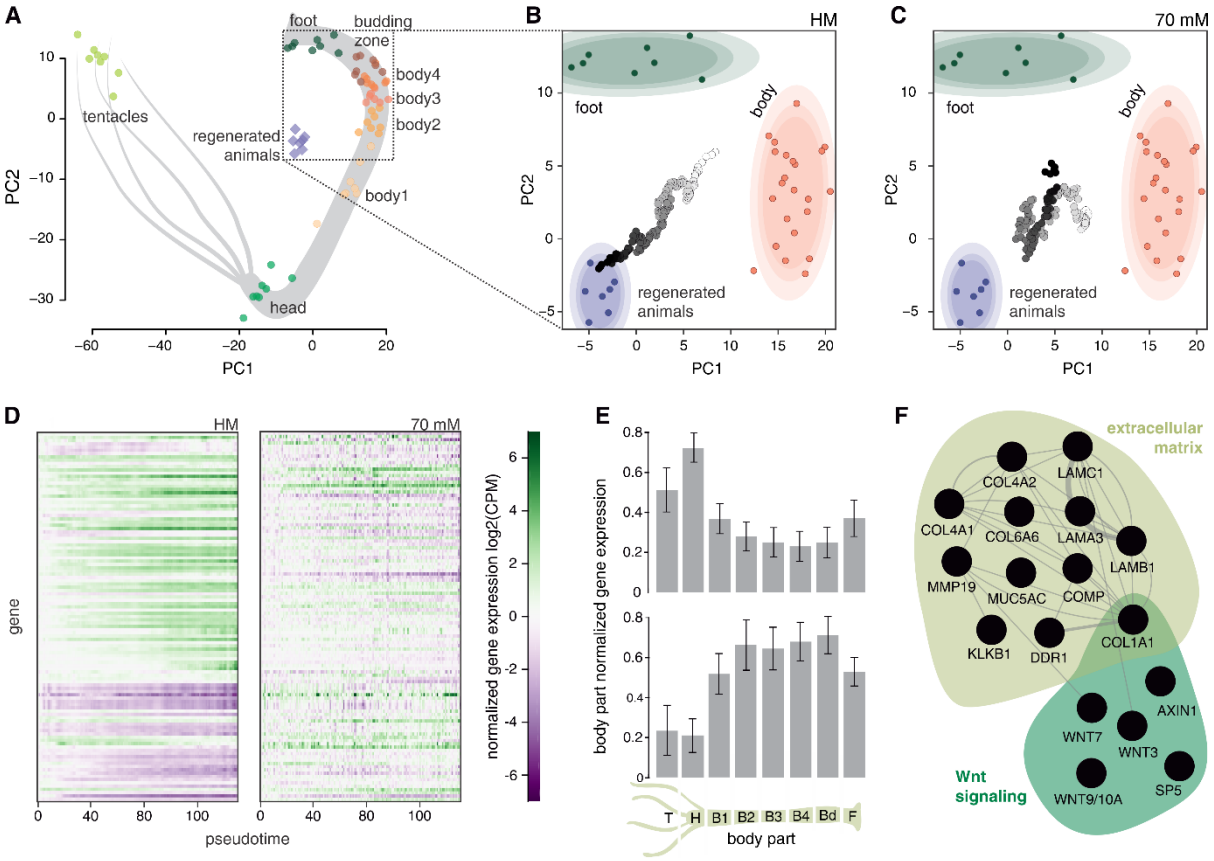

Fig. 3. Transcriptional changes in regenerating spheroids. (A) PCA plot of different body parts based on their transcriptional identity. Full animals regenerated from spheroids (harvested 72 h after cutting) are also included. Dotted box indicates the area enlarged in the following panels. (B – C) Projections of the spheroid time-course data into the body PCA space, with **(B)** and without mechanical input **(C)**. Shaded ovals around the body parts (body2 – body4) and regenerated animals data correspond to 90 %, 80 %, and 70 % gaussian confidence intervals (light to dark shading). The color of the projected time-course data represents the pseudotime progression (from white to black). Each individual dot corresponds to a single spheroid. **(D)** Heatmaps of the behavior of the top 10 % (n=113) genes affected by lack of mechanical simulation in control and isotonic conditions. For each gene, the initial (t^0) $\log_2$(CPM) value was subtracted. **(E)** Average expression patterns in the body for the increasing (upper panel) and decreasing genes (lower panel) from D. The expression data for each gene were normalized to the body part with the highest expression of that gene, before averaging per body part. Error bars show 95 % confidence intervals. **(F)** Subnetworks of genes showing functional enrichment within the upregulated genes, affected by lack of oscillations. Edges indicate physical, genetic, and predicted interactions or coexpression in human cells (data from genemania.org).

Before further examining the head regeneration requirements, we focused on the aboral axis end. The trajectory of spheroids in the isotonic medium moving towards a foot-like identity suggests an interesting possibility to regenerate a foot without the head. This would mean that the axis ends can be largely independently established and differ in the needs for mechanical stimulation. Indeed, when examined for the characteristic foot peroxidase staining, about 50 % of these spheroids are positive for the marker (Fig. 4A-D). Moreover, looking at the expression pattern of known early foot markers, such as *CnNK2* (*27*)and *Dlx1*(*28*), we discovered a small cluster of foot-specific transcription factors with a coordinated temporal behavior (Fig. 4E-F). All these genes show a steep early rise in transcript abundance, followed by a plateau at high expression levels. This progression is not abolished by the absence of mechanical stimulation, even though it becomes more noisy (Fig. 4E), which might account for the decrease in the success of foot regeneration under isotonic conditions. Knockdown, when successful (Fig. S4C), of several of these factors (*Dlx1, Gata3*) also demonstrates their importance for the foot establishment, as it decreases the ability to regenerate a foot after bisection (Fig. 4G). Our data thus support the view that the two poles of the oral/aboral axis function as separate (yet connected) organizing centers (*29*) with differential requirements for mechanical stimulation when being established de novo in the context of tissue spheroids.

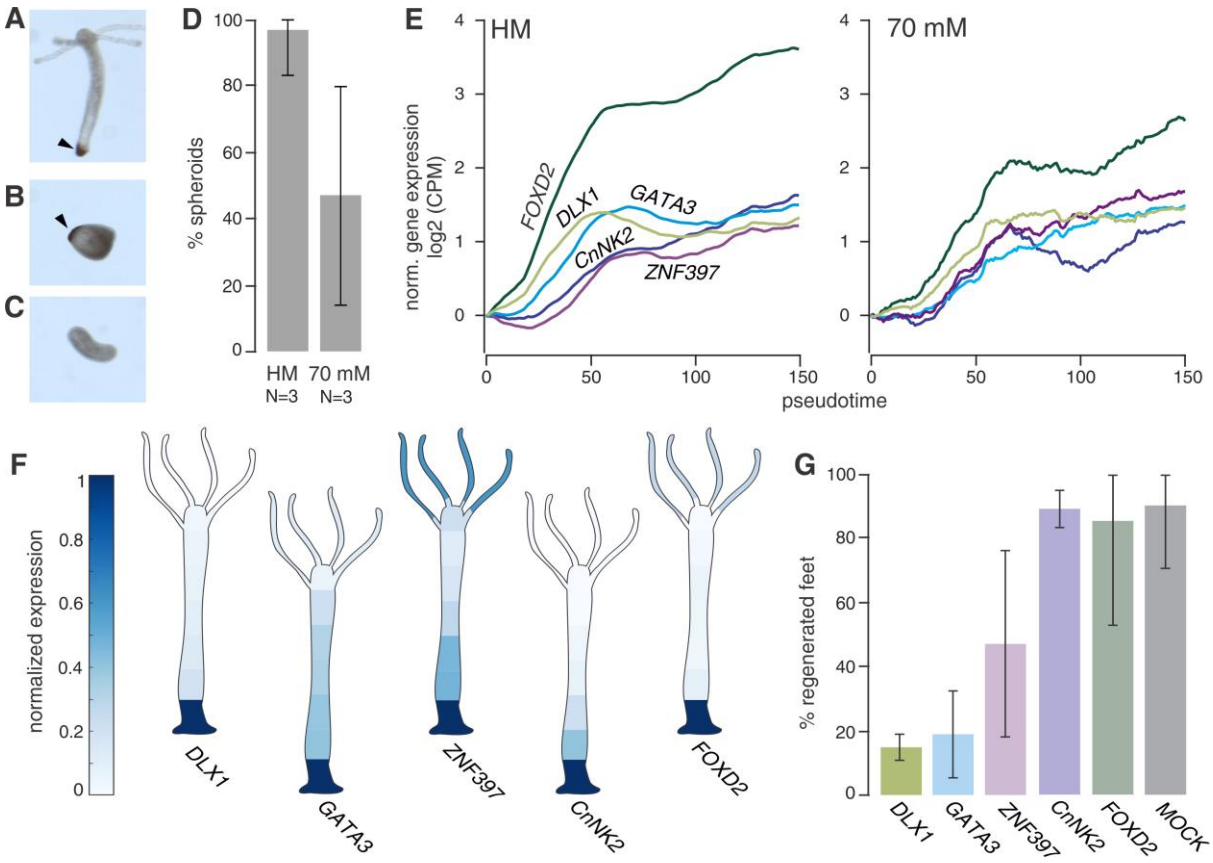

Fig. 4. Foot regeneration without mechanical stimulation. (**A**) Representative spheroid that regenerated under control conditions shows peroxidase staining in the basal disc (foot). (**B**) Similar foot peroxidase staining was observed in some spheroids cultured in 70 mM sucrose in the absence of a head. (**C**) Elongated spheroids developing in the absence of mechanical stimulation do not always have a peroxidase marked foot. (**D**) Quantification of foot marker presence in control (HM) or isotonic medium (70mM sucrose) grown *Hydra* spheroids. Plot shows the average percentages of peroxidase-positive spheroids from 3 independent experiments. Error bars indicate 95% confidence intervals. 42 spheroids were examined in total for the control, and 26 for isotonic conditions. (**E**) Expression patterns of the small cluster of foot-specific transcription factors in control and isotonic medium (70 mM sucrose). Lines indicate moving averages (moving window width is 36 pseudotime points). (**F**) Average body expression patterns of these genes in homeostatic animals (averaged from 8 animals and normalized for each gene to the body part with highest expression level). (**G**) Results of foot regeneration in bisected animals upon knockdown of these transcription factors. Averages from 3 independent experiments are shown.

Wnt3 expression functions as a quantitative readout of tissue stretching

Coming back to the impact of tissue stretching on Wnt signaling, we noticed that the lack of mechanical stimulation affected the expression dynamics of all the canonical Wnt signaling ligands (Fig. 5A-B, Fig. S5A). These genes are activated sequentially during normal regeneration in bisected animals (*16*, *28*) and we observed a similar progression for spheroids. After the pseudotime point 80, most of the transcripts rapidly increase, reflecting a successful establishment of the mouth organizer. However, none of these changes takes place without mechanical stimulation. Interestingly, *Wnt3* expression has a behavior distinct from the other Wnt ligands (Fig. 5B). Previous studies have shown that *Wnt3* is upregulated very early in response to injury (*30*, *21*) and then sustained throughout the regeneration process. Yet, we observe that in isotonic conditions, its expression fails to be sustained and rapidly decreases. While such dynamics can be explained by tissue stretching acting to either stabilize the transcript or activate *Wnt3* transcription, the analysis of intronic vs. exonic reads favors the latter option (Fig. 5C, Fig S5C). Even though both conditions show comparable levels of exonic reads at the beginning of the time course, transcription is clearly more active in *Hydra* medium, as indicated by the levels of intronic reads. As time elapses, the transcript dynamics of the control sample are still predominantly transcription-driven up to the pseudotime point ~100, whereafter mRNA stability/degradation has a more prominent role. This is probably a result of switching on more complex regulations while the organizer is established. Without tissue stretching, however, the intronic counts quickly decrease and plateau at baseline levels, suggesting that the gene transcription is switched off. Subsequently, the exonic reads continue decreasing, as, in the absence of transcription, the temporal development is solely determined by the mRNA degradation. We therefore hypothesized that the

Wnt3 gene transcriptional output functions as a readout of the mechanical input. To test this hypothesis, we performed a qPCR time course under different osmolarities, corresponding to different intensities of mechanical stimulation. As expected, the ability to sustain *Wnt3* expression was anticorrelated with the mechanical input strength (Fig. 5D-E, Fig. S5D-E). To further verify that *Wnt3* transcription is coupled to tissue stretching, rather than tearing upon deflation, we measured *Wnt3* mRNA levels in spheroids that were reintroduced to *Hydra* medium after 12 h preincubation in an isotonic medium. This initial period without oscillations served to lower the *Wnt3* transcript levels. Importantly, our understanding predicts that, when reintroduced to *Hydra* medium, *Wnt3* levels would begin to rise because of tissue stretching before the spheroids collapse for the first time. This is indeed what we observed (Fig. 5F), further arguing for the *Wnt3* transcription to be connected with tissue stretching, rather than deflation, in the context of spheroid oscillations. Since head-regenerating halves of bisected animals also show a decrease of regeneration success in an isotonic medium without oscillations, we investigated whether this results in lower *Wnt3* mRNA levels. Whole mount *in situ* hybridization of such samples has confirmed this assumption. We observe that in the majority of bisected animals without mechanical stimulation the initial expression fails to be sustained (Fig. S5F).

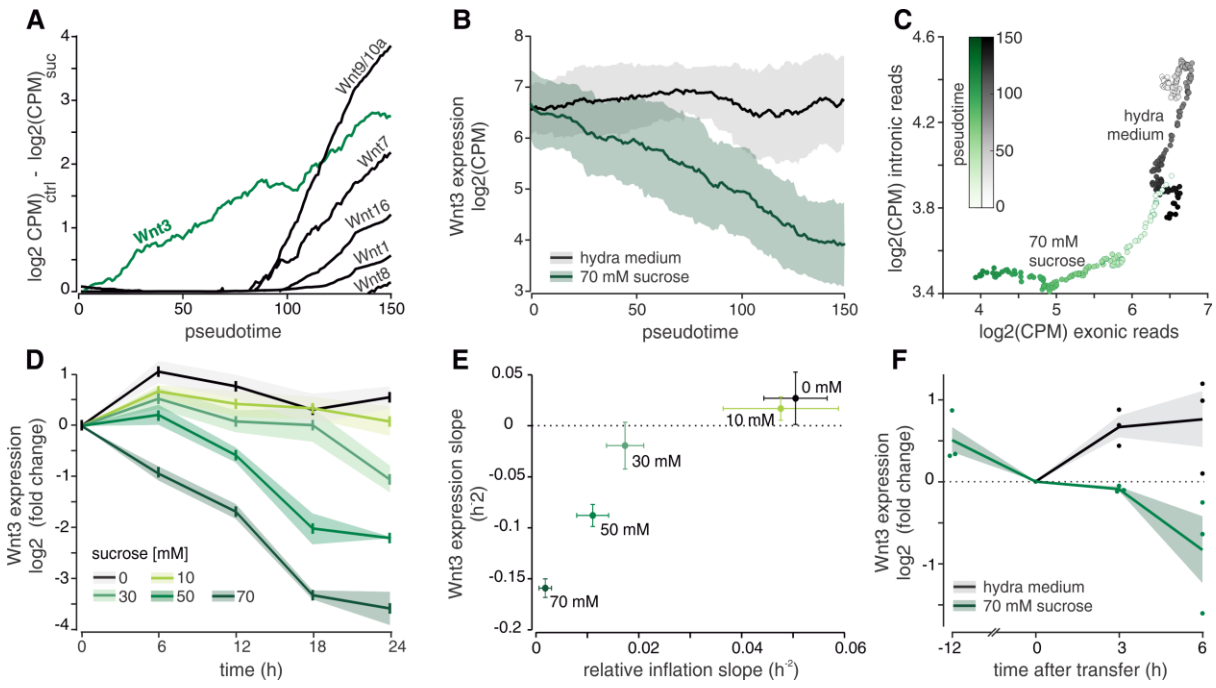

Fig. 5. The relationship between tissue stretching and Wnt3 expression (**A**) Temporal development of the expression differences of canonical Wnt ligands between control and isotonic conditions. (**B**) Wnt3 expression patterns in HM and isotonic medium. In both A and B the lines indicate moving averages (moving window width is 36 pseudotime points). Shaded area represents a moving standard

deviation (window width identical to the mean). (**C**) Scatter plot of intronic versus exonic reads for the Wnt3 transcript from the single-sphere RNA-seq time course. Data were smoothened using a moving average with a window size of 36 pseudotime points (**D**) Wnt3 expression dynamics in different osmolarities, measured with qPCR. Data for each condition were normalized to the initial time point. Shown are averages from 3 independent biological replicates. Shaded areas represent standard error of the mean. (**E**) The relationship between the spheroid inflation rate (slope) and the slope of Wnt3 expression (for raw data see Fig S1a and S5c). The error bars indicate 95% confidence intervals. (**F**) Wnt3 expression in spheroids, preincubated in isotonic medium (70 mM sucrose), upon transfer to HM or continued incubation. Only expanded spheroids before deflation were collected from HM at 3 and 6h after transfer. Data from 3 independent biological replicates, normalized to the transfer time point. Lines indicate averages, shaded area standard error of the mean.

Wnt3 expression is sufficient to rescue the absence of mechanical stimulation

We then asked whether providing Wnt3 would be sufficient to rescue regeneration inthe absence of mechanical stimulation. To this end, we generated animals overexpressing *Wnt3* in the whole ectoderm (Fig. 6A-D), which showed a branched morphology with multiple heads (Fig. 6B). This phenotype is similar to the one observed after β-catenin overexpression (*32*). Interestingly, spheroids derived from these animals were able to regenerate (Fig. 6C), sometimes producing regenerates with multiple tentacles that would later resolve into several heads. Moreover, body column pieces of these animals showed organizer-like properties when transplanted into a wild-type context, as they induced ectopic head formation (Fig. 6D).

Importantly, these animals enable us to examine the sufficiency of *Wnt3* expression for proper regeneration in the absence of mechanical oscillations. Indeed, spheroids derived from the *Wnt3* overexpressing animals were also able to regenerate in isotonic conditions, showing that artificially sustaining the *Wnt3* expression circumvents the need for mechanical stimulation. Interestingly, while the oscillatory behavior is not necessary for these spheroids to regenerate, we also noticed they are able to inflate more before collapsing than the wild-type sphreoids (Fig. 6E, Fig. S5G). One possible explanation of these observations would be a change of tissue mechanical properties upon Wnt3 overexpression. Successful development without oscillations was also observed in an orthogonal experiment with early buds. In this approach, spheroids are derived from early buds and already possess an organizer that renders them unaffected by the lack of mechanical stretching (Fig. 6E-G, Movies S4 – 7). We therefore conclude that sustaining *Wnt3* expression is both necessary and sufficient for successful *Hydra* head organizer regeneration and that it is made possible by its stretching-dependent transcriptional activation.

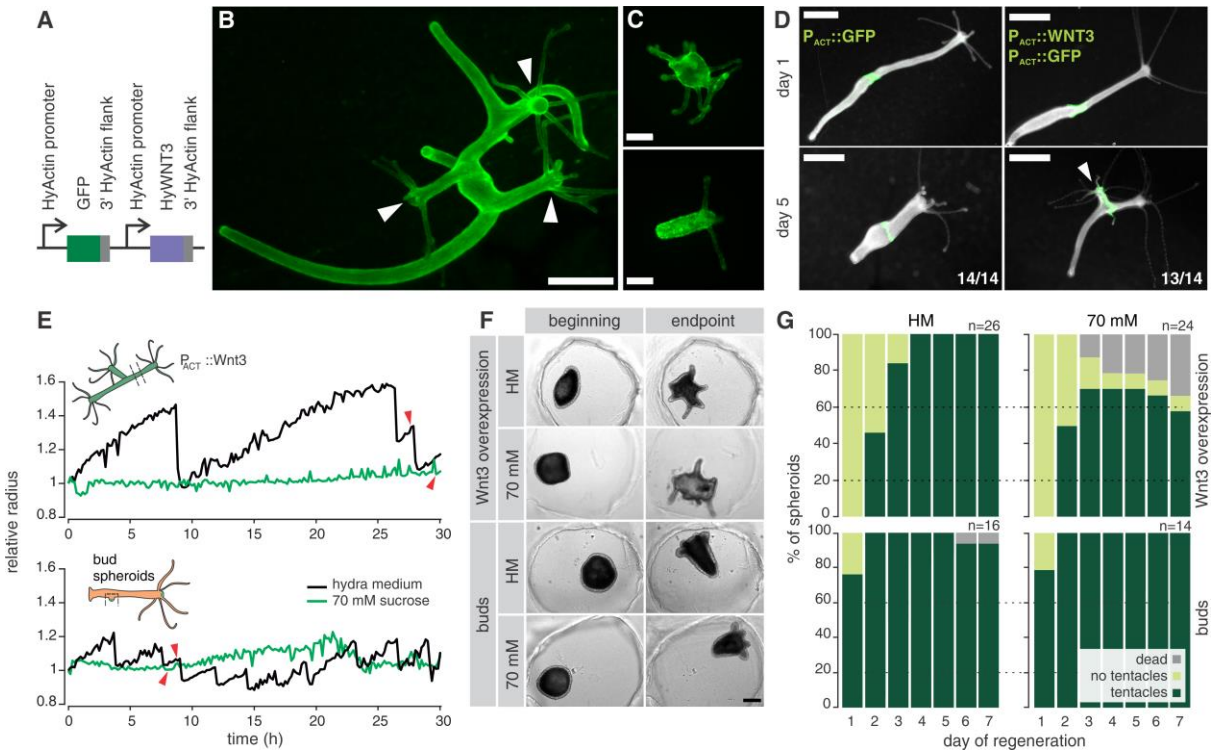

Fig. 6. Rescue of head regeneration in the absence of mechanical stimulation. (**A**) Schematic of the construct used to generate transgenic animals. Both *GFP* and *WNT3* expression is driven by *Hydra* actin promoter and flanked by a 3' UTR of the *Hydra* actin gene. GFP serves as a transgenesis marker (**B**) An example of a fully transgenic individual expressing the construct in the ectoderm and showing a typical branched morphology with ectopic heads (arrowheads). (**C**) Examples of regenerated Wnt3-overexpressing spheroids. Numbers indicate the incidence of the multi-tentacle phenotype in regenerating Wnt3-overexpressing spheroids. Data were pooled from three independent experiments. (**D**) Ectopic head (arrowhead) induction upon grafting tissue (green) from Wnt3-overexpressing animal (right) vs. assimilation of tissue from a control GFP-expressing animal (left). Numbers indicate the number of grafts with identical phenotype to the one shown for each condition (data pooled from three independent experiments). Fluorescence images merged with darkfield images of the entire animals. (**E**) Quantifications of the spheroid behavior for Movies S4 – S7 representative of regeneration rescue in the presence of Wnt3. Red arrowheads indicate the emergence of the first tentacle. (**F**) Snapshots of the initial time points (t = 0 h) and regenerated animals (t > 50 h) from Movies S4 – S7. (**G**) Spheroids derived from Wnt3-overexpressing animals and buds regenerate equally well irrespective of the presence or absence of mechanical stimulation. Cumulative plots of n samples combined from 3 independent replicates. Scale bars in (B) and (D) correspond to 1 mm, in (C) and (F) to 200 µm.

Discussion

Despite the fact that mechanical oscillations are a prominent feature of *Hydra* regeneration from small tissue pieces, their role in this process had long remained elusive. We show that the mechanical stretching, caused by these inflation/deflation cycles, is the critical cue for the *de novo* differentiation of an organizer in this context. Similarly, even when animal halves are establishing a new hypostome after bisection, some level of inflation-driven stretching is required. In this case, the success rate decreases dramatically when the animals are placed in isotonic medium that prevents the osmotic inflations. While we cannot completely exclude the possible side effects of our experimental intervention beyond changing the oscillatory behavior, we do not see evidence for the outcome of the experiments being stress-driven, or dependent on the osmolyte used. Since mechanical oscillations also occur in the re-aggregates of cells from dissociated *Hydra* (*21*), the emergence of organizers there is likely accomplished through a similar mechanism. Moreover, pulsating behavior has also been observed during *Hydra* embryogenesis. After the two epithelial layers are formed, the embryos display rhythmic expansions and contractions that endure until hatching (*33*).Thus, various modes of the oral organizer emergence in *Hydra* are associated with mechanical stimulation in the form of tissue stretching.

The key molecular pathway, which specifies the *Hydra* mouth organizer, is the canonical Wnt signaling (*14*). It has been shown that its ectopic activation can trigger supernumerary organizers in the body column and consecutively, ectopic axis formation (*15*). Among all its ligands, Wnt3 has the most prominent role, as it is the first to be expressed when a new organizer emerges (*16*), and its expression can be maintained through a positive feedback loop (*24*). We see that mechanical oscillations are critical for regulating the *Wnt3* gene expression (Fig. 7), with the levels of transcripts depending quantitatively on mechanical stimulus. Upregulation of Wnt signaling output after mechanical stimulation has been observed during the gastrulation of *Nematostella* (*34*) and zebrafish embryos (*35*) as well. In these cases, the link of the Wnt cascade with mechanics appears to be the phosphorylation of β-catenin. In *Hydra*, such a link is still unknown, but the identification of *Wnt3* as the key target gene enables further investigation of the mechanism that transforms a physical signal into biochemical output. Previous work on the Wnt3 promoter has already identified several regulatory elements (*22*, *30*) that can serve as a departure point for a promising investigation. Nevertheless, the fact that the hypostome axial organizer

emergence is linked molecularly with tissue stretching prompts us to reevaluate the prevailing model on *Hydra* axial patterning.

Hydra axial patterning can be largely explained by a reaction diffusion model proposed originally by A. Gierer and H. Meinhardt (*36*). An activator/inhibitor pair, with the diffusion coefficient of inhibitor being higher than the activator one, is anticipated to be at the core of a mechanism that guarantees local self-activation and long-range inhibition of the organizer identity. In essence, the mechanistic explanation is similar to the one proposed by Turing (*37*) but despite its success in explaining a variety of phenomena, and despite the identification of Wnt3 as the likely head activator (*38*), no activator/inhibitor pair suitable for the particular model has been found. The recent identification of the transcription factor Sp5 as a possible repressor (*30*) also highlighted the need to expand our thinking on how the short-range activation and long-range inhibition can be materialized. Several theoretical models, both in other systems (*39*) and *Hydra* (*40*) have also already considered the option that these signals might be of mechanical nature. Since our results demonstrate a concrete connection between a mechanical property and the expression of a crucial morphogen, they will be valuable for future modelling efforts trying to bridge the current biochemical framework with tissue mechanics.

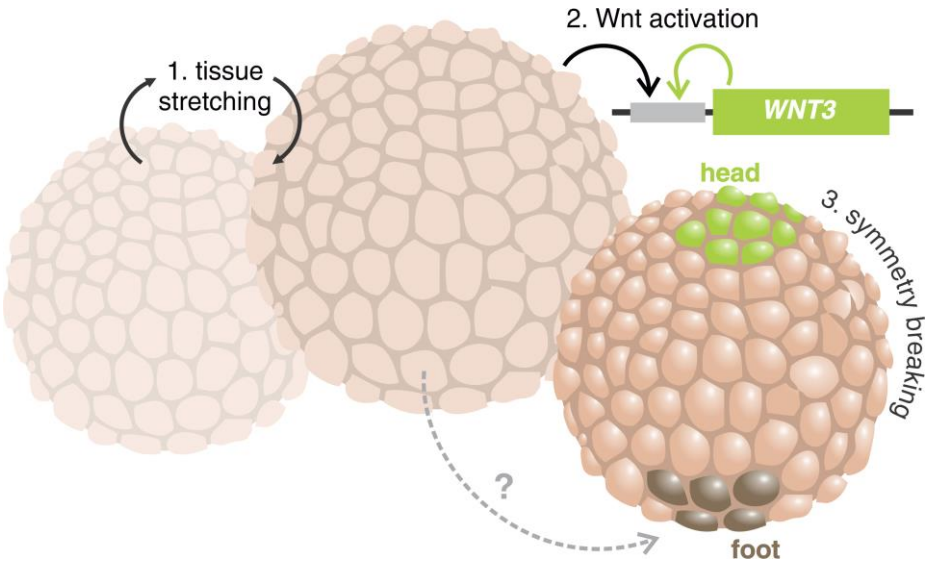

Fig. 7. The role of mechanical oscillations in *Hydra* whole-body regeneration. Mechanical inflation/deflation cycles have a critical role in providing tissue stretching, which activates Wnt3 transcription during *Hydra* regeneration. The expression of this gene can later be self-sustained as is pivotal for specifying the oral pole of the body axis.

The integration of mechanics with biochemical patterning cues remains an open question and is closely related with the spatial specification of the organizer. While all cells of the spheroid are being stretched, only some of them will finally differentiate into the head organizer. We hypothesize that this choice can be driven by the heterogeneity of cells response to mechanical stretching in the tissue, which could result in different levels of *Wnt3* expression across the spheroid. This model is consistent with recent experimental work indicating a role for supracellular actin fibers in positioning the organizer (41, *42*). Moreover, the foot (aboral) pole of *Hydra* body axis emerges in our results as a largely autonomous counterpart to the mouth (oral) pole. Not only can it be established without mechanical oscillations but also seems to be specified faster than the mouth organizer. It is therefore possible that the initially foot-primed cells create an exclusion zone for the hypostome differentiation. Such mechanism would ensure that even if the opposite poles of the axis can emerge independently, they would be properly positioned relative to each other.

Since fluid-filled lumens are one of the leitmotifs of animal morphogenesis (*43*), our system offers an excellent platform to study the general rules of lumen formation and function, in particular the relationship between pressure-dependent cell stretching and cell fate decisions(*3*, *4*). Several developmental contexts where lumen expansion affects cell fate changes have been identified. For example, proper alveolar differentiation in the embryonic lung depends on sufficient mechanical stimulation from the pressure of amniotic fluid (*44*). However, whether the downstream signaling pathways (in this case FGF) also provide a quantitative readout of mechanical stimulation similar to what we describe is not known. While such mechanisms could work with many signaling molecules, the case of Wnt is particularly intriguing thanks to its ancient evolutionary past. The origin of Wnt signaling coincides with the origin of multicellularity (*45*), thus suggesting that its mechanosensitivity in *Hydra* and other cnidarians (*34*) reflects an early evolutionary connection. Whereas first multicellular animals likely had a poor signaling repertoire, the combination of biochemical signals with mechanical cues may have enabled body plan elaboration (*46*), as we report here for *Hydra* spheroids.

Moreover, mechanical input driving Wnt expression is a widespread phenomenon in diverse developmental contexts (*47-49*), as well as in disease (*50*). In particular, tissue stretching seems to activate Wnt-signaling ligands transcriptionally in some of these cases. We thus suggest that this might be a conserved mode of Wnt signaling activation through mechanical stimulation. As we learn more about the upstream mechanosensitive pathways in *Hydra* it will be interesting to see whether only the

regulatory logic is conserved in higher metazoans or also the molecular players and how these evolutionary choices could have impacted the emergence of more complex body plans. Taken together, the mechanism transforming mechanical stimuli into a quantitative transcriptional output, which we have identified in *Hydra*, represents a potentially conserved implementation of mechano-chemical crosstalk in basic morphogenetic processes such as luminogenesis and tissue stretching.

Material and Methods

Animal strains and culture conditions

All experiments were performed using either the AEP or 105 strains of *Hydra vulgaris*. Animals were kept in *Hydra* medium (HM, 1mM $CaCl_2$, 0.2 mM $NaHCO_3$, 0.02 mM KCl, 0.02 mM $MgCl_2$, 0.2 mM Tris-HCl pH 7.4) at 18 ºC and fed with freshly hatched *Artemia* nauplii 3 times a week. Individuals without buds, starved for 24 hours, were used for experiments, if not indicated otherwise. All experiments were performed in accordance with ethical standards and the Swiss national regulations for the use of animals in research.

Spheroid preparation

Details of spheroid generation, imaging and oscillation analysis can be found in a previously published protocol (*51*). Animals were bisected (exact position of the initial cut for different experimental designs is detailed below) and one or several thin tissue rings were obtained by sequential cutting. The rings were then split in 2 - 3 rectangular pieces that were left to close for ca. 2 - 2.5 h in HM or dissociation medium (DM, 3.6 mM KCl, 6 mM $CaCl_2$, 1.2 mM $MgSO_4$, 6 mM sodium citrate, 6 mM sodium pyruvate, 4 mM glucose, 12.5 mM TES, pH 6.9) at room temperature. Properly closed spheroids (typical diameter 300 - 500 µm) were then separated from the pool and used for further experiments.

Live imaging of developing spheroids

Multi-chamber LabTek slides (Nunc) were used for imaging. Spheroids were placed in individual agarose wells (ca. 1 mm in diameter) within the chambers, to retain them in the field of view. The wells were created by coating the bottom of the chambers with a 2-3 mm thick layer of 1% agarose in HM and puncturing holes using a 1 ml micropipette tip after the gel solidified. The chamber was then filled with the desired imaging medium. In case of sucrose treatments, the agarose gel contained sucrose in concentrations equal to the overlaying medium. For inhibitor treatments, drug

concentration in the imaging medium was adjusted, taking the volume of agarose into account. To prevent diluting the imaging medium in the chamber, closed spheroids were first transferred to a dish with bigger volume (ca. 10 ml) of the imaging medium and positioned in the imaging wells only after this wash. Samples were imaged every 10 min at 21 ºC under brightfield illumination using the Nikon Ti2-Eclipse microscope with a 10x CFI Plan Apochromat Lambda objective (Nikon) and iXon-Ultra-888 EMCCD camera (Andor). Images were acquired in the 1024 x 1024 format, with a pixel size of 1.3 µm.

Quantification of oscillation parameters

Brightfield images were batch segmented in Fiji (*52*). A course median filter (radius = 60 px) was first applied, followed by Phansalkar local thresholding (radius = 50 px, r and k parameters = 0) and another round of median filtering (radius = 20 px). The area of segmented objects bigger than 5000 µm^2 including holes was then measured. Radius was calculated from these values, assuming a spherical object. Radius data for each sample were normalized to the starting value and further processed in Matlab using custom functions to extract the slope, amplitude and period of the Phase I oscillations. The number of oscillations and Phase I/II transition was determined manually by two independent experimenters, using a criterion of at least 30% decrease in the amplitude and doubling of the oscillation frequency.

Quantifying average ectoderm thickness

Spheroids from the line *AEP ecto pAct::eGFP* (*53*) were prepared and imaged as previously described. Samples were imaged every 10 min at 21 ºC using the Nikon Ti2-Eclipse microscope with 488 nm laser illumination (Toptica iBeam smart, 500 mW) with a 20x CFI Plan Apochromat Lambda objective (Nikon) and iXon-Ultra-888 EMCCD camera (Andor). Images were acquired in the 1024x1024 format, with pixel size of 0.65 µm. Care was taken to always image the equatorial plane of the spheroid. Images were then processed in Fiji. First, the contrast was adjusted and the images were then smoothed by two iterations of the 3x3 unweighted smoothing function and segmented using the global segmentation function. For each image, two segmentations were generated. One of the entire area of the optical section, including the tissue, and another one of the inner cavity. The radius was then calculated as √(area/π). For each image, the average tissue thickness was taken to be the difference of the two radii.

Plasmid electroporation for sparse GFP labelling of cells

Plasmid DNA of the HotG plasmid (*53*) was extracted from liquid bacterial culture using the EndoFree Plasmid Maxi Kit (Qiagen). 20-25 animals per treatment were transferred into an electroporation cuvette (Gene Pulser / Micro Pulser Electroporation Cuvette 0.4 cm gap; or Bio-Rad electroporation cuvettes 4 mm gap; VWR), washed with MiliQ water twice and then incubated at 4 degrees for 30 minutes followed by RT for 30 minutes. Residual water was removed and 200 µL of a plasmid solution (10 µg plasmid and 10 mM Hepes, to 200 µL) was added to each cuvette. Animals were incubated with this solution for 5 minutes. After relaxation of the animals, two pulses (150 V range) were applied for 75 ms (Gene Pulser II with RF module; Bio-Rad). After electroporation, 500 µL of ice-cold *Hydra* medium was added to the animals. Animals were carefully transferred into a new Petri dish filled with pre-chilled *Hydra* medium. Electroporations were performed in this manner on three days (0, 2 and 4). Animals were used for experiments when first GFP+ cells appeared (~ 1 week after the last electroporation).

Scoring regeneration and Wnt-center appearance in spheroids

Spheroids from the lines *AEP ecto pAct::eGFP* (*53*)and *AEP ecto pAct::dsRed, pWnt3::eGFP* (*24*) were prepared as described above. Animals were bisected at 20% of the body length below the head and one or two rings per animal were generated. Spheroids were left to close in HM. Similar to previous studies (*19*), we used sucrose to alter the medium osmolarity. Sucrose was dissolved in HM to the desired concentration (0, 10, 20, 30, 50 and 70 mM (isotonic)), supplemented with antibiotics (50µg/ml kanamycin, 100µg/ml streptomycin) and filter sterilized. Spheroids were randomly split among the conditions (0 and 70 mM only for Wnt3-reporter line) in 24-well plates, kept at 18 ºC, and scored for the presence of tentacles in 24 h intervals for 7 days. Additionally, the presence of the organizer was assessed in the Wnt3-reporter line spheroids by fluorescence imaging. The Zeiss AxioZoom V.16 fluorescent stereomicroscope with the Zeiss Axiocam MRm CCD camera was used. Finally, the regenerated animals/surviving spheroids were fixed on the 7th day of the time course and stained to determine the presence of the foot.

Experiments with restarted oscillations

AEP ecto pAct::eGFP spheroids were prepared as described above, and the whole population of properly closed spheroids was transferred to 70 mM sucrose in HM to prevent mechanical oscillations. Samples were kept in this medium for 72 h at 18 ºC. Surviving spheroids were then randomly split into two groups and either

transferred to 70 mM sucrose again (controls) or to HM, allowing the mechanical oscillations to restart. Both populations were monitored daily for tentacle appearance as in the previous experiments.

Scoring head regeneration in bisected animals

AEP ecto pAct::eGFP animals were bisected at 50% body length and the halves were kept separately in the wells of 24-well plates at 18 ºC. Tentacle appearance was monitored in 24 h intervals in the foot halves for 5 days.

Peroxidase foot staining

The staining was performed as previously described (*54*). Briefly, animals were relaxed in 2 % urethane in HM and fixed with 4 % paraformaldehyde in HM at 4 ºC overnight. Animals were then washed in PBS + 0.1 % Tween-20 for 5 min and stained for 15 min in the staining solution (0.02 % diaminobenzidine, 0.03 % hydrogen peroxide, 0.25 % Triton-X in PBS). To stop the enzymatic reaction, samples were washed once again in PBS+Tween for 15 min. The whole staining procedure was performed at room temperature with mild agitation.

Imaging and quantification of oscillations in spheroids of different axial origin

To obtain spheroids from different axial positions, the head of the *AEP ecto pAct::GFP* animals was cut away at ~ 10 % of the body length and three rings of tissue were obtained sequentially. Each ring was split into two pieces. Pieces were incubated at room temperature for 2.5 h in DM while closing. To allow backtracking of the piece identity, sister pieces from each ring were kept in separate wells of a 24-well plate, noting the axial position and animal of origin. Similar arrangement was followed for imaging, which otherwise proceeded as described above. Quantifications of oscillation parameters from obtained time-lapse images were also performed as outlined previously.

RNA-sequencing time course of developing spheroids

Over the course of 10 h, few dozens of spheroids were prepared every hour from the 105 strain, let to close for 2 h in DM and then transferred to either HM or HM with 70 mM sucrose. 8 spheroids from each batch were then collected 3 h and 13 h after cutting the last batch, thus creating a time course spanning a window of 22 h. Spheroids were collected individually in 96 well plates in 45 µl of RLT+ buffer (Qiagen) and stored at – 80 °C for a later RNA purification. This was performed using the Zymo Direct-zol MagBead reagents following a modified manufacturer protocol. Briefly, 45µl of Zymo Binding Buffer and 4µl of MagBeads were added to the samples/RLT+ buffer

and incubated for 10min. Beads were washed 3 times with 100% ethanol and incubated with 12.5µl of DNAseI (Zymo) for 10min. The RNA was captured back on the beads using 100µl of MagBead PreWash buffer (10min incubation). After washing the beads 3 times with 100% ethanol, elution was performed with water (13µl) at 55C for 15min. All above incubations were performed at room temperature on a plate shaker unless specified. The resulting RNA quality was assessed using bioanalyser or tapestation RNA HS kit, and concentration determined using Qbit. cDNA amplification was performed using the SmartSeq2 approach as per the original protocol (*55*). Full length cDNA was processed for Illumina sequencing using Tagmentation with an in-house purified Tn5 transposase (*56*): 1ng of amplified cDNA was tagmented in TAPS-DMF buffer (10mM TAPS pH8.5, 5mM MgCl2, 10% DMF), at 55C for 7min. Tn5 was then stripped using SDS (0.04% final) and tagmented DNA was amplified using Phusion High-Fidelity DNA Polymerase (ThermoFisher). PCR was performed in the Phusion HF buffer, with a first extension at 72 °C for 3min, followed by 10 cycles of amplification (95 °C – 30 s, 55 °C –30 s, 72 °C – 30s). Commercial Nextera XT indexes were used for the PCR amplification (1/5 dilution). Final libraries were sequenced on a HiSeq2500 (50cycles single-end) and demultiplexing performed using a standard Illumina bcl2fastq2 pipeline.

Positional RNA-sequencing

Animals of the 105 strain were first bisected at the midpoint between the head and the budding zone. The halves created this way were bisected again in the middle between the head and the previous cut, or the previous cut and the budding zone, respectively, thus creating “body 2” and “body3” segments. Head with tentacles and budding zone with the foot were then removed from the remaining pieces to generate “body1” and “body4” segments. Finally, the budding zone was separated from the foot, using the change of endoderm coloration as a guideline for sectioning. Tentacles were also separated from the head, trying to remove as much of the tentacle tissue as possible. The individual segments were lysed immediately after being cut in 350 ul of RL buffer (Single Cell RNA Purification Kit, Norgen), supplemented with 1 % β-mercaptoethanol, frozen on dry ice and stored at -80 ºC for later RNA isolation. Tentacles of a single animal were pooled as one sample. RNA extraction was performed according to the manufacturer's instructions. Downstream processing of the isolated RNA was identical with the previously described experiment, using the SmartSeq2 protocol and in-house Tn5 transposase. RNA from animals regenerated from spheroids was also isolated and sequences as described here. The spheroids were prepared from the 105 strain, as described in the time course sequencing experiment above and left to regenerate in HM for 72 hours. Individual whole regenerated animals

were then collected in 350 ul of RL buffer in three independent replicates (2-3 animals/replicate).

RNA-seq data alignment and pre-processing

The SmartSeq2 libraries for the spheroid RNAseq generated a total of ~8.9 billion 50nt long reads (accounting for an average sequencing depth of ~25 million reads per spheroid). The Illumina Smartseq2 libraries for the positional and regenerated animals RNA sequencing generated a total of 1.7 billion and 250 million 50nt long reads respectively corresponding to an average depth of ~27 million reads per segment replicate and ~31million reads per regenerated animal. After demultiplexing, reads were aligned against the *Hydra* genome guided by transcriptome annotation (NCBI *Hydra* vulgaris assembly *Hydra*_RP_1.0, NCBI *Hydra* vulgaris annotation release 102) using STAR (*7*) version 2.5.0 with command line parameters: *--outSJfilterReads Unique --outFilterType BySJout --outFilterMultimapNmax 5 --alignSJoverhangMin 8 --alignSJDBoverhangMin 4 --outFilterMismatchNoverLmax 0.1 --alignIntronMin 20 --alignIntronMax 1000000 --outFilterIntronMotifs RemoveNoncanonicalUnannotated --seedSearchStartLmax 50 --twopassMode Basic --genomeChrBinNbits 12 --genomeSAsparseD 2 --quantMode GeneCounts*. Samples with library sizes smaller than 5 million reads were discarded from all subsequent analyses. In total 32/352 spheroid libraries and 1/72 animal segment libraries were removed at this step. The produced gene count tables for all remaining samples were library normalized after excluding from the size factor calculation the top 5 percentiles of highly expressed genes. As the samples along the 22h timeme-course of the spheroids were obtained in two collection sessions (one session for timepoints 1h-11h and one session for timepoints 12-22h), a batch effect was introduced. This manifested as a slight discontinuity both in PCA projections of the samples and in select time-course expression profiles of individual genes. In order to mitigate this effect, we took advantage of the fact that spheroids develop asynchronously (median pseudotime spread per collection point of 1.6h, see section on pseudotime ordering) allowing us to pinpoint samples across batches that nearly overlap in terms of dynamics. The correlation (Spearman's rho) of samples from adjacent timepoints across the two collection series (16 samples collected at 10-11h and 14 samples collected at 12-13h) was calculated to identify pairs of top-3 mutual nearest neighbors (MNNs), corresponding to inferred overlapping samples across batches. These MNN pairs were used to calculate average gene-specific shifts that were then applied as correction factors on all samples from the two batches. This simple strategy efficiently removed the observed discontinuities both in sample

projections and individual gene profiles. The corrected spheroid expression values are used for all downstream analyses.

Pseudotime ordering of spheroids

Individual spheroids evolve asynchronously, with samples collected at a specific experimental time exhibiting technical but also internal developmental time variation. In order to recover the underlying gene expression dynamics, it is therefore necessary to order the samples along an axis corresponding to the temporal evolution of the system and to obtain latent coordinates for each sample on that axis. Our strategy for pseudotime ordering relied on first identifying data features that are smooth functionals of the time variable and subsequently using those features to obtain a 1d projection of the spheroids on a basis that corresponds to the pseudotime axis. This procedure was applied separately to the regular medium and isotonic 22h spheroid time-course datasets sampled at 1h intervals. We begin by selecting the top 50% most variable genes, according to a within-dataset mean-variance trend fit. Each of the first 50 principal components (*P*) of this filtered dataset was fit against a generalized additive model using time (*t*) as the independent variable (function *gam* from the *mgcv* CRAN library, call: *gam(P ~ s(t), method = "GCV.Cp", gamma=1.0)*). The dataset is then reconstructed using only components with gam-fit fdr-adjusted p-values < 0.05 as the rest will contain information almost orthogonal to time dynamics. Next we iterated over all 16, overlapping, 7h time windows and repeated the gam-fitting procedure for the expression of all genes **(G)** to identify individual features that are informative for time-ordering within the corresponding timeframe (function call: *gam(G ~ s(t, k=4), method = "GCV.Cp", gamma=1.25)*). For each 7h time window, 100 1d isomap embeddings were performed using random subsets of half of the respective selected gene expression profiles. Within each 7h window, pseudotime was estimated as the mean of the returned 1d coordinates from the isomap iterations scaled to 7h plus a shift corresponding to the first window timepoint. This procedure returns between 1 and 7 pseudotime estimates per spheroid (depending on how many 7h windows cover the corresponding collection time). A final consensus pseudotime was obtained using the weighted average of the individual estimates with weights determined by the number and gam-fit significance of the genes selected in each respective 7h window.

Projection of segment, regenerated animal, and spheroid data on a common subspace

For the common subspace projection of spheroid, segment and regenerated animal data expression values were first log2 transformed after smoothing using a pseudocount of 8 to shrink effect sizes of lowly expressed genes. The pseudotime-ordered spheroid data were further smoothed using a moving average with a window size of 16 (corresponding to a real-time window of ~2h) since spheroids exhibit considerable technical variation. We then obtained a single eigenvector basis by applying principal component analysis on the animal segment data (base R function *prcomp* with parameters *center=TRUE, scale=FALSE*). Only the intersection of the genes with at least a 2-fold change in gene expression (max absolute delta of 1 for the log transformed values) in both the segment and spheroid datasets were used. Finally, the spheroid and regenerated animal data were projected back to the eigenvector space determined by the animal segment data.

Differential analysis of gene expression in spheroids in hypotonic and isotonic media conditions.

In order to identify genes that are differentially expressed in the hypotonic (HM) and isotonic (70mM glucose medium) conditions we fitted a generalized additive model (GAM) on the delta of the two pseudo-time ordered (PTO) expression time series. First, in order to allow comparisons between the two conditions we had to account for the fact that, after filtering low-depth libraries, we end up with a larger number of spheroids in HM conditions compared to the 70mM conditions (170 vs 150 spheres, see section on RNA-seq data pre-processing). We downsampled the HM data by interpolating to 150 sampling points (t) to acquire two equal-length time series. The difference Δ of the two signals for every gene was scaled and fitted to a GAM (function *gam* from the *mgcv* CRAN library, call: *gam(Δ ~ s (t, k=8), method = "GCV.Cp", gamma=1.0)*). In addition, we calculated effect sizes for each gene between the two conditions as the sum of the absolute values of the difference between the two mean-normalized signals, excluding the highly variable first three timepoints. This procedure allows us to identify genes that differ either in terms of scale or in terms of shape in their gene expression dynamics. Both the fdr-adjusted p-values from the fit (<1e-6) and the calculated effect sizes (>40) were used to select for genes differentially expressed in the two conditions.

Analysis of the changing genes sensitive to mechanical stimulation

The 2269 genes that change their expression at least 2-fold during normal regeneration were clustered in 5 clusters using the *kmeans* function in Matlab. Before clustering, the gene expression time-series of each gene was mean-normalized. To select the top genes sensitive to the removal of mechanical stimulation, we only considered the ones with adjusted P-value $<10^{-6}$. From this pool, the top 10 % were selected based on the sum of differences (n=113). To enable the functional analysis of these genes, their mammalian homologs were then annotated using the available data from *Hydra* genomics databases (see Table S1). GO term enrichment analysis was then performed using GeneMania (genemania.org) separately for members of clusters 3 and 5. Since there were only 3 genes that were members of other clusters, these were left out of the analysis.

Knockdowns of foot-specific transcription factors

Gene knockdowns were performed according to a protocol based on (*57*). Briefly, 20-30 animals per RNAi treatment were incubated at 4 °C for 1 hour and then transferred into an electroporation cuvette (Gene Pulser / Micro Pulser Electroporation Cuvette 0.4 cm gap; Bio-Rad or electroporation cuvettes 4 mm gap; VWR) and washed twice with chilled MiliQ water. Residual water was removed and 200 µL of the siRNA (siRNAs were ordered as 20 bp RNA duplexes from Integrated DNA Technologies (IDT)) solution was added to each cuvette. Each siRNA was diluted in ddH2O to a final concentration of 1.35 µM per treatment. Animals were incubated with the siRNA solution for 5 minutes. After relaxation of the animals, two pulses (150 V range) were applied for 50 ms (Gene Pulser II with RF module; Bio-Rad). After electroporation, 500 µL of ice-cold recovery medium (80 % HM, 20 % v/v dissociation medium) was added to the animals. Animals were carefully transferred into a new Petri dish filled with pre-chilled recovery medium. The next day, the animals were transferred into fresh HM. Three electroporations were performed in this manner with 1 day for recovery in between successive rounds. The animals were then bisected at 50 % body length 2 days after the last electroporation and stained for peroxidase 3 days after bisection, as described above. Total numbers of animals used in all three replicates were 27 *Dlx1*, 29 *Gata3,* 30 *Znf397*, 30 *CnNK2*, 33 *FoxD2*, 33 mock.

Real-time PCR verification of RNAi efficiency

Knockdowns of foot-specific TFs and bisections were performed as described above. On the third day after the bisection, 3 foot-regenerating halves were collected per sample and lysed in 350 ul of RL buffer with 1 % β-mercaptoethanol (Single Cell RNA Purification Kit, Norgen), frozen on dry ice and stored at -80 ºC. After collecting all the samples, RNA was isolated as outlined in the instructions for the kit. The concentration and purity of the extracted RNA was verified using NanoDrop 1000 (Thermo Fisher Scientific). Next, cDNA was prepared with the Oligo(dT)12-18 Primer (Thermo Fisher Scientific) using the High-Capacity cDNA Reverse

Transcription Kit (Applied Biosystems) as per manufacturer's instructions. The qPCR reactions were carried out using the StepOnePlus Real-Time PCR cycler (Thermo Fisher Scientific) with a standard run method. Each reaction contained 10 ng of cDNA, 1x the Platinum SYBR Green qPCR SuperMix-UDG w/ROX (Invitrogen) master mix with 0.25 µM primers in a total volume of 25 µl. The sequences of the primer pairs used are given in Table 1 below. The quantification of gene expression was performed using the StepOne software v 2.3 (Thermo Fisher Scientific).

Table 1. Sequences of primers used in the experiment

gene	forward primer (5′→ 3′)	reverse primer (5′→ 3′)
GAPDH	GACTTGGCCGTATTAACTTGAGC	CTACAAACAAGACGCCCTATTCG
DLX1	GTGAAGATGACGATGAAGATTTAAC	AACGATTTAATTCTCGGAGCTG
GATA3	TAAACCAAAGAGGAGATTGTCAC	ATACTGGTTCACCACTTCCA
ZNF397	AACCAACTCATTCTAGCTGC	TGTGCTTCAATCATTCGTGT
NK2	GGTTTAAGTTGCATGGTTGC	AACTTGGAGATTCACACTTAGG
FOXD2	GCAGTTTTAACGAAGAACACC	TGTCGGGTGAAGCTAAAATG

Real-time PCR time course of Wnt3 expression in different osmolarities

Spheroids of the *105* strain were prepared as described previously, randomly split into 5 groups and incubated in media with different sucrose content (0, 10, 30, 50, 70 mM) at room temperature. Every 6 hours, a sample of 10 spheroids was randomly taken from each of the conditions, lysed in 350 ul of RL buffer with 1 % β-mercaptoethanol (Single Cell RNA Purification Kit, Norgen), frozen on dry ice and stored at -80 ºC. After collecting all the samples, RNA was isolated as outlined in the instructions for the kit. The concentration and purity of the extracted RNA was verified using NanoDrop 1000 (Thermo Fisher Scientific). Next, cDNA was prepared with the Oligo(dT)12-18 Primer (Thermo Fisher Scientific) using the High-Capacity cDNA Reverse Transcription Kit (Applied Biosystems) as per manufacturer's instructions. The qPCR reactions were carried out using the StepOnePlus Real-Time PCR cycler (Thermo Fisher Scientific) with a standard run method. Each reaction contained 10 ng of cDNA, 1x the Platinum SYBR Green qPCR SuperMix-UDG w/ROX (Invitrogen) master mix with 0.25 µM primers in a total volume of 25 µl. The quantification of gene expression was performed using the StepOne software v 2.3 (Thermo Fisher Scientific). Table 2 below shows the sequences of primers used.

Table 2. Sequences of the primers used

gene	forward primer (5′→ 3′)	reverse primer (5′→ 3′)
GAPDH	GACTTGGCCGTATTAACTTGAGC	CTACAAACAAGACGCCCTATTCG
WNT3	TGCAGAAGGAATACGACTGGG	TGCTGGCTGTTGTAATAATTGGG

Real-time PCR time course of Wnt3 expression upon transfer in different media

Spheroids of the *105* strains were prepared as describe above and incubated for 12 h in isotonic medium (HM with 70 mM sucrose). After this initial incubation, the surviving spheroids were randomly split into two groups, one of which was transferred to HM, while the other one was kept in the isotonic medium. Random samples of 9 spheroids were taken from the populations in the beginning of the experiment, after the initial incubation and 3 and 6 hours after transfer. In case of the HM population, care was taken to only include expanded spheroids. Samples were lysed in 350 ul of RL buffer with the addition of 1 % β-mercaptoethanol (Single Cell RNA Purification Kit, Norgen), frozen on dry ice and stored at -80 ºC. Further processing of the samples was identical to the previous experiment.

Generation of transgenic animals overexpressing Wnt3

The transgenesis of animals was performed as previously described (*24*, *53*). Briefly, 2-cell stage embryos were injected with the pAct::GFP, pAct::Wnt3 construct and left to develop. After hatching, the polyps were reared separately and screened for the expression of the transgenesis marker GFP. Fully transgenic animals were then obtained from buds originating in the transgenic cell patches.

Rescue experiments with buds and Wnt-overexpressing spheroids

Animals of the line *AEP ecto pAct::eGFP* with buds in stages 3-4 (staging according to(*58*)) were selected, and tissue rings containing the forming buds were cut. Only the budding fragment of the ring was then excised and allowed to form a spheroid in HM. Given the branched multiheaded morphology of the Wnt-overexpressing *AEP ecto pAct::eGFP, pAct::Wnt3* line, it was not possible to cut tissue rings in a specific axial position. Rings were harvested from sufficiently long body fragments instead and cut into 2-3 fragments as usual. Fragments were left to close in HM. Both types of spheroids were then split between 0 mM and 70 mM sucrose in 24-well plates and scored for tentacle appearance, as detailed above.

Whole mount in situ hybridization

In situ hybridization was performed according to previously published protocols (*59*) with minor modifications. Briefly, animals were fixed at 4 °C in 4% PFA overnight and then de*Hydra*ted in a series of 5 min washes in 25-50-75-100% methanol and incubated overnight in methanol at -20 °C. Rehydration then followed by successive 10 min washes of 75-50-25-0 % methanol in PBS + 0.1 % Tween 20 (PBT). Samples were then treated for 10 min with a 10 µg/ml Proteinase K solution and the reaction was stopped by incubation with 4 mg/ml glycine for 10 min. After 2x 5 min washes with PBT and 2x 5 min washes with 0.1 M triethanolamine solution, samples were treated with acetic anhydride for 2x 5 min, washed in PBT (2x 5min) and refixed in 4% PFA for 20 min. Thorough washing with PBT (5x 5 min) then followed and the animals were heat treated for 30 min at 80 °C. Following preincubation with the hybridization solution for 2 h at 55 °C, DIG-labelled RNA probe dissolved in hybridization solution was added. We used the same *Wnt3* probes previously described (*14*). The samples were incubated with the probes for 3 days and then washed with a series of 75-50-25-0 % solutions of hybridization buffer in 2x SSC. After blocking the samples in 20% sheep serum for 2 h at 4 °C, an incubation with the alkaline phosphatase conjugated anti-DIG antibody followed (overnight, 4 °C). To remove the unbound antibody, 8x 1 h washes with maleic acid buffer were performed, followed by an overnight wash in the same buffer. The next day, samples were treated by NTMT and levamisole, as detailed in the original protocol. Finally, the chromogenic reaction was performed using the BCIP/NBT Color Development Substrate (Promega) according to the manufacturer's instructions.

Transplantation experiments

Transplantation were performed on glass needles, hand-pulled from glass capillaries. Recipient wt AEP animals were bisected at 50% body length and the foot half was driven on the needle longitudinally. For controls, a ring of tissue from the same axial position was cut from the *AEP ecto pAct::eGFP* animals and threaded on the needle. Since it is not possible to match axial positions in the Wnt3 overexpressing animals, we used rings of tissue coming from anywhere in the branched body columns of these animals. The head half of the recipient was then added, thus sandwiching the transplant between the host body halves. Pieces were then secures with a piece of parafilm to prevent sliding of the needle and left for ~ 2h in HM to establish adhesion. After this time, healed grafts were carefully slid off the needle using fine forceps and left to recover. The success of transplantation was evaluated after 24h. Successful transplant were then assessed for ectopic head formation on day 5 after transplantation.

Statistical analysis

All experiments have been performed in at least 3 independent replicates. Details about sample numbers are given in the figures or descriptions of the relevant experiments. Since the nature of the collected data often led to distributions that were not Gaussian, we used the nonparametric Mood's median and Wilcoxon rank sum tests. These tests were performed as two-sided in all cases. For pairwise comparisons, presented in Fig. S1, we used a one-sided paired Student's t-test. Other relevant details are given in the figure legends and experiment descriptions. In all box plots, the central mark corresponds to the median, and the bottom and top box edges indicate the 25^{th} and 75^{th} percentiles, respectively. Whiskers show the range of the data points not considered outliers. Outliers are defined as points that have a value of less than $q_1 - w \times (q_3 - q_1)$, or more than $q_3 + w \times (q_3 - q_1)$. Here, w is the maximum length of the whisker, and q_1 and q_3 correspond to the 25th and 75th percentiles, respectively.

References

1. B. P. Teague, P. Guye, R. Weiss, Synthetic Morphogenesis. *Cold Spring Harbor Perspectives in Biology*. **8**, a023929 (2016).

2. M. N. Shahbazi, Mechanisms of human embryo development: from cell fate to tissue shape and back. *Development*. **147**, dev190629 (2020).

3. E. Hannezo, C.-P. Heisenberg, Mechanochemical Feedback Loops in Development and Disease. *Cell*. **178**, 12–25 (2019).

4. C. Collinet, T. Lecuit, Programmed and self-organized flow of information during morphogenesis. *Nat Rev Mol Cell Biol*. **22**, 245–265 (2021).

5. C. J. Chan *et al.*, *Hydra*ulic control of mammalian embryo size and cell fate. *Nature*. **571**, 112–116 (2019).

6. A. Q. Ryan, C. J. Chan, F. Graner, T. Hiiragi, Lumen Expansion Facilitates Epiblast-Primitive Endoderm Fate Specification during Mouse Blastocyst Formation. *Developmental Cell*. **51**, 684–697.e4 (2019).

7. J. Li *et al.*, The Strength of Mechanical Forces Determines the Differentiation of Alveolar Epithelial Cells. *Developmental Cell*. **44**, 297–312.e5 (2018).

8. K. R. Mosaliganti *et al.*, Size control of the inner ear via *Hydra*ulic feedback. *eLife*. **8** (2019), doi:10.7554/eLife.39596.

9. N. P. Tallapragada *et al.*, Inflation-collapse dynamics drive patterning and morphogenesis in intestinal organoids. *Cell Stem Cell* (2021), doi:10.1016/j.stem.2021.04.002.

10. S. Dasgupta, K. Gupta, Y. Zhang, V. Viasnoff, J. Prost, Physics of lumen growth. *Proc. Natl. Acad. Sci. U.S.A.* **115**, E4751–E4757 (2018).

11. M. C. Vogg, B. Galliot, C. D. Tsiairis, Model systems for regeneration: *Hydra*. *Development*. **146**, dev177212 (2019).

12. K. Chiou, E.-M. S. Collins, Why we need mechanics to understand animal regeneration. *Developmental Biology*. **433**, 155–165 (2018).

13. E. Braun, K. Keren, *Hydra* Regeneration: Closing the Loop with Mechanical Processes in Morphogenesis. *Bioessays*. **40**, e1700204 (2018).

14. B. Hobmayer *et al.*, WNT signalling molecules act in axis formation in the diploblastic metazoan *Hydra*. *Nature*. **407**, 186–189 (2000).

15. M. Broun, L. Gee, B. Reinhardt, H. R. Bode, Formation of the head organizer in *Hydra* involves the canonical Wnt pathway. *Development*. **132**, 2907–2916 (2005).

16. T. Lengfeld *et al.*, Multiple Wnts are involved in *Hydra* organizer formation and regeneration. *Developmental Biology*. **330**, 186–199 (2009).

17. E. N. Browne, The production of new *Hydra*nths in *Hydra* by the insertion of small grafts. *Journal of Experimental Zoology Part A: Ecological Genetics and Physiology*. **7**, 1–23 (1909).

18. M. Broun, H. R. Bode, Characterization of the head organizer in *Hydra*. *Development*. **129**, 875–884 (2002).

19. M. Kücken, J. Soriano, P. A. Pullarkat, A. Ott, E. M. Nicola, An osmoregulatory basis for shape oscillations in regenerating *Hydra*. *Biophysical Journal*. **95**, 978–985 (2008).

20. D. J. Benos, R. G. Kirk, W. P. Barba, M. M. Goldner, Hyposmotic fluid formation in *Hydra*. *Tissue and Cell*. **9**, 11–22 (1977).

21. J. Soriano, S. RUdiger, P. Pullarkat, A. Ott, Mechanogenetic Coupling of *Hydra* Symmetry Breaking and Driven Turing Instability Model. *Biophysical Journal*. **96**, 1649–1660 (2009).

22. J. Soriano, C. Colombo, A. Ott, *Hydra* molecular network reaches criticality at the symmetry-breaking axis-defining moment. *Physical review letters*, ***97***, 258102 (2006).

23. R. Wang, *et al.*, Mouth function determines the shape oscillation pattern in regenerating *Hydra* tissue spheres. *Biophysical journal*, ***117***, 1145-1155 (2019).

24. Y. Nakamura, C. D. Tsiairis, S. Özbek, T. W. Holstein, Autoregulatory and repressive inputs localize *Hydra* Wnt3 to the head organizer. *Proc. Natl. Acad. Sci. U.S.A.* **108**, 9137–9142 (2011).

25. H. K. MacWilliams, *Hydra* transplantation phenomena and the mechanism of *Hydra* head regeneration. II. Properties of the head activation. *Developmental Biology*. **96**, 239–257 (1983).

26. H. Shimizu, Transplantation analysis of developmental mechanisms in *Hydra*. *Int. J. Dev. Biol.* **56**, 463–472 (2012).

27. A. Grens, L. Gee, D. A. Fisher, H. R. Bode, CnNK-2, an NK-2 homeobox gene, has a role in patterning the basal end of the axis in *Hydra*. *Developmental Biology*. **180**, 473–488 (1996).

28. Y. Wenger, W. Buzgariu, C. Perruchoud, G. Loichot, B. Galliot, Generic and context-dependent gene modulations during *Hydra* whole body regeneration. *bioRxiv*, 587147 (2019).

29. H. Meinhardt, A model for pattern formation of hypostome, tentacles, and foot in *Hydra*: how to form structures close to each other, how to form them at a distance. *Developmental Biology*. **157**, 321–333 (1993).

30. M. C. Vogg *et al.*, An evolutionarily-conserved Wnt3/β-catenin/Sp5 feedback loop restricts head organizer activity in *Hydra*. *Nature Communications*. **10**, 312–15 (2019).

31. S. Chera *et al.*, Apoptotic cells provide an unexpected source of Wnt3 signaling to drive *Hydra* head regeneration. *Developmental Cell*. **17**, 279–289 (2009).

32. L. Gee, *et al.,* β-catenin plays a central role in setting up the head organizer in *Hydra*. *Developmental biology*, **340**, 116-124 (2010).

33. V. J. Martin, C. L. Littlefield, W. E. Archer, H. R. Bode, Embryogenesis in *Hydra*. *The Biological Bulletin*. **192**, 345–363 (1997).

34. E. Pukhlyakova, A. J. Aman, K. Elsayad, U. Technau, β-Catenin-dependent mechanotransduction dates back to the common ancestor of Cnidaria and Bilateria. *Proc. Natl. Acad. Sci. U.S.A.* **115**, 6231–6236 (2018).

35. T. Brunet *et al.*, Evolutionary conservation of early mesoderm specification by mechanotransduction in Bilateria. *Nature Communications*. **4**, 2821–15 (2013).

36. A. Gierer, H. Meinhardt, A theory of biological pattern formation. *Kybernetik*. **12**, 30–39 (1972).

37. A. M. Turing, The chemical basis of morphogenesis. *Phil. Trans. of the Royal Soc*. **237**, 37–72 (1952).

38. H. Meinhardt, Modeling pattern formation in *Hydra*: a route to understanding essential steps in development. *Int. J. Dev. Biol.* **56**, 447–462 (2012).

39. J. D. Murray, P. K. Maini, R. T. Tranquillo, Mechanochemical models for generating biological pattern and form in development. *Physics Reports*. **171**, 59–84 (1988).

40. M. Mercker, D. Hartmann, A. Marciniak-Czochra, A Mechanochemical Model for Embryonic Pattern Formation: Coupling Tissue Mechanics and Morphogen Expression. *PLoS ONE*. **8**, e82617–6 (2013).

41. Y. Maroudas-Sacks *et al.*, Topological defects in the nematic order of actin fibres as organization centres of *Hydra* morphogenesis. *Nat. Phys.* **17**, 251–259 (2021).

42. A. Livshits, L. Shani-Zerbib, Y. Maroudas-Sacks, E. Braun, K. Keren, Structural Inheritance of the Actin Cytoskeletal Organization Determines the Body Axis in Regenerating *Hydra*. *Cell Reports*. **18**, 1410–1421 (2017).

43. T. Ruiz-Herrero, K. Alessandri, B. V. Gurchenkov, P. Nassoy, L. Mahadevan, Organ size control via *Hydra*ulically gated oscillations. *Development*. **144**, 4422–4427 (2017).

44. J. Li *et al.*, The Strength of Mechanical Forces Determines the Differentiation of Alveolar Epithelial Cells. *Developmental Cell*. **44**, 297–312.e5 (2018).

45. K. M. Loh, R. van Amerongen, R. Nusse, Generating Cellular Diversity and Spatial Form: Wnt Signaling and the Evolution of Multicellular Animals. *Developmental Cell*. **38**, 643–655 (2016).

46. S. A. Newman, G. Forgacs, G. B. Muller, Before programs: The physical origination of multicellular forms. *Int. J. Dev. Biol.* **50**, 289–299 (2006).

47. R. Baron, M. Kneissel, WNT signaling in bone homeostasis and disease: from human mutations to treatments. *Nat Med*. **19**, 179–192 (2013).

48. B. Cha *et al.*, Mechanotransduction activates canonical Wnt/β-catenin signaling to promote lymphatic vascular patterning and the development of lymphatic and lymphovenous valves. *Genes & Development*. **30**, 1454–1469 (2016).

49. T. Shinozuka, R. Takada, S. Yoshida, S. Yonemura, S. Takada, Wnt produced by stretched roof-plate cells is required for the promotion of cell proliferation around the central canal of the spinal cord. *Development*. **146**, dev159343 (2019).

50. M.-E. Fernandez-Sanchez *et al.*, Mechanical induction of the tumorigenic β-catenin pathway by tumour growth pressure. *Nature*. **523**, 92–95 (2015).

51. Ferenc, J. & Tsiairis, C. D. Studying Mechanical Oscillations during Whole Body Regeneration in *Hydra* in *Whole-Body Regeneration,* B. Galliot, S. Blanchoud, Eds. (Methods in Molecular Biology, Springer, 2021), doi:10.13140/RG.2.2.16577.68961

52. J. Schindelin *et al.*, Fiji: an open-source platform for biological-image analysis. *Nature Methods*. **9**, 676–682 (2012).

53. J. Wittlieb, K. Khalturin, J. U. Lohmann, F. Anton-Erxleben, T. C. G. Bosch, Transgenic *Hydra* allow in vivo tracking of individual stem cells during morphogenesis. *Proc. Natl. Acad. Sci. U.S.A.* **103**, 6208–6211 (2006).

54. S. Hoffmeister, H. C. Schaller, A new biochemical marker for foot-specific cell differentiation in *Hydra*. *Roux's Dev Biol.* **194**, 453-461 (1985).

55. S. Picelli *et al.*, Full-length RNA-seq from single cells using Smart-seq2. *Nat Protoc*. **9**, 171–181 (2014).

56. S. Picelli *et al.*, Tn5 transposase and tagmentation procedures for massively scaled sequencing projects. *Genome Res.* **24**, 2033–2040 (2014).

57. M. Lommel, A. Tursch, L. Rustarazo-Calvo, B. Trageser, T. W. Holstein, Genetic knockdown and knockout approaches in *Hydra*. *bioRxiv,* 230300 (2017).

58. J. J. Otto, R. D. Campbell, Budding in *Hydra* attenuata: bud stages and fate map. *J. Exp. Zool.* **200**, 417–428 (1977).

59. H. Bode, T. Lengfeld, B. Hobmayer, T. W. Holstein, Detection of expression patterns in *Hydra* pattern formation. *Methods Mol. Biol.* **469**, 69–84 (2008).

Acknowledgments

We thank Iskra Katic for performing the RNAi treatments and plasmid electroporations, and Nenad Suknovic (University of Geneva) for the optimized protocol. We would also like to thank the members of the FMI Functional Genomics Facility for performing the RNA-sequencing, the members of the Facility for Advanced Imaging and Microscopy for their support to the imaging part of this work, and Thomas Bosch (Christian-Albrechts-Universität, Kiel) for providing the AEP ecto pAct::GFP *Hydra* line. Finally, we are very grateful to our colleagues Prisca Liberali, Susan Gasser, and Fabian Braukmann, and the two anonymous reviewers for their constructive comments that helped us improve the manuscript.

Funding: This work was supported by the Novartis Research Foundation

Author contributions: JFc and CDT designed the study and wrote the manuscript. JFc, JFi, YN, SS, and CDT performed the experiments. JFc, PP, and CDT analyzed thedata.

Competing interests: The authors declare they have no competing interests.

Data and materials availability: RNA-sequencing data are deposited in the ArrayExpress database under accession numbers E-MTAB-9672 (single spheroid RNA-seq time course), and E-MTAB-9676 (positional RNA-seq). Other relevant data are provided in the manuscript and supplements. Previously unpublished analysis scripts are available at https://doi.org/10.5281/zenodo.5535691

Supplementary Materials

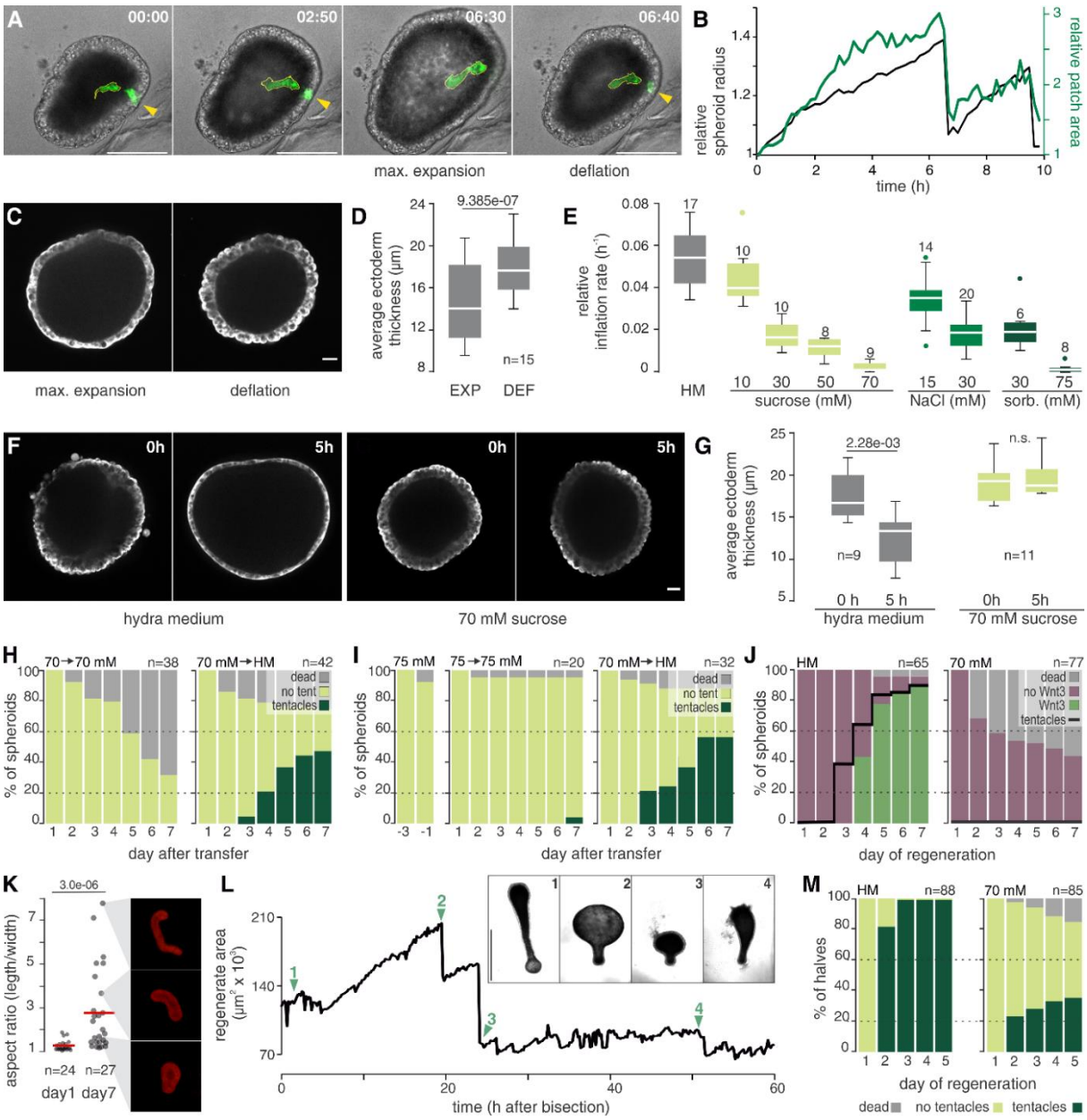

Fig. S1. Mechanical oscillations are required for *Hydra* regeneration

(**A-B**) Individual cells are being stretched during the spheroid expansion. (A) Snapshots of an example oscillating spheroid containing GFP-labelled cells (maximum Z projection of the fluorescent channel overlayed on brightfield images, scale bars 100 µm). Note the concomitant expansion of the green 2-cell patch with the spheroid inflation and its abrupt shrinkage after deflation. As the spheroid expands, another GFP+ cell (yellow arrowhead) moves out the the imaged volume. (B) Quantification of the spheroid radius and the cell area from (A). (**C-D**) Spheroid inflation causes tissue stretching, as evidenced by thinning of the epithelial layer in expanded spheroids. (C) An equatorial optical section of a representative spheroid, ubiquitously expressing GFP in the ectoderm. Spheroid is shown fully expanded (left) and immediately after deflation (right). The time interval between the snapshots was

10 min; scale bar 20 µm. (D) Quantification of tissue thickness before (EXP) and after deflation (DEF) in a population of spheroids. (**E**) Spheroid inflation rate decreases as the osmolarity of the medium increases. Note that this effect manifests independently of the used osmolyte. The number of samples quantified in each condition is indicated above the boxes. See also Fig S2i for details of slope quantification. (**F-G**) Isotonic conditions prevent tissue stretching. (F) Equatorial optical sections of GFP(ecto) spheroids in different media immediately after closing (0h) and 5h later. Note that while the tissue is significantly thinner in the expanding spheroid in *Hydra* medium, no such effect is observed in isotonic medium (70 mM sucrose). Scale bar 20 µm. (G) Quantification of the ectoderm thickness in spheroids from experimental setup shown in (F). (**H**) Regeneration resumes in HM after previous incubation in isotonic medium (70 mM sucrose) for 72 h. (**I**) Experimental setup identical to (H), but using 75 mM sorbitol to create isotonic conditions. (**J**) Quantification of morphological regeneration (tentacle appearance) and molecular symmetry breaking (Wnt3 spot) in a *Wnt3::GFP* reporter line spheroids under control (HM) and isotonic conditions (70 mM sucrose). (**K**) The aspect ratio (length/width) of spheroids in isotonic conditions at the beginning and end of the regeneration time course. N=3 independent experiments. (**L**) Example of an oscillatory behavior in a head-regenerating half of a biseceted animal (Quantification of Movie S3) representative of n=11 samples. Numbered insets correspond to the numbered time points indicated by arrowheads in the plot. To allow clear imaging of the oscillations, without the interference of active regenerate movement, *Hydra* medium with 1 µM linalool was used. (**M**) Head regeneration in the headless halves of bisected animals in control vs. isotonic conditions. Animals were bisected at 50 % body length. Panels (H-J) and (M) show cumulative plots of n samples from 3 independent experiments. P-values in (D) and (G) were calculated using a one-sided paired Student's t-test, in (K) using the Wilcoxon rank-sum test.

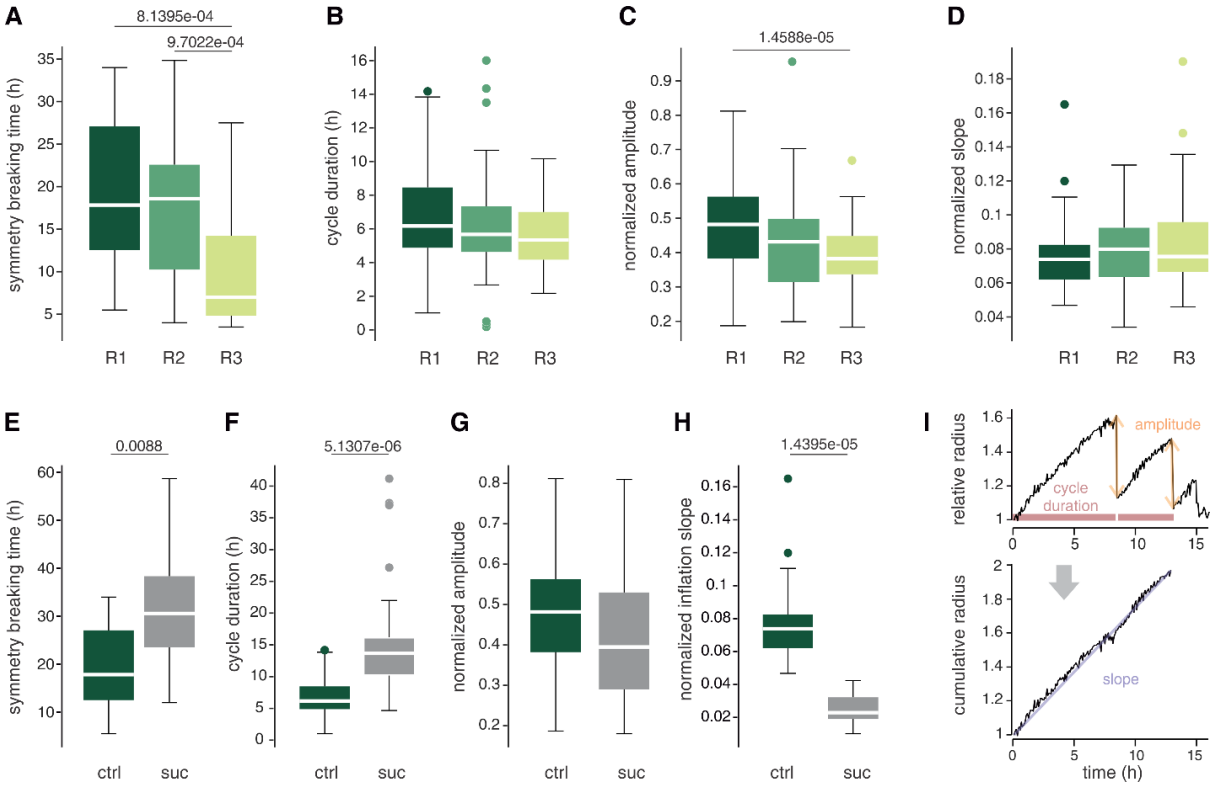

Fig. S2. Quantification of mechanical oscillation parameters

(**A**) Symmetry breaking time, measured as the time of Phase I to Phase II transition for spheroids derived from different axial positions (R1-R3) in control conditions. (**B**) Period of oscillations for the same samples. (**C**) Amplitude of oscillations for the same R1, R2 and R3 samples, indicating the maximum size of the spheroid in each cycle before it ruptures. Note the slight axial gradient of amplitudes, which might suggest a gradient in the resistance of the tissue to rupture. However, this gradient alone is not enough to explain the much more pronounced differences in the requirements for mechanical stimulation among the pieces. (**D**) Slope of inflation. Data shown here (A-D), correspond to the samples in Fig. 2A and are measured on spheroid radius data normalized to the initial size. (**E**) Comparisons of symmetry breaking time for R1 spheroids in control (HM, for samples in Fig. S2A) and in 30 mM sucrose. Similar comparisons for oscillation duration (**F**), oscillation amplitude (**G**) and inflation slope (**H**) which, as expected, decreases significantly, resulting in an increase of the oscillation period. (**I**) An example of the measured parameters. Note that the period and amplitude are quantified for each individual oscillation cycle, while the slope is measured for the entire Phase I, ignoring the deflation events. See (*49*) for details of the quantification procedure. Statistical comparisons were done using the Mood's median test. When significant, P-values are given directly in the plots.

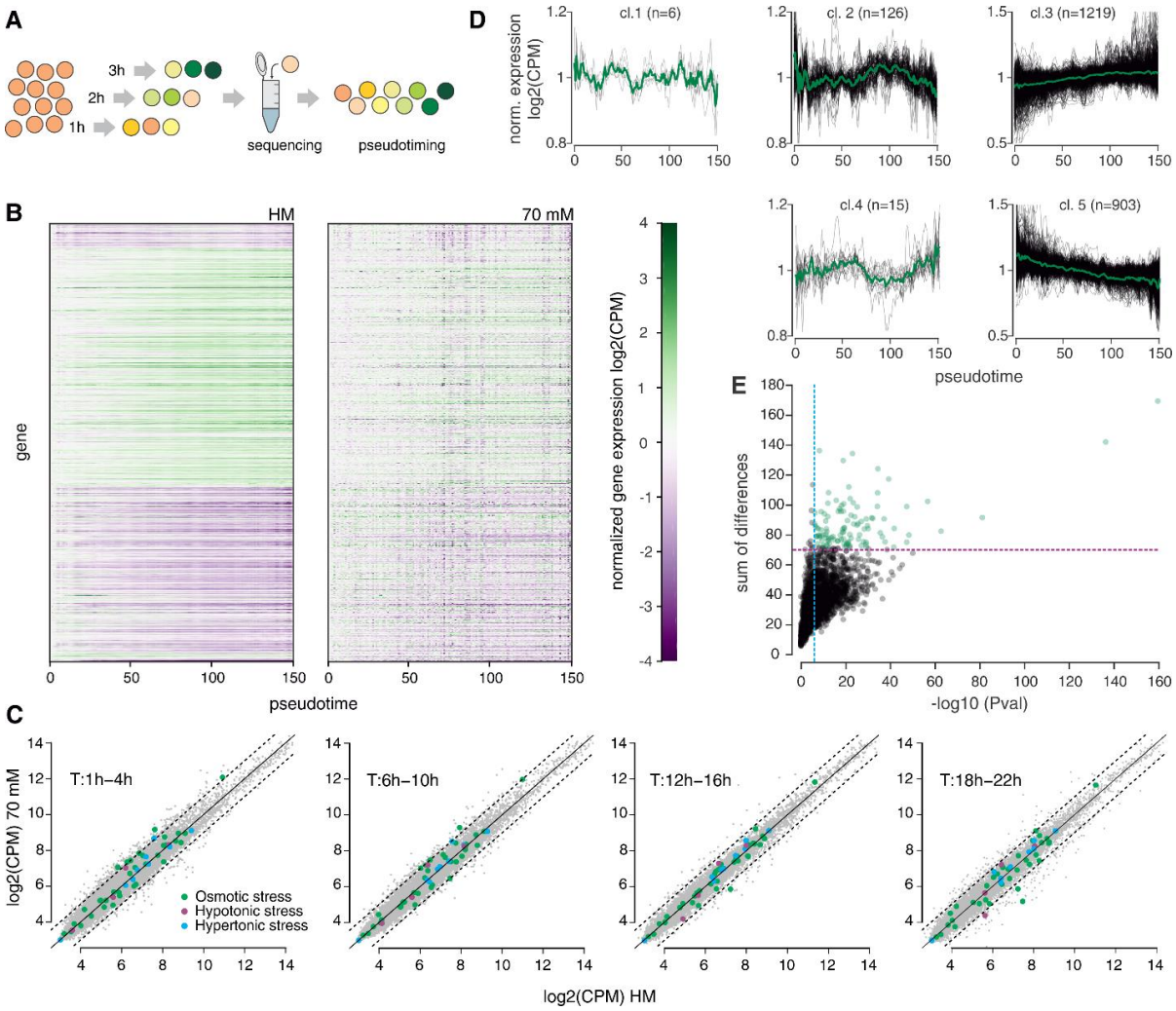

Fig. S3. Time series gene expression profiling for spheroids in control (HM) and isotonic (70mM sucrose) conditions

(**A**) Schematic of the experimental design. Spheroids were left to develop either in HM or isotonic medium after cutting. 8 spheroids were sampled every hour, collected and submitted individually to RNA-sequencing. Transcriptomics data later allowed to reconstruct the temporal development of spheroids (pseudotime) based on the similarity between samples. (**B**) Heatmaps of the temporal progressions for 2269 genes that change their expression at least 2-fold during the course of normal regeneration. Genes are clustered based on their behavior in control conditions. Note that in the isotonic conditions (70 mM sucrose) some of these genes behave differently (presented in Fig 3D), while others remain unaffected. In both datasets, the initial $\log_2$(CPM) values were subtracted for each gene. (**C**) Scatter plots of transcript counts in the isotonic conditions plotted against the control. Data for the indicated time points were averaged. Each dot corresponds to one gene. Genes involved in osmotic stress are highlighted in different colors based on their GO process annotation. Dotted lines indicate 2-fold up- or downregulation. The identity of the highlighted genes is given in Table S1. (**D**) Plots of the average behavior of the 5 gene clusters identified with hierarchical clustering in the control (HM) sample time-series. Black lines show individual genes, while the thick green line is the cluster average. Numbers in parentheses indicate the number of genes in each cluster. (**E**) Selecting the top 10 % mechanosensitive genes. Only genes with a p-value < 10^{-6} for temporal changes in the difference between conditions were considered significant (blue line). Purple line indicates the magnitude-based cutoff (sum of differences between the conditions) for the top 10% of significantly changing genes (green dots).

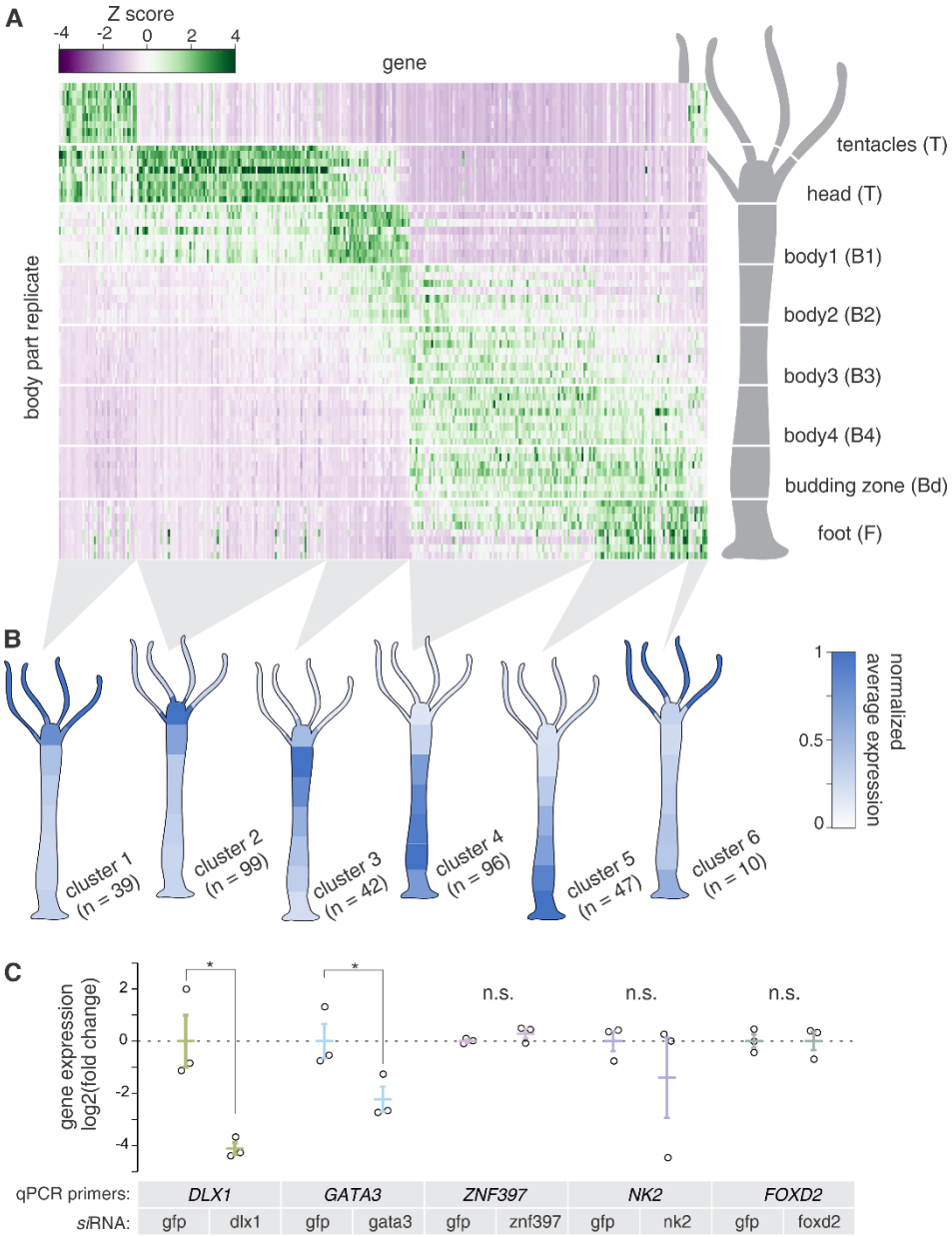

Fig. S4. Gene expression along the *Hydra* Oral/Aboral axis

(**A**) Heatmap of genes with axially graded expression, identified in the positional RNA-sequencing. Rows correspond to individual replicates for each body position. Color coding indicates the Z-score (standard deviations above or below the mean expression of a gene across all segments after collapsing biological replicates). These data were used to generate the PCA map of different positional identities in Fig3A-C. (**B**) Clusters of differentially expressed genes along the O/A axis, identified with k-means clustering. The schematics below show average expression patterns for each cluster, normalized to the body part with highest expression levels. (**C**) Q-PCR quantification of the expression of foot-specific transcription factors upon RNA-interference. Three replicates, each containing 3 regenerated halves per sample, were performed. Animals were bisected at 50% 2 days after the last siRNA electroporation and harvested for RNA extraction 3 days post bisection. Asterisk indicates a P-value < 0.05 from the Wilcoxon rank-sum test

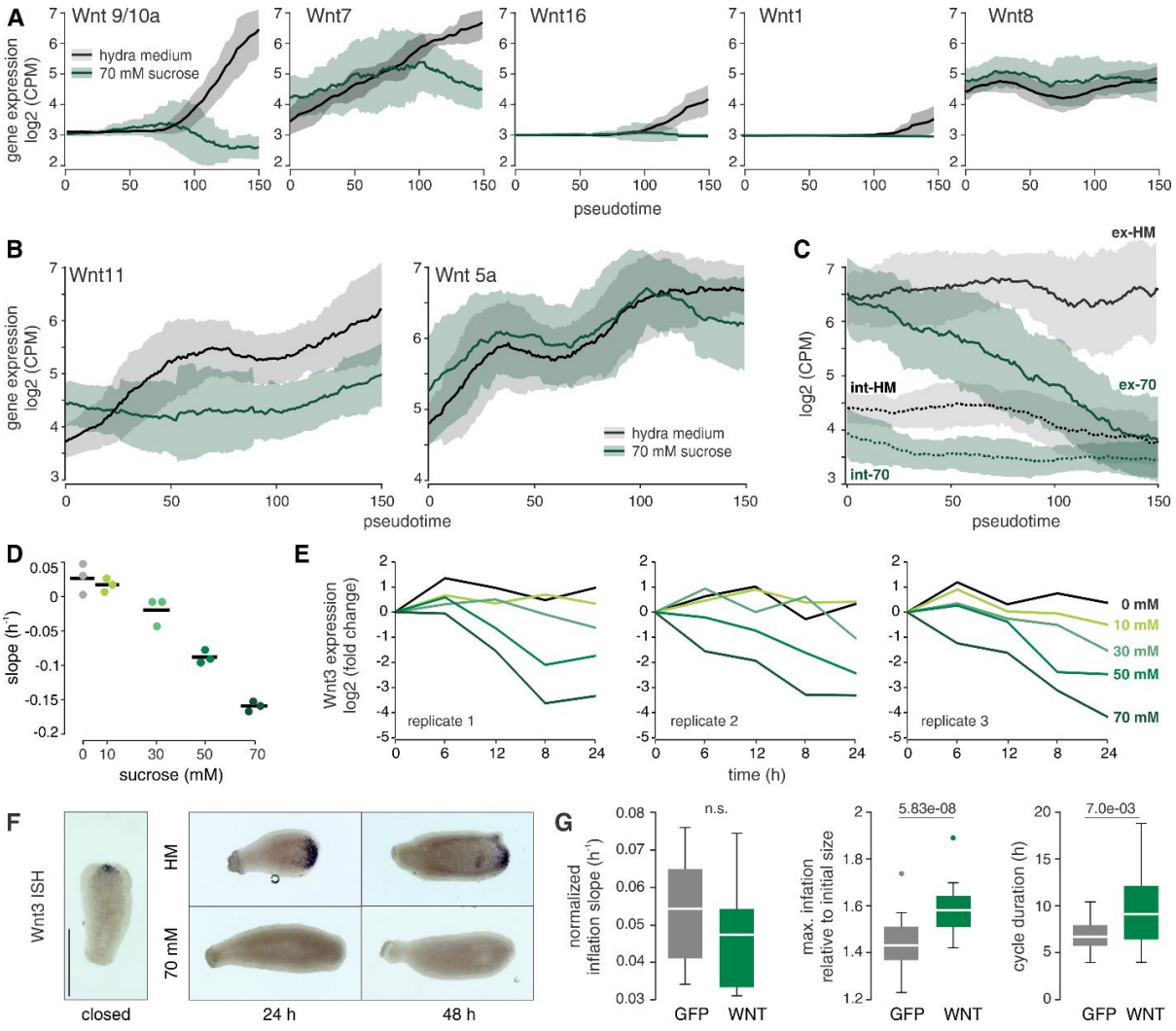

Fig. S5. Wnt signaling depends on mechanical stimulation

(**A**) Temporal gene expression profiles for genes shown in Fig. 6A. (**B**) Differential requirements of mechanical stimulation for the expression of non-canonical Wnt signaling ligands. While the expression pattern of Wnt11 (Wnt/PCP pathway) is sensitive to the removal of mechanical oscillations, Wnt5a (Wnt/Ca^{2+} pathway) does not show changes in the pattern of expression. (**C**) Exonic (solid lines) and intronic (dotted lines) counts for the WNT3 trascript in control (black) and isotonic (green) conditions. Lines in A – C show a moving mean over the temporal (pseudotime) gene expression data and the shaded area represents moving standard deviation. The size of the moving window is 36 pseudotime points. (**D**) Slopes of straight lines fitted on the Wnt3 expression data from Fig 5D. Dots indicate measurements in individual replicates, and lines represent averages. (**E**) Plots of individual replicates of the q-PCR timecourse of WNT3 expression in different osmolarities. For each plot, the lines indicate averages of 3 technical replicates. (**F**) Whole-mount in situ hybridization for the Wnt3 transcript in head-regenerating halves of bisected animals under control and isotonic (70 mM sucrose) conditions. Bisected halves were allowed to close the wound for ~ 1.5 h (closed) and then randomly split between the different media. Representative data are shown. (**G**) Quantification of oscillation parameters in the *ecto pAct::GFP, pAct:Wnt3* spheroids (WNT, n=15). Spheroids from the line *ecto pAct::GFP* were used as a control (GFP, n=17). Wilcoxon rank-sum test was used for statistical comparison.

Table S1. Genes with the osmotic stress functional signature examined in Fig. S3C.

Shading in the table corresponds to the figure colors. The mammalian functional annotation data were acquired form the Molecular Signatures Database (https://www.gsea-msigdb.org/gsea/msigdb/). Corresponding *Hydra* genes were identified using the homolog annotation taken from the *Hydra*2 genome project (https://research.nhgri.nih.gov/*Hydra*/) and the NCBI genome database (https://www.ncbi.nlm.nih.gov/gene). Note that in some cases several *Hydra* genes map to an identical mammalian homolog.

NCBI GeneID	Mammalian homolog	Functional annotation
100197804	*AKR1B1*	Hypertonic response
100214195	*HNMT*	Hypertonic response
100199336	*LETM1*	Hypertonic response
100210191	*MICU1*	Hypertonic response
100198865	*OXT*	Hypertonic response
100198028	*SLC12A2*	Hypertonic response
100208923	*XRCC5*	Hypertonic response
100211211	*XRCC6*	Hypertonic response
105848752	*YBX3*	Hypertonic response
100209595	*CAB39*	Hypotonic response
100198551	*MYLK*	Hypotonic response
100197110	*OXSR1*	Hypotonic response
100210915	*SLC12A6*	Hypotonic response
100202442	*ABCB1*	Response to osmotic stress
101241118	*ABCB1*	Response to osmotic stress
100212701	*ANXA7*	Response to osmotic stress
101238969	*ANXA7*	Response to osmotic stress
105844932	*AQP9*	Response to osmotic stress
100203331	*AQP9*	Response to osmotic stress
100211688	*ATF2*	Response to osmotic stress
100211866	*ATF2*	Response to osmotic stress
100202650	*BAX*	Response to osmotic stress
100203439	*BAX*	Response to osmotic stress
101235784	*CAPN3*	Response to osmotic stress
100204696	*CASP3*	Response to osmotic stress
100212685	*CASP3*	Response to osmotic stress
100202915	*CASP3*	Response to osmotic stress
100198658	*DDX3X*	Response to osmotic stress
100192294	*DDX3X*	Response to osmotic stress
100200171	*DDX3X*	Response to osmotic stress
100213362	*DYSF*	Response to osmotic stress
100208455	*KCNMA1*	Response to osmotic stress
100204742	*KMO*	Response to osmotic stress
100201328	*MAP2K7*	Response to osmotic stress
100213972	*MDR1*	Response to osmotic stress
100199733	*MYLK*	Response to osmotic stress
100211813	*NOLC1*	Response to osmotic stress
101235318	*P53*	Response to osmotic stress

100197078	*PK1L2*	Response to osmotic stress
100207801	*PKD2*	Response to osmotic stress
100198291	*PKD2*	Response to osmotic stress
100207545	*PKD2*	Response to osmotic stress
100206298	*S12A2*	Response to osmotic stress
100204936	*SERPINB6*	Response to osmotic stress
100215837	*SORD*	Response to osmotic stress
100203619	*TP53*	Response to osmotic stress
100215316	*WNK3*	Response to osmotic stress
100205438	*ZFP36L1*	Response to osmotic stress

Table S2. Top 10% genes sensitive to the removal of mechanical stimulation.

The annotation of mammalian homologs is taken from the *Hydra*2 genome project and the ncbi genome database. Only genes, for which a mammalian homolog could be found, were used in downstream GO terms analysis. Cluster identities correspond to those in Fig S3b-c.

NCBI GeneID	Mammalian homolog	Adjusted P-value	Sum of differences (A.U.)	Cluster
100198792	*NPC2*	4.6326E-09	136.092381	5
100205069		6.9999E-24	134.095417	5
100213913		3.1262E-35	123.973407	5
100204588	*DMRT1*	3.6722E-13	107.95492	5
100200513	*H4-16*	1.6495E-57	102.175059	5
100200175	*PAX3*	3.2117E-24	101.235388	5
100197450		7.4321E-13	100.906573	5
100210977		7.4045E-10	95.3031152	5
100211420		3.3403E-23	92.9587732	5
101235091	*BPI*	7.3336E-25	91.9228974	5
105847657		4.6034E-30	90.4197589	5
100200125		6.7357E-12	89.0720116	5
100204140	*SLC36A1*	3.6431E-20	84.6764672	5
105846366		3.1009E-12	83.8653636	5
101235129		7.1214E-10	83.1229474	5
105846591		2.1964E-12	81.9765514	5
100204267	*H4-16*	2.5964E-36	81.1650399	5
100192253	*MDN1*	7.8772E-10	79.260342	5
101237889		6.3432E-09	79.0574564	5
100215610		1.1107E-07	78.8610029	5
101241797		9.9278E-08	78.6866458	5
100214145	*ARF1*	3.3494E-37	78.4883676	5
100210142		2.5949E-09	78.1921106	5
100204912	*FAXC*	3.6078E-13	77.8118357	5
105848556		7.8388E-19	76.6290038	5
100205153		4.0525E-13	76.6027665	5
100198375	*UBE2M*	3.0794E-10	75.8575807	5
101239409	*CHST11*	6.3026E-13	75.6299749	5
105845131		4.9111E-22	75.131633	5
105850420		6.0134E-30	74.830474	5
101240945		3.0763E-21	73.637984	5
100205795	*HEXA*	2.8568E-12	73.0806362	5
100207977	*CHAC1*	7.7933E-11	72.7090957	5
100206276	*SPIRE1*	7.7358E-28	72.6416818	5
100204652	*M1AP*	1.5981E-10	71.0456557	5
100213095	*CHST1*	3.3537E-15	70.7990643	5
100205814		6.5178E-20	100.53371	4
105850674		6.6341E-07	87.1054945	4
100210377		5.7241E-12	80.1938687	4

105847121		8.6105E-20	77.1119522	4
100215038	*WNT9/10a*	1.809E-160	169.212235	3
100214793		3.717E-137	141.847658	3
101234798	*MMP19*	1.1136E-19	129.449635	3
100211747	*HPGDS*	4.6766E-40	117.071199	3
100214868	*WNT7*	3.2928E-22	111.795984	3
100212279		4.1605E-35	107.875029	3
100203050	*WNT3*	7.9199E-23	104.022471	3
100206447	*DDR1*	1.3286E-16	102.877443	3
100209110		5.9247E-19	99.3826011	3
101240588	*COL4A1*	5.6316E-35	98.8317157	3
105847477	*KLKB1*	3.9643E-48	98.6953477	3
105843060	*MTPN*	5.8948E-26	98.4730393	3
105846947	*DMBT1*	4.3646E-18	97.1788779	3
100201149	*GOLGB1*	1.1656E-18	95.571484	3
100199145		9.7521E-20	95.5645877	3
100213338		1.6442E-17	95.4806636	3
100203315		3.821E-07	94.5783671	3
100215832		2.6035E-11	93.8196351	3
100210883	*ZIC4*	7.0249E-13	92.0023137	3
100198091		5.6989E-82	91.3725492	3
100205589	*ZSWIM6*	1.9592E-32	91.0877752	3
101235638	*MC1R*	5.9506E-33	90.7801104	3
100215883		5.4484E-38	90.4575232	3
100214647	*COL4A2*	1.2705E-21	89.3511821	3
100197980	*AGO2*	8.6049E-28	88.7448567	3
100197276	*LAMB1*	2.3072E-26	87.2690407	3
100215810	*MUC5AC*	2.1317E-24	87.0480783	3
100208937		6.3469E-26	86.3673867	3
100211987	*COL1A1*	1.4675E-30	85.9500703	3
100213961		3.2435E-07	85.6512258	3
105843397	*SUCNR1*	5.8369E-08	84.5183252	3
100200109	*AGO1*	3.3473E-20	84.2078428	3
100205317	*BCR*	1.5419E-42	84.0707399	3
100201345		6.9752E-31	83.9326117	3
105843191	*SMYD4*	1.4373E-08	83.900393	3
100209165	*PXN*	4.0241E-29	83.720318	3
101237470	*SP5*	1.6895E-19	83.4839872	3
100203539	*SBF2*	1.8026E-63	82.2574124	3
100212732	*ZNFX1*	6.561E-20	81.8082977	3
100200618	*LAMA3*	2.2243E-19	81.5123445	3
100205218	*COL4A1*	1.2508E-22	80.0568453	3
100211594	*SH3RF1*	4.5916E-27	79.8703778	3
100214250	*COMP*	4.0807E-49	79.7026634	3
100205822		8.7407E-11	79.6388417	3
100214706	*ZNFX1*	1.3698E-08	79.6088021	3
105847351		1.9103E-18	79.5634631	3
105847324		3.6577E-15	78.590009	3

100203271		2.2374E-14	77.9479218	3
100204823		5.0267E-12	77.8807991	3
101234364	*ZNFX1*	2.9224E-23	77.5378183	3
100204347		1.5128E-26	76.8581599	3
100211037	*PITX1*	1.9622E-15	76.6511158	3
100202525		3.0872E-17	75.9005866	3
100207920	*TIMP3*	3.1925E-17	75.6159102	3
101240985	*COL6A6*	8.2395E-29	75.1719549	3
100208925	*TRPV3*	1.9281E-38	75.1135063	3
101239940	*HECTD1*	3.9643E-48	74.9103455	3
101240505	*COL4A1*	1.4454E-21	74.5043193	3
100215811	*ANKRD52*	1.3513E-13	74.1728462	3
105844127		4.9043E-22	73.8252026	3
105849579		3.1318E-08	73.7209731	3
100215286	*COL6A6*	3.3727E-20	73.6005058	3
100205070		6.2009E-30	73.3631814	3
100200555		1.0528E-12	72.4081638	3
100207691	*LAMC1*	8.1635E-23	72.3880374	3
100199754	*COL1A1*	3.3394E-21	72.28531	3
101239232	*ANKRD28*	1.9786E-20	71.8506799	3
100209738	*SF3B1*	2.3597E-42	71.6429143	3
100209752		1.3275E-10	71.6130722	3
100206389	*AXIN1*	1.545E-22	71.4835447	3
100202503		9.9044E-09	71.324878	3
101239976	*TFPI*	1.9211E-17	70.8434945	3
100205900	*BANK1*	5.3075E-30	71.5096716	2

Table S3. Functional annotation enrichment of the upregulated and downregulated genes from the top 10 % mechanosensitive genes.

Only the dominant clusters of genes were analyzed since the number of members of the other clusters within the set was negligible and not sufficient to analyze enrichment. Green shading indicates functional terms related to extracellular matrix and yellow shading indicated functional terms related to Wnt signaling. Note that there were no retinoic acid signaling genes. The enrichment of this signature is generated by Wnt signaling genes, as they often crosstalk to the retinoic signaling. No significantly enriched functional signatures were found for cluster 5.

upregulated in control (cluster 3)	
Functional category	False discovery rate
extracellular matrix part	3.80E-13
extracellular matrix structural constituent	1.66E-10
endoplasmic reticulum lumen	1.48E-09
frizzled binding	6.43E-09
collagen catabolic process	5.38E-08
multicellular organismal catabolic process	1.01E-07
collagen metabolic process	4.34E-07
multicellular organismal macromolecule metabolic process	5.77E-07
multicellular organismal metabolic process	8.98E-07
basement membrane	9.62E-07
cell fate commitment	2.32067E-06
gene silencing by RNA	3.9343E-06
skeletal system development	1.01115E-05
Wnt signaling pathway	1.30022E-05
response to retinoic acid	1.42522E-05
collagen	2.1533E-05
platelet-derived growth factor binding	2.46334E-05
gene silencing by miRNA	3.37478E-05
basal lamina	3.37921E-05
posttranscriptional gene silencing by RNA	4.85417E-05
posttranscriptional gene silencing	4.85417E-05
gene silencing	4.85456E-05
receptor agonist activity	5.83005E-05
cellular response to retinoic acid	5.86821E-05
G-protein coupled receptor binding	0.000107706
Golgi lumen	0.000151083
forebrain development	0.000158994
canonical Wnt signaling pathway	0.000195776
downregulated in control (cluster 5)	
Functional category	False discovery rate
intracellular lipid transport	0.124710452
amino acid transport	0.188127412
sulfur compound metabolic process	0.242697813
organic anion transport	0.477999928
carnitine transmembrane transport	0.498036189

organic acid transport	0.498036189
carboxylic acid transport	0.498036189
amino-acid betaine transport	0.498036189
carnitine transport	0.498036189
biotin metabolic process	0.498036189

Supplementary Movies

Movie S1.

Control spheroid imaged in *Hydra* medium.
Movie S2.

Control spheroid imaged in isotonic medium with 70 mM sucrose.
Movie S3.

Oscillations of a head-regenerating half from a bisected animal in *Hydra* medium.
Movie S4.

Wnt-overexpressing spheroid imaged in *Hydra* medium.
Movie S5.

Wnt-overexpressing spheroid imaged in isotonic medium with 70 mM sucrose
Movie S6.

Bud spheroid imaged in *Hydra* medium.
Movie S7.

Bud spheroid imaged in isotonic medium with 70 mM sucrose

II.1.2. β-catenin as a Potential Link between Wnt Signaling and Tissue Stretching

Thanks to its dual role as a mechanosensitive junctional component and transcriptional activator in the canonical Wnt signaling pathway, β-catenin is an excellent candidate for connecting tissue stretching with Wnt3 expression in our system. To investigate its dynamics in regenerating spheroids, we took advantage of a β-cat::GFP C-terminal fusion transgenic line (generated by Yukio Nakamura, University of Aberdeen), which harbors a random integration of the fusion construct in the genome of ectodermal cells. Spheroids in standard conditions usually displayed abundant nuclear β-catenin during the initial time points, which did not seem to be spatially restricted within the spheroid. This early ubiquitous nuclear localization is probably connected to injury-related Wnt upregulation (Cazet et al., 2021; Lengfeld et al., 2015). Subsequently, the nuclear GFP signal would disappear and later show up again but only within a spatially constrained patch of cells (Fig. II.1-1. A-B). Interestingly, we never observed this patch of nuclear β-catenin appearing before the first spheroid deflation (Fig. II.1-1. C). Since technical limitations of the imaging did not allow imaging the full spheroid, it was not always possible to track the patch and assess its stability, due to the spheroid rotation. However, in cases where the patch remained in the field of view throughout the time course, it appeared stable and coincided with the location of the future head (Fig. II.1-1. D).

We then decided to investigate the relationship between the nuclear β-cat^{+} patch appearance and the spheroid deflation. The observation that β-catenin only became nuclear after at least one spheroid deflation was suggestive of a causal relationship. While mechanical changes associated with the tissue rupture could force the protein to become nuclear, such a mechanism would seemingly contradict our previous findings that the spheroids rely on a continuous measure of tissue stretching rather than counting the elapsed cycles (Fig. 2 in II.1.1). To test whether the nuclear localization of β-catenin indeed followed spheroid deflation, we slowed down the oscillations using intermediate osmolyte concentrations (30 mM sucrose or sorbitol). In these conditions, the patch of β-cat^{+} nuclei appeared already during the first inflation, indicating its independence from the spheroid deflation (Fig. II.1.-2. A). Moreover, the absolute time interval within which the patch first appears seemed to have remained the same irrespective of the experimental manipulation (Fig. II.1.-2. B). Similar results were obtained when investigating the dependence between the original spheroid tissue axial position and the nuclear β-catenin patch emergence. Thus, the observed differences in symmetry breaking times between spheroids derived from different axial positions (Fig. S2A in II.1.1) cannot be attributed to different temporal dynamics of β-catenin nuclearization.

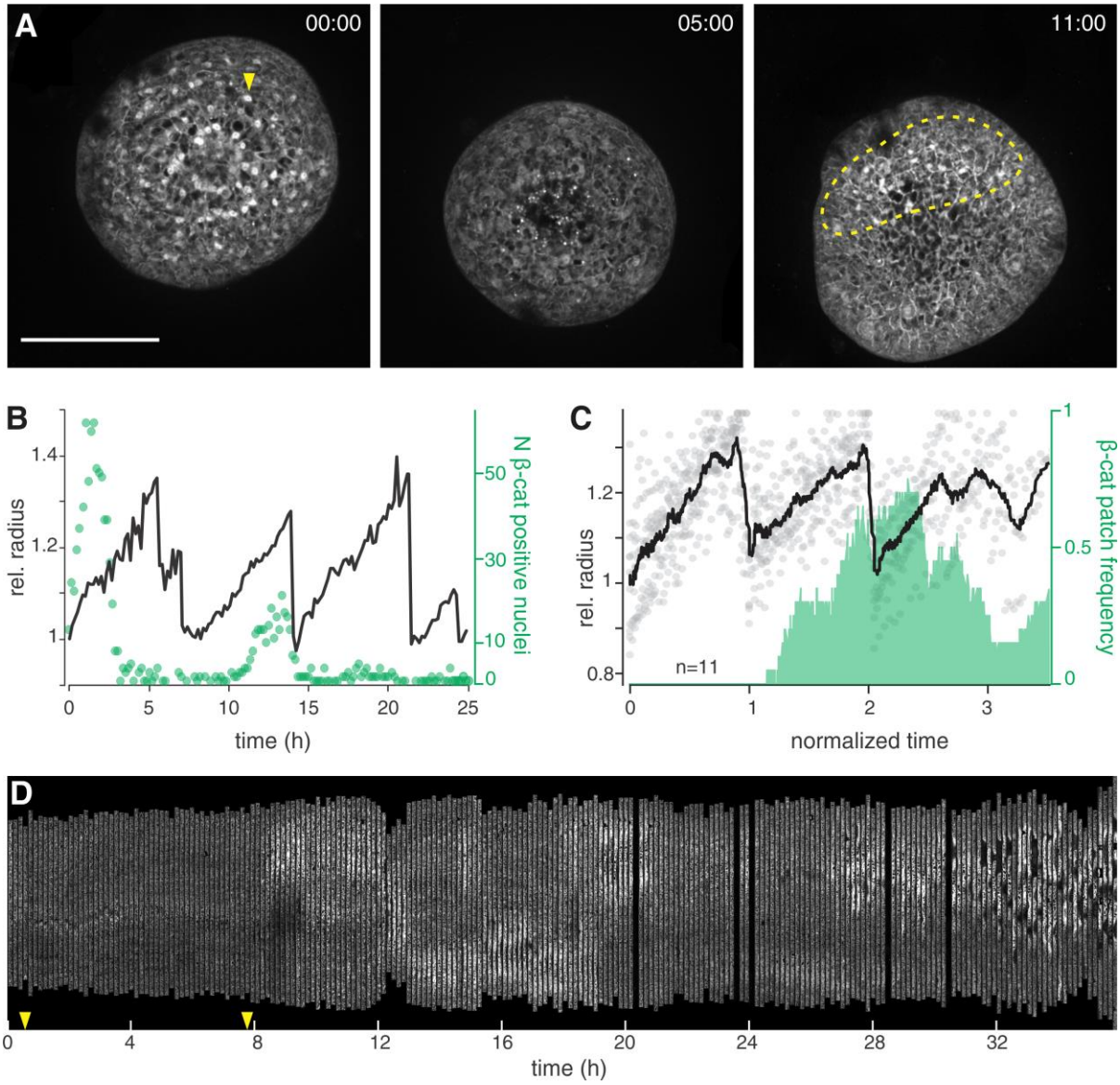

Fig. II.1-1. Localized patch of nuclear β-catenin in regenerating spheroids. (**A**) Typical temporal dynamics of β-cat$^+$ nuclei (yellow arrowhead) in spheroids. Very early after the spheroid closure (left), the protein appears nuclear in the majority of cells. This pattern is then lost (center) and reappears only in a subset of cells (right, dotted line). Maximum Z projections, scale bar 100 μm. (**B**) Quantification of the oscillatory behavior and number of positive nuclei in the spheroid from (A). (**C**) Quantification of the average oscillatory behavior and the appearance of nuclear β-catenin patch in several spheroids. The black line represents averaged radius behavior while points represent measurements from individual spheroids. One time unit corresponds to the average duration of the first oscillation. (**D**) Montage of straightened segmented ectodermal tissue layer from a single spheroid, in which the patch of β-cat$^+$ nuclei (light area) was visible throughout the course of regeneration. Yellow arrowheads indicate deflations.

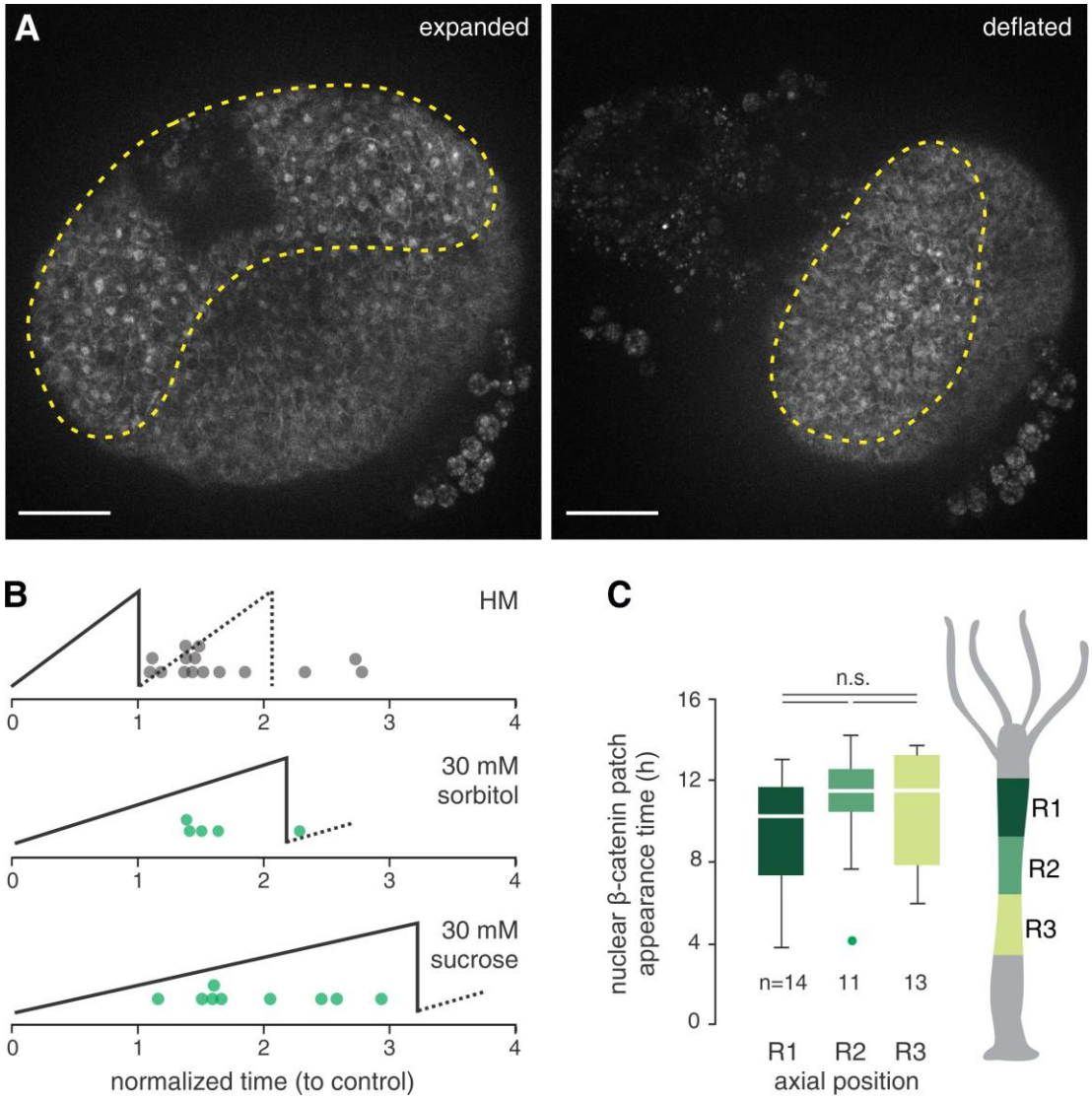

Fig. II.1-2. The timing of β-catenin nuclear localization does not depend on spheroid deflation or tissue axial origin. (**A**) A patch of nuclear β-catenin (dotted lines) present already before the first deflation, in a spheroid cultured in 30 mM sucrose. The time difference between the shown maximum Z projections is 10 min. Scale bars 100 µm. (**B**) Quantification of the nuclear β-catenin patch appearance in spheroids cultured in *Hydra* medium, 30 mM sorbitol, and 30 mM sucrose. Time is normalized to the average duration of the first oscillation in control conditions. (**C**) The relationship between the original axial position of the spheroid tissue and the timing of nuclear β-cat^{+} patch appearance.

Interestingly, when using higher sucrose concentrations, we also observed that the nuclei became less clearly defined. In isotonic conditions (70 mM sucrose) the localized patch of β-cat^{+} nuclei did not appear at all (Fig. II.1.-3), suggesting that the level of tissue stretching might be influencing the amounts of nuclear β-catenin rather than the timing of its localization there. However, this qualitative result would need to be verified quantitatively, ideally using a double transgenic line harboring a nuclear marker in addition to the β-catenin::GFP fusion. This would allow segmenting the nuclei and measuring changes of nuclear β-catenin fluorescence intensity over time.

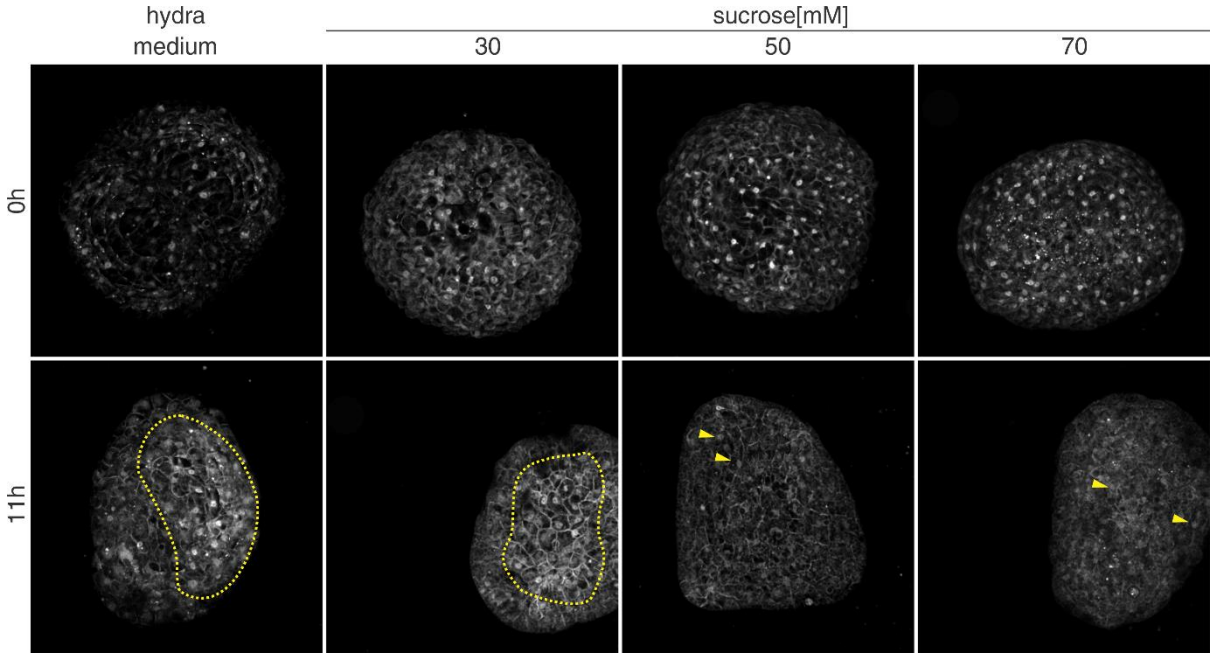

Fig. II.1-3. B-cat nuclear patch intensity seems to correlate with the intensity of tissue stretching. Representative images, illustrating the behavior of β-catenin in different osmolarities. The initial global nuclear localization, responding to the wound, can be seen and is comparable in all conditions (top row). However, the subsequent localized patch of β-cat^{+} nuclei is only clearly visible in the control and 30 mM sucrose samples (yellow dotted lines). In the higher concentrations, potentially positive nuclei are sparsely visible (yellow arrowheads), but without a nuclear counterstain cannot be clearly identified. All images come from the same biological replicate and were imaged using the same microscope settings.

II.1.3. Wnt3 Promoter Analysis to Uncover Candidate Mechanoresponsive Transcription Factors

To unbiasedly select other candidate factors that could regulate *Wnt3* expression in response to tissue stretching, we performed transcription factor (TF) binding site prediction in the 1500 bp region upstream of the *Wnt3* transcription start site. Using the motif data from the JASPAR database (Sandelin et al., 2004), we were able to detect *bona fide* binding sites for 343 animal transcription factors. This set was reduced to 63 based on literature mining, focusing on factors having genetic interactions with the *Wnt3* gene, regulators of Wnt signaling, or involved in mechanosensing. We were then able to identify homologs for 32 of these genes in the *Hydra* genome. Since the transcription factor, involved in transforming mechanical signals to *Wnt3* expression would have to be present in body column cells from the beginning of the regeneration process, we further reduced the candidate group (based on the positional RNA-seq data) only to genes expressed throughout the body column (Fig II.1-4. A). This gave us 15 candidate genes (Fig. II.1-4. B), which were pre-screened for head regeneration phenotypes upon knockdown.

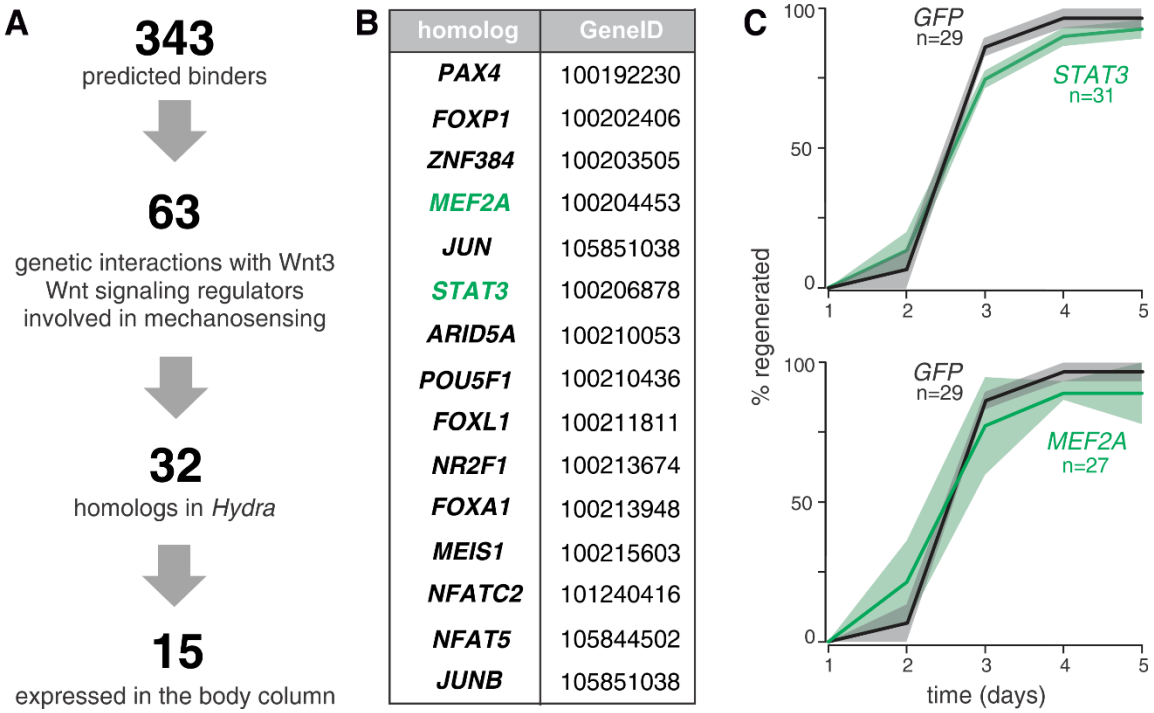

homolog	GeneID
PAX4	100192230
FOXP1	100202406
ZNF384	100203505
MEF2A	100204453
JUN	105851038
STAT3	100206878
ARID5A	100210053
POU5F1	100210436
FOXL1	100211811
NR2F1	100213674
FOXA1	100213948
MEIS1	100215603
NFATC2	101240416
NFAT5	105844502
JUNB	105851038

Fig. II.1-4. Selection and testing of candidate TFs that modulate Wnt3 expression in a mechanically-dependent manner. (**A**) Selection strategy. (**B**) Selected candidate transcription factors. Genes highlighted in green showed an improvement of head regeneration upon RNAi in the preliminary screening. (**C**) Follow-up RNAi experiments did not support the altered regeneration phenotype upon knockdown of *STAT3* or *MEF2A*. Lines represent averages of 3 independent replicates (with a total of n animals). Shaded areas indicate 95% confidence intervals of the mean. The control samples are identical in both cases.

While we did not observe any phenotypes for most of the candidate genes, *Mef2A* and *Stat3* were an interesting exception, as their knockdown seemed to improve head regeneration. This might indicate that they function as *Wnt3* repressors, which are being removed from the promoter or downregulated through the Wnt-enhancing action of tissue stretching. However, subsequent RNAi experiments did not confirm this initial observation, in both cases producing results comparable to control (Fig. II.1-4.). Thus, this attempt to identify potential *Wnt3* regulators responsive to tissue mechanics was not successful. In the future, changes of the selection pipeline and/or improved knockdown methods might produce more favorable results.

Additionally, we also explored the possible usefulness of the regeneration deficient *reg-16 Hydra* strain (gift of Hiroshi Shimizu, Mishima Hydra Laboratory) for identifying such regulators. This strain was one of the mutant lines generated by sexual inbreeding of animals isolated from the same pond (Sugiyama & Fujisawa, 1977a). It shows a strongly reduced head regeneration capacity, but the existing head maintenance and budding do not appear affected (Sugiyama & Fujisawa, 1977b). Moreover, it seems to have a normal injury response (Kobatake & Sugiyama, 1989; Rentzsch et al., 2007) and can be rescued by ectopically provided Wnt3 (Lengfeld et al., 2009), suggesting a defect of organizer initiation during regeneration, upstream of the self-sustaining Wnt3 loop. We thus hypothesized that the mechanism transforming mechanical stimuli to Wnt3 expression might be defective in these animals. Such explanation would be consistent with our previous observations of significantly hindered (but not abolished) head regeneration in bisected animals under isotonic conditions (Fig. S1M and S5F in II.1.1.). To investigate this possibility further, we decided to sequence the *Wnt3* promoter of *reg-16* animals, since the genetic basis of their phenotype remains unknown. We scored the head regeneration in the aboral halves upon bisection at 50% body length and used the oral halves to further propagate the animals, divided into subcultures based on individual regeneration phenotypes (Fig. II.1-5. A). We then used the aboral halves for DNA extraction and sequencing once the regeneration time course was finished. As expected, we obtained a mixture of normally regenerating animals and others either showing delays or complete non-regeneration. Interestingly, however, when the asexual progeny of non-regenerating animals was bisected again, it showed a similar ratio of these two outcomes, suggesting an inherently probabilistic nature of the phenotype (Fig. II.1-5. B-C). This was consistent with the sequencing results, where all animals were found to carry the same mutations irrespective of their regeneration phenotype (Fig. II.1.-5. D). In total, we detected 8 mutations in the *Wnt3* promoter region of *reg-16* (one insertion and 7 substitutions, Fig. II.1.-5. E and Appendix 1), none of which was directly affecting

known functional TF binding sites. Interestingly, however, one of the nucleotide substitutions is located in between two neighboring Tcf binding sites, both essential for a proper organizer function (Nakamura et al., 2011). It might therefore affect the proper assembly of TF complexes involved in the organizer maintenance. Several of the detected mutations also do not seem to change TF binding site predictions significantly in comparison to the wt sequence, suggesting that they might reflect natural sequence variability. Other mutations, however, seem to have functional consequences (Appendix 2). For example, the -1250 G>A substitution appears to potentially create a new Hox factor binding site. Interestingly, such potentially functionally significant mutations are localized in the part of the Wnt3 promoter previously termed as the activator element (Nakamura et al. 2011), further supporting their likely influence on the Wnt3 gene expression regulation.

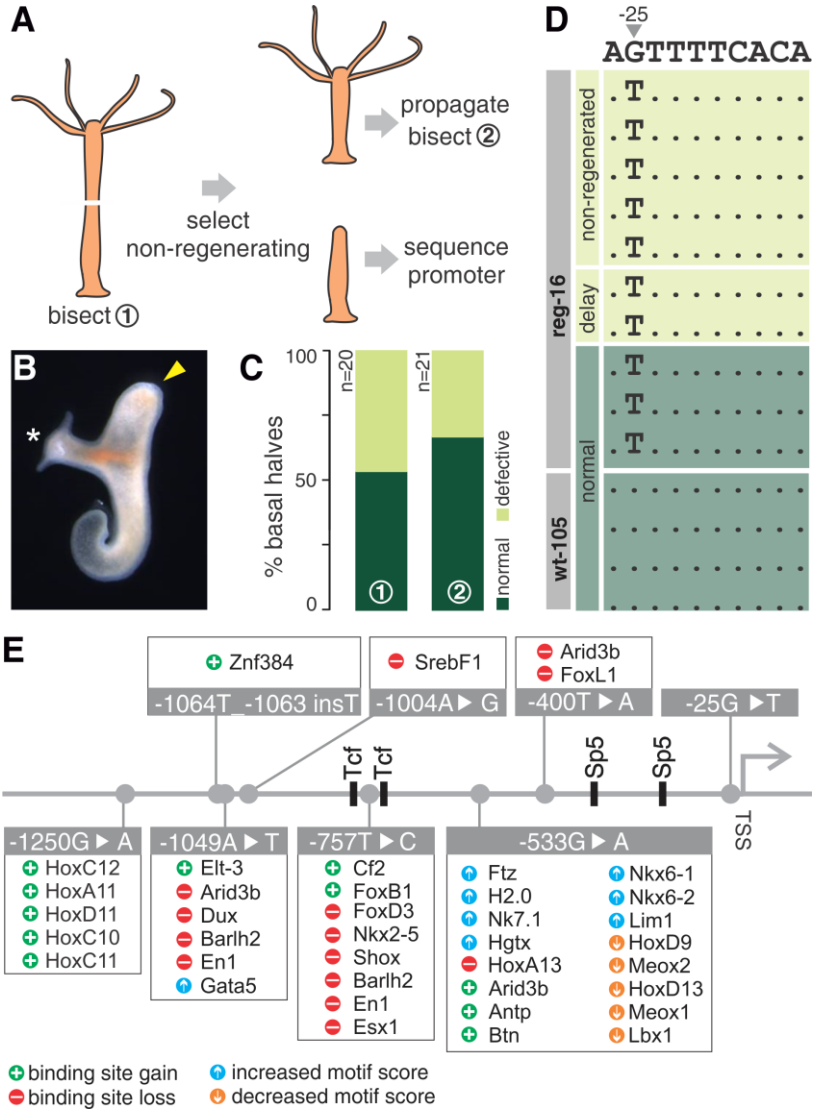

Fig. II.1-5. Phenotypes of the *reg-16* mutant and potentially affected binding sites in the Wnt3 promoter. (**A**) The strategy to select head-regeneration deficient individuals from the culture and propagate them. (**B**) An example of a non-regenerating foot half 5 days post bisection. The cut surface (arrowhead) is healed but does not show signs of head regeneration Asterisk indicates a newly forming bud. (**C**) The probabilistic nature of head regeneration deficit in the *reg-16* animals. Initially, about half of the bisected animals show head regeneration defects (1) and a similar ratio is obtained after re-bisecting the offspring of these animals (2). Animals that do not regenerate a head by 3 days post bisection are considered to have defective regeneration. (**D**) Despite different regeneration pheno-types, all the sequenced reg-16 individuals share the same mutations in the Wnt3 promoter. Here shown on the example of the -25G>T substitution. Dots in the alignment indicate nucleotides identical to the reference sequence. (**E**) Schematic representation of the mutations in the Wnt3 promoter and potential most significantly affected transcription factor binding sites. The position of intact *Tcf* and *Sp5* binding sites is also indicated. TSS – transcription start site.

II.1.4. Discussion

Our results, connecting the amounts of tissue stretching with *Wnt3* transcriptional activation, open several questions for further investigation. In particular, how is the emerging mouth organizer localized if all the spheroid cells experience stretching and should produce Wnt3. A likely explanation is the cell-to-cell variability of mechanical properties, which would lead to variable amounts of tissue stretching across the spheroid. As a result, different amounts of Wnt3 protein will be made in different areas of the spheroid and could drive localized symmetry breaking (Fig. II.1-6. A). Indeed, imaging reveals that the spheroid tissue is more stretched in some areas than in others, giving further support to this idea (Fig. II.1-6. B). It will therefore be pivotal to investigate whether the more stretched parts show higher Wnt3 expression and are the sites of symmetry breaking and head formation.

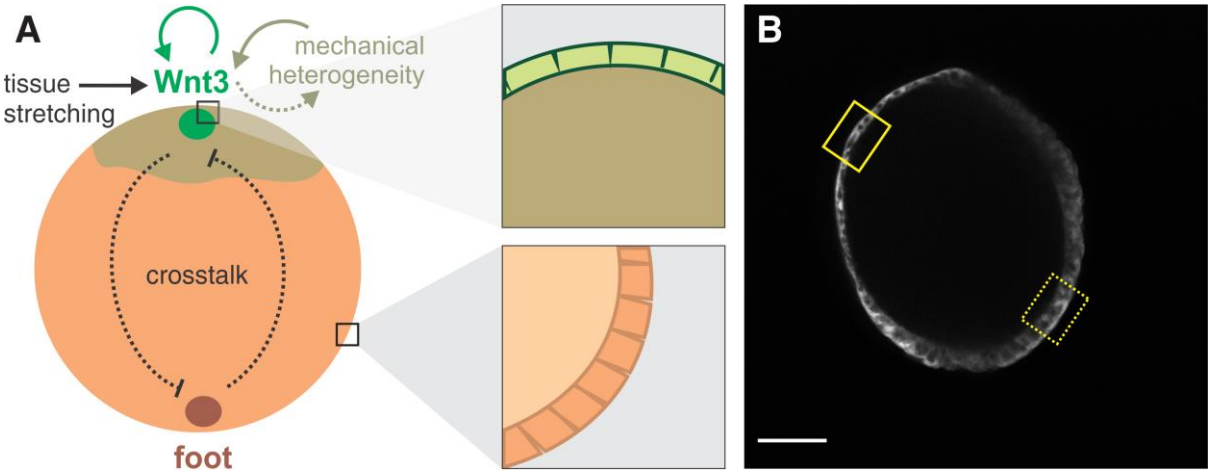

Fig. II.1-6. Mechanical asymmetries in spheroids as potential drivers of the head organizer positioning. (**A**) The proposed model for head organizer positioning in regenerating *Hydra* spheroids. In a freshly generated tissue spheroid, Wnt3 expression is sustained through tissue stretching as a result of mechanical oscillations. Even though all cells are being stretched and capable of differentiating to the organizer, the location of the organizer can be specified through local bias of tissue mechanical properties, signaling crosstalk with the surrounding, and the developing foot organizer. Symmetry breaking happens once a small group of cells with sufficiently high Wnt3 levels is established and the Wnt3 expression then becomes self-sustaining. This then initiated the downstream organizer program. (**B**) Equatorial optical section through an expanded *pAct::GFPecto* spheroid, illustrating heterogeneities in tissue stretching. Note the much thinner wall on one side (full line rectangle), compared to a less stretched thicker tissue (dotted rectangle) on the other side. Scale bar 50 µm.

Interestingly, another mechanism for localizing the head organizer was proposed recently, relying on the organization of supracellular actin muscle fibers (Livshits et al., 2017). These fibers run perpendicular to the body axis in the endoderm and parallel to it in the ectoderm, coalescing at the poles of the animal (Fig. II.1-7. A). When a tissue

piece, excised from the body column, folds into a spheroid, two such coalescence points are created, and the regenerated head position coincides with one of them (Fig. II. 1-7. B). The authors argue that this coalescing actin fiber topology therefore drives head organizer specification. However, such explanation contradicts previous findings in reaggregates (Seybold et al. 2016), which lose the organized actin network during tissue dissociation into single cells. While the fiber network begins reappearing upon reaggregation, it is disorganized and does not have a common directionality until after symmetry breaking. At this point, the fibers will begin to reorient towards the newly formed organizer (Fig. II.1-7. C). Another recent study has also highlighted the general ability of Wnt-primed tissue to reorganize and attract the supracellular actin fibers (Wang et al., 2020). Thus, instead of driving the organizer localization *per se*, the supracellular actin network topology can likely bias its positioning through the influence on tissue mechanical properties. Such view where the structure of actin fibers is a part of the mechanochemical feedback loop controlling *Wnt3* expression, and itself being shaped by it, would be compatible with our model presented above. Assuming that we correctly predict the more stretched parts of spheroids to be the sites of higher *Wnt3* expression and symmetry breaking, another interesting prediction emerges, that the actin fiber coalescence points should also be located there, since they would be responsible for allowing the tissue to stretch more.

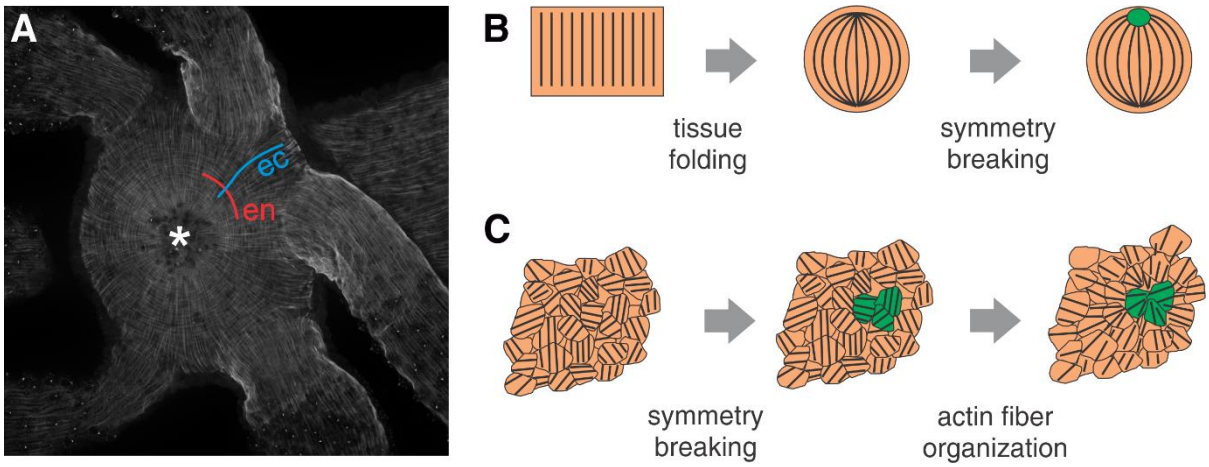

Fig. II.1-7. Supracellular actin fibers and the head organizer positioning. (**A**) Supracellular actin fiber organization in the *Hydra* head revealed by phalloidin staining. Ectodermal fibers (ec) run parallel to the axis and coalesce in the mouth (asterisk). Endodermal fibers (en) run perpendicular to them. (**B**) Rectangular pieces cut from the body column can retain intact fibers that seem to bias the localization of the future organizer. (**C**) In reaggregates, supracellular actin organization is lost and reemerges as a network of randomly oriented fibers. Once the symmetry is broken, the organizer guides actin fiber repositioning. Cartoons based on Livshits et al. (2017) and Seybold et al. (2016).

The second key outstanding question concerns sensing of the mechanical stimuli by *Hydra* cells and translating them to chemical signals. We attempted to explore the possible mechanisms by investigating the dynamics of β-catenin and searching for binding sites of potentially mechanosensitive transcription factors in the *Wnt3* promoter. Neither of these approaches yielded conclusive results thus far.

While live imaging of β-catenin during spheroid regeneration brought interesting results, their interpretation is highly dependent on the current experimental limitations, namely the inability to image the entire spheroid and the lack of a nuclear marker. In a minority of cases, we observe the patch of β-cat^{+} nuclei to be stable and give rise to the future hypostome. However, in most spheroids it seems to disappear and reemerge later. Although such dynamic behavior would add an interesting dimension to understanding the role of β-catenin, we are currently not able to distinguish actual fluctuations from artefacts generated by the spheroid movement. For example, a stable patch moving out of the field of view due to spheroid rotation. Thus, to be able to assess the nuclear β-catenin patch stability and dynamics, it will be crucial to employ a different imaging strategy, such as lightsheet microscopy, allowing to image the entire spheroid. This can be coupled with "tissue tattoo" approaches, using photoconvertible dyes (Maroudas-Sacks et al., 2021) to create reference points for tracking the spheroid movement. Similarly, combining the reporter line with a nuclear marker (e.g. *H2B::mCherry*) would allow monitoring β-catenin translocation in and out of the nuclei and help quantitatively dissect the tentative relationship between overall stretching amounts and nuclear levels of the protein presented in Fig. II.1.-3. It would also facilitate correlating the protein localization dynamics with areas of differential tissue stretching in the spheroid.

Irrespective of technical concerns, determining whether the observed nuclear translocation of β-catenin is a cause or consequence of Wnt signaling activation is extremely important for interpreting our results. To this end, a *Wnt3* FISH time course in spheroids can be used to investigate the spatiotemporal behavior of *Wnt3* transcription and compared with the β-catenin localization data. The patch of β-cat^{+} nuclei might precede increased *Wnt3* expression in the cells, indicating the role of β-catenin in sensing mechanical stimuli. An intriguing mechanism for such sensing was recently shown to function in human embryonic stem cells, where mechanical stretching increases the release of β-catenin from junctions through its phosphorylation and thus activates Wnt signaling (Muncie et al. 2020). Alternatively, even if β-catenin itself was involved in sensing tissue mechanics in our system, the required initial nuclear levels could be below the dynamic range of the reporter.

In this case, the β-cat^{+} nuclei would only be visible as a result of high Wnt activation levels in the respective cells, compared to the rest of the spheroid. The same would be true if β-catenin was not part of the mechanosensing mechanism. However, its nuclear localization would still be a valuable indirect measure of Wnt signaling activity in both scenarios, which can be correlated with other cellular properties such as deformation or position within the spheroid.

Regardless of the precise relationship between tissue stretching and β-catenin nuclear localization, the patch of positive nuclei appears surprisingly early during spheroid development. Molecular symmetry is therefore broken early, at least in relation to Wnt activation. As shown in Fig. II.1.-2, its timing also seems independent from the original axial position, suggesting that it cannot account for the previously observed differences of mouth establishment timing in spheroids (Fig. 2 and S2, section II.1.1). A possible alternative explanation is that initiating the organizer program requires different duration of mechanically sustained *Wnt3* expression, depending on the axial position. Since different Wnt ligands are expressed sequentially during organizer establishment (Fig. 5, section II.1.1. and Lengfeld et al. 2015), this hypothesis can be tested by comparing the temporal dynamics of their expression in spheroids originating from very different axial positions. Rather than the organizer itself, the downstream mouth opening stabilization, could also be affected. In either case, such graded timing differences could result from an inhibitory gradient in the body column.

To complement focusing on β-catenin as a potential candidate, we also implemented untargeted search strategies, based on *in silico* predictions of TF binding sites in the *Wnt3* promoter. We subsequently tested how knockdowns of the selected factors influenced head regeneration. Interestingly, none of the 15 selected factors has shown a significant phenotype. Although this likely stems from insufficient RNAi efficiency, other explanations should also be considered. Since our predictions are based on transcription factor binding motifs from other metazoan species, varying levels of conservation for different factors can influence the accuracy of the prediction (Villar et al., 2014). Some of the predicted sites might not be functional or could be bound by other proteins. Similarly, some *Hydra* TFs might recognize motifs different from those in the database and would not be identified in the analysis. Moreover, even though the *Hydra* genome contains most transcription factor families, they usually have a smaller number of individual members (Chapman, Kirkness, Simakov et al. 2010), which complicates homolog annotation. One possibility to improve chances of identifying the correct candidates might be relaxing selection criteria, such as motif conservation threshold, or not requiring known involvement in Wnt regulation

or mechanosetransduction. However, this would likely lead to a dramatic increase of candidate gene numbers. Alternatively, the recent ATAC-seq data for homeostatic and regenerative *Hydra* are becoming available (Cazet et al., 2021; Siebert et al. 2019; Murat et al., 2019), can be used to pinpoint *Wnt3* promoter regions relevant for TF binding in different conditions. In combination with improved knockdown and knockout approaches, these strategies should allow more thorough experimental verification of computational predictions.

Analogous challenges also apply for the orthogonal experiments with the *reg-16* mutant line. While dysfunctional coupling between tissue stretching and *Wnt3* expression could be a possible explanation of its phenotype, the promoter sequencing did not identify a clear candidate mutation. The causal mutation affecting DNA binding might be instead present in the TF itself rather than its binding site. Changes in the expression levels of a Wnt3-regulatory TF could also produce the observed phenotype, for example by altering its availability. Importantly, the regeneration defect might be of a different nature. Therefore, further explorations of the genetic makeup and transcriptional programs will be helpful for providing clues to understand this phenotype. Additional operational tests will involve imaging *reg-16* spheroids. If the coupling of tissue stretching with *Wnt3* expression is affected, we would expect the spheroids that fail to regenerate to keep oscillating in Phase I. regime, unable to break symmetry. Moreover, *reg-16* spheroids should be more sensitive to increased medium osmolarity than wt spheroids, and completely fail to regenerate at lower than isotonic osmolyte concentrations. An intriguing alternative explanation is that the defect decreases the strength of the *Wnt3* expression positive feedback loop, possibly as a result of the mutation between a tandem of Tcf binding sites in its promoter. This idea can be tested both *in vivo* and i*n vitro* using previously implemented approaches, such as binding assays and reporter lines (Nakamura et al. 2011). Even though the molecular analysis of the *reg-16* line might not uncover intermediate steps of the mechanics/Wnt crosstalk, going beyond its phenotype, known for decades, will hopefully shed light on how the mouth organizer is established and regulated.

Jaroslav Ferenc and Charisios Tsiairis conceived and designed the experiments
Jaroslav Ferenc performed all the experiments and analysis, except of the following contributions from other FMI members: Jan Eglinger made the Knime workflow for segmenting and straightening ectoderm images, Panagiotis Papasaikas performed the binding site analysis of Wnt3 promoter, and Iskra Katic performed siRNA electroporations.

II.2. Body Patterning in Homeostatic *Hydra*

II.2.1. Positional RNA-sequencing to Uncover Downstream Effectors of Wnt Signaling Involved in Body Patterning

Although the evidence concerning Wnt signaling involvement in *Hydra* body axial patterning is plentiful, very little is known about the downstream pathways, which regulate the specification of different body parts. To gain insight into these aspects of patterning, we performed positional RNA-sequencing of Wnt-activator treated animals (10 µM alsterpaullone) and compared it to the control conditions. We only kept the animals in the drug solution for 24h and cut the pieces for sequencing immediately after the treatment to avoid observing artifacts due to later effects, such as the ectopic tentacle and organizer formation in the body column. Even though, the overall pattern of body part identities remained largely unchanged, all other body parts became more head-like after the treatment as expected (Fig. II.2-1. A-B).

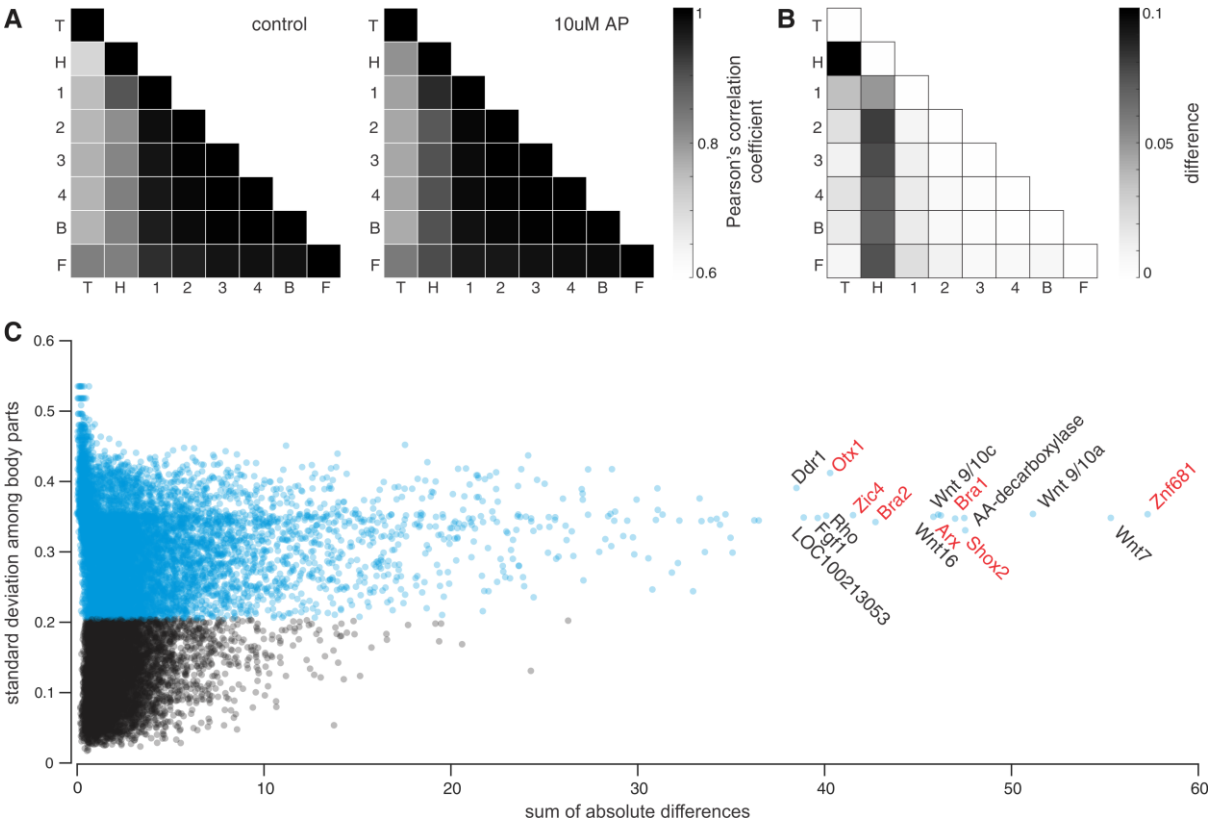

Fig. II.2-1. Comparison the axial gene expression patterns in wt and AP-treated animals. (**A**) Heatmaps of pairwise correlations of gene expression between body pieces of control and AP-treated animals. (**B**) Heatmap of the subtraction (AP – control) of the correlation matrices in (A). (**C**) Scatter plot of differentially expressed genes. Top changing genes are annotated, with transcription factors highlighted in red. Genes with non-uniform axial pattern (standard deviation of normalized expression among body parts > 0.2) are shown in blue. The sum of absolute differences is a sum of the absolute values of the $\log_2$ fold changes of all body positions for a given gene.

Looking at the genes with strongest expression changes across all body pieces we noticed that most of them have a non-uniform axial expression pattern in control conditions, suggesting that the Wnt signaling targets are indeed primarily body part specific or expressed in gradients (Fig. II.2-1. C).

The top hits, assessed by the overall change, also included several known Wnt-signaling targets, such as *brachyury* homologs *Bra1* and *Bra2* (Fig. II.2-2. A). Interestingly, *hyTcf* was also significantly upregulated (Fig. II.2-2. A). Unlike in other organisms, where the Tcf factors are usually ubiquitously expressed, the expression of *Hydra* Tcf is concentrated along the hypostome with a slight gradient in the body column (Hobmayer et al., 2000). Thus, the strength of Wnt signaling output in *Hydra* not only depends on the availability of Wnt ligands and β-catenin, but also Tcf molecules. Our data now suggest that *Tcf* positively regulates its own expression. This might be an additional mechanism for reinforcing (canonical) Wnt signaling, apart from the previously described positive autoregulation of Wnt3 expression (Nakamura et al., 2011).

In further analysis, we focused on transcription factors with changing expression and used interaction data from mammalian cells to approximate their regulatory relationships (Fig. II.2-2. B). While this dataset failed to capture some known regulatory interactions, occurring in *Hydra,* such as the direct regulation of *Sp5* by Tcf (Vogg et al., 2019), other clues pointed out its usefulness for predicting previously undescribed ones. For example, the genes *Znf397* and *FoxD2*, coding for transcription factors involved in foot specification (according to our data in Fig. 4, section II.1.1.), appear to be direct targets of Tcf. Consistently with this hypothesis, they show a strong downregulation upon Wnt activation, which can be one of the mechanisms of head/foot antagonism.

To begin further exploring the possible direct targets of Tcf, we selected 4 genes for knockdown (*Zic4, Meis1, FoxA2*, and *Pitx1*), covering a range of connectivities and modes of regulation (Fig. II.2-2. B, white asterisks). We assessed head and foot regeneration in the bisected animals, as well as macroscopic phenotypes (e.g. ectopic tentacles) in intact animals, upon RNAi. Interestingly, none of the knockdowns presented a significant phenotype in any of the scored conditions (data not shown).

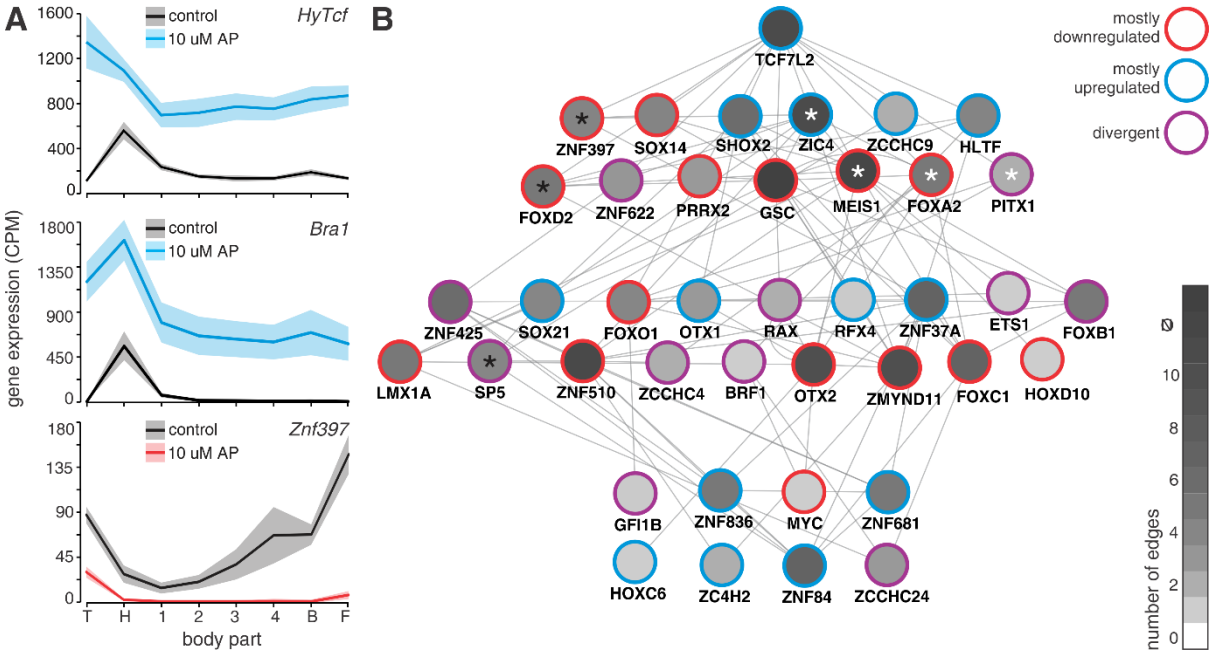

Fig. II.2-2. Relationships of the differentially expressed transcription factors with Tcf. (**A**) Examples of axial expression profiles for selected genes in control conditions and upon AP treatment. Lines indicate averages among the replicates and shaded areas correspond to 95 % confidence intervals. The plot color in AP conditions is blue for upregulated genes and red for downregulated ones. (**B**) A network of physical, genetic, and predicted interactions in human cells (data from genemania.com). The hierarchy reflects whether a given factor has a direct connection to Tcf or indirect through one or several other factors. The color intensity for each node represents a total number of edges connected to it. The outline color of each node reflects whether a particular gene is upregulated (blue) or downregulated (red) in most of the body parts. Cases where the differences diverge across the body are highlighted in purple. White asterisks indicate genes selected for knockdown and black asterisks mark the genes, for which the knockdown phenotype was already known.

II.2.2. Zic4, a Key Regulator of Epithelial Differentiation

The results, presented in this chapter, are part of a manuscript prepared jointly with the Galliot lab (University of Geneva).

However, *Zic4*, a Wnt-responsive transcription factor, expressed in the head and tentacles (Fig. II.2-3 A-C) showed an unexpected phenotype of ectopic peroxidase staining in the tentacle tips upon knockdown (Fig. II.2-3 D-F). This staining is a characteristic feature of basal disk cells (Hoffmeister and Schaller, 1985) and we routinely perform it at as a part of RNAi experiments to assess potential foot-related phenotypes. This observation was thus indicating that, upon *Zic4* knockdown, the tentacles might change their identity to that of a basal disk.

Our collaborators in the Galliot group were also investigating this gene as a target of the Wnt inhibitor *Sp5* (Vogg et al. 2019), previously identified by them. *Sp5* was suspected to be an activator of *Zic4* (Fig. II.2-4. A) since its downregulation also resulted in a decrease of *Zic4* expression. The phenotype of *Sp5* knockdown resembles

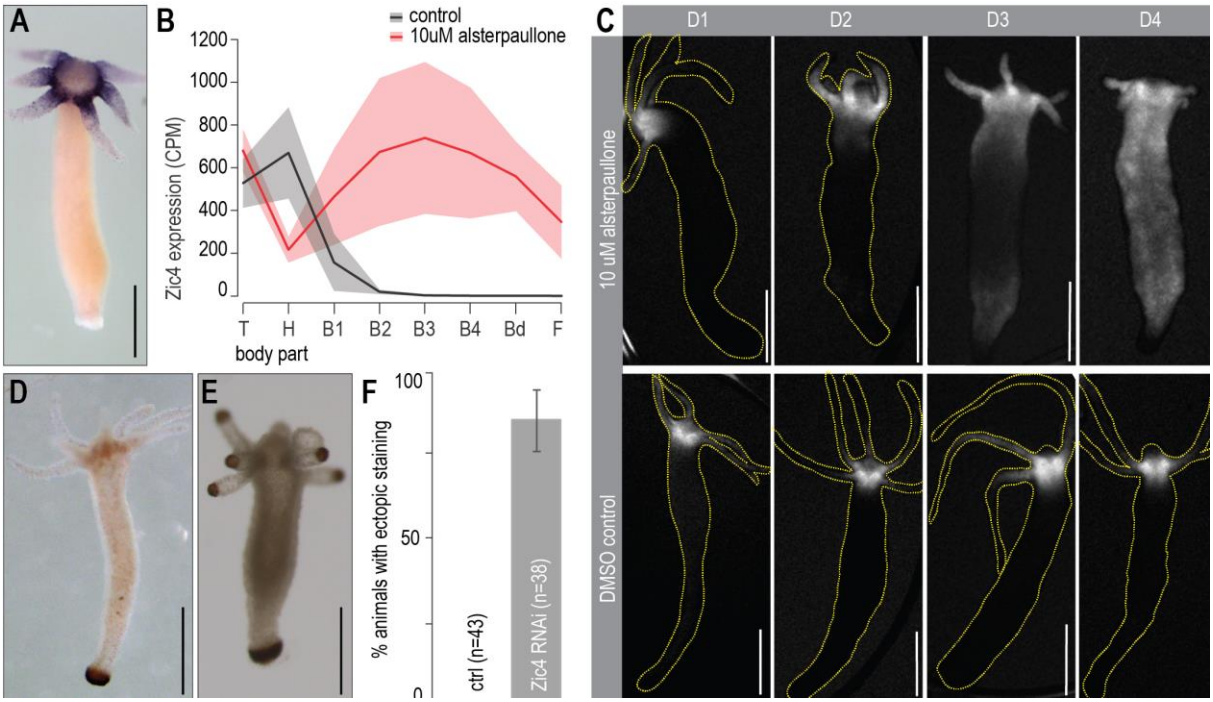

Fig. II.2-3. Zic4 expression patterns and knockdown phenotype. (**A**) Whole-mount *in situ* hybridization of Zic4. (**B**) Expression pattern of Zic4 in the control positional RNA-seq data (black) and the positional sequencing after the 24h 10 µM alsterpaullone treatment (red). Line indicates average of the replicates and shaded areas indicate 95% confidence intervals. (**C**) The change of Zic4 expression pattern in the *pZic4::GFP* reporter line (Galliot lab) during continuous alsterpaullone treatment. (**D-E**) Chromogenic peroxidase stainings in the RNAi animals. (D) control RNAi, (E) Zic4 RNAi, notice the ectopic staining in tentacle tips. (**F**) Quantification of the incidence of ectopic peroxidase staining in the tentacles of Zic4 RNAi animals. A total of n animals from 3 replicates. Error bars indicate 95% confidence intervals. Scale bars 500 µm.

Wnt-signaling activation and manifests as ectopic heads (Vogg et al., 2019a). Interestingly, it was mainly in the tentacles of these ectopic oral structures, where the peroxidase staining was present, with the original tentacles being almost completely negative (Fig. II.2-4. B). Double *Zic4/Sp5* knockdown resulted in an even stronger phenotype of multiheaded animals with very short peroxidase-positive tentacles, including the ones of the original head (Fig. II. 2-4. C-D). Moreover, the morphology of the peroxidase$^+$ tentacle cells closely resembled the morphology of basal disk cells, further pointing in the direction of a cell fate transformation (Fig. II. 2-4. D and G).

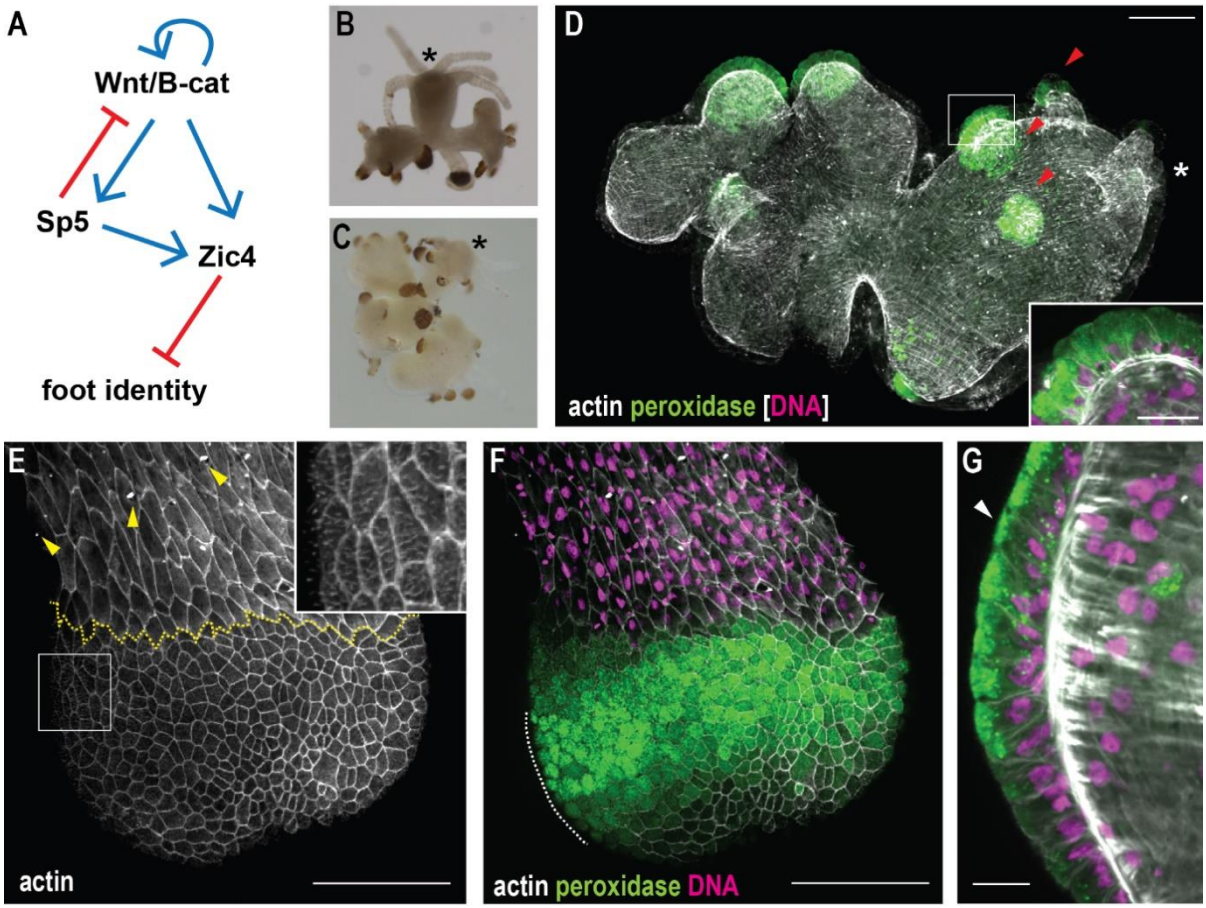

Fig. II.2-4. The regulatory relationship of Zic4 and Sp5 and the phenotype of their double knockdown. (**A**) The proposed regulatory relationships of the Wnt/B-catenin signaling and the transcription factors Zic4 and Sp5. (**B-D**) Representative images of Sp5 (B) and Zic4/Sp5 (C-D) knockdown animals, 7 days after the last siRNA electroporation. Note the presence of ectopic heads with short peroxidase$^+$ tentacles. Asterisks indicate the original mouth position. (B-C) chromogenic peroxidase staining, (D) fluorescent peroxidase staining. In the double knockdowns, the original tentacles are also very short, peroxidase$^+$, and with cellular morphology resembling that of a basal disk (cf. inset in D with G). (**E**) The distinctive morphology of basal disk cells as shown in phalloidin staining. Note the typical ciliated cells (inset) and the basal disk area being completely free of nematocytes (yellow arrowheads). Yellow dotted line marks the basal disk boundary. (**F**) High levels of peroxidase activity are typical for basal disk cells. (**G**) Optical section along the white dotted line in (F) showing the characteristic inverted triangle shape of the basal disk mucous cells with apically concentrated peroxidase granules (white arrowhead) and basaly positioned nuclei. Images (D-F) are standard deviation Z projections of surface tissue layer, scale bars 50 µm. Inset in (D) and (G) are middle plane confocal sections, scale bars 20 µm.

To test this hypothesis, we performed RNA-sequencing of tentacles from the knockdowns, separating original and ectopic tentacles in samples where they both occur. Since especially in the *Zic4* individual knockdown, the peroxidase staining appears almost exclusively at the distal ends of the tentacles, we sequenced the proximal (base) and distal (tip) tentacle portions separately whenever the tentacle length allowed. The results have shown a significant upregulation of foot-specific markers across all samples accompanied by variable levels of downregulation of tentacle markers (Fig. II.2-5). The strength of both changes seemed to have been correlated with the phenotype strength. For example, the short and strongly peroxidase^{+} tentacles of the *Sp5* RNAi animals showed both a stronger upregulation of foot markers and stronger downregulation of tentacle-specific genes than the original tentacles of the same animals. Similarly, rather than expressing different subclusters of marker genes, tentacle tips and bases mostly differed in the strength of gene expression changes. Since peroxidase overexpression can also be a hallmark of stress-response, we used the sequencing data to verify that it is a reliable basal disk marker in our setting. Surveying all the peroxidase genes annotated in the *Hydra* genome, we found that only the three foot-specific ones were highly and consistently upregulated in all RNAi conditions, supporting the usefulness of peroxidase staining as a basal disk marker (Fig. II.2-6).

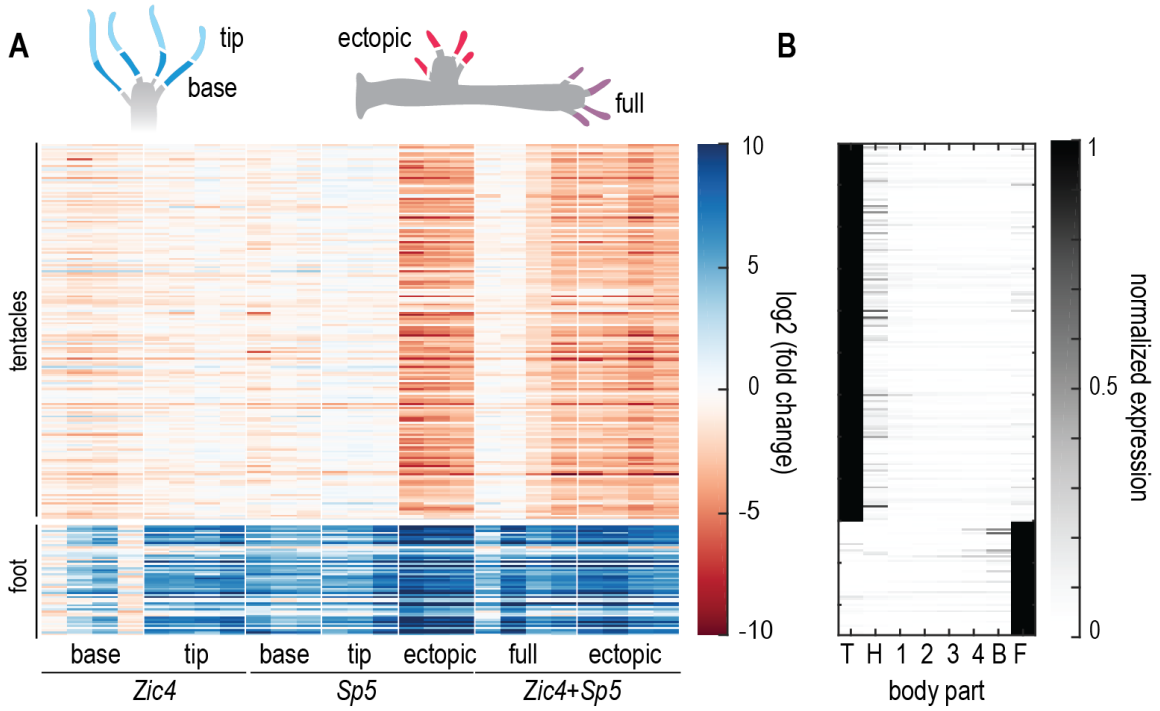

Fig. II.2-5. RNA-sequencing of tentacles from Zic4 and Sp5 RNAi animals. (**A**) Expression pattern of tentacle- and foot-specific genes in the samples of tentacles from RNAi animals. Lines in the heatmap represent individual genes and columns are different replicates. Cartoons indicate the different types of tentacle samples collected. For the original tentacles of the Zic4 and Sp5 RNAi animals, the proximal

(base) and distal (tip) halves were collected separately and pooled. The ectopic tentacles of the Sp5 and double knockdown (ectopic), as well as original tentacles of the double knockdown (full), were harvested without performing this step, since they were too short. (**B**) Axial expression pattern of marker genes from (A) in the wt positional RNA-seq dataset. The expression of each gene is normalized to the body part with its highest expression.

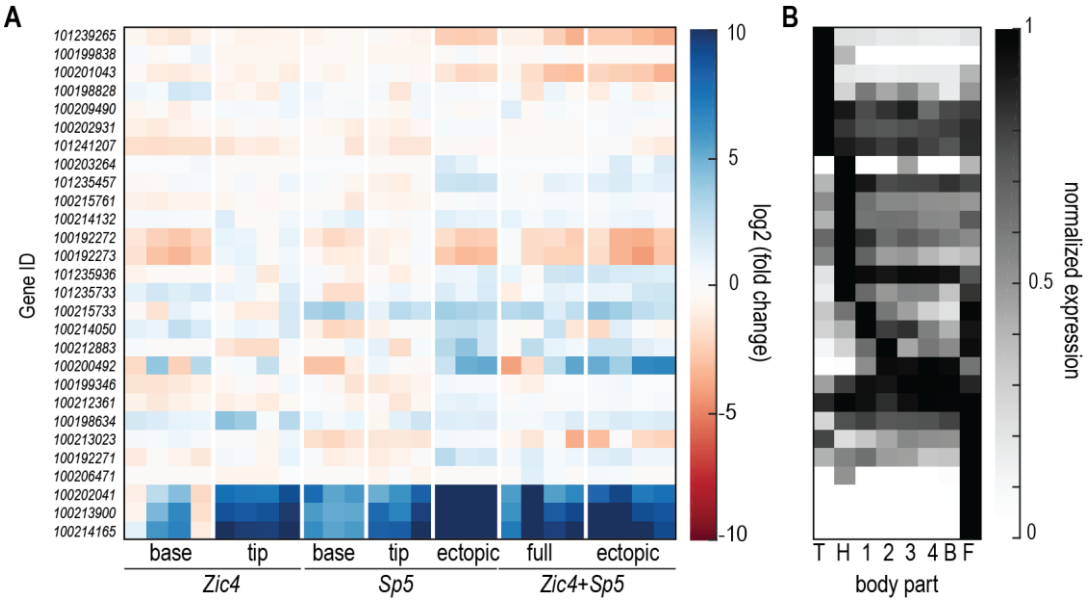

Fig. II.2-6. Upregulation of foot-specific peroxidases upon Zic4 and Sp5 RNAi. (**A**) Epression of all the *Hydra* peroxidase genes in the different RNAi conditions. (**B**) Axial expression pattern of these genes in the wt positional RNA-seq dataset. The expression of each gene is normalized to the body part with its highest expression.

Given these results, we were interested to see where do the knockdown samples cluster, when projected into the PCA space of tissue identities. This PCA space was generated (analogously to Fig. 3 in II.1.1) using all the axially variable genes from our positional RNA-sequencing dataset. Contrary to our expectations, most of the RNAi tentacles aggregated in close proximity of the negative controls and reference samples (Fig. II.2-7. A). However, since the bulk RNA-sequencing presents an averaged picture, this might be the result of only some tentacle cells being transformed and others remaining unaffected. For example, if only the tentacle epithelial cells assumed a foot-like identity while the differentiated interstitial lineage progeny (e.g. nematocytes, specific neurons) remained unchanged, we might expect a similar outcome. To evaluate this hypothesis, we constructed the PCA space selecting only the subsets of variable genes expressed either in the epithelial or interstitial cells (selection of genes according to Siebert et al. 2019). Interestingly, in the epithelial PCA, RNAi controls still cluster with the reference samples but the other RNAi samples move on a line between the tentacle and foot identity, suggesting that some of the epithelial cells indeed become foot-like. On the other hand, the interstitial PCA closely mirrors

the picture obtained when all axially variable genes are used to construct the PCA space. This result is consistent with the assumption that the differentiated cells of interstitial lineage are predominantly unaffected by the *Zic4* and/or *Sp5* knockdowns.

In all three plots, the ectopic tentacle samples appear to be closest to the reference foot samples, matching with the previous observation of the strongest upregulation of foot and downregulation of tentacle markers in these conditions. We speculate that such strong phenotype may result from these tentacles being generated *de novo* due to the knockdown. While epithelial cells follow signals from the ectopic organizers to form new tentacles, migrating interstitial cells might receive conflicting clues if the battery cell differentiation is simultaneously affected. Another noteworthy observation is the high variability of the original tentacle samples from double knockdowns. In these animals with the strongest phenotype, the original head is often indistinguishable from the ectopic ones. We thus selected rare animals with a weaker phenotype for sequencing, to be able to make this distinction. The data therefore reflect the spread within weaker phenotype rather than the typical stronger phenotype.

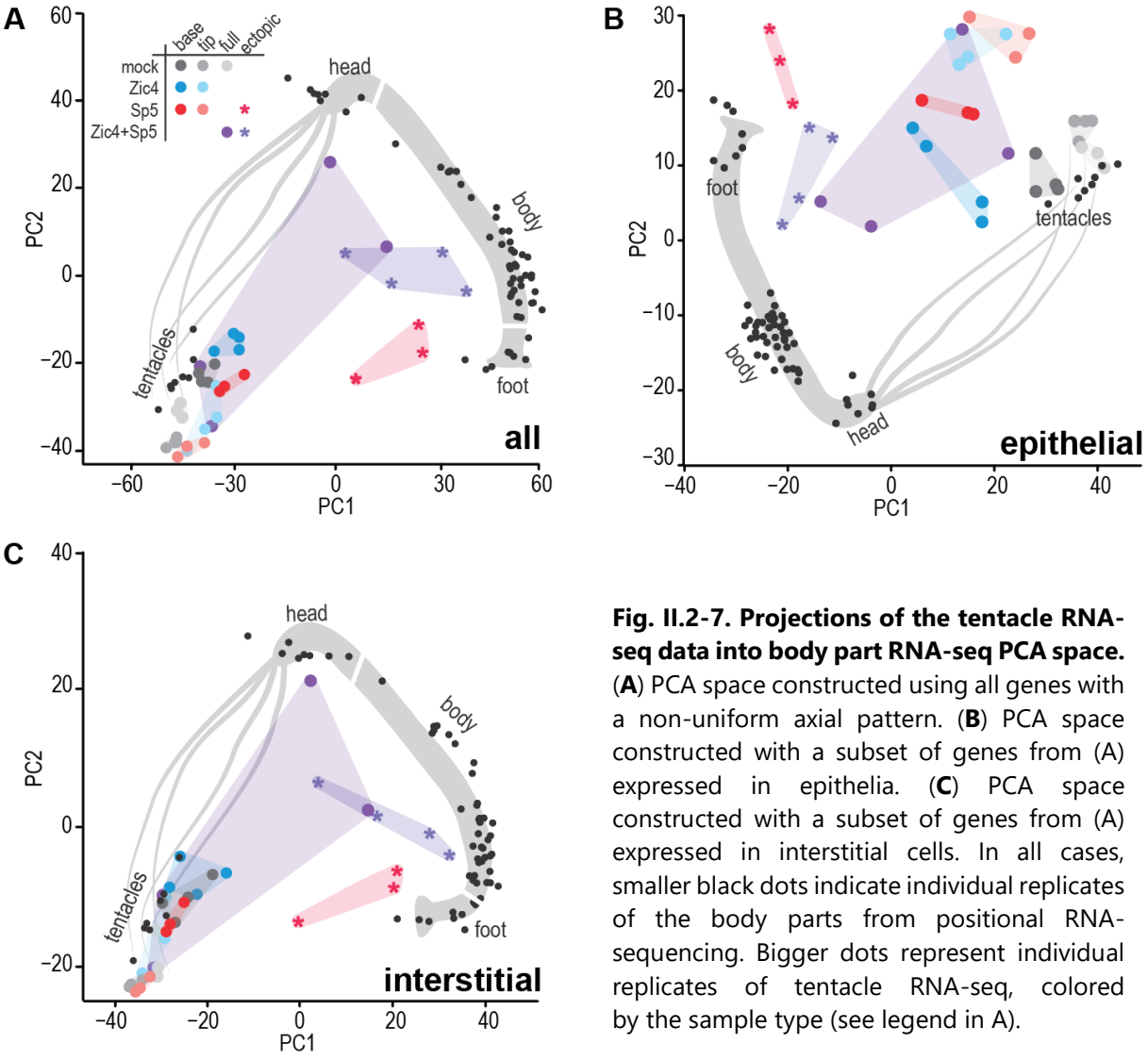

Fig. II.2-7. Projections of the tentacle RNA-seq data into body part RNA-seq PCA space. (**A**) PCA space constructed using all genes with a non-uniform axial pattern. (**B**) PCA space constructed with a subset of genes from (A) expressed in epithelia. (**C**) PCA space constructed with a subset of genes from (A) expressed in interstitial cells. In all cases, smaller black dots indicate individual replicates of the body parts from positional RNA-sequencing. Bigger dots represent individual replicates of tentacle RNA-seq, colored by the sample type (see legend in A).

Seeing both the morphological and transcriptional evidence of foot-specific epithelial differentiation occurring in the tentacles of knockdown animals, we were wondering whether it happens by misdifferentiation of ectodermal cells arriving into the tentacles or transdifferentiation of already existing battery cells. We thus decided to investigate whether intermediates, having characteristics of both the battery and basal disk cells, can be found in the tentacles. Such results would strongly suggest transdifferentiation. We chose the double knockdown because of its enhanced phenotype and analyzed tentacles from an early time point (2 days after the second electroporation). These tentacles did indeed contain peroxidase^{+} cells already, indicating basal disk fate, however many of them were still harboring nematocytes, pointing to their battery cell

origin (Fig. II.2-8. C-D). At the same time, the number of residing nematocytes was drastically reduced, compared to the untransformed neighbors. Thus, it seems that the battery cells begin losing nematocytes and transdifferentiate into basal disk cells, upon the downregulation of *Zic4* (and *Sp5*).

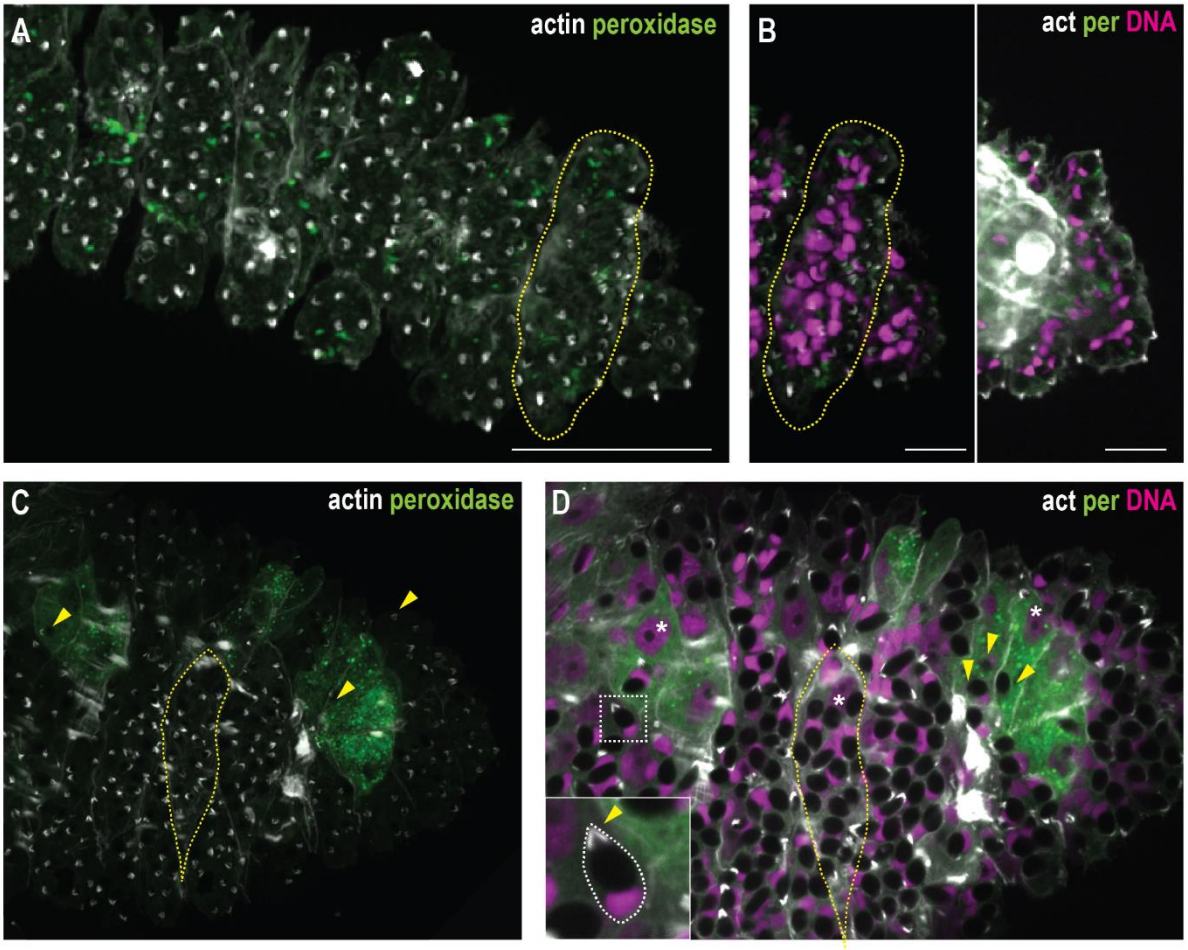

Fig. II.2-8. Transdifferentiation of tentacle battery cells. (**A)** Standard deviation Z-projection of phalloidin-stained control tentacle, negative for peroxidase. Note the oblong battery cells (yellow dotted line) filled with nematocytes, which are visible by their apical actin staining (yellow arrowheads). (**B**) Details of the battery cell structure including nematocyte nuclei. Z-projection (left) and an optical section through the tentacle middle plane (right). The cell encircled in the yellow dotted line is identical to the one in (A). (**C**) Standard deviation Z-projection of a phalloidin-stained tentacle upon *Zic4/Sp5 RNAi.* Note that the peroxidase-positive transformed cells harbor only a few nematocytes (yellow arrowheads), compared to the untransformed cells around. (**D**) Optical section through the middle plane of the tentacle shown in (C). Yellow arrowheads indicate the nematocytes retained in peroxidase$^+$ cells. Note also the marked lack of nematocyte nuclei within the transformed cells. Asterisks mark epithelial nuclei. Inset shows an enlarged nematocyte, highlighting its typical pear-like shape with the apical actin staining and basally-positioned highly condensed nucleus. Scale bars: 50 µm (A, C-D), 20 µm (B).

Interestingly, when looking at the functional annotation of genes showing at least twofold upregulation across all the original tentacles samples (Appendices 2-3), we noticed a strong bias for cell cycle and division related signatures, coming from a cluster of 19 genes (Fig. II.2-9. A).

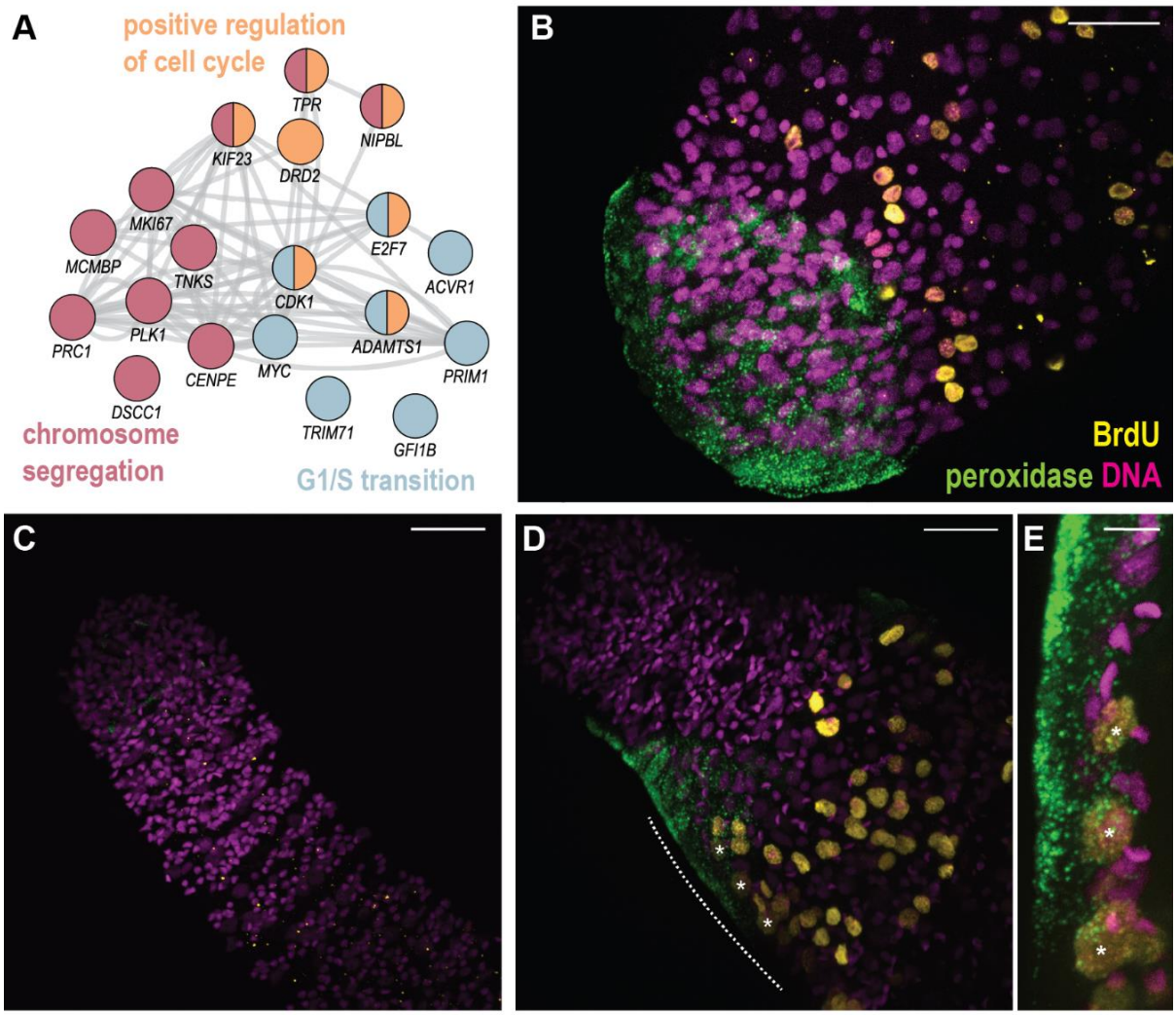

Fig. II.2-9. Transdifferentiation is accompanied by cell cycle reentry. (**A**) Subnetwork of 19 genes consistently upregulated in tentalces across all RNAi conditions color coded according to GO terms. Edges indicate genetic/physical interactions, colocalization and/or coexpression in human cells. Data from genemania.org. (**B-D**) Standard deviation Z-projections of samples stained for peroxidase and BrdU upon RNAi. (B) Foot of a control animal. Note that the peroxidase^{+} basal disk cells are BrdU^{-}. (**C**) Control tentacle, negative for both markers. (D) Zic4/Sp5 RNAi tentacle, showing partially overlapping domains of positive peroxidase and BrdU staining. (**E**) Confocal section through the tentacle shown in (D) along the dotted white line. Epithelial nuclei marked by asterisks are identical in both pictures. Scale bars 50 µm (B-D), 20 µm (E).

This indicated that the change of cell fate might be accomplished through indirect transdifferentiation (Sisakhtneshad and Matin, 2012) involving proliferating intermediates. Indeed, many epithelial cells in the early Zic4/Sp5 knockdown tentacles were $BrdU^+$, which is not a usual characteristic of the terminally differentiatied basal disk or battery cells (Fig. II.2-9. B-D). However, only a small fraction of the $BrdU^+$ cells were also $peroxidase^+$ and *vice versa* (Fig. II.2-9. D-E), consistent with the idea that the cells become only transiently proliferative and then lose this characteristic during differentiation to another cell type. While treatment with hydroxyurea, a DNA synthesis inhibitor, prevented transdifferentiation, the cells did not actually seem to divide on the way to acquiring new identify (Galliot lab, data not shown), Thus, instead of proliferation, transient reentry into the cell cycle might be required for the observed cell fate changes.

We were also curious, how Zic4 accomplishes the suppression of basal disk differentiation and decided to investigate binding sites in the promoters of foot-specific genes upregulated across all RNAi conditions (Fig. II.2-10. A). Strikingly, none of them contained *bona fide* Zic4 binding sites, arguing against the direct suppression by the Zic4 protein itself. However, several other TF binding motifs were enriched among these genes, some in a great majority of them. Further search for Zic4 binding sites in the promoters of these TFs (Fig. II.2-10. A, blue dots), revealed a cluster of 7 of them (*Nfat5, Gata3, Sry, FoxI1, Hhex, Rax2, Prrx2*, and *Awh*), which are themselves probable Zic4 targets, and their binding sites are highly enriched in the promoters of the downstream foot-specific genes.

Two possible wiring scenarios for suppressing the foot differentiation in tentacles, downstream of Zic4, through some of these TFs exist (Fig II.2-10. B). First, if the intermediate TF was stimulating basal disk differentiation, we would expect it to be expressed in the foot area under normal conditions and repressed by Zic4. Alternatively, the intermediate factor can be suppressing the basal disk fate and promoting tentacle battery cell differentiation. In this case, it would be positively regulated by Zic4 and should have a similar axial expression pattern in control conditions. We therefore turned to the positional RNA-seq data and investigated the expression patterns of our candidate TFs. Given the criteria above, three genes emerged as particularly promising. *Nfat5* and *FoxI1* are both expressed in the tentacles and downregulated across all replicates upon *Zic4* knockdown. They would therefore fit the criteria for basal disk repressors positively regulated by Zic4. Conversely, *Gata3* is predominantly expressed in the foot and upregulated after *Zic4* RNAi. Moreover, we have previously shown that this transcription factor is indeed important for foot specification (Fig. 4 in II.1.1). Future experimental efforts can be aimed at verifying

these candidates by respective combined knockdown/overexpression approaches and investigating the functionality of Zic4 binding sites in their promoters.

In summary, we have identified a novel regulator of epithelial differentiation operating downstream of the canonical Wnt signaling, which is crucial for tentacle battery cell specification. Our results also point out a potential general framework for understanding the epithelial cell type specification in *Hydra*.

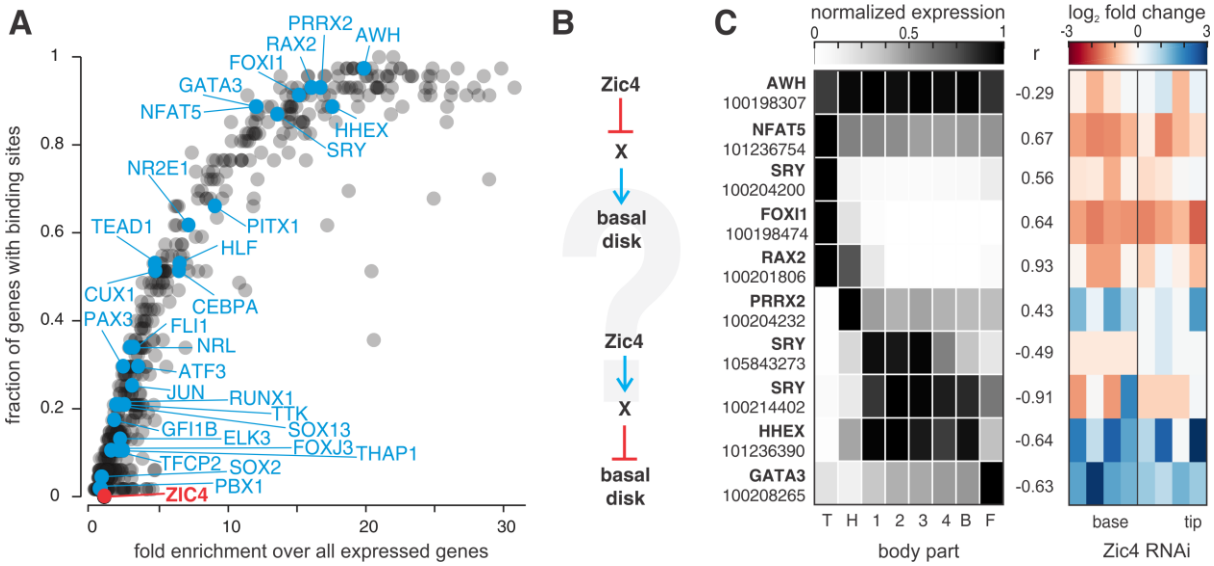

Fig. II.2-10. Potential downstream targets of Zic4 regulating foot differentiation. (**A**) Analysis of binding sites in the promoters of foot-specific genes upregulated upon Zic4 RNAi. Each dot represents a single transcription factor. Zic4 is shown in red. Transcription factors, whose promoters contain at least one *bona fide* Zic4 binding site, are highlighted in blue. (**B**) The two possible ways Zic4 can suppress basal disk differentiation via an intermediate transcription factor. (**C**) Expression patterns and changes of the highest-scoring transcription factors from (A). Left, axial expression patterns in the wt positional RNA-seq dataset. The expression of each gene is normalized to the body part with its highest expression. The value of Pearson's correlation coefficient (r) with the Zic4 axial expression pattern is indicated next to the rows. Right, expression changes in tentacles upon the downregulation of Zic4.

II.2.3. Using Mass spectrometry Imaging to Identify Small Molecules Potentially Involved in Patterning

A significant constrain for identifying potential (diffusive) morphogens can often be visualizing their distribution in the tissue of interest. This is especially challenging for non-protein signaling factors. However, tools, such as mass spectrometry imaging are promising to remove such obstacles. Here, unlike in conventional mass spectrometry experiments, the concentrations of different molecular entities are measured in tissue sections, rather than in a liquid extract. This allows rasterized point-by-point measurements and later reconstruction of a molecule's spatial distribution (Ly et al., 2016). Mass spectrometry imaging was successfully employed for investigating a range of questions such as the cell compartmentalization in ciliates (Kompauer et al., 2017), metabolic markers of tumors in comparison to surrounding normal tissue (Buck et al., 2015), or symbiosis between bacteria and mollusks (Geier et al., 2020).

We decided to test whether we could use this technique to find metabolites potentially functioning as signals in patterning. The aim was to compare metabolite distribution in normal conditions and under alsterpaullone treatment. Since we already generated the positional sequencing data in such conditions, this would also allow comparisons of the metabolite distribution with expression patterns of their production and degradation enzymes. After treating the animals for 24 h with either DMSO or 10 µM alsterpaullone, paraffin sections were prepared to be used for measurements (Fig. II.2-11). Thanks to the *Hydra* anatomy, a single longitudinal section captures all body parts and cell types in the animal. The imaging was performed in three independent replicates. More than 2500 different metabolites were detected in each sample.

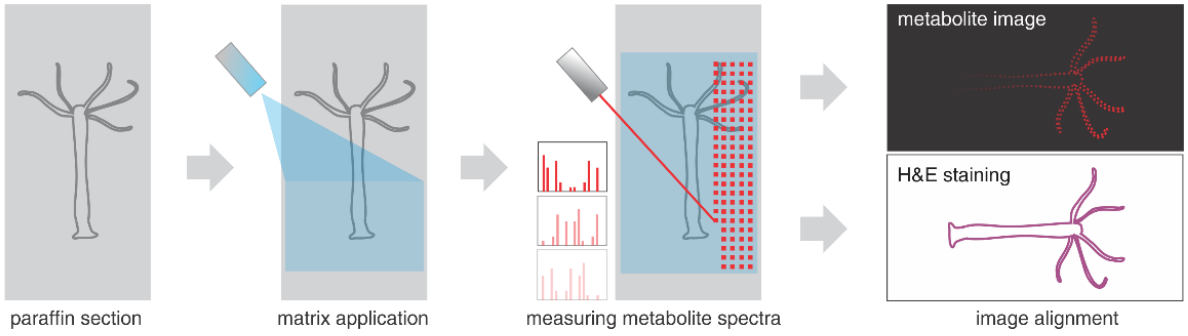

Fig. II.2-11. Matrix-assisted laser desorption/ionization (MALDI) mass spectrometry imaging of *Hydra* sections. After 24 h of control or alsterpaullone treatment, standard paraffin sections are prepared and mounted on slides with conductive coating. Matrix to help molecular ionization is then applied by spreading and the mass spectra are measured point by point in a raster-like fashion. The sample can then be stained with standard histological techniques and the reconstructed image of metabolite distribution aligned with the sample. Based on Ly et al. (2016).

Although we have not performed a comprehensive analysis of this recent data yet, some interesting molecules were already identified. Two classes of sulphonic acids (Fig. II.2.12. A) provide an interesting example. They are both found in differentiated body parts with an additional body column gradient for the isomers of lower molecular weight (Fig. II.2.12. B). Upon Wnt activation, the amounts of both types of sulphonic acids increase in the body column, leading to flattening of their gradients. Interestingly, these metabolites share a production enzyme, the cholesterol sulphotransferase Sult2B1, which is upregulated in many tumors and was found to promote epithelial to mesenchymal transition (EMT) in a Wnt-dependent manner (Yang et al., 2019; Geese et al., 2001). However, whether the sulphonic acids have any regulatory functions *per se* is not known. The expression profile of the *Hydra Sult2* (Fig. II.2.12. C) homolog can in both cases largely explain the metabolite distribution under control conditions. Interestingly, the relatively minor changes of *Sult2* expression pattern upon Wnt activation do not seem to account for the observed metabolite distribution changes. It might be possible that Wnt also influences the activity of Sult2, distribution of its substrates, or expression and activity of the respective degradation enzymes.

This example demonstrates the usefulness of the approach for identifying graded small molecules with spatial distribution influenced by the Wnt signaling, which could serve as yet unknown patterning signals. Once the dataset is thoroughly examined, functional testing of selected candidates will be decisive for choosing some of them to be further verified.

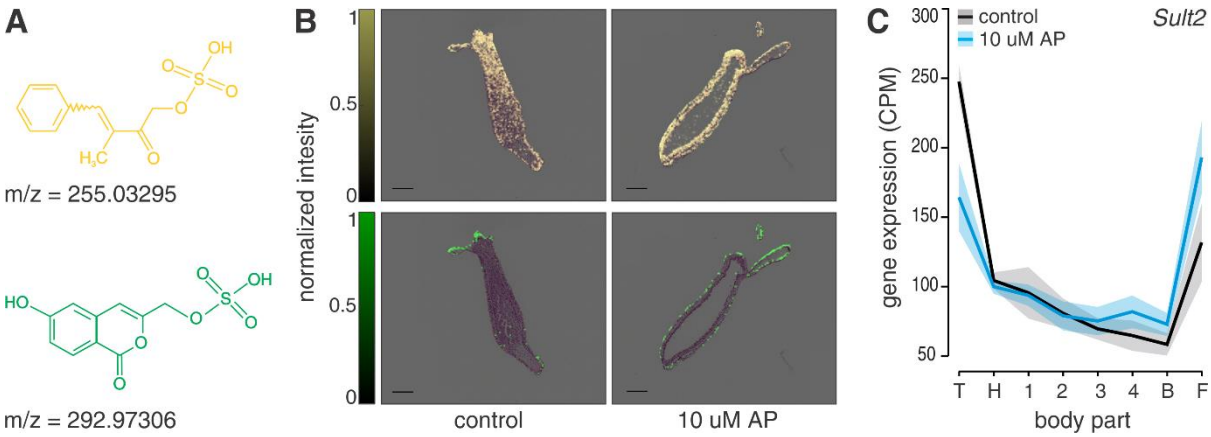

Fig. II.2-12. Two sulphonic acid classes with a Wnt-sensitive distribution pattern in the body. (**A**) Formulas of the some of the isomers corresponding to the m/z values: [(3-methyl-2-oxo-4-phenylbut-3-en-1-yl)oxy]sulfonic acid (top), and [(5-hydroxy-1-oxo-1H-isochromen-3-yl)methoxy]-sulfonic acid (bottom) (**B**) Representative images of the distribution of these two sulphonic acids in control conditions and after alsterpaullone treatment. (**C**) Expression pattern of Sult2 gene, coding the enzyme, which produces both molecules. Black line indicates average across all replicates in control, and the blue line in alsterpaullone conditions. Shaded areas correspond to 95 % confidence intervals.

II.2.4. Discussion

Even though *Hydra* patterning and the underlying cell differentiation processes are well understood on the cellular level, their molecular underpinnings, especially for epithelial cells, remain unclear. In this work, we have found the transcription factor Zic4 to be a crucial regulator of tentacle identity, operating downstream of canonical Wnt signaling. Zic4 appears to be necessary for battery cell differentiation and maintenance, as evidenced by the transdifferentiation of these cells to basal disk identity upon its knockdown. Zic4 is also a direct target of Wnt repressor Sp5 and their double knockdown enhances the phenotype. From the available data it is not clear, however, whether Sp5 has a Zic4-independent role in controlling cell fates or its downregulation simply lowers the amounts of Zic4 even further than in the single knockdown conditions. Additional results (Galliot lab) indicate that such effect exists but is rather small.

Interestingly, the cell identity change seems to involve indirect transdifferentiation, i.e. changing identity through partially dedifferentiated proliferating intermediates. Similar processes have been observed during inner ear hair cell regeneration in chicken (Roberson et al., 2014), lens regeneration in axolotl (Tsonis et al., 2004), and are suggested to be part of the adult bone marrow cell plasticity in mammals (Herzog and Krause, 2003). However, despite the presence of $BrdU^+$ cells in tentacles upon Zic4/Sp5 knockdown, suggesting an ongoing DNA synthesis (and thus cell cycle reentry), we did not find any evidence of cell division taking place (no phospho-histone 3 staining positive cells in the tentacles or mitotic cells in the macerated single cell preparations were observed in the Galliot lab). Thus, it is unclear whether the cell cycle reentry and/or mitotic division is required for the cell fate change upon Zic4 downregulation. One possible explanation could be that epithelial cells are arrested in different phases of the cell cycle before differentiating to distinct cell types. For example, if battery cell precursors were arrested in G1 phase before differentiating but basal disk precursors in G2, this short cell cycle reentry would allow the cells to proceed until the next differentiation checkpoint. While intriguing, this hypothesis is not supported by the existing evidence, which strongly suggests that both the battery and basal disk cells are G2-arrested (Buzgariu et al., 2014, Dübel and Schaller, 1990). An alternative explanation can be deduced from the axial expression pattern of the cell division/cycle associated genes upregulated upon Zic4 knockdown (Fig. II.2-13). Under normal conditions, these genes are strongly downregulated in tentacles but not in the foot. Therefore, their downregulation is either not necessary for cell cycle pausing in differentiated basal disk cells, or they are regulated in a different (and possibly more complex) manner. The transient burst of BrdU incorporation could then be explained

as a byproduct of their upregulation, that is later suppressed by a different mechanism ensuring cell cycle pausing during the basal disk differentiation. Alternatively, higher expression of these genes might even be required for successful basal disk specification. To better understand the requirements for cell division and cycle reentry during the battery cell to basal disk transdifferentiation, it will be helpful to use inhibitors that block the cell cycle progression in different stages and evaluate their impact on the cell fate change.

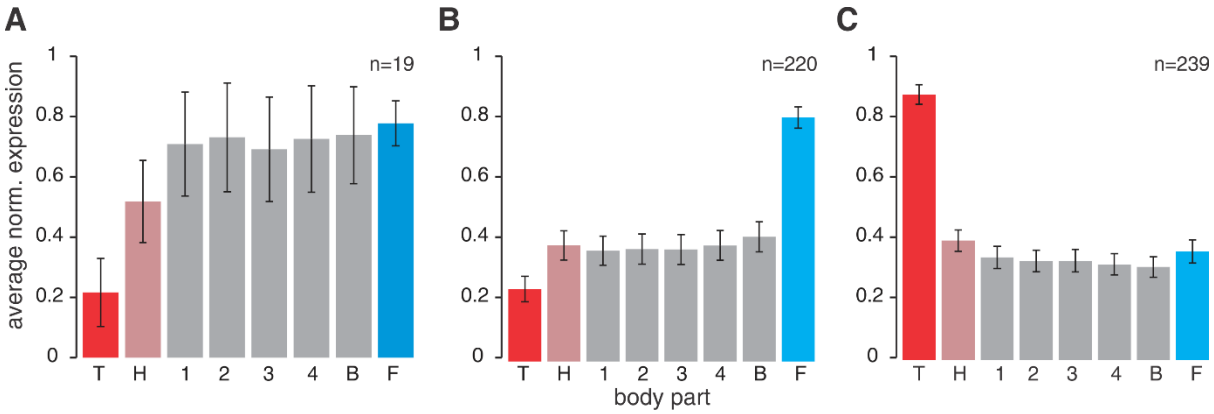

Fig. II.2-13. Average axial patterns of gene clusters differentially expressed in original tentacles upon Zic4/Sp5 knockdowns. (**A**) The cluster of 19 upregulated genes that share cell division and cycle related functional signatures. (**B**) All upregulated genes (at least twofold). (**C**) All downregulated genes (at least twofold). The colors of bars distinguish different body parts and are added to aid visual comparison.

The fact that, after downregulating *Zic4*, battery cells change identity to another differentiated cell type rather than simply staying differentiated of dedifferentiating also potentially reveals more general principles of patterning and differentiation in *Hydra* (Fig. II.2-14). Since cell can still successfully differentiate after the knockdown, they are most likely perceiving extrinsic differentiation clues (for example diffusible morphogens, tissue curvature, etc.). Moreover, because they adopt a basal disk identity, this might be the default epithelial cell differentiation trajectory in *Hydra*, as also suggested by our previous experiments on spheroids (Fig. 4 in II.1.1). Importantly, in this view, the differentiation signals could be identical on either end of the animal, because their interpretation at the oral end would be altered by the Wnt organizer presence. Alternatively, a cross-antagonistic system of transcription factors, akin to the one regulating vertebrate hematopoietic lineage specification, might be at work in *Hydra* epithelia. The two main lineages of hematopoietic cells – myeloid and erythroid are specified by the interplay of two transcription factors (Gata1 and Pu.1),

the lineage commitment ultimately depending on which of them is prevalent in each cell (Grad and Enver, 2009; Arinobu et al. 2007). In this case, the depletion of one of the factors also leads to the respecification of cells to the opposite lineage identity (Galloway et al., 2005). Interestingly, the "zones of influence" of these transcription factors can also be spatially separated as is the case in zebrafish embryos, where erythroid precursors have an anterior origin, and myeloid precursors originate posteriorly (Rhodes et al., 2005). If such a mechanism was guiding *Hydra* epithelial differentiation, the best candidate for the Zic4 antagonist based on our data would be Gata3. However, since *Gata3* knockdown does not seem to produce the transdifferentiation of basal disk into battery cells, this mechanism seems unlikely. To understand the control of epithelial differentiation in *Hydra* it will therefore be important to not only interrogate the TF network wiring, but also perform experiments deciphering the nature of their interactions. For example, animal lines ectopically expressing *Zic4* will elucidate whether it is also sufficient to drive the emergence of new ectopic tentacles. It would be equally interesting to investigate the foot differentiation in such animals, or the ability of Zic4 excess to recue battery cell specification in the ectopic heads upon *Sp5* RNAi (assuming that the ectopic head phenotype is not affected by *Zic4* overexpression). Similarly, if Gata3 crosstalks with Zic4, we would either expect a rescue of the transdifferentiation phenotype or inability to form tentacles upon *Zic4/Gata3* double knockdown.

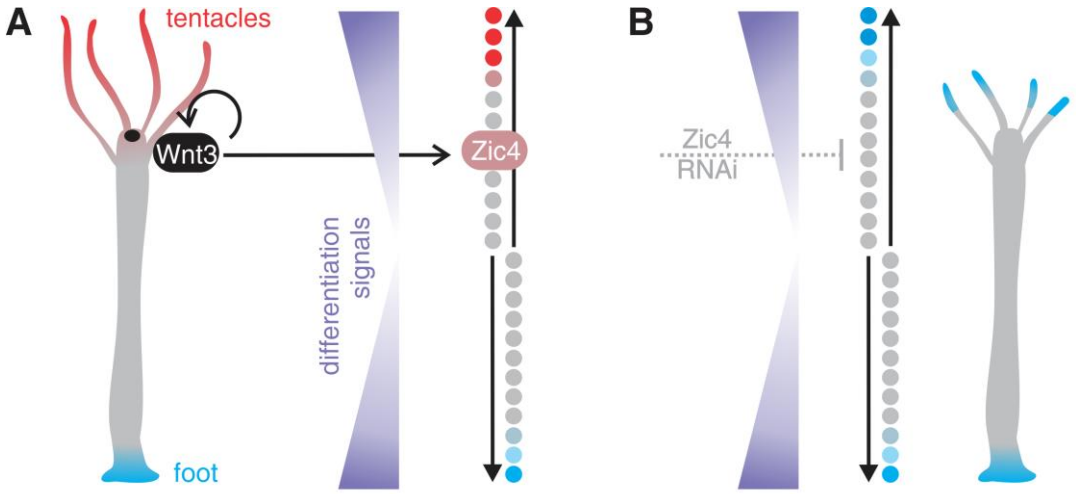

Fig. II.2-14. The proposed framework for cell differentiaton in *Hydra* and the role of *Zic4*. (**A**) In normal conditions, the epithelial cells perceive differentiation signals upon arriving at the ends of the animal. If no specific clues are present, the default differentiation path generates the foot. However, near the Wnt organizer, cells will start expressing *Zic4*, which inhibits the foot identity and instructs tentacle differentiation instead. (**B**) Upon *Zic4* knockdown, cells still perceive the generic differentiation signals and thus assume the foot identity on either side of the axis.

The Zic transcription factors constitute a small gene family that is conserved across almost all metazoans except ctenophores and sponges (Layden et al., 2010). Their biological roles are also largely conserved, including, most prominently, mesoderm patterning, and neural or sensory cell specification (for review see Aruga and Hatayama, 2018). The regulation by and crosstalk with the Wnt pathway also appear to be conserved features of Zic factors. In many animals, they are not only regulated by the Wnt/β-catenin signaling (Satou and Imai, 2018; Vasquez-Doorman and Petersen, 2014; Gamse and Sive, 2001) but also modulate it through interactions with Tcf factors (Fujimi et al., 2012, Pourebrahim et al., 2011). Previous studies in *Hydra* (Lindgrens et al., 2004) have shown that another Zic family member (termed *HyZic*, since it was presumed to be the only Zic factor in the *Hydra* genome) is involved in nematocyte differentiation, which would be in line with the conserved role of sensory cell specification. Even though they do not possess mesodermal tissue, many of the factors, repurposed for mesoderm specification later in evolution (*brachyury*, *mef2, snail, foxA, twist*), are expressed around the oral pole of *Hydra* and other cnidarians (Technau and Steele; 2011, Technau, 2001). Thus, the involvement of *Zic4* in the *Hydra* oral end patterning is also consistent with its later recruitment for mesodermal roles alongside the genes mentioned above. Interestingly, the expression patterns of two Zic genes (*NvzicC* and *NvzicD*) of the sea anemone *Nematostella vectensis* closely resemble the expression patterns of *Zic4* and *HyZic* (Layden et al., 2010), indicating that the roles of these genes are also conserved within the cnidarian phylum.

The successful identification of *Zic4* provides motivation for further exploring the rich positional RNA-seq datasets. It would not only be interesting to further investigate the functions of other candidate target genes but also more closely inspect the spatial aspect of their regulation by Wnt. For example, many suspected direct targets (like *Tcf* or *Bra1/2*) show a simple pattern of up- or downregulation in all body positions. Other genes have divergent patterns of differential expression, suggesting more complex regulation. *Zic4* itself, although a direct target, is downregulated in the head and upregulated across all the other positions, likely due to several feedback loops active in the oral area. Yet other even more interesting cases, such as *FoxB2*, have divergent regulation connected with the axis ends (e.g. downregulation at the oral pole and upregulation at the aboral pole). Systematic investigation of these patterns, especially in combination with temporal data (i.e. positional sequencing at different time points after the addition of alsterpaullone), could allow reconstructing the connectivity and topology of genetic networks driving *Hydra* patterning downstream of the canonical Wnt signaling.

Alternatively, the positional RNA-seq datasets can be exploited in combination with the mass spectrometry imaging data. One intriguing possibility is uncovering molecules, which simultaneously have a graded distribution and a tightly restricted localization of their production enzymes, suggesting a potential role as diffusible morphogens. Similar approach can also be adopted for the previously identified morphogenetic peptides to investigate the span of their distribution in the body column. As we have also demonstrated, mass spectrometry imaging is a valuable tool to identify potential signaling molecules coupled with specific body parts or signaling pathways. We plan to functionally evaluate these molecules by treating intact and regenerating animals, as well as by performing knockdowns of the respective production/degradation enzymes. Such experiments would open the doors into the emerging field of metabo-developmental crosstalk.

Developmental processes in animals are long known to be behaving differently depending on nutrient and energy availability (Zhang et al., 2018). However, more recent work indicates that cellular metabolic status can be linked with cell differentiation and proliferation (Ly et al., 2020). Stem cells appear to be more glycolytic across different models, compared to their differentiated offspring (Cliff et al., 2017). Using the overall metabolite distribution, we could determine whether this is also true in *Hydra*, which would argue for an evolutionary ancient origin of such duality. Moreover, while certain metabolites have been already shown to act as epigenetic regulators (Gándara and Wappner, 2018) or directly interact with signaling cascades (Miyazawa and Aulehla., 2018), more are likely to be discovered. For example, the sulphonic acids mentioned above can be just byproducts of promiscuous enzymatic activity or uncharacterized signaling molecules. It is intriguing to think that these metabolites could be mediating the effects of *Sult2B* upregulation on EMT. The approaches presented here can help uncover other such factors, broadening our understanding of signals involved in tissue patterning.

Jaroslav Ferenc and Charisios Tsiairis conceived and designed the experiments

Jaroslav Ferenc performed all the experiments and analysis, except of the following contributions from other FMI members and external collaborators: RNA sequencing was performed by the FMI Genomic Facility, Panagiotis Papasaikas processed the RNA-seq data, performed the principal component analysis and projections, as well as TF binding site analysis, Jacqueline Ferralli performed the Zic4 whole-mount ISH, Iskra Katic performed siRNA electroporation, Clara Nuninger performed the BrdU staining, Hans-Rudolf Hotz processed the raw MALDI data and generated output images. The MALDI mass spectrometry imaging was performed in the laboratory of Axel Walch (Helmholtz Zentrum, Munich).

III. Material and Methods

III.1. Studying Mechanical Oscillations during Whole Body Regeneration in *Hydra* (book chapter in press)

The following manuscript is part of the book „Whole-Body Regeneration" (eds. S. Blachoud & B. Galliot) in the „Methods in Molecular Biology" series (Springer).

Authors

Jaroslav Ferenc[1, 2] and Charisios D. Tsiairis[1, 3]

Affiliations

1 – Friedrich Miescher Institute for Biomedical Research, Maulbeerstrasse 66, 4058 Basel, Switzerland
2 – University of Basel, Petersplatz 1, 4001 Basel, Switzerland
3 – Corresponding author: charisios.tsiairis@fmi.ch

Abstract

Cells of the freshwater cnidarian *Hydra* possess an exceptional regeneration ability. In small groups of these cells, organizer centers emerge spontaneously and instruct the patterning of the surrounding population into a new animal. This property makes them an excellent model system to study the general rules of self-organization. A small tissue fragment or a clump of randomly aggregated cells can form a hollow spheroid that is able to establish a body axis *de novo*. Interestingly, mechanical oscillations (inflation/deflation cycles of the spheroid) driven by osmosis accompany the successful establishment of axial polarity. Here we describe different approaches for generating *Hydra* tissue spheroids, along with imaging and image analysis techniques to investigate their mechanical behavior.

1 Introduction

Hydra is a simple freshwater animal composed of two epithelial layers, gastrodermis and epidermis, and organized along a single oral/aboral axis. Its regenerative capacities and amenability to experimental manipulation have made it a rich source of insights about regenerating missing body parts already at the dawn of modern experimental biology ***(1)***. Experiments where regeneration has been challenged, as well as transplantation experiments, have substantially shaped the theories of biological pattern formation ***(2-3)***. Importantly, *Hydra* does not only offer a platform for manipulating existing patterns but also for observing their emergence *de novo*. This was shown when cells from dissociated body columns were reaggregated and they managed to recreate functional animals in a few days ***(4-5)***. Astonishingly, unlike organoid systems, they are able do so without the external addition of signaling factors (see ***(1)*** for further comparison with organoids).

Initially, the cells in the aggregates sort to re-establish the epidermal and gastrodermal layers thus creating a symmetric hollow epithelial spheroid composed of cells whose positional identity along the main body axis is to be specified ***(6)***. After approximately 24 hours, symmetry is broken and Wnt-expressing organizing centers start to emerge. These centers guide the appearance of head structures at the oral end of the axis ***(7)***. The role of Wnt signaling as a key driver of oral identity is well established both in the homeostatic conditions and in regenerating *Hydra* ***(8-9)***. Depending on the size of the aggregates and the axial origin of dissociated tissue, one or more organizing centers can appear ***(10)***. A similar fate awaits spheroids created from small tissue fragments ***(11)***. When a small piece of the body column tissue is excised, it will fold into a hollow spheroid, visually indistinguishable from the one created from reaggreragated cells. Since all the cells have a shared identity, body poles need to be defined in this case as well. Wnt signaling centers will emerge and eventually develop into new animal heads.

Interestingly, regenerating spheroids of any origin experience cycles of inflations and deflations on the way to symmetry breaking ***(12)***. These mechanical oscillations are osmotically driven and appear to be important for proper regeneration ***(13)***. Water from the hypotonic medium is entering the cells, which pump it inside the spheroid cavity to maintain their osmotic balance ***(14)***. As a result, the whole spheroid inflates until reaching a threshold of tissue rupture. The accumulated liquid is thus released, the spheroid deflates and the cycle is repeated. During the spheroid development, the profile of oscillations changes. Initial high amplitude and low frequency oscillations (termed Phase I oscillations) eventually transition to faster cycles with lower amplitude

(Phase II oscillations). This is a hallmark of symmetry breaking and reflects the emergence of a stable mouth opening that releases the accumulated liquid under lower pressures ***(15)***.

Spheroids prepared from small tissue fragments or by single cell re-aggregation (Fig. 1) are useful to study these mechanical events during regeneration. However, one method might suit specific experimental demands better than the other. Making reaggregates is more laborious, yet offers better control of the spheroid size by using a fixed number of cells. In addition, different cell populations (e.g. expressing different fluorescent markers) can be mixed in one aggregate. Cut tissue pieces, on the other hand, preserve tissue integrity, close faster, and allow better selection of original tissue axial position. Importantly, such spheroids also retain supracellular actin myofibers, which have been recently implicated in mechanically guiding the axis emergence ***(16)***. These structures dissolve upon tissue dissociation and begin to reappear with random orientation in the aggregates. Moreover, they only seem to align and reorient after the symmetry has been broken ***(17)***. This difference thus offers an opportunity to dissect the impact of these actin structures on the tissue mechanical and biological properties.

Importantly, *Hydra* spheroids as an experimental model system do not only offer versatile starting conditions. Additional advantages include short regeneration time, simple culture conditions, amenability to imaging and experimental manipulations. Perturbing the osmolarity by adding solutes, such as sucrose or sorbitol, to the medium allows slowing down the oscillations in a concentration-dependent manner ***(13)***. Different small molecules (e.g. cytoskeleton-affecting drugs) have also been used to perturb the oscillation dynamics. For example, treatment with the Rho-kinase inhibitor Y-27632 results in a sigmoidal rather than linear inflation behavior ***(18)***. Furthermore, since similar oscillations occur in many other cyst-like structures ***(19)***, *Hydra* spheroids offer a unique system to tackle the biological significance of such phenomena. In the following protocols, we detail techniques for making *Hydra* spheroids both from cells originating from dissociated animals and cut tissue pieces (see Fig. 1). Instructions and tools for live imaging and computational extraction of basic oscillation characteristics from the acquired image data are also provided.

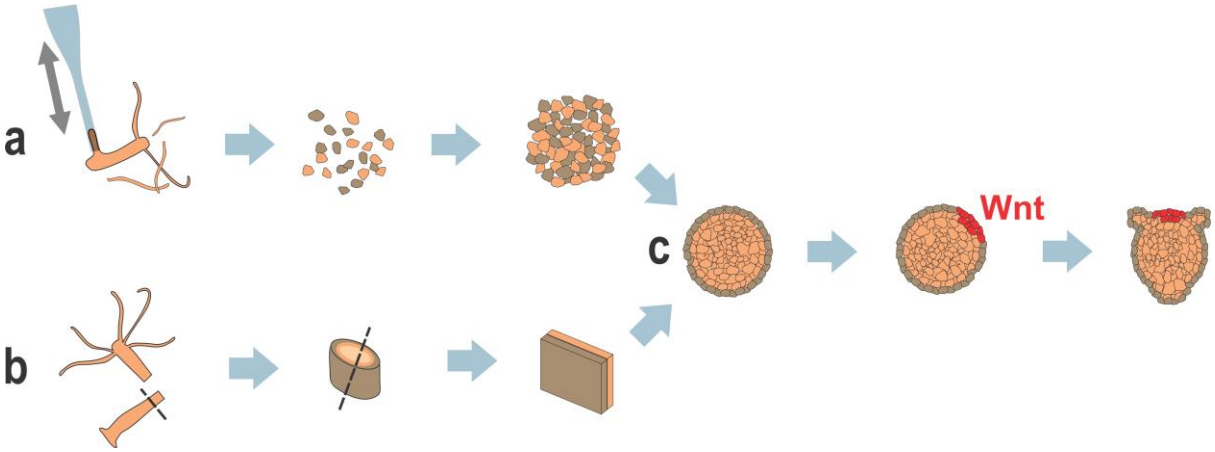

Figure 1. Overview of spheroid preparation and development. (**a**) using cut pieces as starting material, (**b**) using cells from dissociated body colums, (**c**) both methods generate spheroids that will break symmetry and regenerate into full animals.

2 Materials

Use distilled water to prepare all the solutions. If not indicated otherwise, solutions can be stored at room temperature.

2.1 Culture media and animal handling

1. M-solution: 0.1 M Tris-HCl, 0.1 M $NaHCO_3$, 0.01 M KCl, 0.01 M $MgCl_2$, pH 7.4. Filter sterilize.
2. Calcium chloride solution: 1 M $CaCl_2$. Filter sterilize.
3. *Hydra* medium: 2mL M-solution, 1mL calcium chloride solution in 1L water (*see* **Note 1**).
4. Handling pipettes: Flame the tip of Pasteur pipettes for a few seconds using a Bunsen burner to blunt the edges.
5. Agarose gel: 1 % (w/v) agarose boiled in *Hydra* medium. Can be stored for 1 – 2 weeks.
6. Imaging chamber: Multi-chamber glass-bottom imaging slides covered with 2mm of Agarose gel (*see* **Note 2**).

2.2 Cutting and dissociating animals

1. Microsurgical scalpel (e.g. MICRO FEATHER 15° or 45° ophthalmic incision scalpels, *see* **Note 3**).
2. Stereomicroscope.
3. ***Dissociation medium:*** 3.6 mM KCl, 6 mM $CaCl_2$, 1.2 mM $MgSO_4$, 6 mM sodium citrate, 6 mM sodium pyruvate, 4 mM glucose, 12.5 mM TES-HCl, pH 6.9.

Add antibiotics (0.05 g/L kanamycin, 0.1 g/L streptomycin) and filter sterilize. This solution can be stored at 4 °C for a month.

4. ***Reaggregate medium 1:*** A 1:3 mixture of Hydra medium and dissociation medium
5. ***Reaggregate medium 2:*** A 1:1 mixture of Hydra medium and dissociation medium
6. ***Reaggregate medium 3:*** A 3:1 mixture of Hydra medium and dissociation medium
7. Dissociation pipettes: Flame Pasteur pipettes to obtain a narrow opening smaller than 1 mm in diameter. This requires some practice.
8. 0.4 ml microcentrifuge tubes (e.g. APEX Scientific mini).

3 Methods

3.1 Spheroid preparation from cut tissue pieces

1. Fill the lid of a 90 mm Petri dish with *Hydra* medium.
2. Transfer a few animals into the dish using a handling pipette.
3. Orient the animals with the help of the handling pipette so that they are lying flat and wait until they relax (*see* **Note 4**).
4. Bisect the body column in 50 % of its length with a swift movement of the blade (*see* **Note 5** and **Note 6**).
5. Allow the bisected halves to relax again. The tissue immediately next to the cut should appear slightly swollen.
6. Make a second cut just below the swelling to obtain a ring of tissue (see Fig. 2A). Rings can be taken from both halves of the animal.
7. Cut the ring open.
8. Perform another cut in the middle of the resulting tissue stripe to create two pieces of equal size. (see Fig. 2B, **Note 7** and **Note 8**).
9. Transfer the pieces into a 35 mm Petri dish with *Hydra* medium (*see* **Note 9**).
10. Let them close for 2 – 2.5 hours (*see* **Note 10**).

3.2 Spheroid preparation from dissociated body tissue

1. Fill the lid of a 90 mm Petri dish with *Hydra* medium.
2. Transfer ca. 30 *Hydra* into the dish using a handling pipette.
3. Orient the animals with the help of the pipette so that they are lying flat and wait until they relax (*see* **Note 4**).
4. Cut away the heads of the animals (cut below the tentacles).

5. Cut away the feet (cut above the less pigmented zone) of the animals (*see* **Note 11**).
6. Transfer the resulting body columns into a 15 mL Falcon tube with 3 mL of dissociation medium.
7. Vortex briefly and wait until the body columns settle at the bottom of the tube.
8. Remove as much of the medium as possible.
9. Add 3 mL of dissociation medium.
10. Slowly pipette the medium in and out of a dissociation pipette (approximately 20 times) to begin dissociating the body column. Avoid introducing any bubbles. The medium should become cloudy.
11. Let the suspension sit for about 2 min to allow the sedimentation of bigger tissue pieces.
12. Carefully transfer as much of the cell suspension as possible to a new 15 mL tube without disturbing the sediment.
13. Repeat steps 9 – 12 twice with the leftover sediment. Pool all cell suspensions in one tube. You should have collected 9 – 10 mL of the cell suspension after the third round of dissociation.
14. Centrifuge the collected cell suspension for 5 min at 4 °C and 150 rcf.
15. Discard most of the supernatant (leave just enough to cover the pellet).
16. Resuspend the pellet in 3 mL of dissociation medium (*see* **Note 12**).
17. Cut the caps of the 0.4 mL microcentrifuge tubes away.
18. Fill the tubes with 400 µL of the cell suspension. Pipette the liquid slowly down the side of the tube to avoid creating bubbles. If there is a bubble at the bottom of the tube, tap the tube to release it (*see* **Note 13**).
19. Position a maximum of four 0.4 ml tubes per 50 mL Falcon tubes.
20. Centrifuge the 50 mL Falcons for 5 min at 4 °C and 150 rcf (see Fig. 2E and **Note 14**).
21. Carefully remove the microcentrifuge tubes from Falcon tubes using forceps.
22. Add a small amount of dissociation medium to overfill the tube slightly.
23. Fill a 90mm Petri dish with 40ml of dissociation medium.
24. Quickly invert the tubes upside down and place them into the dish with dissociation medium. The tubes should be standing upright with openings completely submerged in the liquid (see Fig. 2F and **Note 15**).
25. Wait 10 - 30min for the aggregates to detach from the tubes and descend into the dish (*see* **Note 16**).
26. Gently remove the microcentrifuge tubes from the Petri dish.
27. Wait 1 h and carefully transfer the aggregates the reaggregate medium 1 using a handling pipette.

28. Wait 1h and transfer the aggregates into the reaggregate medium 2
29. Wait 1 h and transfer the aggregates into the reaggregate medium 3 (*see* **Note 17** and **Note 18**).
30. Culture the aggregates in Hydra medium at 18 – 23 °C until regeneration is complete.

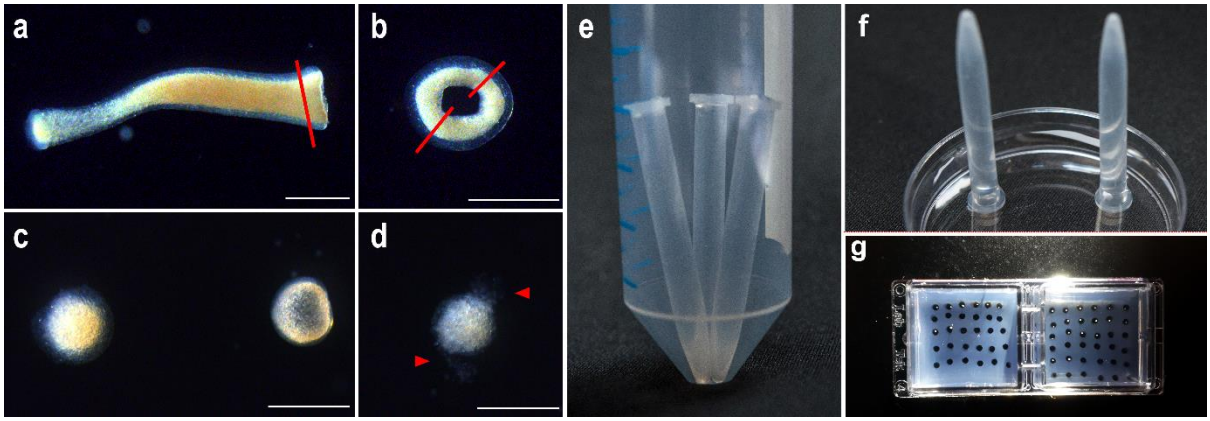

Figure 2. Critical steps in spheroid preparation protocols. (**a**) foot half of a bisected animal (note the slight tissue swelling next to the cut side), red line indicates the position of the next cut, (**b**) ring of tissue, red lines indicate the positions of cuts to prepare fragments of equal size that will give rise to spheres, (**c**) properly closed spheroids just after closing (left), and after inflation begun (right), (**d**) improperly closed spheroid releasing cells (arrowheads), (**e**) tubes with cell suspension positioned in a 50 ml falcon tube and ready for centrifugation, (**f**) tubes standing in a dish of dissociation medium before the release of aggregates, (**g**) spheroids mounted in the agarose wells in imaging chamber. All scale bars correspond to 500 µm.

3.3 Imaging

1. Boil the 1 % agarose gel (see **Note 19**).
2. Pipette the agarose to the imaging chambers. The agarose layer should cover the flat bottom of the chamber and be approximately 2 mm thick (see **Note 20**).
3. Incubate the chambers at 4 °C until the gel solidifies.
4. Create wells in the imaging chamber using a 1000 µl micropipette with the tip attached (see **Note 21**): Depress the plunger and push the tip through the agarose layer. Rotate the pipette slightly to make sure that the agarose is cut. Release the plunger to suck out the cut piece and take the tip out of the agarose. Create as many wells as necessary for the number of spheroids you intend to image (*see* **Note 22**).

5. Fill the chambers up with *Hydra* medium (*see* **Note 23**). If air becomes trapped in the wells, release the bubbles by flushing them with a stream of medium from a pipette.
6. Select properly formed spheroids (see Fig. 2C-D, **Note 24** and **Note 25**).
7. Using a handling pipette, carefully transfer spheres to individual wells in agarose (*see* **Note 26**). Take care to avoid getting the spheroids in contact with the liquid/air interface, as they will be torn apart by the surface tension. Instead of forcing the spheroids into the wells, hover them over and wait for them to descend by gravity (see Fig. 2G).
8. Cover the imaging chamber with a lid and place it on the microscope stage.
9. Image in transmitted light with an inverted microscope at temperatures below 23 °C (*see* **Note 27** and **Note 28**). Use magnification that allows fitting the whole agarose well into the field of view. Adjust the light settings so that the spheroid has good contrast against the background – the center of the spheroid will become more transparent as it inflates (see Fig. 3A).

3.3 Image segmentation and quantification of oscillation parameters

1. Load the acquired images into ImageJ and apply a coarse median filter (radius = 75 µm, *see* **Note 29**).
2. Use the Phansalkar segmentation method (radius = 65 µm, Parameter 1 and 2 = 0, parameters 1 and 2 correspond to the k and r values in the Phansalkar thresholding method, respectively ***(20)***) in "Auto Local Threshold" function (*see* **Note 30**).
3. Apply the "Fill holes" function.
4. Apply a median filter with a radius of 25 µm.
5. Visually inspect the accuracy of the segmentation (see Fig. 3B and **Note 31**). ImageJ macro for batch segmentation that follows this protocol is provided in Table 1.
6. Use the "Analyze Particles" function to measure the size of segmented objects. Include particles bigger than 5000 μm^2.
7. Load the area measurements into Matlab (*see* **Note 32**)
8. Convert the area measurement into radius according to the formula $r=(S/\pi)^{1/2}$, where S is the measured area and r is the estimated radius.
9. Normalize the radius data per sample by dividing them with the respective initial values.
10. Use the "findcollapse" function (Table 2) to detect the time and amplitude of spheroid deflations (*see* **Note 33**).
11. Use the "sphereslope" function (Table 3, *see* **Note 34**) to extract the inflation slope.

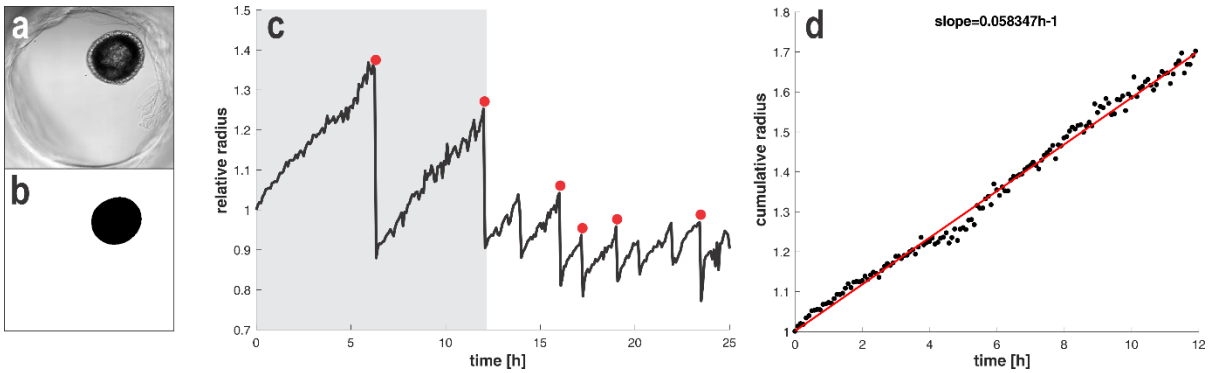

Figure 3. Imaging setup and image analysis. (a) proper imaging setup, (**b**) shows the image from (**a**) segmented using the described strategy, (**c**) example of a relative radius trace, shaded area indicates Phase I oscillations, deflation points detected by the "findcollapse" function with a threshold of 1.15 are shown as red dots, (**d**) plot generated using the "sphereslope" function for the Phase I data in **c**, black dots indicate the corrected radius (note the absence of deflation), the fitted line is shown in red.

4 Notes

1. The stock solutions should not be mixed before adding them to the water. This will cause the salts to precipitate.
2. We use Lab-Tek (Nunc) or µ-Slide (ibidi) chambers for imaging. Multiwell plates can also be used; however, they are more prone to medium evaporation. Evaporation changes the osmolarity of the medium and impacts on the characteristics of the oscillations.
3. Microsurgical blades from different manufacturers are suitable for cutting. The angle of the blade is a matter of experimenters' preference.
4. Use non-budding animals. Be consistent with the feeding status of animals used for experiments since this can influence the results. We typically use animals starved for 24 hours.
5. If reusing the scalpel, clean the blade with 70 % ethanol beforehand. The blade should be sharp and cut through the tissue effortlessly. Use a new scalpel if the blade is damaged. Cut edges that appear squeezed, or release threads of cells are an indication of a worn-out blade, too.
6. Body columns can be bisected at different levels, depending on the experimental requirements, for example to assess the influence of axial position on regeneration.
7. It is not recommended to cut the ring with a single cut. This usually creates more damage to the resulting pieces than necessary.
8. Depending on the proportions of the ring, the animal, and the desired spheroid size, adapt the number of pieces that are cut from one ring. We typically use tissue pieces with the shorter side of ~ 100 – 150 µm and the longer side of ~ 300 – 500

µm. Animals of some strains (e.g. 105) are thinner and dividing the ring into two equally sized pieces might result in spheroids that are too small to develop properly. In that case, trim the open ring to the desired size and discard the smaller piece. Similarly, thicker rings can be divided into 3 or more pieces.

9. Repeat steps 4 – 6 in section 3.1 if you want to obtain more rings/spheres from the same animal.

10. Tissue pieces from the AEP strain close better than the 105 or Basel strains. To increase the success of closing, dissociation medium can be used instead of the *Hydra* medium.

11. Steps 1 – 5 in section 3.2 can be omitted but we highly recommend cutting the differentiated parts away before starting the experiments.

12. To ensure having a single cell suspension, the resuspended cells can be passed through a cell strainer (30 µm pore size).

13. Less than 400 µL of cell suspension can be used, depending on the desired aggregate size and dissociation efficiency. Always fill up the rest of the tube with dissociation medium.

For better reproducibility among experiments, cell concentration should be determined using a counting chamber and aggregates prepared with the same number of cells. In our experience, a few thousands of epithelial cells should be used to prepare an aggregate of a final size comparable to a cut spheroid.

14. To achieve proper pellet formation, the tubes should be almost vertical during centrifugation. Different rotors might allow for such arrangements even without the use of falcon tubes as we describe here. If you want to prepare aggregates with patches of different cells (e.g. expressing two different fluorescent markers), centrifuge first the smaller population of cells, which should form the patch. Then replace the supernatant with the suspension of the other cell population and repeat the centrifugation step.

15. The liquid column inside the tubes should be continuous with the medium inside the dish. If you notice any bubbles created at the interface while positioning the tubes, remove them from the dish, add dissociation medium as in step 22 in section 3.2, and place them back into the dish.

16. Some aggregates may take longer to detach. These samples often do not develop as well as the faster detaching ones.

17. While performing steps 27 – 29 in section 3.2, you should see the cells sorting and reestablishing the epithelial layers. If you want to image cell sorting, start imaging after the transfer to reaggregate medium 2 and keep the aggregates in this solution.

18. The aggregates should stay in the reaggregate medium 3 for 1 – 2 h before starting the imaging. By this time, the epidermal and gastrodermal layers should be reestablished, which is a sign of successfully completed cell sorting. Depending on the size of the aggregates, cell type ratios, and *Hydra* strain, the sorting might take longer. In that case, we recommend prolonging the second incubation (reaggregate medium 2). The duration is best determined empirically. Ultimately, the epidermal layer should be continuous, flat and cells should not be released from spots in the surface.

19. Even though the agarose gel can be stored in a closed flask and re-melted when needed, imaging chambers with agarose should always be prepared fresh (e.g. while the spheroids are closing). This prevents the gel in the chamber from drying out and shrinking. Always change tips when pipetting warm agarose to prevent volume changes as the tip heats up.

20. It's important to compensate for the presence of agarose in the well when doing chemical treatments. Thermostable compounds (e.g. sucrose) can be added directly to the agarose. Prepare 2 % agarose in *Hydra* medium and mix it, after boiling, with an equal volume of 2x concentrated compound solution. Pipette into the chambers as described. If this approach is not feasible (e.g. for thermolabile molecules), adjust the concentration of the compound, taking the total volume of medium plus agarose into account.

21. The wells prevent the spheroids from escaping the field of view during imaging. However, they are spacious enough to allow spheroid expansion without imposing any mechanical constrains.

22. You can use a 1000 µl pipette tip or a Pasteur pipette connected to suction to punch the wells and suck out the excess agarose. Alternatively, wells can also be cast using the 200 µl tips or similar custom-made inserts. Position the inserts immediately after pouring liquid agarose into the chambers and make sure they are touching the bottom of the slide. Let the agarose solidify and release the insert afterward by carefully wiggling it out of the gel.

23. Various osmolytes (such as sucrose and sorbitol) can be used to osmotically alter the properties of the oscillations. For example, adding 30 mM sucrose approximately doubles the period of Phase I oscillations. If using sucrose or sorbitol, we recommend adding antibiotics to the medium (0.05 g/L kanamycin, 0.1 g/L streptomycin) and filter sterilizing it.

24. Properly closed cut spheroids should not be releasing threads of cells and should appear round. The typical size range varies between 300 – 500 µm in diameter. If the spheroids seem to be closing but the closure point is still visible as a furrow, extend the closing time by 30 min. If you are using *Hydra* medium for closing the

spheroids, some of them may already start inflating after the tissue closes (see Fig 2C). The success rate of closing is strain dependent. We typically observe about 70-95 % of successfully closed spheroids in *Hydra* medium for the AEP strain but a much lower percentage (50-75 %) for the 105 strain. The usual causes of unsuccessful closing include cutting with a blunt blade, damage while handling the cut pieces, and poor health of the animals.

25. Properly formed spheroids from dissociated cells should be indistinguishable from the spheroids prepared from tissue pieces. Similarly, if the aggregates appear fluffy and/or are releasing threads of cells, they should not be used for further experiments.

26. If the imaging medium is not identical with the closing medium, include an additional washing step. Put the spheroids first into a dish with the imaging medium and only then transfer them to the imaging chambers to avoid changing the composition of medium there. Alternatively, the medium in the chamber can also be exchanged after positioning all the spheres in agarose.

27. Adjust the parameters of imaging to fit your experimental needs. We routinely image for 60 hours with a time step of 10 min.

28. This setup is also useful for fluorescence imaging. The bottom half of the sphere can be imaged with good results using a confocal microscope.

29. The filter radii are given in µm to be universally applicable. However, the functions in ImageJ require values in pixels. Calculate those according to the pixel size of your image.

30. Global segmentation can also be used but this algorithm tends to outperform it in more challenging situations.

31. Common segmentation challenges include cells extruded by the spheroid, agarose pieces in the wells and uneven illumination. Depending on the specific sample, it might be possible to alleviate these issues by adjusting brightness and contrast of the image before segmentation, applying shading and background corrections, or by using trainable segmentation algorithms. It is also helpful to only perform the segmentation on the area inside of the agarose well.

32. The analysis pipeline can also be implemented in other environments using the information on the algorithm rationale in the following notes and comments within the respective Matlab functions.

33. The collapses are detected by dividing the radius values of neighboring time points. For this, the function requires specifying a threshold, which also allows adjusting the sensitivity of detection. We usually use a threshold of 1.15 for Phase I oscillations (see Fig. 3C). The amplitude is then calculated as the difference between these points when a collapse is detected.

34. This function uses the same deflation detection method as "findcollapse" and uses the amplitude values to correct for the shifts created by spheroid deflations. A straight line is then fitted to the corrected data. This allows measuring the overall slope for long periods, such as the whole Phase I duration (see Fig. 3D). To enable slope measurements for different time windows (e.g. one oscillation), the function requires the user to specify an interval for this measurement.

Tables

Table 1. Image segmentation macro that can be used for batch processing in ImageJ. Adjust the parameters to fit the pixel size of your images as described in **Note 29**.

```
run("8-bit");

run("Median...", "radius=60 stack");

run("Auto Local Threshold", "method=Phansalkar radius=50 parameter_1=0
parameter_2=0 white stack");

run("Fill Holes", "stack");

run("Median...", "radius=20 stack");
```

Table 2. The 'findcollapse' function. This function identifies deflations and outputs for each instance the time (as frame of the time course) and the amplitude (as the difference of relative radius). Inputs: rad – relative radius data as a column vector, threshold - threshold for detecting the collapse. We recommend a threshold of 1.15 for Phase I oscillations.

```
function [frame,amplitude]=findcollapse(rad,threshold)
if ~iscolumn(rad)
   error('expect rad to be a column vector');
end
amplitude = -diff(rad);
b = rad(1:end-1)./rad(2:end);
frame = (2:(length(rad)))';
frame(b <= threshold) = [];
amplitude(b <= threshold) = [];
end
```

Table 3. The 'sphereslope' function. This function extracts the slope of inflation for a specified period of the time course and plots the fit if requested. Inputs: rad - relative radius data as a column vector, threshold - threshold for detecting the collapse, tinterval - time step of imaging in minutes, frstart - defines the beginning (frame in the time course) of the measuered interval, frstop - defines the end of the measured interval, varargin - use either 'plot' or 'noplot' depending on your preferences. If nothing is specified for varargin, the default option is no plot.

```
function slope = sphereslope(rad,threshold,tinterval,frstart,frstop,varargin)
if ~isempty(varargin)
   switch varargin{1}
      case 'plot'
         gen_plot = true;
      case 'noplot'
         gen_plot = false;
      otherwise
         error('plot options are plot and noplot')
   end
else
   gen_plot = false;   % default plot option
end
if ~iscolumn(rad)
   error('expect rad to be a column vector');
end
% detecting collapses and correcting for them
a = -diff(rad);
b = rad(1:end-1)./(rad(2:end));
corrad = rad + [0;cumsum(a.*(b > threshold))];
% linear fit
time = ((0:(length(rad)-1))*(tinterval/60))';
P = polyfit(time(frstart:frstop),corrad(frstart:frstop),1);
slope = P(1);
% plot result
if gen_plot
   scatter(time(frstart:frstop),corrad(frstart:frstop),15,'k','o','filled')
   yfit = P(1)*time + P(2);
   title(['slope=',num2str(slope),'h-1'])
   ylabel('cumulative radius')
   xlabel('time [h]')
   hold on;
```

```
   plot(time(frstart:frstop),yfit(frstart:frstop),'r','LineWidth',2);
   hold off;
end
end
```


Acknowledgments

We thank Jacqueline Ferralli for useful additions to the protocols and Melinda Liu Perkins (UC Berkeley) for helpful suggestions on the Matlab functions. Our research is supported by the Novartis Research Foundation and by the Schweizerischer Nationalfonds zur Förderung der Wissenschaftlichen Forschung (grant 31003A_182674).

References

1. Vogg, M. C., Galliot, B., Tsiairis, C. D. (2019). Model systems for regeneration: Hydra. *Development*, *146*(21).
2. Wolpert, L., A. Hornbruch, M. R. B. Clarke. "Positional information and positional signalling in Hydra." *American Zoologist* 14, no. 2 (1974): 647-663.
3. Meinhardt, H. (1993). A model for pattern formation of hypostome, tentacles, and foot in hydra: how to form structures close to each other, how to form them at a distance. *Developmental biology*, *157*(2), 321-333.
4. Noda, K. (1971). Reconstitution of dissociated cells of hydra. *Zool. Mag.*, *80*, 99-101.
5. Gierer, A., Berking, S., Bode, H. et al. (1972). Regeneration of hydra from reaggregated cells. *Nature New Biology*, *239*(91), 98-101.
6. Technau, U., Holstein, T. W. (1992). Cell sorting during the regeneration of Hydra from reaggregated cells. *Developmental biology*, *151*(1), 117-127.
7. Sato, M., Sawada, Y. (1989). Regulation in the numbers of tentacles of aggregated hydra cells. *Developmental biology*, *133*(1), 119-127.
8. Hobmayer, B., Rentzsch, F., Kuhn et al. (2000). WNT signalling molecules act in axis formation in the diploblastic metazoan Hydra. *Nature*, *407*(6801), 186-189.
9. Lengfeld, T., Watanabe, H., Simakov, O. et al. (2009). Multiple Wnts are involved in Hydra organizer formation and regeneration. *Developmental biology*, *330*(1), 186-199.
10. Technau, U., von Laue, C. C., Rentzsch, F. et al. (2000). Parameters of self-organization in Hydra aggregates. *Proceedings of the National Academy of Sciences*, *97*(22), 12127-12131.
11. Bode, P. M., Bode, H. R. (1984). Formation of pattern in regenerating tissue pieces of Hydra attenuata: II. Degree of proportion regulation is less in the hypostome and tentacle zone than in the tentacles and basal disc. *Developmental biology*, *103*(2), 304-312.

12. Fütterer, C., Colombo, C., Jülicher, F. et al. (2003). Morphogenetic oscillations during symmetry breaking of regenerating Hydra vulgaris cells. *EPL (Europhysics Letters)*, *64*(1), 137.

13. Kücken, M., Soriano, J., Pullarkat, P. A. et al. (2008). An osmoregulatory basis for shape oscillations in regenerating hydra. *Biophysical journal*, *95*(2), 978-985.

14. Benos, D. J., Kirk, R. G., Barba, W. P. et al. (1977). Hyposmotic fluid formation in Hydra. *Tissue and Cell*, *9*(1), 11-22.

15. Soriano, J., Colombo, C., Ott, A. (2006). Hydra molecular network reaches criticality at the symmetry-breaking axis-defining moment. *Physical review letters*, *97*(25), 258102.

16. Livshits, A., Shani-Zerbib, L., Maroudas-Sacks, Y. et al. (2017). Structural inheritance of the actin cytoskeletal organization determines the body axis in regenerating hydra. *Cell reports*, *18*(6), 1410-1421.

17. Seybold, A., Salvenmoser, W., Hobmayer, B. (2016). Sequential development of apical-basal and planar polarities in aggregating epitheliomuscular cells of Hydra. *Developmental biology*, *412*(1), 148-159.

18. Sander, H., Pasula, A., Sander, M. et al. (2020). Highly coordinated mechanical motion mediated by the microtubule cytoskeleton is a pivotal element of de-novo symmetry breaking in hydra spheroids. *bioRxiv*.

19. Ruiz-Herrero, T., Alessandri, K., Gurchenkov, B. V. et al. (2017). Organ size control via hydraulically gated oscillations. *Development*, *144*(23), 4422-4427.

20. Phansalkar, N., More, S., Sabale, A., Joshi, M. (2011). Adaptive local thresholding for detection of nuclei in diversity stained cytology images. In *2011 International Conference on Communications and Signal Processing* (pp. 218-220). IEEE.

III.2. Additional Methods

This section contains details of experimental procedures not mentioned in sections II.1.1 and III.1. or substantially deviating from them

Live imaging of the β-catenin::GFP spheroids

Spheroids from the *AEP β-cat::GFPecto* line were prepared by cutting tissue pieces and mounted for imaging as described above. The imaging was performed using a Nikon Ti2-Eclipse spinning disk confocal microscope with a Yokogawa CSU W1 scanning unit and an iXon-Ultra 888 EMCCD camera (Andor). Toptica iBeam Smart 488 nm (500mW) laser was used for exciting the fluorophore and samples were imaged using a 20x air CFI P-Apo Lambda objective (NA=0.75, Nikon). For each sample, 9 Z-sections were acquired with a spacing of 9 µm every 10 min for a total time course duration of 60 h. The imaging chamber was kept within the temperature range of 20 – 22 °C.

Detection of nuclear B-cat spots

To automatically detect B-cat$^+$ nuclei, the maximum Z-projections were processed using the functionalities from the TrackMate plugin (Tinevez et al. 2017) in Fiji. The LoG spot detector was used (estimated blob size = 10µm, median filter =ON, subpixel localization = ON) and the false positives (autofluorescent spots in the endoderm) were filtered based on the standard deviation of intensity.

In silico prediction of potential TF binding sites in the Wnt3 promoter

The promoter sequence (1500bt upstream of transcription start site) was first soft-masked for the presence of simple mono-, di- and tri-nucleotide repeats. Putative TFBS were identified using the JASPAR2018 and TFBSTools Bioconductor packages: First the set of JASPAR2018 "CORE" frequency matrices were converted to position weight matrices (function toPWM, type="log2probratio") using a pseudocount of 4 and a flat nucleotide background. The promoter sequence was queried using the searchSeq function (min.score 90%). The results were finally filtered to remove duplicates resulting from hits on palindromic oligonucleotides. For further analysis only transcription motifs with a score ≥ 10 were considered as hits.

Selecting and testing candidate transcription factors

Transcription factors, having *bona fide* binding sites in the *Wnt3* promoter were then investigated for genetic interactions with the Wnt3 genes and other canonical Wnt signaling ligands using the data from the GeneMania databases (genemania.com). This information was further supplemented by literature mining for the same functions and known implication in mechanosensing. To identify *Hydra* homologs of these genes, we

relied on the NCBI *Hydra vulgaris* annotation (release 102) and the Hydra2.0 project annotation (research.nhgri.nih.gov/hydra/), verifying each hit by an amino acid blast search. Finally, only genes expressed in all parts of the body column in our positional RNA-seq dataset were selected for the RNAi screening. siRNA electroporation was performed as described in section II.1.1. Animals were bisected at 50 % body length 2 days after the 3rd electroporation and scored once every 24 h for the presence of tentacles as a morphological marker of head regeneration. Scoring was carried out for 5 days.

Regeneration assays and Wnt3 promoter analysis in reg-16 animals

Animals were bisected at 50% body length and let to regenerate in *Hydra* medium at 18°C, scoring the head regeneration every 24 h for 5 days. The oral halves were then grouped based on the regeneration phenotypes of corresponding aboral halves and maintained as separate cultures. After the regeneration time course ended, the genomic DNA was extracted from the aboral halves using the Blood and Tissue DNA kit (Qiagen) according to the manufacturer's instructions. The genomic segment 1500 bp upstream of the *Wnt3* transcription start site was then PCR amplified. Reaction composition: 10 ng gDNA, 0.2 mM dNTPs, 5µM forward and reverse primers, 1x Phusion HF buffer (NEB), 2U Phusion DNA polymerase (NEB). Reaction conditions: 30s - 98 °C, 40x (10s - 98 °C, 30s - 54 °C, 1 min – 72 °C), 10 min – 72 °C. The PCR products were subsequently gel purified using the QIAquick Gel Etraction Kit (Qiagen) according to the manufacturer's instructions and sent for sequencing (Microsynth). The sequencing primers (table below) were identical to PCR primers used, with an added primer in the middle of the template for improved coverage.

Primer name	Sequence 5' -> 3'
pWnt3_FWD	GCTACTGGATACCAAACCAT
pWNt3_REV	AGCAAAGTACTTACATCCAGA
pWNT3_middle	ATTGTTGGCAAAGTAGTTG

The obtained sequenced were then stitched and aligned with the genomic reference sequence (Appendix IV.1) using the GENtle software (Manske, 2006) and subjected to binding site prediction as described above for the wt sequence. The results were then compared to obtain a list of potentially affected binding sites (Appendix IV.2). For binding site gain/loss, we only considered those with a motif score of ≥10. To be considered as a hit for increased/decreased binging, we required a change of motif score of of at least ±2.

Positional RNA-sequencing of alsterpaullone-treated animals and data analysis.

Non-budding animals of the 105 strain were treated for 24 h with a 10 µM alsterpaullone solution in *Hydra* medium, then let to recover for 1 h in normal *Hydra* medium without alsterpaullone. Subsequently, the animals were sectioned and the individual pieces processed as described for the positional sequencing of control animals in II.1.1.

To obtain the parwise correlation matrices between body parts for control and alsterpaullone conditions, the average CPM values for each gene and body part were calculated and the average values used as input for the *corr* function in Matlab R2016b (function arguments: type = Pearson, rows = pairwise).

The sum of absolute log2fold differences was calculated by first adding 1 to both the control and alsterpaullone average CPM matrices. The log2fold changes in alsterpaullone conditions compared to control were then calculated and their absolute values summed per gene.

Zic4 reporter line time course with alsterpaullone

The animals of the P_{Zic4}*::GFP* reporter line were constantly incubated in 10 µM alsterpaullon solution in *Hydra* medium (or a corresponding DMSO solution) for 4 days, and imaged once every 24 h, using the Axiovert 200m fluorescence microscope (Zeiss) with a 2.5x Plan Neofluar objective (Zeiss) and the CoolSnap HQ monochrome camera (Photometrics). For imaging, living animals were mounted in a drop a medium between two coverslips, using pieces of twice folded parafilm as spacers.

Chromogenic peroxidase staining in RNAi animals

Zic4, Sp5 and double RNAi was perfomed as described in section II.1.1. After the third electroporation, animals were kept in culture for additional 7 days and fed on *Artemia* nauplii 3x during this period. At the end of this period, animals were fixed for peroxidase staining. After relaxing in 2% urethane, animals were fixed overnight at 4 °C in 4 % PFA in *Hydra* medium. The next day they were washed in PBT (PBS + 0.1 % Tween-20) for 5 min and then stained for 15 min using the following staining solution: 0.02 % diaminobenzidin, 0.25 % Triton-X, 0.03 % H_2O_2 in PBS. The chromogenic reaction was then stopped by a subsequent 15 min wash in PBT. All steps were performed at room temperature with mild agitation. Stained samples were imaged

using the Axiozoom V16 microscope (Zeiss) with the Zeiss 0.5x PlanApoZ objective (Na = 0.15) and AxioCam ICc5 camera (Zeiss).

RNA sequencing of tentacles from the RNAi animals

RNAi was perfomed as described in section II.1.1. After the third electroporation, animals were kept in culture for additional 7 days and fed on *Artemia* nauplii 3x during this period. Tentacles were harvested for sequencing at the end of this time period. For one sample, tentacles from one animal were pooled. In case of the Zic4 and Sp5 RNAi animals, tentacles of the original head were split into proximal (base) and distal halves (tips) before pooling. Tentacles of the original heads in the double knockdown, as well as tentacles of the ectopic heads were collected full, since they were too short for splitting. Corresponding control samples (full and split) were also obtained from the control GFP RNAi animals. All samples were collected in 350 µl of the RT lysis buffer (Norgen) supplemented with 1 % mercaptoethanol and frozen at – 80 °C for later RNA extraction. RNA was extracted according to the manufacturer's instructions and sequenced in house according to the procedures described in section II.1.1.

Analysis of the tentacle RNA- sequencing data

The raw RNA-sequencing reads were quality-checked and processed to obtain library-normalized counts as detailed in section II.1.1 above. To generate log2fold differences, normalized counts (CPM) were used. Zeros were eliminated by adding 1 to each indivdual value. Identical control samples were then averaged in this CPM+1 matrix and used to calculate the log2 fold change for corresponding samples: GFP tips were used as a control for Zic4 tips and Sp5 tips, GFP base as a control fro Zic4 base and Sp5 base, and GFP full as a control for Zic4/Sp5 full, Zic4/Sp5 ectopic and Sp5 ectopic.

Selection of tentacle and foot marker genes and differential analysis of their expression

The foot and tentacle specific markers were selected based on the average expression profiles in the positional RNA-seq data. Genes with low expression were first filtered out of this dataset (average CPM ≤ 200 in the body part with the lowest expression), and the remaining values normalized for each gene to the body position with its maximum expression. Then, genes with a value of 1 in tentales or foot were only retained in the dataset. The specificity for foot/tentacles was determined as a difference of the weighted sum of the remaining body parts to the investigated position. For example, for calculating tentacle specificity, the following formula would be used: $T_{specificity} = w_{tent}.CPM_{tent} – (w_{head}.CPM_{head} + w_{body1}.CPM_{body1} + … + w_{foot}.CPM_{foot})$, where *w* is the weight, assigned to each position according to the table below.

	tentacles	head	body1	body2	body3	body4	budding	foot
Tspecific	9	2	3	4	5	6	7	8
Fspecific	8	7	6	5	4	3	2	9

The weighting scheme is designed to penalize distant positions more, to avoid picking genes that have similar high expression levels in both foot and tentacles. Finally, genes with a specificity score of ≥ 5 were retained and considered marker genes for either position.

Fluorescent peroxidase staining and imaging of Zic4/Sp5 RNAi animals

Zic4/Sp5 RNAi was performed as described in section II.1.1. above. For endpoint whole mounts, animals were collected 7 days after the 3rd siRNA electroporation. For early stages of tentacle transformation, only 2 electroporations were performed and animals were collected 2 days after the second electroporation. Animals were relaxed in 2% urethane and fixed overnight in 4% PFA. For staining, the samples were first washed for 5 min in PBST (PBS + 0.1 % Tween-20) and then stained for 15 min in the staining solution containing 1x Alexa Fluor 488 Tyramide Reagent (Thermo Fisher), 0.25 % Triton-X, and 0.03 % H_2O_2 in PBS. Afterward, one quick wash with PBST was performed, followed by another 15 min PBST wash. Actin and DNA were then stained using a solution of 10 µg/ml Hoechst 33258 (Sigma Aldrich) and 200 pM Phalloidin-Atto565 (Sigma Aldrich) in PBS. After 10 min of incubation in the staining solution in the dark, 3 washes with PBST were performed. If needed, the tentacles and feet of the animals were cut and mounted between two coverslips using a ProLong Gold Antifade mounting medium (Thermo Fisher). The samples were imaged using a Nikon Ti2-Eclipse spinning disk confocal microscope with a Yokogawa CSU W1 scanning unit and an iXon-Ultra 888 EMCCD camera (Andor). Toptica iBeam Smart 405 nm (300 mW), 488 nm (500 mW), and Cobolt Jive 561 nm (200 mW) lasers were used for exciting the fluorophores. Samples were imaged using a 60x oil CFI P-Apo Lambda objective (NA=1.4, Nikon). For each sample, several Z-sections were acquired with a spacing of 2 µm, covering the visible Z range.

BrdU staining and imaging

Zic4/Sp5 RNAi animals 2 days after the second electroporation were incubated for 6 h with a freshly prepared 5 mM BrdU (Sigma Aldrich) solution in HM. After 6 washes in HM, the animals were relaxed in 2% urethane and fixed overnight in 4 % PFA. The next day, tiramide staining was performed as described above and the samples were re-fixed in 4% PFA in PBST for 2 h at 4°C and subsequently dehydrated in 100 % methanol

overnight at -20 °C. The next day, samples were rehydrated in successive washes of 75 – 50 - 25 % methanol in PBST, followed by 4 x 10 min washes with PBST and permeabilized for 1 h using 1 % Triton-X in PBS. After a 30 min incubation in 2.5 M HCl, 10 quick washes in PBST and 2 x 5 min washed in PBST, samples were incubated in a blocking solution of 2 % BSA in PBS for 1 h at RT. Incubation with the primary antibody (diluted 1:20) then followed – first, 1 h at 37 °C and then at °C overnight. After the antibody removal, two quick washes with PBST, and 4x 10 min PBST washes, the samples were incubated with 1:500 diluted secondary antibody (anti-mouse-Alexa467, abcam) for 4 h at RT. 5x 5 min PBST washes followed and the samples were then counterstained With Hoechst 33258 and mounted as described above. If not specified otherwise, all the reagents, used in this protocol, were from the BrdU labeling and detection kit (Sigma Aldrich / Roche). Imaging was also performed as described above, except for using the appropriate lasers to excite the fluorophores: Toptica iBeam Smart 405 nm (300 mW), 488 nm (500 mW), and 639 nm (500 mW).

Paraffin section preparation and MALDI imaging

Non-budding animals of the 105 strain were treated for 24 h with 10 µM alsterpaullone or a corresponding amount of DMSO in HM. Then, the animals were fixed overnight in 4 % PFA and dehydrated in the TCP 15 Duo tissue processor (Medite) using a standard setup. After paraffin embedding, 4 µm thick longitudinal sections to be used for the analysis were prepared. MALDI imaging was performed as described previously (Ly et al., 2016; Buck et al., 2015). Briefly, global metabolomic imaging was carried out on a Bruker Solarix 7 T FT-ICR MS (Bruker Daltonics), controlled by ftmsControl (v.2.2.0, Bruker Daltonics) and flexImaging (v.5.0, Bruker Daltonics). All samples were analyzed in negative ion mode over a mass range of m/z 75–1100 with a 1 M data point transient (0.367 s duration) and an estimated resolution of 49,000 at m/z 400. On-line calibration was performed using the 9-aminoacridine hydrochloride monohydrate matrix peak as reference mass. The lateral resolution was set to 15 µm. The Smartbeam-II Nd:YAG (355 nm) laser frequency was set to 1000 Hz. Metabolite distribution was visualized from the measured data using the Cardinal MSI package in R/Bioconductor.

Epilogue

Your inner *Hydra*

On account of faculty departures, I ended up directing the human anatomy course at a medical school… At first glance, you couldn't have imagined a worse candidate for the job of training the next generation of doctors: I'm a paleontologist who has spent most of his career working on fish. It turns out that being a paleontologist is a huge advantage in teaching human anatomy. Why? The best road maps to human bodies lie in the bodies of other animals. Neil Shubin

In his book, *Your Inner Fish*, Neil Shubin compares the human body to an old house that went through several renovations over the decades of its existence. A new owner, planning to do yet another remodeling, and looking at the plans of wiring and plumbing, might struggle to comprehend why it all seems so chaotic. Trying to memorize the layout of the human nervous system, a medical student might be asking very similar questions. In both cases, the *status quo* emerged by evolving over time rather than being rationally redesigned every so often. If we looked at the older house plans, we might appreciate that the weird presence of power plugs in some places and their absence in others could be explained by previous layouts of the rooms. Similarly, the explanations for sometimes absurd anatomical layouts of our own bodies, can be found in the anatomy of our ancestors. Many people have pointed out that the same is true for gene regulatory networks, signaling pathways, and other principles that guide building these bodies. While always functional, evolutionary solutions are far from always being elegant or optimal. And they are very rarely new – most of the time, evolution just combines and repurposes old solutions in fascinating new ways. Simple models, such as *Hydra*, nematodes, flies, and organoids look nothing like us, yet they have been instrumental for understanding principles used to build such complex structures as the old house of our body.

Old houses are full of surprises and there is no reason to expect that this one is any different. Who knows what can we find if we explore it using the torch of *Hydra* biology. Answers to the question of why we do not regenerate well? New ways of telling cells what we want them to do? Whatever the results, the excitement of finding out will surely be nothing short of the excitement experienced by a boy looking for treasures in the attic of his grandparents' house.

Appendices

App. 1. Alignment of *Wnt3* promoter sequences from the wild type 105 and *reg-16 Hydra* strains

The positions different between the two sequences are highlighted in yellow. Other highlighted parts of the sequence correspond to binding sites, for which there is previous functional evidence in the literature – *Tcf* (green) and *Sp5* (blue).

```
wt_105  TTATTACTAATATAACTATTATTAATCTAAAACAGTGGAATAAACATTTAGAATATTGTT
reg_16  TTATTACTAATATAACTATTATTAATCTAAAACAGTGGAATAAACATTTAGAATATTGTT

GACTTCATATTCGCCTAAAAAGCATATGTTTACATTTTTTATTAAGTAATTATCTTTGTTTGGCATTT
GACTTCATATTCGCCTAAAAAGCATATGTTTACATTTTTTATTAAGTAATTATCTTTGTTTGGCATTT

AATAATATTAAAAAGTATTCGTCACCAAAACTCTGCTTTTTCAAATTTATAAATTTATGTTAACGTTA
AATAATATTAAAAAGTATTCGTCACCAAAACTCTGCTTTTTCAAATTTATAAATTTATGTTAACGTTA

AAACAATGCATCAATGCATTGAACGTTTTTTTAATGGAAAAATTAACAATTTTGCTATCTTTATAAGT
AAACAATGCATCAATGCATTGAACGTTTTTTTAATGGAAAAATTAACAATTTTACTATCTTTATAAGT

TTGTTTAGTTTCAAGTTTTATATAATGTAGCTTGAGTGTAAAAATATTATTTGAGTCTAACAATAAAT
TTGTTTAGTTTCAAGTTTTATATAATGTAGCTTGAGTGTAAAAATATTATTTGAGTCTAACAATAAAT

CTAAAATAACTTTTTGTTGATGCTAGATTTTATACATCTTTAACAGCTATGGCGCCAAAAGAGACAGC
CTAAAATAACTTTTTGTTGATGCTAGATTTTATACATCTTTAACAGCTATGGCGCCAAAAGAGACAGC

GGGTGTTTTATTGAGCTACGCAGTTATTGTTTTTTT_AAATTCAGTCTTAATCAAATGTTAACAAATA
GGGTGTTTTATTGAGCTACGCAGTTATTGTTTTTTTTAAATTCAGTCTTTATCAAATGTTAACAAATA

AAAATCCTGATTGCATCCCAATCAGCTCATTTGGAATATGTTATGACCAACCAAATTGTTGGCAAAGT
AAAATCCTGATTGCATCCCAATCAGCTCGTTTGGAATATGTTATGACCAACCAAATTGTTGGCAAAGT

AGTTGTAAATTATGATGTCATCTTCTTATAGGAAAATGACATCAGTAAATAATCGTCAGAAAAAAACG
AGTTGTAAATTATGATGTCATCTTCTTATAGGAAAATGACATCAGTAAATAATCGTCAGAAAAAAACG

TCAGAAAACAAGTGACGTATTATAATTTTGTTTATAATATACATATATATATATAAAACTCATCGATG
TCAGAAAACAAGTGACGTATTATAATTTTGTTTATAATATACATATATATATATAAAACTCATCGATG

ACAAAACAATGACCAATAAAATATTCCTTTGATAGAGTCTCCTAATATGTTATCTTGGTAATTTGTAC
ACAAAACAATGACCAATAAAATATTCCTTTGATAGAGTCTCCTAATATGTTATCTTGGTAATTTGTAC

AATTATTTTATTAAATGTTTATCAATTAATGATAAATTTAAACTTATAGAGATATTTGCAATGTTGAT
AACTATTTTATTAAATGTTTATCAATTAATGATAAATTTAAACTTATAGAGATATTTGCAATGTTGAT

AAAAAAGATGTCGATAACATATTAACGAAATAGTATATGAATATAAACATATAATATTATCATATATA
AAAAAAGATGTCGATAACATATTAACGAAATAGTATATGAATATAAACATATAATATTATCATATATA

TTATGCACATCAAGTTTTATGTTTACTGACGTTTCCCTGCCTTCTAACTCCTACCTGCACAAAAAGCT
TTATGCACATCAAGTTTTATGTTTACTGACGTTTCCCTGCCTTCTAACTCCTACCTGCACAAAAAGCT

TGAACTTTTATATTTTTTAATTAGTATAAGCAAATAGACGTCTTAAAGTTAAATCGATACTTCTTTAA
TGAACTTTTATATTTTTTAATTAATATAAGCAAATAGACGTCTTAAAGTTAAATCGATACTTCTTTAA

AATCTTTACAAACATTACCATGTGAAATATTTGGCTTAATATATCAGAACAGCTATATCAATTTCACT
AATCTTTACAAACATTACCATGTGAAATATTTGGCTTAATATATCAGAACAGCTATATCAATTTCACT
```

GTAATTTTATCGCACTGTGCTTATTATTAGATATTCAATAACCCATTGTGAAAAGGCTTAAACCCGTT
GTAATTTTATCGCACTGTGCATATTATTAGATATTCAATAACCCATTGTGAAAAGGCTTAAACCCGTT

TTTACTTTGTTGCTTTAAAGGTTTGATTTAACTAACCGCTAATCATTATAAAAAGTTATAAATTTATA
TTTACTTTGTTGCTTTAAAGGTTTGATTTAACTAACCGCTAATCATTATAAAAAGTTATAAATTTATA

AAAATTTATCTCTGCAAAAAAAGATTTAACATTAACACAACTACTACAAAAATCTATCTCAGGATACT
AAAATTTATCTCTGCAAAAAAAGATTTAACATTAACACAACTACTACAAAAATCTATCTCAGGATACT

GTCAAAAAGTTAAACAGGTCATTAAAGTTAACTTTTGTCAAAGCGGTATCCCTATTCCAAAAGTTTCA
GTCAAAAAGTTAAACAGGTCATTAAAGTTAACTTTTGTCAAAGCGGTATCCCTATTCCAAAAGTTTCA

ACGTAACCGTGTCAATTCTTTACATAGCAAATAGAAAGGGTCACCGATTAAAGAAAATAATAAAAGGA
ACGTAACCGTGTCAATTCTTTACATAGCAAATAGAAAGGGTCACCGATTAAAGAAAATAATAAAAGGA

TTCACACGTGCTAATCGTGCGCTTTAAAGATGACTGATTGTTTCTAACTTTATTTGAAATTTCACAAG
TTCACACGTGCTAATCGTGCGCTTTAAAGATGACTGATTGTTTCTAACTTTATTTTAAATTTCACAAG

AAAAGTTTTCACA
AAAAGTTTTCACA

App. 2. Predicted transcription factor binding sites in the *Wnt3* promoter affected by the mutations found in the reg-16 strain

Data for binding sites shown in Fig. II.1.-5. Rdis TSS – relative distance from the transcription start site. Diff – difference between the motif score in the reg16 and wt strains. Shading corresponds to the colors used in the figure.

type of change	start	end	rdist TSS	score 105	score reg16	diff	strand	name
loss	740	751	-760	11.34	0.00	-11.34	+	Foxd3
loss	739	745	-761	9.03	0.00	-9.03	-	Nkx2-5
loss	488	497	-1012	11.26	0.00	-11.26	+	SREBF1
loss	488	497	-1012	12.15	0.00	-12.15	-	SREBF2
loss	444	454	-1056	10.05	0.00	-10.05	+	Arid3b
loss	958	967	-542	10.77	0.00	-10.77	-	HOXA13
gain	430	441	-1070	0.00	15.37	15.37	-	ZNF384
gain	961	971	-539	0.00	15.36	15.36	-	Arid3b
gain	647	656	-853	0.00	13.79	13.79	+	Cf2
gain	649	658	-851	0.00	13.79	13.79	+	Cf2
gain	651	660	-849	0.00	12.85	12.85	+	Cf2
gain	645	654	-855	0.00	12.43	12.43	-	Cf2
gain	245	255	-1255	0.00	11.71	11.71	-	HOXC12
gain	244	255	-1256	0.00	11.17	11.17	-	Hoxa11
gain	447	454	-1053	0.00	11.11	11.11	+	elt-3
gain	962	968	-538	0.00	11.00	11.00	-	Antp
gain	648	658	-852	0.00	10.91	10.91	+	FOXB1
gain	647	657	-853	0.00	10.91	10.91	-	FOXB1
gain	649	659	-851	0.00	10.91	10.91	-	FOXB1
gain	245	254	-1255	0.00	10.90	10.90	-	HOXD11
gain	962	969	-538	0.00	10.87	10.87	-	Ubx
gain	962	972	-538	0.00	10.47	10.47	+	Arid3b
gain	245	254	-1255	0.00	10.43	10.43	-	HOXC10
gain	962	968	-538	0.00	10.23	10.23	-	btn
gain	245	255	-1255	0.00	10.07	10.07	-	HOXC11
increase	960	967	-540	7.96	11.30	3.34	+	NKX6-1
increase	961	967	-539	9.62	12.28	2.66	+	al
increase	961	967	-539	8.21	10.85	2.64	-	CG15696-RA
increase	960	967	-540	7.69	10.27	2.59	+	NKX6-2
increase	961	967	-539	9.78	12.28	2.50	-	Lim1
increase	961	967	-539	8.51	10.93	2.42	-	ftz
increase	961	967	-539	7.49	9.82	2.32	-	H2.0
increase	961	967	-539	6.86	9.08	2.22	-	CG4328-RA
increase	959	969	-541	11.03	13.24	2.21	-	mix-a
increase	446	453	-1054	7.18	9.32	2.14	-	GATA5
increase	961	967	-539	8.10	10.16	2.06	-	NK7.1
increase	961	967	-539	9.01	11.01	2.00	-	hbn
increase	961	967	-539	9.97	11.97	2.00	-	repo
increase	961	967	-539	8.87	10.87	2.00	-	HGTX
decrease	958	967	-542	11.36	9.19	-2.17	-	Hoxd9
decrease	959	967	-541	13.30	10.84	-2.46	+	Vsx2
decrease	959	968	-541	11.37	8.81	-2.56	+	MEOX2
decrease	958	967	-542	12.48	8.86	-3.62	-	HOXD13
decrease	959	968	-541	12.13	8.31	-3.82	-	MEOX1
decrease	960	967	-540	13.18	8.45	-4.74	+	LBX1

App. 3. Genes up- and downregulated in the original tentacles upon *Zic4* and/or *Sp5* knockdown

The table below lists genes that are upregulated or downregulated at least twofold in the original tentacles across all three RNAi conditions (*Zic4*, *Sp5*, *Zic4/Sp5*). Mammalian homolog annotation is taken from the NCBI *Hydra* genome data and the *Hydra* 2.0 project.

Upregulated genes				Downregulated genes			
GeneID	Homolog	GeneID	Homolog	GeneID	Homolog	GeneID	Homolog
101239789	ABR	105850352	Pkd1l2	100203582	AAEL6169	101234549	RNF32
100210091	ACVR1	105845159	PKHD1L1	101237372	ABCA2	100203629	ROBO3
100206071	Adam12	100205568	Plk1	100199215	Adam9	100205768	Sacs
100208289	ADAMTS1	100206541	PRC1	101238755	ADGRG4	105843825	Scp2
105844515	Adamts2	100206443	Prim1	105849252	ADGRG4	101241822	SHPRH
100209499	ADCY9	100201316	Psmd1	100270692	AGRN	100208526	SLC26A11
100200794	ADGRG4	101238484	PTPN13	100197540	aguA	100200481	SLC26A11
100205679	ADGRL2	100197272	PTPRS	100215094	Ak5	100213140	Slc7a9
105844049	ADRA1A	101235051	ptrB	101236346	amiD	100197225	Snx33
105846686	AHR	100210636	rapB	100197902	Asic1	100214575	Sox14
100205450	ALOX5	101241134	RERG	100214732	At3g176	105846505	SPR
100213999	ANKLE1	105849684	Rnf213	105845013	ATF7IP	100209288	TBX3
101234454	ANKRD52	100215907	rsgI5	100212925	ATP1A1	105846236	tcmO
100213900	APX1	101241110	Sart3	101235090	Bgb	101237961	tcmO
100214165	APX1	105845326	selenon	105847444	C5AR1	100213558	TEP1
101238888	ARMC3	101237795	sens	100209768	ca2	100208566	tes
100214999	ASPM	100199160	SMAD4	100202430	ca2	100207025	THIO
105849235	azin2	100196975	SOS2	101235784	CAPN3	100198301	tmem175
100200894	C2CD5	100212484	SPAN	100208228	CASP3	100214937	TMEM65
100205167	CD163	100213985	SSUH2	100212346	CD63	100202765	TNXB
100203266	cdk1	101236263	Syt11	105844958	CDC27	100215665	TROP1
101241452	CENPE	100198801	TCNA	100210111	CENPJ	100203455	ucpB
100212386	CHS6	105850864	tdcB	100208689	CFP	100200825	vipA
100202965	CHT3	100208998	TEF	105848966	Chadl	101236687	V-RYK
105844213	cnr1a	105847586	THBS1	100200022	Chdh	101235119	ZBTB4
101236800	comA	100201190	TIC32	100206783	CHRNA1	100209117	Zcchc24
100214911	Crip1	101241044	TLN1	100209558	Cirl	105843206	ZNF25
100201765	Csgalnact1	100214927	Tmem175	100212785	COL12A1	no annotated homologs	
100197334	cyp17a1	100200954	TNC	100197108	cptp	105846402	105843613
100215560	dfa	105844854	Tnks	100213225	CTRC	100212700	105845955
105850420	dmbx1b	101235534	TOB1	101236489	CYBB	100210765	105845966
100204588	DMRT2	100200884	Tpr	100196976	cyn-5	101237147	105846001
101234551	dop-4	101237000	TRIM71	100209412	CYP4V2	100213636	100207462
105844578	dop-4	105844769	TSPAN11	105845172	DD3-3	100203936	105846077
100198376	drc7	101238520	UBE4B	105847951	DDB_G282895	101240212	101236986
105845218	DRD2	100202679	WDR17	100206697	DGCR6	105846547	100209373
101240578	drn-1	100197163	wnt11	100200072	DIRAS1	100214004	105846238
100212332	dscc1	100208923	XRCC5	105848978	Dnase1l3	100207142	100197241
100203927	E2F7	101238022	yfkN	105849343	Dnase1l3	105848240	100201931
100204327	Ercc3	no annotated homologs		100210049	dram1	100199459	105846858
100204612	Fat4	100205034	100202793	105849770	drn-1	105850037	105847004
101236336	FGF1	101234820	105846310	101237220	dut	101239931	100211379
101239906	FGF7	105844896	100202039	100200336	elovl5	100214063	105847127
105843568	FGF8	101239929	105846384	100215335	fd96Ca	105850905	100204518
100197691	FKBP5	101238258	100197942	100202133	FGFR3	100206674	105847527
105847336	Fkrp	100205589	105846997	100204239	Flnc	100201614	101238033
105844391	Frzb	100198538	100207257	100198474	foxi1	105851027	105847668
100198071	FUCTA	100204542	105847121	101238695	foxi1	105843186	100207118
101236668	FUT3	100199661	101241808	100215619	FUCTA	105843282	100202799
101237636	GABPB2	105849132	100215485	101237130	FUT8	100197524	101241836

100199858	GAD2	105850306	105847573	100198022	gelsolin	100213157	105848049
101234300	Gal3st2	100203490	100210266	105845705	GPR1	105843410	101235343
101237080	Gal3st3	101238403	105847978	100215065	Grm7	101240162	100215873
100199508	Galnt13	105843104	105848121	101237171	Grm8	105843516	105848313
100204399	Galr2	100204912	101241576	100199051	HCRTR2	100208799	105848323
100208265	gata2	100198316	101237281	101236405	Hgsnat	100198147	100210217
105847942	GFI1B	100199767	105848420	100213161	Hln	101237210	105848466
105846415	Glipr2	100213943	105848649	100214713	HMCN1	105843898	105848540
100208558	GLIPR2	105843301	105848775	100198699	Hmcn1	101241401	105848569
100212131	glul	100192232	101236532	100205154	Hmcn1	100212741	100202099
100207674	GLUL	101237499	100209978	100204780	ITPK1	100212453	105848632
105849107	GPR19	101239543	101236745	100214532	KCNA2	100208696	105848635
101239493	Gpr98	100198634	100209643	105843806	kcna2	101236602	105848636
105847599	Grm3	100198704	101236937	100210973	kcna2	100210032	100205443
100197148	Hmcn1	105843489	100205558	100210833	Kctd16	101236166	100209175
105847153	Hmcn1	100204278	100208201	100203494	KLF11	100202183	105848950
101241572	Hmcn1	101235703	105849850	101240913	kug	105844503	105848959
101237827	Hps5	105843845	101241784	105847914	Lgr5	100202839	105849386
105844459	HTR4	105843865	100200514	100212598	MAPK6	100213741	100208172
100201235	INTU	105843959	100202041	100197844	meig1	101240726	105849528
100202151	itga4	100202073	105850460	105844936	MGAT5	100213736	101234545
101238114	ITGB6	101236448	100206919	100200666	MGAT5	100215835	100207228
100202465	Kcnh6	105844432		100206688	MGAT5	100201167	105850440
100209617	KIF23	101234322		101237025	MGAT5B	100207688	
100198304	lhx5	100203288		101241127	MGAT5B	100204915	
101239718	LMX1A	100212027		101238598	MPC1	105844978	
100211539	LTA4H	101238148		100197870	nas-14	100200907	
105845876	Ltbp4	101241526		100207091	nas-15	100208937	
105845875	Ltbp4	100213623		100206128	nas-4	101238924	
105846042	Ltbp4	100202150		105844647	NCF2	101237622	
105845990	mcmbp	101238326		100212833	NCF2	100200139	
101240402	Megf6	100204479		100215618	NDB1	100201643	
100205951	MKI67	105845224		101234629	Nid2	105845369	
100200988	MMP25	100206390		100204761	NR2E1	101236026	
100215810	MUC5AC	100205981		100201578	Oat	100199435	
105844435	MYC	100204208		100203531	PANK4	100213338	
100212949	Myo1a	101236711		105851019	PAQR5	105845520	
100208067	myoM	101237124		105847287	Pigl	100206417	
100211197	Nfic	101237124		105845064	pkbA	100211831	
100201760	NIPBL	105845407		100199344	plekhf2	105845582	
105843835	Npy4r	100204611		105844596	PPP1R12A	100201803	
105843641	OPN4	105845745		100205678	Psma4	105845617	
101234579	Os4g573	100205709		100211897	RAB3B	105845756	
100199257	pan	105845815		101238409	rab6	100205676	
100214107	PKD1L2	101235710		101240509	RASL12	101235313	
100203937	Pkd1l2	100197250		105845225	RF_381	100206648	
100213839	Pkd1l2	105845995		100203825	rimK	100211650	
100208450	Pkd1l2	101239228		105846190	rnf213a	100199604	

App. 4. Functional annotation of genes from Appendix 3

The results were generated based on human datasets using GeneMania (genemania.org). The genes in Appendix 3, for which a mammalian homolog can be found, were used as an input.

Functional annotation	false discovery rate
upregulated genes	
mitotic sister chromatid segregation	2.97E-08
chromosome segregation	2.97E-08
sister chromatid segregation	2.97E-08
mitotic nuclear division	5.49E-08
nuclear chromosome segregation	7.48E-08
spindle	7.60E-07
regulation of chromosome organization	8.52952E-06
microtubule cytoskeleton organization involved in mitosis	2.49714E-05
regulation of cell division	5.97193E-05
spindle organization	0.000231363
spindle assembly	0.000610462
mitotic spindle	0.000625484
mitotic spindle organization	0.000902317
mitotic spindle assembly	0.000902317
cell cycle G1/S phase transition	0.003154902
positive regulation of cell cycle process	0.003599593
ATPase activity	0.003599593
chromosomal region	0.006798297
cell division	0.00778426
negative regulation of chromosome organization	0.008124668
chromosome separation	0.008340476
regulation of cytokinesis	0.008398615
serine/threonine protein kinase complex	0.009477784
metaphase/anaphase transition of mitotic cell cycle	0.011666994
regulation of metaphase/anaphase transition of cell cycle	0.01193788
positive regulation of cell cycle	0.01193788
metaphase/anaphase transition of cell cycle	0.013839632
regulation of mitotic sister chromatid separation	0.014130048
mitotic sister chromatid separation	0.014130048
mitotic cell cycle checkpoint	0.014538522
motor activity	0.015547708
regulation of chromosome separation	0.015722194
positive regulation of chromosome organization	0.015722194
protein kinase complex	0.015722194
regulation of sister chromatid segregation	0.018082057
negative regulation of mitotic cell cycle	0.019053153
spindle assembly checkpoint	0.019053153
negative regulation of mitotic metaphase/anaphase transition	0.019053153

mitotic spindle checkpoint	0.019053153
spindle checkpoint	0.019053153
negative regulation of mitotic cell cycle phase transition	0.020106819
negative regulation of mitotic sister chromatid separation	0.020159199
negative regulation of mitotic nuclear division	0.020159199
nuclear envelope disassembly	0.02134141
maintenance of sister chromatid cohesion	0.02134141
negative regulation of metaphase/anaphase transition of cell cycle	0.02134141
neural precursor cell proliferation	0.021568191
negative regulation of sister chromatid segregation	0.022597799
negative regulation of mitotic sister chromatid segregation	0.022597799
urogenital system development	0.022776008
negative regulation of chromosome segregation	0.023343152
regulation of protein kinase C signaling	0.023343152
establishment of chromosome localization	0.023343152
negative regulation of chromosome separation	0.023343152
cytokinesis	0.02425028
negative regulation of cell cycle phase transition	0.024986053
regulation of chromosome segregation	0.024986053
chromosome localization	0.024986053
membrane disassembly	0.025908117
protein kinase C signaling	0.025908117
negative regulation of cyclase activity	0.025908117
positive regulation of cell division	0.027445489
regulation of mitotic sister chromatid segregation	0.027445489
mitotic sister chromatid cohesion	0.030023288
angiogenesis	0.030023288
negative regulation of lyase activity	0.030023288
cyclic-nucleotide-mediated signaling	0.039834065
G2/M transition of mitotic cell cycle	0.040611279
protein localization to chromosome	0.042117104
cell cycle G2/M phase transition	0.043164619
regulation of mitotic metaphase/anaphase transition	0.043164619
negative regulation of nuclear division	0.043164619
sprouting angiogenesis	0.049971581
regulation of cell cycle G2/M phase transition	0.055300928
regulation of cell cycle G1/S phase transition	0.060088085
regulation of adenylate cyclase activity	0.063381991
cell cycle checkpoint	0.065988912
G protein-coupled receptor signaling pathway, coupled to cyclic nucleotide second messenger	0.067139651
regulation of angiogenesis	0.068309628
cellular response to ionizing radiation	0.069037328
microtubule	0.069037328
neuropeptide receptor activity	0.069037328
positive regulation of DNA biosynthetic process	0.071466766

cellular response to fibroblast growth factor stimulus	0.074984454
adrenergic receptor signaling pathway	0.074984454
lyase activity	0.074984454
metaphase plate congression	0.078891
renal system development	0.079954683
G1/S transition of mitotic cell cycle	0.081893981
cyclin-dependent protein kinase holoenzyme complex	0.082028164
cellular response to radiation	0.095161491
antigen processing and presentation via MHC class II	0.096861944
downregulated genes	
oxidoreductase activity, acting on NAD(P)H, oxygen as acceptor	0.000221423
sphingolipid transporter activity	0.005169094
phagocytic vesicle	0.006285781
antigen processing and presentation of exogenous peptide antigen via MHC class I	0.015784923
antigen processing and presentation of peptide antigen via MHC class I	0.026013825
oxidoreductase activity, acting on NAD(P)H	0.038552324
ceramide binding	0.087941024
catalytic activity, acting on a glycoprotein	0.093951241
antigen processing and presentation of exogenous peptide antigen	0.093951241
secondary lysosome	0.093951241
antigen processing and presentation of exogenous antigen	0.093951241

References

Aragona, M., Panciera, T., Manfrin, A., Giulitti, S., Michielin, F., Elvassore, N., ... & Piccolo, S. (2013). A mechanical checkpoint controls multicellular growth through YAP/TAZ regulation by actin-processing factors. *Cell*, *154*(5), 1047-1059.

Arinobu, Y., Mizuno, S. I., Chong, Y., Shigematsu, H., Iino, T., Iwasaki, H., ... & Akashi, K. (2007). Reciprocal activation of GATA-1 and PU. 1 marks initial specification of hematopoietic stem cells into myeloerythroid and myelolymphoid lineages. *Cell stem cell*, *1*(4), 416-427.

Aruga, J., & Hatayama, M. (2018). Comparative genomics of the Zic family genes. In: *Zic family*, Aruga, J. ed. 3-26.

Aulehla, A., Wiegraebe, W., Baubet, V., Wahl, M. B., Deng, C., Taketo, M., ... & Pourquié, O. (2008). A β-catenin gradient links the clock and wavefront systems in mouse embryo segmentation. *Nature cell biology*, *10*(2), 186-193.

Barkai, N., & Shilo, B. Z. (2009). Robust generation and decoding of morphogen gradients. *Cold Spring Harbor perspectives in biology*, *1*(5), a001990.

Bedzhov, I., Bialecka, M., Zielinska, A., Kosalka, J., Antonica, F., Thompson, A. J., ... & Zernicka-Goetz, M. (2015). Development of the anterior-posterior axis is a self-organizing process in the absence of maternal cues in the mouse embryo. *Cell research*, *25*(12), 1368-1371.

Benham-Pyle, B. W., Pruitt, B. L., & Nelson, W. J. (2015). Mechanical strain induces E-cadherin–dependent Yap1 and β-catenin activation to drive cell cycle entry. *Science*, *348*(6238), 1024-1027.

Benos, D. J., Kirk, R. G., Barba, W. P., & Goldner, M. M. (1977). Hyposmotic fluid formation in Hydra. *Tissue and Cell*, *9*(1), 11-22.

Bode, H. R., & Flick, K. M. (1976). Distribution and dynamics of nematocyte populations in Hydra attenuata. *Journal of cell science*, *21*(1), 15-34.

Boehm, A. M., Khalturin, K., Anton-Erxleben, F., Hemmrich, G., Klostermeier, U. C., Lopez-Quintero, J. A., ... & Bosch, T. C. (2012). FoxO is a critical regulator of stem cell maintenance in immortal Hydra. *Proceedings of the National Academy of Sciences*, *109*(48), 19697-19702.

Bosch, T. C. (2007). Why polyps regenerate and we don't: towards a cellular and molecular framework for Hydra regeneration. *Developmental biology*, *303*(2), 421-433.

Bosch, T. C., & Fujisawa, T. (2001). Polyps, peptides and patterning. *BioEssays*, *23*(5), 420-427.

Bosch, Thomas CG, Friederike Anton-Erxleben, Georg Hemmrich, and Konstantin Khalturin. "The Hydra polyp: nothing but an active stem cell community." *Development, growth & differentiation* 52, no. 1 (2010): 15-25.

Bremer, J. L. (1932). The presence and influence of two spiral streams in the heart of the chick embryo. *American Journal of Anatomy*, *49*(3), 409-440.

Brennecke, J., Aravin, A. A., Stark, A., Dus, M., Kellis, M., Sachidanandam, R., & Hannon, G. J. (2007). Discrete small RNA-generating loci as master regulators of transposon activity in Drosophila. *Cell*, *128*(6), 1089-1103.

Brinkmann, F., Mercker, M., Richter, T., & Marciniak-Czochra, A. (2018). Post-Turing tissue pattern formation: Advent of mechanochemistry. *PLoS computational biology*, *14*(7), e1006259.

Broun, M., Gee, L., Reinhardt, B., & Bode, H. R. (2005). Formation of the head organizer in hydra involves the canonical Wnt pathway.

Browne, E. N. (1909). The production of new hydranths in hydra by the insertion of small grafts. *Journal of Experimental Zoology*, *7*(1), 1-23.

Brunet, T., & King, N. (2017). The origin of animal multicellularity and cell differentiation. *Developmental cell*, *43*(2), 124-140.

Brunet, T., Bouclet, A., Ahmadi, P., Mitrossilis, D., Driquez, B., Brunet, A. C., ... & Farge, E. (2013). Evolutionary conservation of early mesoderm specification by mechanotransduction in Bilateria. *Nature communications*, *4*(1), 1-15.

Buck, A., Ly, A., Balluff, B., Sun, N., Gorzolka, K., Feuchtinger, A., ... & Walch, A. (2015). High-resolution MALDI-FT-ICR MS imaging for the analysis of metabolites from formalin-fixed, paraffin-embedded clinical tissue samples. *The Journal of pathology*, *237*(1), 123-132.

Buzgariu, W., Crescenzi, M., & Galliot, B. (2014). Robust G2 pausing of adult stem cells in Hydra. *Differentiation*, *87*(1-2), 83-99.

Caliari, S. R., Perepelyuk, M., Cosgrove, B. D., Tsai, S. J., Lee, G. Y., Mauck, R. L., ... & Burdick, J. A. (2016). Stiffening hydrogels for investigating the dynamics of hepatic stellate cell mechanotransduction during myofibroblast activation. *Scientific reports*, *6*(1), 1-10.

Camazine, S., Deneubourg, J. L., Franks, N. R., Sneyd, J., Theraula, G., & Bonabeau, E. (2020). *Self-organization in biological systems*. Princeton university press.

Campbell, R. D. (1979). Development of hydra lacking interstitial and nerve cells ("epithelial hydra"). *Determinants of spatial organization*, 267-293.

Campbell, R. D., & David, C. N. (1974). Cell cycle kinetics and development of Hydra attenuata: II. Interstitial cells. *Journal of cell science*, *16*(2), 349-358.

Cazet, J. F., Cho, A., & Juliano, C. E. (2021). Generic injuries are sufficient to induce ectopic Wnt organizers in Hydra. *Elife*, *10*, e60562.

Chan, C. J., & Hiiragi, T. (2020). Integration of luminal pressure and signalling in tissue self-organization. *Development*, *147*(5), dev181297.

Chan, C. J., Costanzo, M., Ruiz-Herrero, T., Mönke, G., Petrie, R. J., Bergert, M., ... & Hiiragi, T. (2019). Hydraulic control of mammalian embryo size and cell fate. *Nature*, *571*(7763), 112-116.

Chapman, G. B., & Tilney, L. G. (1959). Cytological studies of the nematocysts of Hydra: I. Desmonemes, isorhizas, cnidocils, and supporting structures. *The Journal of Cell Biology*, *5*(1), 69-77.

Chapman, G. B., & Tilney, L. G. (1959). Cytological studies of the nematocysts of Hydra: II. The stenoteles. *The Journal of Cell Biology*, *5*(1), 79-83.

Chapman, J. A., Kirkness, E. F., Simakov, O., Hampson, S. E., Mitros, T., Weinmaier, T., ... & Steele, R. E. (2010). The dynamic genome of Hydra. *Nature*, *464*(7288), 592-596.

Cliff, Tim S., and Stephen Dalton. "Metabolic switching and cell fate decisions: implications for pluripotency, reprogramming and development." *Current opinion in genetics & development* 46 (2017): 44-49.

Cormier, S. M., & Hessinger, D. A. (1980). Cnidocil apparatus: sensory receptor of Physalia nematocytes. *Journal of ultrastructure research*, *72*(1), 13-19.

Cox, D. N., Chao, A., & Lin, H. (2000). Piwi encodes a nucleoplasmic factor whose activity modulates the number and division rate of germline stem cells. *Development*, *127*(3), 503-514.

David, C. N. (2012). Interstitial stem cells in Hydra: multipotency and decision-making. *International Journal of Developmental Biology*, *56*(6-7-8), 489-497.

David, C. N., & Campbell, R. D. (1972). Cell Cycle Kinetics and Development of Hydra Attenuata: I. Epithelial Cells. *Journal of cell science*, *11*(2), 557-568.

David, C. N., & Gierer, A. (1974). Cell cycle kinetics and development of Hydra attenuata: III. Nerve and nematocyte differentiation. *Journal of Cell Science*, *16*(2), 359-375.

Davis, L. E. (1973). Histological and ultrastructural studies of the basal disk of Hydra. *Zeitschrift für Zellforschung und Mikroskopische Anatomie*, *139*(1), 1-27.

Dillon, R., Maini, P. K., & Othmer, H. G. (1994). Pattern formation in generalized Turing systems. *Journal of Mathematical Biology*, *32*(4), 345-393.

Dorland, Y. L., & Huveneers, S. (2017). Cell–cell junctional mechanotransduction in endothelial remodeling. *Cellular and Molecular Life Sciences*, *74*(2), 279-292.

Driever, W., & Nüsslein-Volhard, C. (1988). A gradient of bicoid protein in Drosophila embryos. *Cell*, *54*(1), 83-93.

Dübel, S., & Schaller, H. C. (1990). Terminal differentiation of ectodermal epithelial stem cells of Hydra can occur in G2 without requiring mitosis or S phase. *The Journal of cell biology*, *110*(4), 939-945.

Dumortier, J. G., Le Verge-Serandour, M., Tortorelli, A. F., Mielke, A., De Plater, L., Turlier, H., & Maître, J. L. (2019). Hydraulic fracturing and active coarsening position the lumen of the mouse blastocyst. *Science*, *365*(6452), 465-468.

Dupont, S., Morsut, L., Aragona, M., Enzo, E., Giulitti, S., Cordenonsi, M., ... & Piccolo, S. (2011). Role of YAP/TAZ in mechanotransduction. *Nature*, *474*(7350), 179-183.

Dupre, C., & Yuste, R. (2017). Non-overlapping neural networks in Hydra vulgaris. *Current Biology*, *27*(8), 1085-1097.

Durdu, S., Iskar, M., Revenu, C., Schieber, N., Kunze, A., Bork, P., ... & Gilmour, D. (2014). Luminal signalling links cell communication to tissue architecture during organogenesis. *Nature*, *515*(7525), 120-124.

Engler, A. J., Sen, S., Sweeney, H. L., & Discher, D. E. (2006). Matrix elasticity directs stem cell lineage specification. *Cell*, *126*(4), 677-689.

Fang, D., Hawke, D., Zheng, Y., Xia, Y., Meisenhelder, J., Nika, H., ... & Lu, Z. (2007). Phosphorylation of β-catenin by AKT promotes β-catenin transcriptional activity. *Journal of Biological Chemistry*, *282*(15), 11221-11229.

Fernandez-Sanchez, M. E., Barbier, S., Whitehead, J., Béalle, G., Michel, A., Latorre-Ossa, H., ... & Farge, E. (2015). Mechanical induction of the tumorigenic β-catenin pathway by tumour growth pressure. *Nature*, *523*(7558), 92-95.

Fujimi, T. J., Hatayama, M., & Aruga, J. (2012). Xenopus Zic3 controls notochord and organizer development through suppression of the Wnt/β-catenin signaling pathway. *Developmental biology*, *361*(2), 220-231.

Fujisawa, Toshitaka, and Eisuke Hayakawa. "Peptide signaling in Hydra." *International Journal of Developmental Biology* 56, no. 6-7-8 (2012): 543-550.

Fütterer, C., Colombo, C., Jülicher, F., & Ott, A. (2003). Morphogenetic oscillations during symmetry breaking of regenerating Hydra vulgaris cells. *EPL (Europhysics Letters)*, *64*(1), 137.

Galloway, J. L., Wingert, R. A., Thisse, C., Thisse, B., & Zon, L. I. (2005). Loss of gata1 but not gata2 converts erythropoiesis to myelopoiesis in zebrafish embryos. *Developmental cell*, *8*(1), 109-116.

Gamba, A., Nicodemi, M., Soriano, J., & Ott, A. (2012). Critical behavior and axis defining symmetry breaking in Hydra embryonic development. *Physical review letters*, *108*(15), 158103.

Gamse, J. T., & Sive, H. (2001). Early anteroposterior division of the presumptive neurectoderm in Xenopus. *Mechanisms of development*, *104*(1-2), 21-36.

Gándara, L., & Wappner, P. (2018). Metabo-Devo: A metabolic perspective of development. *Mechanisms of development*, *154*, 12-23.

Gartner, Z. J., & Hu, J. L. (2021). Guiding tissue-scale self-organization. *Nature Materials*, *20*(1), 2-3.

Gee, L., Hartig, J., Law, L., Wittlieb, J., Khalturin, K., Bosch, T. C., & Bode, H. R. (2010). β-catenin plays a central role in setting up the head organizer in hydra. *Developmental biology*, *340*(1), 116-124.

Geese, W. J., & Raftogianis, R. B. (2001). Biochemical characterization and tissue distribution of human SULT2B1. *Biochemical and biophysical research communications*, *288*(1), 280-289.

Geier, B., Sogin, E. M., Michellod, D., Janda, M., Kompauer, M., Spengler, B., ... & Liebeke, M. (2020). Spatial metabolomics of in situ host–microbe interactions at the micrometre scale. *Nature Microbiology*, *5*(3), 498-510.

Gierer, A., & Meinhardt, H. (1972). A theory of biological pattern formation. *Kybernetik*, *12*(1), 30-39.

Gierer, A., Berking, S., Bode, H., David, C. N., Flick, K., Hansmann, G., ... & Trenkner, E. (1972). Regeneration of hydra from reaggregated cells. *Nature New Biology*, *239*(91), 98-101.

Gomez, C., Özbudak, E. M., Wunderlich, J., Baumann, D., Lewis, J., & Pourquié, O. (2008). Control of segment number in vertebrate embryos. *Nature*, *454*(7202), 335-339.

Graf, T., & Enver, T. (2009). Forcing cells to change lineages. *Nature*, *462*(7273), 587-594.

Green, J. B., & Sharpe, J. (2015). Positional information and reaction-diffusion: two big ideas in developmental biology combine. *Development*, *142*(7), 1203-1211.

Gregor, T., Bialek, W., Van Steveninck, R. R. D. R., Tank, D. W., & Wieschaus, E. F. (2005). Diffusion and scaling during early embryonic pattern formation. *Proceedings of the National Academy of Sciences*, *102*(51), 18403-18407.

Guder, C., Pinho, S., Nacak, T. G., Schmidt, H. A., Hobmayer, B., Niehrs, C., & Holstein, T. W. (2006). An ancient Wnt-Dickkopf antagonism in hydra.

Hannezo, E., & Heisenberg, C. P. (2019). Mechanochemical feedback loops in development and disease. *Cell*, *178*(1), 12-25.

Hartl, M., Glasauer, S., Gufler, S., Raffeiner, A., Puglisi, K., Breuker, K., ... & Hobmayer, B. (2019). Differential regulation of myc homologs by Wnt/β-Catenin signaling in the early metazoan Hydra. *The FEBS journal*, *286*(12), 2295-2310.

Hausmann, K., & Holstein, T. (1985). Sensory receptor with bilateral symmetrical polarity. *Naturwissenschaften*, *72*(3), 145-147.

Heisenberg, C. P., & Bellaïche, Y. (2013). Forces in tissue morphogenesis and patterning. *Cell*, *153*(5), 948-962.

Hemelrijk, C. K., & Hildenbrandt, H. (2012). Schools of fish and flocks of birds: their shape and internal structure by self-organization. *Interface focus*, *2*(6), 726-737.

Herzog, E. L., Chai, L., & Krause, D. S. (2003). Plasticity of marrow-derived stem cells. *Blood*, *102*(10), 3483-3493.

Heyn, H., Ferreira, H. J., Bassas, L., Bonache, S., Sayols, S., Sandoval, J., ... & Larriba, S. (2012). Epigenetic disruption of the PIWI pathway in human spermatogenic disorders. *PloS one*, *7*(10), e47892.

Hiscock, T. W., & Megason, S. G. (2015). Mathematically guided approaches to distinguish models of periodic patterning. *Development*, *142*(3), 409-419.

Hobmayer, B., Rentzsch, F., Kuhn, K., Happel, C. M., von Laue, C. C., Snyder, P., ... & Holstein, T. W. (2000). WNT signalling molecules act in axis formation in the diploblastic metazoan Hydra. *Nature*, *407*(6801), 186-189.

Hobmayer, E., Holstein, T. W., & David, C. N. (1990). Tentacle morphogenesis in hydra. II. Formation of a complex between a sensory nerve cell and a battery cell. *Development*, *109*(4), 897-904.

Hoffmeister, S., & Schaller, H. C. (1985). A new biochemical marker for foot-specific cell differentiation in hydra. *Wilhelm Roux's archives of developmental biology*, *194*(8), 453-461.

Hu, K. (2019). On mammalian totipotency: What is the molecular underpinning for the totipotency of zygote?. *Stem cells and development*, *28*(14), 897-906.

Johnson, C. P., Tang, H. Y., Carag, C., Speicher, D. W., & Discher, D. E. (2007). Forced unfolding of proteins within cells. *Science*, *317*(5838), 663-666.

Juliano, C. E., Reich, A., Liu, N., Götzfried, J., Zhong, M., Uman, S., ... & Lin, H. (2014). PIWI proteins and PIWI-interacting RNAs function in Hydra somatic stem cells. *Proceedings of the National Academy of Sciences*, *111*(1), 337-342.

Kirby, T. J., & Lammerding, J. (2018). Emerging views of the nucleus as a cellular mechanosensor. *Nature cell biology*, *20*(4), 373-381.

Kishimoto, Y., Murate, M., & Sugiyama, T. (1996). Hydra regeneration from recombined ectodermal and endodermal tissue. I. Epibolic ectodermal spreading is driven by cell intercalation. *Journal of Cell Science*, *109*(4), 763-772.

Kobatake, E., & Sugiyama, T. (1989). Genetic analysis of developmental mechanisms in hydra. XIX. Stimulation of regeneration by injury in the regeneration-deficient mutant strain, reg-16. *Development*, *105*(3), 521-528.

Komekado, H., Yamamoto, H., Chiba, T., & Kikuchi, A. (2007). Glycosylation and palmitoylation of Wnt-3a are coupled to produce an active form of Wnt-3a. *Genes to Cells*, *12*(4), 521-534.

Kompauer, M., Heiles, S., & Spengler, B. (2017). Atmospheric pressure MALDI mass spectrometry imaging of tissues and cells at 1.4-µm lateral resolution. *Nature methods*, *14*(1), 90-96.

Kücken, M., Soriano, J., Pullarkat, P. A., Ott, A., & Nicola, E. M. (2008). An osmoregulatory basis for shape oscillations in regenerating hydra. *Biophysical journal*, *95*(2), 978-985.

Lagache, T., Hanson, A., Fairhall, A., & Yuste, R. (2020). Robust single neuron tracking of calcium imaging in behaving Hydra. *bioRxiv*.

Layden, M. J., Meyer, N. P., Pang, K., Seaver, E. C., & Martindale, M. Q. (2010). Expression and phylogenetic analysis of the zic gene family in the evolution and development of metazoans. *EvoDevo*, *1*(1), 1-16.

Le Thomas, A., Rogers, A. K., Webster, A., Marinov, G. K., Liao, S. E., Perkins, E. M., ... & Tóth, K. F. (2013). Piwi induces piRNA-guided transcriptional silencing and establishment of a repressive chromatin state. *Genes & development*, *27*(4), 390-399.

Lengfeld, T., Watanabe, H., Simakov, O., Lindgens, D., Gee, L., Law, L., ... & Holstein, T. W. (2009). Multiple Wnts are involved in Hydra organizer formation and regeneration. *Developmental biology*, *330*(1), 186-199.

Leost, M., Schultz, C., Link, A., Wu, Y. Z., Biernat, J., Mandelkow, E. M., ... & Meijer, L. (2000). Paullones are potent inhibitors of glycogen synthase kinase-3β and cyclin-dependent kinase 5/p25. *European journal of biochemistry*, *267*(19), 5983-5994.

Li, J., Wang, Z., Chu, Q., Jiang, K., Li, J., & Tang, N. (2018). The strength of mechanical forces determines the differentiation of alveolar epithelial cells. *Developmental cell*, *44*(3), 297-312.

Li, Z., Lee, H., & Zhu, C. (2016). Molecular mechanisms of mechanotransduction in integrin-mediated cell-matrix adhesion. *Experimental cell research*, *349*(1), 85-94.

Lim, R. S., Anand, A., Nishimiya-Fujisawa, C., Kobayashi, S., & Kai, T. (2014). Analysis of Hydra PIWI proteins and piRNAs uncover early evolutionary origins of the piRNA pathway. *Developmental biology*, *386*(1), 237-251.

Lindgens, D., Holstein, T. W., & Technau, U. (2004). Hyzic, the Hydra homolog of the zic/odd-paired gene, is involved in the early specification of the sensory nematocytes.

Livshits, A., Shani-Zerbib, L., Maroudas-Sacks, Y., Braun, E., & Keren, K. (2017). Structural inheritance of the actin cytoskeletal organization determines the body axis in regenerating hydra. *Cell reports*, *18*(6), 1410-1421.

Lo, C. M., Wang, H. B., Dembo, M., & Wang, Y. L. (2000). Cell movement is guided by the rigidity of the substrate. *Biophysical journal*, *79*(1), 144-152.

Loh, K. M., van Amerongen, R., & Nusse, R. (2016). Generating cellular diversity and spatial form: Wnt signaling and the evolution of multicellular animals. *Developmental cell*, *38*(6), 643-655.

Lohmann, J. U., & Bosch, T. C. (2000). The novel peptide HEADY specifies apical fate in a simple radially symmetric metazoan. *Genes & development*, *14*(21), 2771-2777.

Lohmann, J. U., & Bosch, T. C. (2000). The novel peptide HEADY specifies apical fate in a simple radially symmetric metazoan. *Genes & development*, *14*(21), 2771-2777.

Lu, F. I., Thisse, C., & Thisse, B. (2011). Identification and mechanism of regulation of the zebrafish dorsal determinant. *Proceedings of the National Academy of Sciences*, *108*(38), 15876-15880.

Ly, A., Buck, A., Balluff, B., Sun, N., Gorzolka, K., Feuchtinger, A., ... & Walch, A. (2016). High-mass-resolution MALDI mass spectrometry imaging of metabolites from formalin-fixed paraffin-embedded tissue. *Nature protocols*, *11*(8), 1428-1443.

Ly, C. H., Lynch, G. S., & Ryall, J. G. (2020). A metabolic roadmap for somatic stem cell fate. *Cell metabolism*, *31*(6), 1052-1067.

MacWilliams, H. K. (1982). Pattern formation in Hydra head regeneration. *American Zoologist*, *22*(1), 17-26.

MacWilliams, H. K. (1983). Hydra transplantation phenomena and the mechanism of hydra head regeneration: II. Properties of the head activation. *Developmental biology*, *96*(1), 239-257.

MacWilliams, H. K. (1983). Hydra transplantation phenomena and the mechanism of Hydra head regeneration: I. properties of the head inhibition. *Developmental biology*, *96*(1), 217-238.

Manske, M. (2006). *GENtle, a free multi-purpose molecular biology tool* (Doctoral dissertation, Universität zu Köln).

Maroudas-Sacks, Y., Garion, L., Shani-Zerbib, L., Livshits, A., Braun, E., & Keren, K. (2021). Topological defects in the nematic order of actin fibres as organization centres of Hydra morphogenesis. *Nature Physics*, *17*(2), 251-259.

Meinhardt, H. (2012). Modeling pattern formation in hydra: a route to understanding essential steps in development. *International Journal of Developmental Biology*, *56*(6-8), 447-462.

Mercker, M., Hartmann, D., & Marciniak-Czochra, A. (2013). A mechanochemical model for embryonic pattern formation: coupling tissue mechanics and morphogen expression. *PloS one*, *8*(12), e82617.

Mercker, M., Kazarnikov, A., Tursch, A., Özbek, S., Holstein, T. W., & Marciniak-Czochra, A. (2021). How Dickkopf molecules and Wnt/beta-catenin interplay to self-organise the Hydra body axis. *bioRxiv*.

Mercker, M., Köthe, A., & Marciniak-Czochra, A. (2015). Mechanochemical symmetry breaking in Hydra aggregates. *Biophysical journal*, *108*(9), 2396-2407.

Miura, T., Shiota, K., Morriss-Kay, G., & Maini, P. K. (2006). Mixed-mode pattern in Doublefoot mutant mouse limb—Turing reaction–diffusion model on a growing domain during limb development. *Journal of theoretical biology*, *240*(4), 562-573.

Miyazawa, H., & Aulehla, A. (2018). Revisiting the role of metabolism during development. *Development*, *145*(19), dev131110.

Mueller, J. F. (1950). Some observations on the structure of hydra, with particular reference to the muscular system. *Transactions of the American Microscopical Society*, *69*(2), 133-147.

Muncie, J. M., Ayad, N. M., Lakins, J. N., Xue, X., Fu, J., & Weaver, V. M. (2020). Mechanical tension promotes formation of gastrulation-like nodes and patterns mesoderm specification in human embryonic stem cells. *Developmental Cell*, *55*(6), 679-694.

Murad, R., Macias-Muñoz, A., Wong, A., Ma, X., & Mortazavi, A. (2019). Integrative analysis of Hydra head regeneration reveals activation of distal enhancer-like elements. *bioRxiv*, 544049.

Murthy, S. E., Dubin, A. E., & Patapoutian, A. (2017). Piezos thrive under pressure: mechanically activated ion channels in health and disease. *Nature reviews Molecular cell biology*, *18*(12), 771-783.

Nakamura, Y., Tsiairis, C. D., Özbek, S., & Holstein, T. W. (2011). Autoregulatory and repressive inputs localize Hydra Wnt3 to the head organizer. *Proceedings of the National Academy of Sciences*, *108*(22), 9137-9142.

Naujok, O., Lentes, J., Diekmann, U., Davenport, C., & Lenzen, S. (2014). Cytotoxicity and activation of the Wnt/beta-catenin pathway in mouse embryonic stem cells treated with four GSK3 inhibitors. *BMC research notes*, *7*(1), 1-8.

Negrete, J., & Oates, A. C. (2021). Towards a physical understanding of developmental patterning. *Nature Reviews Genetics*, 1-14.

Noda, K. (1971). Reconstitution of dissociated cells of hydra. *Zool. Mag.*, *80*, 99-101.

Nüchter, T., Benoit, M., Engel, U., Özbek, S., & Holstein, T. W. (2006). Nanosecond-scale kinetics of nematocyst discharge. *Current Biology*, *16*(9), R316-R318.

Oberlender, S. A., & Tuan, R. S. (1994). Expression and functional involvement of N-cadherin in embryonic limb chondrogenesis. *Development*, *120*(1), 177-187.

Otto, J. J., & Campbell, R. D. (1977). Budding in Hydra attenuata: bud stages and fate map. *Journal of Experimental Zoology*, *200*(3), 417-428.

Panciera, T., Azzolin, L., Cordenonsi, M., & Piccolo, S. (2017). Mechanobiology of YAP and TAZ in physiology and disease. *Nature reviews Molecular cell biology*, *18*(12), 758-770.

Peebles, F. (1897). Experimental studies on Hydra. *Archiv für Entwicklungsmechanik der Organismen*, *5*(4), 794-819.

Perruchoud, C., ... & Galliot, B. (2019). An evolutionarily-conserved Wnt3/β-catenin/Sp5 feedback loop restricts head organizer activity in Hydra. *Nature communications*, *10*(1), 1-15.

Petersen, C. P., & Reddien, P. W. (2009). Wnt signaling and the polarity of the primary body axis. *Cell*, *139*(6), 1056-1068.

Pfeifer, R., Lungarella, M., & Iida, F. (2007). Self-organization, embodiment, and biologically inspired robotics. *science*, *318*(5853), 1088-1093.

Philipp, I., Aufschnaiter, R., Özbek, S., Pontasch, S., Jenewein, M., Watanabe, H., ... & Hobmayer, B. (2009). Wnt/β-catenin and noncanonical Wnt signaling interact in tissue evagination in the simple eumetazoan Hydra. *Proceedings of the National Academy of Sciences*, *106*(11), 4290-4295.

Porcher, A., & Dostatni, N. (2010). The bicoid morphogen system. *Current biology*, *20*(5), R249-R254.

Pourebrahim, R., Houtmeyers, R., Ghogomu, S., Janssens, S., Thelie, A., Tran, H. T., ... & Tejpar, S. (2011). Transcription factor Zic2 inhibits Wnt/β-catenin protein signaling. *Journal of Biological Chemistry*, *286*(43), 37732-37740.

Priya, R., Allanki, S., Gentile, A., Mansingh, S., Uribe, V., Maischein, H. M., & Stainier, D. Y. (2020). Tension heterogeneity directs form and fate to pattern the myocardial wall. *Nature*, *588*(7836), 130-134.

Pukhlyakova, E., Aman, A. J., Elsayad, K., & Technau, U. (2018). β-Catenin–dependent mechanotransduction dates back to the common ancestor of Cnidaria and Bilateria. *Proceedings of the National Academy of Sciences*, *115*(24), 6231-6236.

Puram, S. V., & Bonni, A. (2013). Cell-intrinsic drivers of dendrite morphogenesis. *Development*, *140*(23), 4657-4671.

Ramdas, N. M., & Shivashankar, G. V. (2015). Cytoskeletal control of nuclear morphology and chromatin organization. *Journal of molecular biology*, *427*(3), 695-706.

Rentzsch, F., Guder, C., Vocke, D., Hobmayer, B., & Holstein, T. W. (2007). An ancient chordin-like gene in organizer formation of Hydra. *Proceedings of the National Academy of Sciences*, *104*(9), 3249-3254.

Rhodes, J., Hagen, A., Hsu, K., Deng, M., Liu, T. X., Look, A. T., & Kanki, J. P. (2005). Interplay of pu. 1 and gata1 determines myelo-erythroid progenitor cell fate in zebrafish. *Developmental cell*, *8*(1), 97-108.

Roberson, D. W., Alosi, J. A., & Cotanche, D. A. (2004). Direct transdifferentiation gives rise to the earliest new hair cells in regenerating avian auditory epithelium. *Journal of neuroscience research*, *78*(4), 461-471.

Roca-Cusachs, P., Gauthier, N. C., Del Rio, A., & Sheetz, M. P. (2009). Clustering of α5β1 integrins determines adhesion strength whereas αvβ3 and talin enable mechanotransduction. *Proceedings of the National Academy of Sciences*, *106*(38), 16245-16250.

Rodrigues, M., Leclère, P., Flammang, P., Hess, M. W., Salvenmoser, W., Hobmayer, B., & Ladurner, P. (2016). The cellular basis of bioadhesion of the freshwater polyp Hydra. *BMC Zoology*, *1*(1), 1-15.

Röper, J. C., Mitrossilis, D., Stirnemann, G., Waharte, F., Brito, I., Fernandez-Sanchez, M. E., ... & Farge, E. (2018). The major β-catenin/E-cadherin junctional binding site is a primary molecular mechano-transductor of differentiation in vivo. *Elife*, *7*, e33381.

Ruiz-Herrero, Teresa, Kévin Alessandri, Basile V. Gurchenkov, Pierre Nassoy, and Lakshminarayanan Mahadevan. "Organ size control via hydraulically gated oscillations." *Development* 144, no. 23 (2017): 4422-4427.

Ryan, A. Q., Chan, C. J., Graner, F., & Hiiragi, T. (2019). Lumen expansion facilitates epiblast-primitive endoderm fate specification during mouse blastocyst formation. *Developmental cell*, *51*(6), 684-697.

Sacks, P. G., & Davis, L. E. (1979). Production of nerveless Hydra attenuata by hydroxyurea treatments. *Journal of Cell Science*, *37*(1), 189-203.

Sanchez-Esteban, J., Cicchiello, L. A., Wang, Y., Tsai, S. W., Williams, L. K., Torday, J. S., & Rubin, L. P. (2001). Mechanical stretch promotes alveolar epithelial type II cell differentiation. *Journal of Applied Physiology*, *91*(2), 589-595.

Sandelin, A., Alkema, W., Engström, P., Wasserman, W. W., & Lenhard, B. (2004). JASPAR: an open-access database for eukaryotic transcription factor binding profiles. *Nucleic acids research*, *32*(suppl_1), D91-D94.

Sander, H., Pasula, A., Sander, M., Giri, V., Terriac, E., Lautenschlaeger, F., & Ott, A. (2020). Symmetry breaking and de-novo axis formation in hydra spheroids: the microtubule cytoskeleton as a pivotal element. *bioRxiv*.

Sarras Jr, M. P., Madden, M. E., Zhang, X., Gunwar, S., Huff, J. K., & Hudson, B. G. (1991). Extracellular matrix (mesoglea) of Hydra vulgaris: I. Isolation and characterization. *Developmental biology*, *148*(2), 481-494.

Satou, Y., & Imai, K. S. (2018). Ascidian Zic Genes. In: *Zic family*, Aruga, J. ed., 87-106.

Saunders, J. W. (1966). Death in embryonic systems. *Science*, *154*(3749), 604-612.

Schaller, H. C. (1973). Isolation and characterization of a low-molecular-weight substance activating head and bud formation in hydra.

Schaller, H., & Gierer, A. (1973). Distribution of the head-activating substance in hydra and its localization in membranous particles in nerve cells.

Schmidt, T., & David, C. N. (1986). Gland cells in Hydra: cell cycle kinetics and development. *Journal of cell science*, *85*(1), 197-215.

Schwarz, C., & Hadjantonakis, A. K. (2020). Cells under Tension Drive Gastrulation. *Developmental Cell*, *55*(6), 669-670.

Shahbazi, M. N. (2020). Mechanisms of human embryo development: from cell fate to tissue shape and back. *Development*, *147*(14), dev190629.

Shimizu, H. (2012). Transplantation analysis of developmental mechanisms in Hydra. *International Journal of Developmental Biology*, *56*(6-7-8), 463-472.

Sick, S., Reinker, S., Timmer, J., & Schlake, T. (2006). WNT and DKK determine hair follicle spacing through a reaction-diffusion mechanism. *Science*, *314*(5804), 1447-1450.

Siebert, S., Anton-Erxleben, F., & Bosch, T. C. (2008). Cell type complexity in the basal metazoan Hydra is maintained by both stem cell based mechanisms and transdifferentiation. *Developmental biology*, *313*(1), 13-24.

Siebert, S., Farrell, J. A., Cazet, J. F., Abeykoon, Y., Primack, A. S., Schnitzler, C. E., & Juliano, C. E. (2019). Stem cell differentiation trajectories in Hydra resolved at single-cell resolution. *Science*, *365*(6451).

Sisakhtnezhad, S., & Matin, M. M. (2012). Transdifferentiation: a cell and molecular reprogramming process. *Cell and tissue research*, *348*(3), 379-396.

Soh, R., Hardy, A., & Zur Nieden, N. I. (2021). The FOXO signaling axis displays conjoined functions in redox homeostasis and stemness. *Free Radical Biology and Medicine*.

Solnica-Krezel, L., & Sepich, D. S. (2012). Gastrulation: making and shaping germ layers. *Annual review of cell and developmental biology*, *28*, 687-717.

Soriano, J., Rüdiger, S., Pullarkat, P., & Ott, A. (2009). Mechanogenetic coupling of Hydra symmetry breaking and driven Turing instability model. *Biophysical journal*, *96*(4), 1649-1660.

Soriano, J., Rüdiger, S., Pullarkat, P., & Ott, A. (2009). Mechanogenetic coupling of Hydra symmetry breaking and driven Turing instability model. *Biophysical journal*, *96*(4), 1649-1660.

Spink, K. E., Fridman, S. G., & Weis, W. I. (2001). Molecular mechanisms of β-catenin recognition by adenomatous polyposis coli revealed by the structure of an APC–β-catenin complex. *The EMBO journal*, *20*(22), 6203-6212.

SUGIYAMA, T., & FUJISAWA, T. (1977). Genetic analysis of developmental mechanisms in hydra I. Sexual reproduction of Hydra magnipapillata and isolation of mutants. *Development, Growth & Differentiation*, *19*(3), 187-200.

Sugiyama, T., & Fujisawa, T. (1977). Genetic analysis of developmental mechanisms in hydra: III. Characterization of a regeneration deficient strain. *Development*, *42*(1), 65-77.

Sunyer, R., & Trepat, X. (2020). Durotaxis. *Current Biology*, *30*(9), R383-R387.

Tajik, A., Zhang, Y., Wei, F., Sun, J., Jia, Q., Zhou, W., ... & Wang, N. (2016). Transcription upregulation via force-induced direct stretching of chromatin. *Nature materials*, *15*(12), 1287-1296.

Teague, B. P., Guye, P., & Weiss, R. (2016). Synthetic morphogenesis. *Cold Spring Harbor perspectives in biology*, *8*(9), a023929.

Technau, U., & Steele, R. E. (2011). Evolutionary crossroads in developmental biology: Cnidaria. *Development*, *138*(8), 1447-1458.

Technau, U., von Laue, C. C., Rentzsch, F., Luft, S., Hobmayer, B., Bode, H. R., & Holstein, T. W. (2000). Parameters of self-organization in Hydra aggregates. *Proceedings of the National Academy of Sciences*, *97*(22), 12127-12131.

Thompson, D. A. W. (1917). *On growth and form*. Cambridge

Tinevez, J. Y., Perry, N., Schindelin, J., Hoopes, G. M., Reynolds, G. D., Laplantine, E., ... & Eliceiri, K. W. (2017). TrackMate: An open and extensible platform for single-particle tracking. *Methods*, *115*, 80-90.

Trembley, A. (1744). *Mémoires, pour servir à l'histoire d'un genre de polypes d'eau douce, à bras en forme de cornes* (Vol. 1). Chez Jean & Herman Verbeek.

Tsonis, P. A., Madhavan, M., Tancous, E. E., & Del Rio-Tsonis, K. (2004). A newt's eye view of lens regeneration. *International Journal of Developmental Biology*, *48*(8-9), 975-980.

Turing, A. (1952). Chemical Basis of Morphogenesis. *Philosophical Transactions Royal Society B*. *237*(641), 3-72

Uhler, C., & Shivashankar, G. V. (2017). Regulation of genome organization and gene expression by nuclear mechanotransduction. *Nature reviews Molecular cell biology*, *18*(12), 717-727.

Valenta, T., Hausmann, G., & Basler, K. (2012). The many faces and functions of β-catenin. *The EMBO journal*, *31*(12), 2714-2736.

Van Helvert, S., Storm, C., & Friedl, P. (2018). Mechanoreciprocity in cell migration. *Nature cell biology*, *20*(1), 8-20.

Vásquez-Doorman, C., & Petersen, C. P. (2014). zic-1 Expression in Planarian neoblasts after injury controls anterior pole regeneration. *PLoS genetics*, *10*(7), e1004452.

Villar, D., Flicek, P., & Odom, D. T. (2014). Evolution of transcription factor binding in metazoans—mechanisms and functional implications. *Nature Reviews Genetics*, *15*(4), 221-233.

Vining, K. H., & Mooney, D. J. (2017). Mechanical forces direct stem cell behaviour in development and regeneration. *Nature reviews Molecular cell biology*, *18*(12), 728-742.

Vogg, M. C., Beccari, L., Ollé, L. I., Rampon, C., Vriz, S., Perruchoud, C., ... & Galliot, B. (2019). An evolutionarily-conserved Wnt3/β-catenin/Sp5 feedback loop restricts head organizer activity in Hydra. *Nature communications*, *10*(1), 1-15.

Vogg, M. C., Galliot, B., & Tsiairis, C. D. (2019). Model systems for regeneration: Hydra. *Development*, *146*(21), dev177212.

Wang, H., Swore, J., Sharma, S., Szymanski, J., Yuste, R., Daniel, T., ... & Fairhall, A. L. (2020). From neuron to muscle to movement: a complete biomechanical model of Hydra contractile behaviors. *bioRxiv*.

Wang, R., Steele, R. E., & Collins, E. M. S. (2020). Wnt signaling determines body axis polarity in regenerating Hydra tissue fragments. *Developmental Biology*, *467*(1-2), 88-94.

Wartlick, O., Kicheva, A., & González-Gaitán, M. (2009). Morphogen gradient formation. *Cold Spring Harbor perspectives in biology*, *1*(3), a001255.

Watanabe, M., & Kondo, S. (2015). Is pigment patterning in fish skin determined by the Turing mechanism?. *Trends in Genetics*, *31*(2), 88-96.

Webster, G. (1966). Studies on pattern regulation in hydra: II. Factors controlling hypostome formation.

Willert, K., & Nusse, R. (2012). Wnt proteins. *Cold Spring Harbor perspectives in biology*, *4*(9), a007864.

Wilson, A., Murphy, M. J., Oskarsson, T., Kaloulis, K., Bettess, M. D., Oser, G. M., ... & Trumpp, A. (2004). c-Myc controls the balance between hematopoietic stem cell self-renewal and differentiation. *Genes & development*, *18*(22), 2747-2763.

Wittlieb, J., Khalturin, K., Lohmann, J. U., Anton-Erxleben, F., & Bosch, T. C. (2006). Transgenic Hydra allow in vivo tracking of individual stem cells during morphogenesis. *Proceedings of the National Academy of Sciences*, *103*(16), 6208-6211.

Wolpert, L. (1969). Positional information and the spatial pattern of cellular differentiation. *Journal of theoretical biology*, *25*(1), 1-47.

Wolpert, L., Hornbruch, A., & Clarke, M. R. B. (1974). Positional information and positional signalling in Hydra. *American Zoologist*, *14*(2), 647-663.

Yang, Q., Xue, S. L., Chan, C. J., Rempfler, M., Vischi, D., Maurer-Gutierrez, F., ... & Liberali, P. (2021). Cell fate coordinates mechano-osmotic forces in intestinal crypt formation. *Nature Cell Biology*, 1-12.

Yang, X., Du, X., Sun, L., Zhao, X., Zhu, J., Li, G., ... & Wang, Z. (2019). SULT2B1b promotes epithelial-mesenchymal transition through activation of the β-catenin/MMP7 pathway in hepatocytes. *Biochemical and biophysical research communications*, *510*(4), 495-500.

Yao, T. (1945). Studies on the organizer problem in Pelmatohydra oligactis: I. The induction potency of the implants and the nature of the induced hydranth. *Journal of Experimental Biology*, *21*(3-4), 147-150.

Yost, C., Torres, M., Miller, J. R., Huang, E., Kimelman, D., & Moon, R. T. (1996). The axis-inducing activity, stability, and subcellular distribution of beta-catenin is regulated in Xenopus embryos by glycogen synthase kinase 3. *Genes & development*, *10*(12), 1443-1454.

Zhang, J., Zhao, J., Dahan, P., Lu, V., Zhang, C., Li, H., & Teitell, M. A. (2018). Metabolism in pluripotent stem cells and early mammalian development. *Cell metabolism*, *27*(2), 332-338.

Zhu, M., & Zernicka-Goetz, M. (2020). Principles of Self-Organization of the Mammalian Embryo. *Cell*, *183*(6), 1467-1478.Vogg, M. C., Beccari, L., Ollé, L. I., Rampon, C., Vriz, S.,

Zuzarte-Luis, V., & Hurle, J. M. (2004). Programmed cell death in the developing limb. *International Journal of Developmental Biology*, *46*(7), 871-876.

Abbreviations

AP	alsterpaullone
B1 – B4 (or 1 – 4)	body1 – body 4
Bd (or B)	budding zone
BrdU	5-bromo-2′-deoxyuridine
CPM	counts per million
DM	dissociation medium
EMT	epithelial to mesenchymal transition
F	foot
FFPE	formalin-fixed paraffin-embedded
FGF	fibroblast growth factor
FISH	fluorescent *in situ* hybridization
GFP	green fluorescent protein
GM model	Gierer-Meinhardt model
H	head
H&E	hematoxylin and eosin staining
HM	*Hydra* medium
i-cells	interstitial cells
ISH	*in situ* hybridization
MALDI	matrix-assisted laser desorption/ionization
MSI	mass spectrometry imaging
N	number of independent experimental replicates or number of objects in a plot
n	number of samples or technical replicates
NA	numerical aperture
PBS	phosphate-buffered saline
perox	peroxidase
PFA	paraformaldehyde
RD	reaction-diffusion
RNAi	RNA interference
RNA-seq	RNA sequencing
RT	room temperature
SD	standard deviation
siRNA	small interfering RNA
SSC	saline-sodium citrate buffer
suc	sucrose
T	tentacles
TES	2-{[1,3-Dihydroxy-2-(hydroxymethyl)propan-2-yl]amino}ethane-1-sulfonic acid
TF	transcription factor
β-cat	β-catenin

Curriculum vitae // Jaroslav Ferenc

Research Experience

2016 – 2022	**Ph.D. student – Tsiairis lab | FMI Basel (CH**) Self-organization, patterning, and tissue mechanics in *Hydra*
2014 – 2016	**MSc student – Tomaska lab | Comenius University (SK)** Telomeres as potential oxidative stress sensors
7/2013 – 9/2013	**Research intern – Bollenbach lab | IST Austria (AT)** Gene expression dynamics during interspecific bacterial interactions
2011 – 2014	**Research intern – Tomaska lab (Comenius University)** Extranuclear functions of mammalian telomerase

Education

2016 – 2022	**Ph.D. in Molecular Biology** *summa cum laude* FMI Basel / University of Basel Thesis: Dynamics of Tissue Patterning in *Hydra*
7/2019 – 8/2019	**Santa Barbara Advanced School of Quantitative Biology** Kavli Institute for Theoretical Physics / UC Santa Barbara (USA)
2014 – 2016	**MSc in Genetics** *with distinction* Comenius University in Bratislava Thesis: Nucleomitochondrial Communication in *Saccharomyces cerevisiae* via Telomeres
2011 – 2014	**BSc in General Biology** *with distinction* Comenius University in Bratislava Thesis: Evolutionary Biochemistry

Selected Awards

2021	EIPOD fellowship for postdoctoral research at EMBL Heidelberg
2016	Outstanding Master Thesis Award
2014	Talents of the New Europe grant for young scientists and artists
2014	Ministry of Education Scholarship
2014	Award of the Chancellor of Comenius University
2011	International Sustainable World Project Olympiad, silver medal
2010	European Union Contest for Young Scientists, special prize
2010	Int. Environment and Sustainability Olympiad, gold medal

TEACHING & OTHER ACTIVITIES

2019 – 2021	**Introduction to Biology course (University of Basel)** Tutoring a group of undergraduate students
2012 – present	**General Biology course (Comenius University)** Guest lecture on principles of self-organization
2018, 2021	**International Biology Olympiad** Jury member
2011 – present	**Slovak Biology Olympiad** Jury member and tasks author

PUBLICATIONS

Ferenc, J., & Tsiairis, C. D. (2022).
Studying Mechanical Oscillations during Whole Body Regeneration in Hydra.
In *Whole-Body Regeneration*, B. Galliot, S. Blanchoud, eds.
(Methods in Molecular Biology, Springer), *in press*

Misailidis, G., Ferenc, J., & Tsiairis, C. D. (2022).
Self-organization of tissues through biochemical and mechanical signals.
In *Modeling of Biomaterials* (Springer), Malek, J., Suli, E. eds., *in press*

Ferenc, J., Papasaikas, P., Ferralli, J., Nakamura, Y., Smallwood, S., & Tsiairis, C. D. (2021).
Mechanical oscillations orchestrate axial patterning through Wnt activation in Hydra. *Science Advances*, 7(50), eabj6897.

Vogg, M. C., Ferenc, J., Buzgariu, W. C., Perruchoud, C., ... & Tsiairis, C. D. (2021).
The transcription factor Zic4 acts as a transdifferentiation switch.
bioRxiv. https://www.biorxiv.org/content/10.1101/2021.12.22.473838v1.full.pdf

Ferenc, J.,* Červenák, F.,* Birčák, E.,* ... & Tomáška, Ľ. (2018).
Intentionally flawed manuscripts as means for teaching students to critically evaluate scientific papers.
Biochemistry and Molecular Biology Education, 46(1), 22-30.

Simonicova, L., Dudekova, H., Ferenc, J., ... & Tomaska, L. (2015).
Saccharomyces cerevisiae as a model for the study of extranuclear functions of mammalian telomerase. *Current genetics*, 61(4), 517-527.